ABSTRACT

Title of Dissertation: EXPERIMENTAL AND COUPLED CFD/CSD INVESTIGATION OF FLEXIBLE MAV-SCALE FLAPPING WINGS IN HOVER

James Lamel Lankford
Doctor of Philosophy, 2018

Dissertation directed by: Dr. Inderjit Chopra
Department of Aerospace Engineering

Due to their potential to expand our sensing and mission capabilities in both military and civilian applications, micro air vehicles (MAVs) have recently gained increased recognition. However, man-made MAVs have struggled to meet the aerodynamic performance and maneuvering capabilities of biological flapping wing flyers (small birds and insects) which operate at MAV-scales (Reynolds numbers on the order of 10^3–10^4). Several past studies have focused on developing and analyzing flapping-wing MAV designs due to the possibility of achieving the increased lift, performance and flight capabilities seen in biological flapping wing flyers. However, there are still a lack of baseline design principles to follow when constructing a flexible flapping wing for a given set of wing kinematics, target lift values, mission capabilities,

etc. This is due to the limited understanding of the complex, unsteady flow and aeroelastic effects intrinsic to flexible flapping wings.

In the current research, a computational fluid dynamics (CFD) solver was coupled with a computational structural dynamics (CSD) solver to simulate the aerodynamics and inherent aeroelastic effects of a flexible flapping wing in hover. The coupled aeroelastic solver was validated against experimental test data to assess the predictive capability of the coupled solver. The predicted and experimental results showed good correlation over several different test cases. Experimental tests included particle image velocimetry (PIV) measurements, instantaneous aerodynamic force measurements and dynamic wing deformation recordings via a motion capture system. The aeroelastic solver was able to adequately predict the process of leading edge vortex (LEV) formation and shedding observed during experimentation. Additionally, the instantaneous lift and drag force-time histories as well as passive wing deformations agreed satisfactorily with the experimental measurements.

The coupled CFD/CSD solver was used to determine how varied wing structural compliance influences aerodynamic force production, temporal and spatial evolution of the flowfield and overall wing performance. Results showed that for the wings tested, decreasing wing stiffness, especially toward the wing root, increased the time-averaged aerodynamic lift with minimal effect on drag. This is primarily due to prolonged sustainment of the LEVs produced during flapping and suggests that aeroelastic tailoring of flapping wings could improve performance.

EXPERIMENTAL AND COUPLED CFD/CSD INVESTIGATION OF FLEXIBLE MAV-SCALE FLAPPING WINGS IN HOVER

by

James Lamel Lankford

Dissertation submitted to the Faculty of the Graduate School of the
University of Maryland, College Park, in partial fulfillment
of the requirements for the degree of
Doctor of Philosophy
2018

Advisory Committee:
Dr. Inderjit Chopra, Chair/Advisor
Dr. James D. Baeder
Dr. Anubhav Datta
Dr. Darryll J. Pines
Dr. Balakumar Balachandran

To my wife, parents, brother and sister

Acknowledgements

Pursing my PhD has been one of the most challenging and most rewarding experiences of my life and I want to thank God for helping me through it all. I'm also certain that I wouldn't have been able to complete this journey without the support and encouragement from a number of people. First, I'd like to sincerely thank my adviser Dr. Inderjit Chopra for taking me on as one of his students. Under his guidance I've grown to become a better engineer and truly appreciate all he's done in furthering my professional development as a research scientist. I also want to thank my committee members Dr. James Baeder, Dr. Darryll J. Pines, Dr. Anubhav Datta and Dr. Balakumar Balachandran for their guidance and mentorship throughout this process. I'd also like to thank Dr. James E. Hubbard and Dr. Anya Jones for their assistance during my PhD journey.

I want to acknowledge and express gratitude to the Micro Autonomous Systems and Collaborative Technology Alliance (MAST-CTA) for their support of this research. I also want to thank the ARCS Metro Washington Chapter and the Lockheed-Martin Corporation for their help in funding my academic studies.

I want to give a special thanks to all my friends and colleagues in the rotorcraft center. In particular, I wish to thank Elizabeth, Will, Elena, Dan and Stacey for making my time in the rotorcraft center that much more enjoyable. I especially want to thank Dr. David Mayo for being a great friend and mentor. His work ethic and positive attitude toward his work left a lasting influence on me and I attribute a lot of my early success in graduate school to having worked with him. I'm also grateful for my friends

Helene and Abbey. Your conversations really helped motivate me through the last leg of this journey and I'm glad I had a chance to meet you two.

I must graciously thank my wife Bianca Lankford for supporting me throughout this entire process. The sacrifice, encouragement and continued love she provided was truly a blessing. I also want to thank my parents (James and Myrthlyn Lankford) as well as my brother Darryl and sister Shanique for their understanding, patience and support while I was working toward my PhD. Lastly, I want to sincerely thank my friends Justin Harper and Justin Smith for their support and inspiration during my academic career and making sure I always keep things in perspective.

Table of Contents

List of Tables

List of Figures

Nomenclature

AR	Wing aspect ratio, $AR = b / \bar{c}$
C_D	Drag coefficient
C_L	Lift coefficient
D	Drag
D_{plate}	Isotropic plate bending coefficient, $D_{plate} = Eh^3/[12(1-\nu^2)]$
E	Young's modulus
L	Lift
L/D	Lift-to-Drag Ratio
L/P	Power Loading
P	Power
S	Wing planform area
T	Period of a flap cycle
V_{tip}	Wing tip velocity
b	Wing span
$\bar{c}$	Wing mean chord
f	Flap frequency (in Hz)
h	Wing thickness
r	Radial position along the span
t	Time
u,v,w	Flow velocity in x,y,z directions respectively

Γ	Circulation
Π_1	Aeroelastic scaling parameter
Ω	Flap frequency (in rad/s)
ν	Poisson's ratio
π_1	Natural frequency-based aeroelastic scaling parameter

ϕ	Flap angle
ϕ_{amp}	Flap amplitude
ω	Vorticity
ω_n	Natural frequency (in rad/s)

List of Abbreviations

1D	One Dimensional
2D	Two Dimensional
3D	Three Dimensional
CAD	Computer-Aided Design
CFD	Computational Fluid Dynamics
CSD	Computational Structural Dynamics
DIC	Digital Image Correlation
GTOW	Gross Take Off Weight
IDW	Inverse Distance Weighting
LEV	Leading Edge Vortex
MAV	Micro Air Vehicle
PIV	Particle Image Velocimetry
RANS	Reynolds-Averaged Navier-Stokes

Chapter 1 Introduction

1.1 Motivation for the Development of Micro Air Vehicles (MAVs)

Within both the military and civilian sectors, there is an increasing demand for the use of unmanned aircraft. Unmanned aerial vehicles (UAVs) offer a wide range of mission profile capabilities with reduced operational cost and minimized safety risks because a pilot is not needed in the vehicle for operation. Powered UAVs were initially developed and tested in the early 1900s [1] mainly for military use. Over time as the technology matured, their use became more widespread within military operations. Notable current UAVs include the MQ-1 *Predator* developed by General Atomics [2] as well as the Northrop Grumman RQ-4 *Global Hawk* [3] and MQ-8 *Fire Scout* [4]. Figs. 1.1 – 1.3 provide images of these UAVs.

Figure 1.1: General Atomics MQ-1 *Predator*

Figure 1.2: Northrop Grumman RQ-4 *Global Hawk*


Figure 1.3: MQ-8 *Fire Scout*

Applications for UAVs in the military sector include reconnaissance and intelligence gathering as well as precision missile strike missions. The absence of a pilot allows for increased flight endurance because the flight time is no longer limited to the physical capabilities of the pilot. UAVs are also more readily utilized in high-risk environments because there is no risk of injury or loss of life to the pilot. However, widespread use of UAVs in both military and civilian sectors has been limited due to the high cost of the vehicles. For example, in 2013 the RQ-4 *Global Hawk* cost approximately $131 million per vehicle and that cost rises to $222 million per vehicle when including research and development costs [5].

The aforementioned UAVs are equivalent in size to full-scale piloted aircraft, which is partly responsible for the relatively high cost of the vehicles. Over recent decades, the continual decrease in the size, robustness and price of electronic devices has resulted in a surge of interest in the development of smaller unmanned micro air vehicles (MAVs). The Defense Advanced Research Projects Agency (DARPA) issued a challenge in 1997 that called for the development of a vehicle with no dimension greater than 15 cm (6 inches), a gross takeoff weight not exceeding 100 grams and a flight endurance of 60 minutes [6]. The dimension and weight requirements from the 1997 DARPA challenge are what many in the aerospace field use to define the MAV class of aircraft. However, over time this definition has become more relaxed and many of the aircraft described as MAVs have weights or dimensions greater or less than those specified in the challenge. In general, MAVs are small, lightweight flying platforms which, due to their size, are maneuverable in confined environments and easily portable such that they can be carried by a single person. Given their small size, MAVs are relatively inexpensive to manufacture and operate making them beneficial for a number of emerging mission roles.

Regarding military and law enforcement applications, MAVs can be used for reconnaissance missions providing increased situational awareness for soldiers in the field. MAVs can also be used in search and rescue missions to aid in finding people trapped in confined or highly inaccessible areas such as mines, caves, tunnel systems, etc. Additional military/law enforcement mission profiles include border/perimeter patrol as well as crowd monitoring at large public events.

In the civilian sector, MAVs may be used for the monitoring and inspection of large infrastructure including bridges, pipelines and powerlines [7,8]. They can also aid in the agricultural sector by monitoring crop yields over vast acres of land which would save farmers both time and money [9]. In disaster relief efforts, MAVs can be used to explore areas which may be inaccessible or hazardous for people to explore. For example, MAVs were used to explore areas affected during the Fukushima Daiichi nuclear power plant disaster [10]. The high levels of radiation in the area make it extremely difficult and dangerous for humans to directly investigate. However, MAVs can be used to assess the damage of the nuclear reactors at the site and provide investigators vital information in the effort of decommissioning the power plant.

The market for vehicles capable of meeting many of the missions discussed has steadily been increasing. This has led to the creation of numerous MAVs with varied configurations and attributes. As interest and technological potential for the widespread use of micro air vehicles continues to grow, it has become increasingly imperative to be able to assess the performance and efficiency of a given MAV design and determine if it can meet the requirements of a given mission profile.

1.2 Fixed-wing MAVs

Fixed-wing MAVs are the most technologically mature of the types of MAV configurations under discussion. A major benefit of fixed-wing designs is that they are relatively simplistic. They typically have very few moving parts to achieve powered, controllable flight. The main powered components are normally the propulsion system and actuators for control surfaces. Fixed-wing MAVs currently claim some of the

highest flight times and cruise speeds in their class. Also, fixed-wing MAV designs demonstrate higher aerodynamic efficiency characteristics in comparison to other MAV configurations. A drawback of fixed-wing MAV configurations is that they are not able to hover and must maintain a degree of forward speed to remain in flight. This significantly limits their use in confined spaces where operating at low-speeds and maintaining maneuverability is important.

An example of one of the earliest, sophisticated fixed-wing MAV designs is the *Black Widow* developed by AeroVironment [11]. A picture of the Black Widow can be seen in Fig. 1.4. The *Black Widow* was designed using a multidisciplinary design optimization paired with a genetic algorithm to optimize the design of the aircraft. The vehicle has a gross takeoff weight of 80 grams, wing span of 15.24 cm (6 inches), a flight endurance of 30 minutes and top speed of 13.4 $m\text{-}s^{-1}$ (30 mph). A video camera is attached to the MAV to provide real-time color video to the pilot to aid in operation of the vehicle. Through the design of the vehicle, it was found that optimizing the propulsion system is key to maximizing the endurance of the vehicle and the use of the multidisciplinary design optimization was important in improving the design of the vehicle.

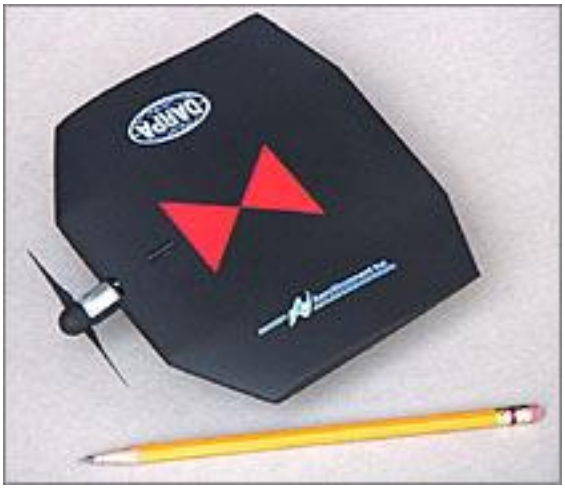

Figure 1.4: AeroVironment *Black Widow*

Since the development of the *Black Widow*, a number of fixed-wing MAVs have been developed. Researchers from Ghent University in Belgium developed a multidisciplinary design optimization methodology to design fixed-wing MAVs given a set of geometrical constraints [12]. A prototype vehicle (*UGMAV25)* was designed using the methodology discussed in [12]. Numerical and empirical models are used to determine the aerodynamic forces of the wing, propeller, vertical tail and control surfaces. The multidisciplinary design optimization consisted of an endurance optimization, an internal component selection analysis and a dynamic analysis to assess the stability, controllability and maneuverability of the vehicle. The final vehicle design had a wing span of 25 cm, mass of 58 grams and achieved a flight time of 17 minutes. A photo of the *UGMAV25* is shown in Fig. 1.5.

Figure 1.5: *UGMAV25* from Ref. [12]

Aurora Flight Sciences has developed the *Skate* MAV (shown in Fig. 1.6) designed for use in tactical mission scenarios as well as scientific endeavors where unmanned flight is beneficial [13]. The *Skate* has a wingspan of 0.61 m (2 ft), weight of approximately 1 kg (2 lbs), a flight endurance of 1 hour and can operate for ranges up to 5 km (3.1 miles).

Figure 1.6: Aurora Flight Sciences Skate MAV

The United States Air Force has implemented the use of AeroVironment's *WASP III* as a part of its Battlefield Air Targeting Micro Air Vehicle Small Unmanned Aircraft System [14]. The *WASP III*, shown in Fig. 1.7a, has a wingspan of 72.3 cm (28.5 inches), mass of 450 grams (~1 lb), a top speed of 17.9 m-s^{-1} (40 mph) and maximum altitude of 305 m (1000 ft). AeroVironment has since improved upon the design creating the *WASP AE* MAV which is depicted in Fig. 1.7b.

(a) *WASP III* MAV (b) *WASP AE* MAV

Figure 1.7: Fixed-wing MAVs developed by AeroVironment

There has also been interest in the use of flexible wings for fixed-wing MAV configurations. Wings constructed with a membrane may provide a level of passive or active wing morphing that can be used to increase performance in certain situations or act as a means of flight control [15,16]. A micro air vehicle with a membrane-based wing design was developed by Ifju et al. [16] at the University of Florida. At angles of attack below stall, the flexible wing and an equivalent rigid wing exhibit similar aerodynamic performance. However, at high angles of attack, the flexible wing was able to produce equivalent levels of lift, compared to the rigid wing, but with a slightly higher lift-to-drag ratio.

Flexible wings were also implemented on the Battlefield Air Targeting Camera (BATCAM) autonomous MAV [17,18]. Wind tunnels tests were conducted on the MAV with flexible wings in place as well as rigid wings. Results showed that the rigid

wings produced higher lift-to-drag ratios compared to the flexible wing. The flexible wings also exhibited a decreased lift curve slope compared to the rigid wings. However, a major driver in the use of flexible wings was to allow for them to fold so that the MAV could be stored in a circular tube for ease of portability. This demonstrates that flexibility in fixed-wing MAVs may provide advantages in terms of practicality and usage and that performance may not be the driving metric for a given design.

1.3 Rotary-wing MAVs

Rotary-wing MAVs are a rapidly growing class of small unmanned aircraft systems (sUAS) in which the lifting surface or surfaces are constantly rotated to generate lift. This allows for the air velocity over the lifting surface to be independent of the vehicle body's motion, enabling them to hover and operate well at low forward speeds. In comparison to fixed-wing MAVS, rotary-wing MAVs are typically more maneuverable. Because of this, rotary-wing MAVs are ideal for operating in confined spaces or tasks involving stationary observation.

A drawback of rotary-wing MAVs is that they are less efficient with regard to producing lift. Figure of Merit (FM), which is a means of measuring hover efficiency, for manned full-scale single main rotor aircraft can be as high as 0.8. However, most rotary-wing MAVs have FM values between 0.45 – 0.60 [19]. A means of improving hover efficiency is by increasing the disk area of the rotor (i.e. reducing disk loading). However, that would require an increase in size which is contrary to the geometric constraints imposed on most MAV designs. Currently there are a large variety of

rotary-wing MAV designs, but the majority of them can be separated into 3 categories: single rotor, coaxial rotor and multi-rotor designs.

1.3.1 Single Rotor MAVs

Many single rotor designs have been developed in academia as well as in industry. At the University of Maryland, work has gone into developing a number of single main rotor MAV designs [20–22]. Typically, one issue with a single main rotor design is that some mechanism is needed to counteract the torque created by spinning the rotor. Generally, a tail rotor is used to provided anti-torque, but its incorporation comes at the expense of decreased compactness of the design. Hrishikeshavan et al. [22] designed a shrouded single main rotor MAV with anti-torque vanes named the *TiShrov*. The *TiShrov* (shown in Fig. 1.8) uses the anti-torque vanes exposed to the downwash from the rotor to counteract the main rotor torque. The shroud provides an extra performance benefit while also protecting the rotor from the outside environment. Performance studies found that the shroud resulted in a 40% increase in power loading increasing the payload capability of the vehicle.

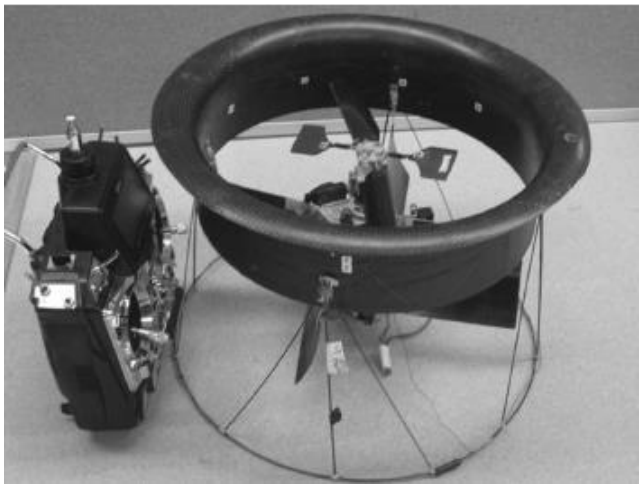

Figure 1.8: *TiShrov* MAV from Ref. [22]

The *Black Hornet Nano* (shown in Fig. 1.9) is designed by Prox Dynamics [23] and has a single main rotor and tail rotor configuration. The vehicle has an area footprint of approximately 10 × 2.5 cm^2 (4 × 1 in^2), a mass of 16 grams (0.5 oz), and a flight time of approximately 20 minutes. It's capable of reaching speeds of 4.9 $m\text{-}s^{-1}$ (11 mph) and is equipped with three video cameras, which can stream live video to the operator.

Figure 1.9: *Black Hornet Nano* by Prox Dynamics

1.3.2 Coaxial Rotor MAVs

Several rotary-wing MAVs concepts have opted for a coaxial design [24–27]. In a coaxial design, two counter-rotating sets of rotor blades act along the same axis of rotation. This configuration does increase the complexity of the design as well as the overall weight of the vehicle. However, the use of counter-rotating rotors negates the need for a means of generating anti-torque and allows the overall design to be more compact. Also, given the size constraints of most MAVs, a coaxial design enables

greater thrust production from the vehicle without increasing the vehicle's overall footprint.

At the University of Maryland, Bohorquez et al. worked to design, build and test a coaxial rotary-wing MAV [20,28]. The work of Bohorquez was based on improving a previous coaxial MAV design by Samuel et al. [29]. Experimental tests, blade element momentum theory (BEMT) based trade studies and high-fidelity CFD parametric studies were conducted to determine how the design could be modified to improve its hover efficiency. The final prototype of the vehicle is shown in Fig. 1.1.

More recently, researchers at the University of Pennsylvania have developed a coaxial MAV that operates without a swashplate [30]. The vehicle has a weight of 227 grams, a rotor diameter of 30 cm and vehicle height of 16.3 cm. The blade attachments are designed in a manner such that lead-lag motion is coupled to blade pitch motion. The motor torque is modulated to cause the blade to pitch during rotation and effectively allow for cyclic pitch control. This control scheme minimizes hub component weight as well as design complexity.

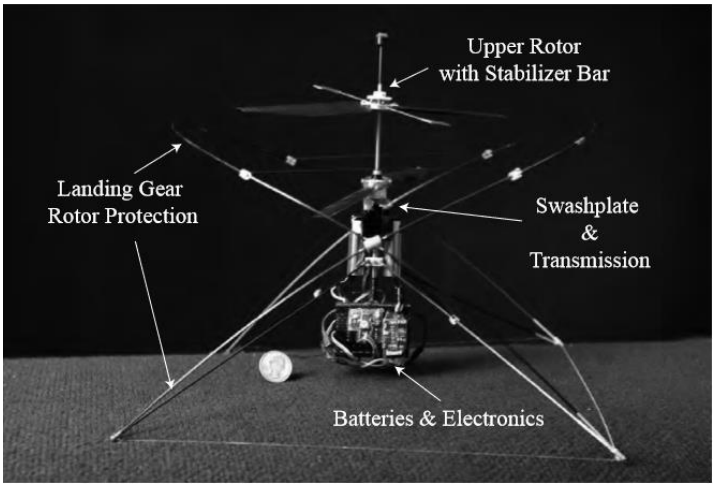

Figure 1.10: Coaxial MAV prototype from Ref. [28]

1.3.3 Multi-rotor MAVs

In recent years, there has been a significant increase in the development and production of multi-rotor MAV designs within both the military and civilian sectors. For the sake of discussion, a multi-rotor MAV is a vehicle with more than two rotors which rotate about independent axes. Many multi-rotor designs consist of four rotors and are referred to as quadrotor MAVs. Quadrotor MAVs consist of two clockwise rotating rotors and two counter-clockwise rotating rotors in order to provide a balance in torque. Quadrotor MAVs can either have fixed or variable pitch blades. In the case of fixed pitch rotors, control of the vehicle is achieved by independently varying the revolutions per minute (RPM) of the rotors.

Multirotor MAVs use for photography, videography and general recreation within the civilian sector has significantly increased. This has led to the emergence of companies such as DJI and Parrot. Vehicles such as the Parrot *Bebop 2* [31] have a typical 4 rotor configuration. Select vehicles are made up of more than 4 rotors, such as the DJI S900 [32], which is composed of 6 rotors. Examples of the two vehicles are shown in Fig. 1.11. While including more rotors drives up vehicle power consumption, it provides the benefit of increased stability and redundancy in case of rotor failure.

(a) Parrot *Bebop 2* (b) DJI S900

Figure 1.11: Commercial multi-rotor MAVs

AeroVironment has developed the *Snipe Nano UAS* [33] which is shown in Fig. 1.12. The *Snipe Nano UAS* is a quadrotor MAV with a mass of 140 grams (4.9 oz) and flight endurance of approximately 15 minutes. It has a maximum flight speed of approximately 9.8 m-s^{-1} (22 mph) and is capable of operating in wind speeds of 10 kts and gusts of 20 kts. The vehicle is equipped with video cameras to provide live video feeds to the operator and is useful for reconnaissance and surveillance missions.

Figure 1.12: AeroVironment *Snipe Nano UAS*

1.3.4 Unconventional Rotary-wing MAVs

The most common types of rotary-wing MAVs were discussed in the previous sub-sections. However, there are some notable rotary-wing MAVs that don't fit into the aforementioned categories. For example, the *Robotic Samara* (Fig. 1.13) is a monocopter MAV created at the University of Maryland whose design is based on the seed pods of the Samara tree [34].

Figure 1.13: The *Robotic Samara* MAV from Ref. [34]

Another type of vehicle is the cycloidal rotor MAV. Cycloidal rotors have been developed at the University of Maryland for a number of years [35–37]. In a cycloidal rotor, the span of the rotor blades lies in the same direction as the axis of rotation. The rotor rotates in a paddle wheel-like fashion to enable the blade to generate lift. Pitching of the cyclorotor blades is varied such that lift production in achieved at the top and bottom of the blade rotation. A picture depicting a cyclocopter can be seen in Fig. 1.14. Cyclocopters have a relatively complex rotor design and the rotor blades and hub comprise a larger fraction of the vehicle weight. However, cycloidal rotors have been shown to have higher Figures of Merit and lower power consumption in forward flight compared to conventional rotary-wing MAVs [35,36].

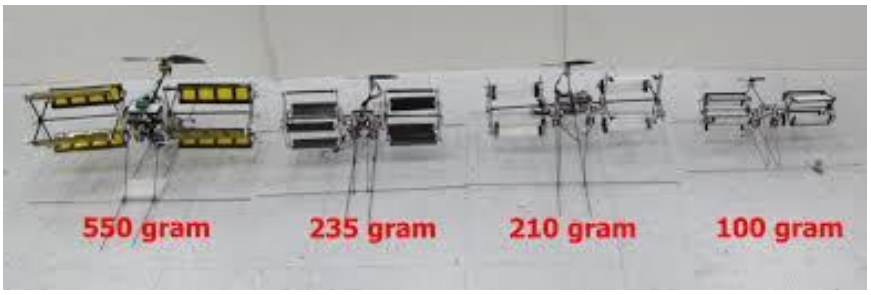

Figure 1.14: Various cycloidal rotor MAV designs

1.4 Flapping-wing MAVs

Current MAV systems based on conventional aircraft designs, (i.e. fixed-wing and rotary-wing designs) suffer from decreased lifting force generation and as such degraded aerodynamic efficiency [38,39]. The major factor for the lowered aerodynamic performance can be attributed to Reynolds numbers effects which will be discussed more depth in Section 1.5. MAVs typically operate at low Reynolds numbers ($O\sim10^4$) and many studies have found that operating at such Reynolds numbers can cause degraded lift-to-drag ratios, increased drag coefficient magnitudes and increased susceptibility to flow transition and separation [40].

In nature, there are numerous animals (i.e. small birds and insects) that are of comparable size to desired man-made MAVs, however they fly effortlessly. These animals have managed to overcome many of the challenges of flying at low Reynolds numbers even in gusty environments. Natural flyers exhibit a periodic, flapping motion of their wings in order to achieve flight. Attention has focused on flapping-wing micro air vehicle (FMAV) designs because of the potential for increased lift capability, aerodynamic performance, gust tolerance and maneuverability exhibited by biological flapping wing flyers, which operate in the same aerodynamic regime. One drawback of

FMAVs is that they inherently have unsteady wing kinematics. Creating the reciprocating flapping wing motion can lead to complexities in the vehicle design as well as produce cyclical loads which can exacerbate fatigue stresses on various components. Another issue is that FMAVs rely on unsteady aerodynamics to achieve flight and currently we have a limited understanding with regard to designing a vehicle that utilizes those unsteady mechanisms. Means of developing a flapping-wing design and accurately assessing its performance characteristics is still an open field of study. In general, FMAVs can be separated into two categories: ornithopters and entomopters.

1.4.1 Ornithopters – Flap Kinematics

Ornithopters are flapping wing aerial vehicles where the wing flapping kinematics emulate that of avian animals or bats. While there may be some variance, avian-like flap kinematics primarily result in the wing flapping mostly in the vertical plane. Figure 1.15 provides an illustration of avian flap kinematics. A flap cycle for avian-like flap kinematics can be broken down into two components: a downstroke and an upstroke. During the downstroke, the wing is extended to aid in the generation of positive lift. Active twisting of the wings is performed by the flying animal through the change of wing pitch along the span. Typically, the wings are twisted to result in nose-down pitching the leading edge toward the wing tip. This is to aid in the generation of positive lift force as well as propulsive thrust. During the upstroke, the wing is retracted to minimize the drag produced. Negative angles of attack along the wing produce propulsive thrust during the upstroke but also work to produce some negative lift. The wings need to be appropriately actuated to produce net positive lift and propulsive

thrust over the course of a flap cycle. Lift is primarily produced along the inboard portion of the wing while propulsive thrust is generated more toward the wing tip.

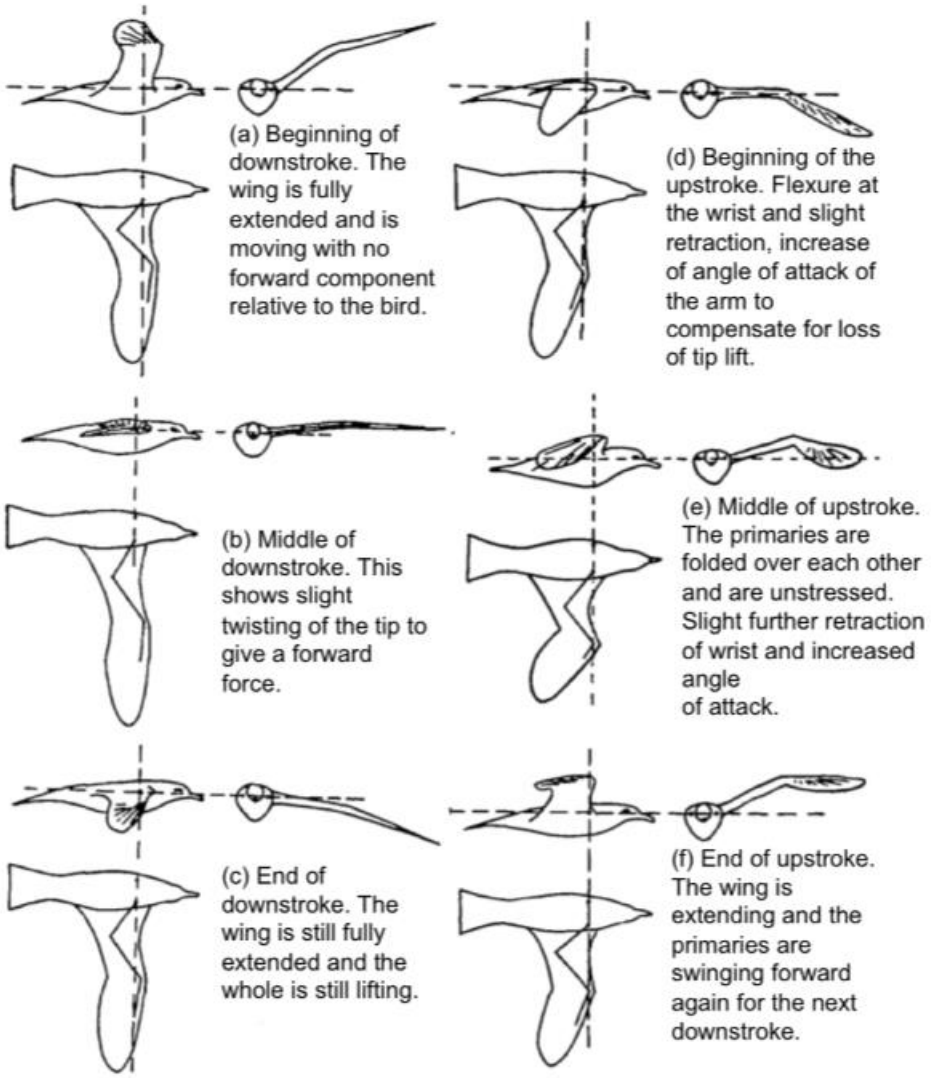

Figure 1.15: Illustration of avian flap kinematics. Adopted from Ref. [41]

1.4.2 Ornithopters – Select Vehicles

Odyssey (Fig. 1.16a) is a flapping wing MAV developed at the University of Maryland that's been used as a testbed for flapping wing experimental studies [42]. It is based off of the ornithopter design proposed by Kinkade [43]. It has a mass of

approximately 450 grams and is capable of 30-minute flight times. *Robo Raven* (Fig. 1.16b) is another flapping-wing MAV developed at the University of Maryland [44]. It was designed with independent control of each wing to expand the flight envelope of the vehicle. The wings are created using stiff carbon fiber rods with a Mylar film covering. *Robo Raven* has a total mass of 290 grams, wing span of 1.17 m and an operating flap frequency of 4 Hz.

(a) *Odyssey* MAV

(b) *Robo Raven* MAV

Figure 1.16: Ornithopters developed at the University of Maryland

The *Microbat* is a palm-sized ornithopter developed by AeroVironment [45]. The vehicle has a wing span of 9 inches, overall length of 6 inches and a mass of 12.5 grams. The flight time of the vehicle was limited to approximate 40 seconds. A picture of the *Microbat* can be seen in Fig. 1.17.

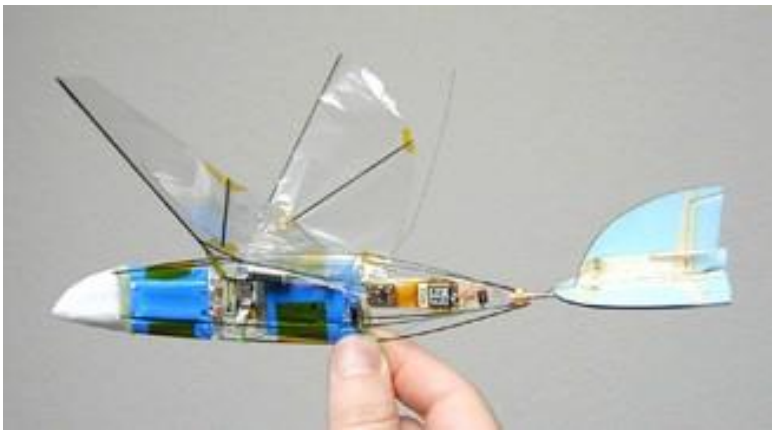

Figure 1.17: The AeroVironment *Microbat*

The *DelFly Micro*, created at TU Delft, has a wing span of 10 cm and a total vehicle mass of 3.07 grams [46]. It has an onboard transmitter as well as a camera as payload. The vehicle has been able to achieve forward flight work is geared toward expanding its flight capabilities.

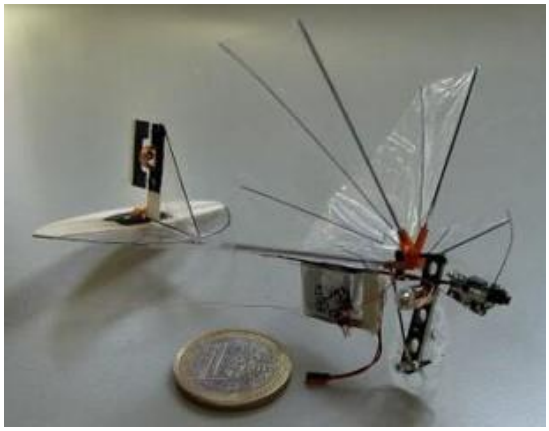

Figure 1.18: TU Delft *DelFly Micro* from Ref. [46]

1.4.3 Entomopters – Flap Kinematics

Entomopters are flapping wing aerial vehicles where the wing flapping kinematics emulate that of insects. Insect-like flap kinematics result in the wing flapping occurring mostly in the horizontal plane. Figure 1.19 provides an illustration of insect flap kinematics. During insect-like flap kinematics, the wing is actuated in a mostly horizontal stroke plane. Similar to avian-like flap kinematics, the flap cycle can be broken down into a downstroke and upstroke. Even more so, a given stroke can be decomposed into a translational component and a stroke reversal component.

During wing translation, the wing is held at a relatively fixed pitch angle. At the end of a flap stroke, the wing must twist or rotate about its span to allow for a positive angle of attack as it begins to move in the opposite direction. This action is known as stroke reversal. Most animals which utilize insect-like flap kinematics have minimal to no direct control over the pitching of their wings. The wing twist during flapping is often due to aerodynamic and inertial forces acting on the wing. An exception to this are hummingbirds which have active control over their wings due to their musculoskeletal system. In normal hovering flight the downstroke and upstroke are symmetric. Changes to the flap plane, wing pitch angle, or stroke amplitude to allow for maneuvering and stability during flight.

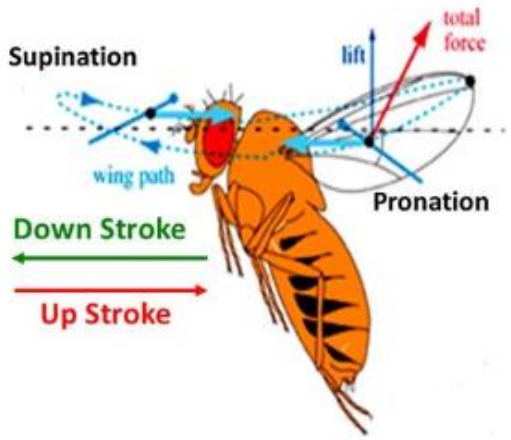

Figure 1.19: Illustration of insect flap kinematics. Adopted from Ref. [47]

1.4.4 Entomopter – Select Vehicles

One flapping-wing vehicle that utilizes insect-like flap kinematics is the *Mentor* MAV [48]. The vehicle utilizes two sets of flapping wings (4 wings total) to generate lift and balance side-to-side flapping forces. Two versions of the vehicle were built: one powered by an internal combustion engine and another powered by an electric motor. Each vehicle had a maximum span of 14 inches and operated at a flap frequency of 30 Hz. However, the mass of the vehicles differed where the internal combustion engine-based vehicle had a mass of 580 grams and the electric motor-based vehicle had a mass of 440 grams. Onboard fuel stores allowed for up to 6 minutes of flight times for the internal combustion engine-based design. However, the electric motor-based design was limited to flight time of approximately 20 seconds due to power draw restrictions from the battery.

Figure 1.20: *Mentor* MAV developed at the University of Toronto [48]

The *DelFly II* is one in a series of flapping-wing MAVs developed at the Technical University of Delft [46,49]. The *DelFly II* (Fig. 1.21) has a total mass of 16 grams and wing span of 28 cm. Unlike the original *DelFly* (also known as the *DelFly I*), the *DelFly II* was designed to allow for hovering flight. In addition to hovering flight, the vehicle can achieve a maximum forward flight speed of 7.0 $m\text{-}s^{-1}$ as well as fly backwards at a speed of 1.0 $m\text{-}s^{-1}$.

RoboBee, displayed in Fig. 1.22, is an at-scale, insect-sized flapping-wing vehicle developed at Harvard [50]. The vehicle has a mass of 80 milligrams and the wings are actuated using piezoelectric bimorphs. Benchtop tests showed that the vehicle was able to produce enough vertical lift to takeoff. However, it is not currently onboard battery powered and must be powered by an external source in a tethered mode.

Figure 1.21: The TU Delft *DelFly II*

Figure 1.22: Harvard *RoboBee* described in Ref. [50]

The *Nano Hummingbird* was developed by AeroVironment in response to DARPA's Nano Air Vehicle (NAV) program [51]. Figure 1.23 provides an image of the *Nano Hummingbird*. The *Nano Hummingbird* has a mass of 19 grams, wing span of 16.5 cm and is capable of a maximum forward flight speed of 6.7 m-s^{-1}. The vehicle carried a video camera capable of streaming color video to a remote ground station. A unique characteristic of the vehicle is that it's able to maintain control flight solely through actuation of its wings.

Figure 1.23: *Nano Hummingbird* discussed in Ref. [51]

The *Robotic Hummingbird*, shown in Fig. 1.24, is a flapping wing MAV design that was initially began development at the University of Maryland and has since continued development at Texas A&M University [52]. The vehicle was designed over several iterations with the final design having a wing span of 12 inches and operates at a flap frequency of 22 Hz with a total mass of 62 grams. The wings are actuated using a unique "modified 5-bar" mechanism which helps to amplify the output of a conventional crank-rocker four-bar mechanism.

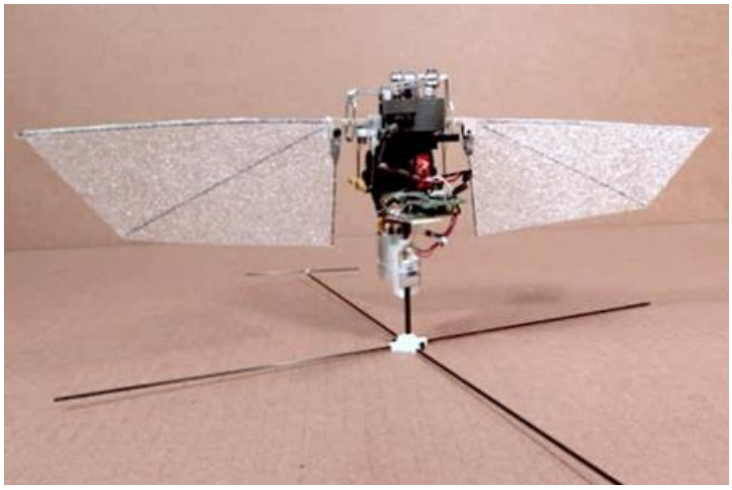

Figure 1.24: Texas A&M *Robotic Hummingbird* discussed in Ref. [52]

BionicOpter is a dragonfly inspired flapping-wing MAV created by Festo [53]. The vehicle was constructed with a dragonfly-like design with a pair of forewings and a pair of hindwings. *BionicOpter* has a wingspan of 63 cm, overall length of 44 cm and a gross take-off weight of 175 grams. A brushless motor was used to actuate the four wings as well as adjust the flap frequency. The wing flap amplitude and wing twist of each wing were independently controlled through eight servos. A picture of the *BionicOpter* can be seen in Fig. 1.25.

Figure 1.25: *BionicOpter* developed by Festo [53]

Table 1.1 provides an overview of some of the flapping-wing MAVs discussed in this section including information on their respective vehicle masses, flight times and the institution at which they were created.

Table 1.1**: Selected list of current FMAV designs**

Name	Institution	Mass	Flight Time	Hover-capable
RoboBee	Harvard	80 mg	----	Yes
Microbat	AeroVironment	12.5 g	< 1 min	No
DelFly II	TU Delft	16.0 g	9 min	Yes
Nano Hummingbird	AeroVironment	19.0 g	4 min	Yes
Robotic Hummingbird	Texas A&M	62.0 g	~ 1 min	Yes
BionicOpter	Fresto (Germany)	175 g	----	Yes
Robo Raven	Univ. of Maryland	290 g	5 min	No
Odyssey	Univ. of Maryland	450 g	25 – 30 min	No
Mentor	Univ. Toronto	580 g	6 min	Yes

1.5 Challenges Associated with MAV Design

Many unique challenges arise when considering the design, manufacturing and operation of vehicles at MAV-scale. Given their small size, issues arise when considering how to power the vehicle, utilization of appropriate sensors and integration of other mechanical components. More importantly, the flow phenomena and characteristics exhibited by lifting surfaces differ at MAV-scales in comparison to the full-scale conventional aircraft. This is due to low Reynolds number effects. Reynolds number is defined in the equation below:

$$Re = \frac{\rho V L}{\mu} \tag{1.1}$$

where ρ is the fluid density, V is reference velocity, L is the characteristic length and μ is the dynamic viscosity of the fluid. Physically, Reynolds number represents that ratio of inertial forces to viscous forces acting in a given flow. Typical full-scale aircraft

operate at Reynolds number on the order of 10^6 – 10^7. In this range of Reynolds numbers, viscous effects are minimal and can assumed to act within a thin boundary layer near the wing surface [54].

MAVs operate at Reynolds numbers on the order of 10^4 – 10^5. At these low-Reynolds number ranges viscous effects play a much more significant role in the aerodynamics resulting in some adverse effects. At low-Reynolds numbers, there is an increase in skin friction drag and airfoils are also more susceptible to flow separation. This leads to decreased maximum lift coefficients, increased drag coefficients and overall lowered aerodynamic efficiency. Figure 1.26 provides plots, presented by McMasters and Henderson [55], illustrating the effects of Reynolds number on lift-to-drag ratio and maximum lift coefficient.

Lift-to-drag ratio (L/D) is a measure of efficiency for airfoils where larger L/D values signify greater efficiency. When examining L/D (Fig. 1.26a), "smooth" airfoils outperform "rough" airfoils for Reynolds number greater than 10^5. However, for Reynolds numbers less than 10^5, smooth airfoils exhibit a significant reduction in L/D due to low-Reynolds number effects. In Fig. 1.26b, the maximum lift coefficient generated by the airfoil can be seen to drop as Reynolds number is decreased.

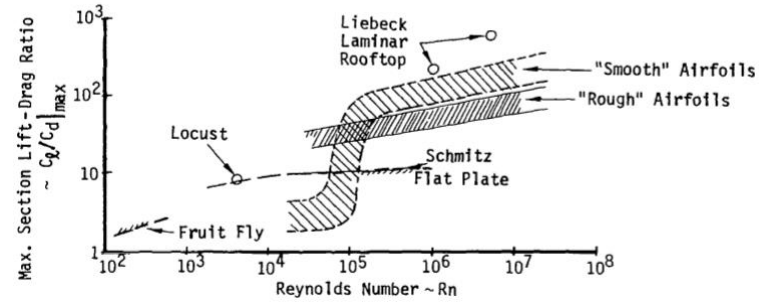

(a) Lift-to-drag ratio vs Reynolds number

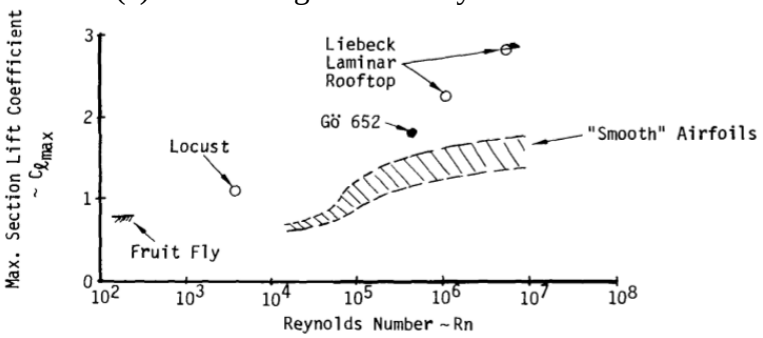

(b) Maximum sectional lift coefficient vs Reynolds number

Figure 1.26: Plot illustrating Reynolds number effects. Adopted from Ref. [55]

Similar conclusions can be drawn when analyzing the hover efficiency of rotors at low-Reynolds numbers. One means of assessing the hover efficiency of a vehicle is by its power loading. Power loading $\left(PL = \frac{T}{P}\right)$ is the ratio of vertical thrust generated by a vehicle per unit of power needed to generate said thrust. Power loading provides a metric to compare the efficiency of various hover-capable vehicles. Figure 1.27 shows plots of power loading versus disk loading for a variety of hover capable vehicles. Note that disk loading $\left(DL = \frac{T}{A_e}\right)$ is the ratio of thrust produced divided by the effective area swept out by the lifting surface and is analogous to wing loading for fixed-wing aircraft. Disk loading effects power loading through the equation below:

$$PL = \frac{\sqrt{2\rho} * FM}{\sqrt{DL}} \tag{1.2}$$

where ρ is the density of the operating fluid and *FM* is the figure of merit of the aerodynamic system. From Eq. (1.2), a decrease in disk loading leads to an increase in power loading. In Fig. 1.27, the constant lines in the plot are constant values of figure of merit. The figure of merit tends to be greater for helicopters in comparison to more conventional small-scale rotors.

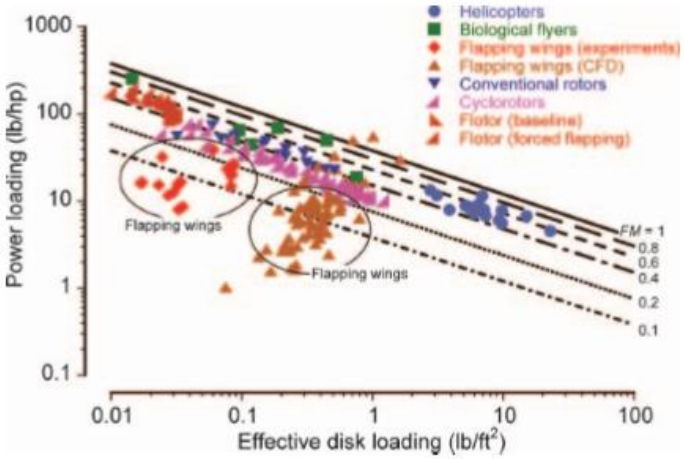

Figure 1.27: Power loading vs disk loading for a range of hover-capable vehicles. Adopted from Ref. [56]

A major factor that influences the efficiency of a given configuration (lift-to-drag ratio or power loading) is the geometry of the wing/rotor. With respect to lift-to-drag ratio, higher aspect ratio wings tend to have better lift-to-drag ratios for a given airfoil cross-section. With respect to power loading, rotors with larger disk areas have better hover efficiency for a given thrust produced. However, given the size constraints placed on MAVs, increases in wing aspect ratio or rotor disk area are limited.

Outside of the wing planform or rotor geometry, the airfoil geometry can have a significant effect on the aerodynamic characteristics of an airfoil. At the Reynolds numbers associated with full-scale conventional aircraft, airfoils typically have a

rounded leading edge and gradually taper toward a sharp trailing edge as they tend to exhibit better aerodynamic performance. Studies by Laitone showed that thin cambered plates outperformed NACA 0012 airfoils when comparing L/D and lift curve slope at low-Reynolds numbers [57]. Figure 1.28 provides the L/D versus angle of attack and lift coefficient versus angle of attack plots from Ref. [57]. Similar results were found in separate studies by Mueller [40] and by Hein and Chopra [58] regarding the improved performance of thin cambered airfoils subject to low Reynolds number flows. The airfoil profiles of many natural wing flyers exhibit those of thin cambered airfoils [59]. Insect wings typically have sharp leading and trailing edges with a low thickness-to-chord ratio.

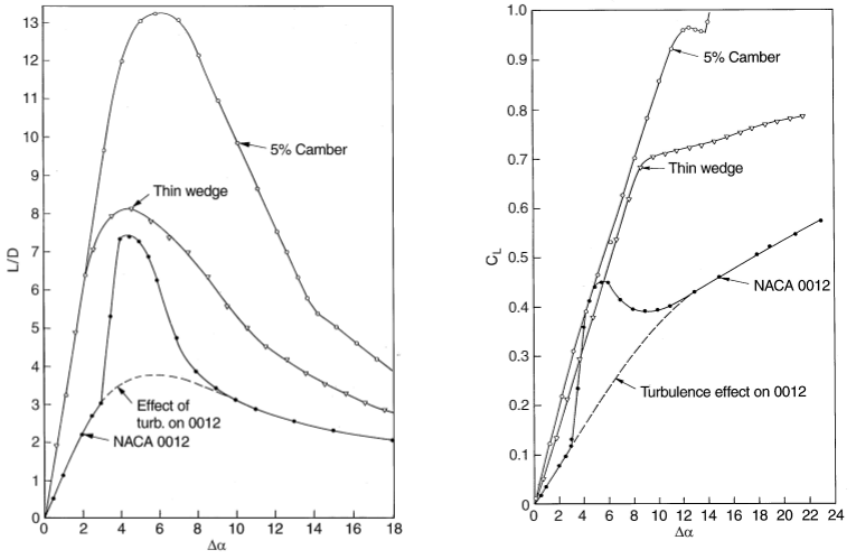

Figure 1.28: Plots of lift-to-drag ratio and lift coefficient vs angle of attack from Ref. [57]

Nature has managed to overcome many of the barriers that have plagued the development of man-made MAVs. Most of the flying animals that are at the desired scale of MAVs utilize flapping wings to achieve flight. The “Great Flight Diagram”

shown in Fig. 1.29 illustrates the efficiency of natural flyers at MAV-scale. Thus, it serves to further explore the flapping-wing design concept to make man-made vehicles which can match or exceed the performance and maneuverability seen in natural flyers.

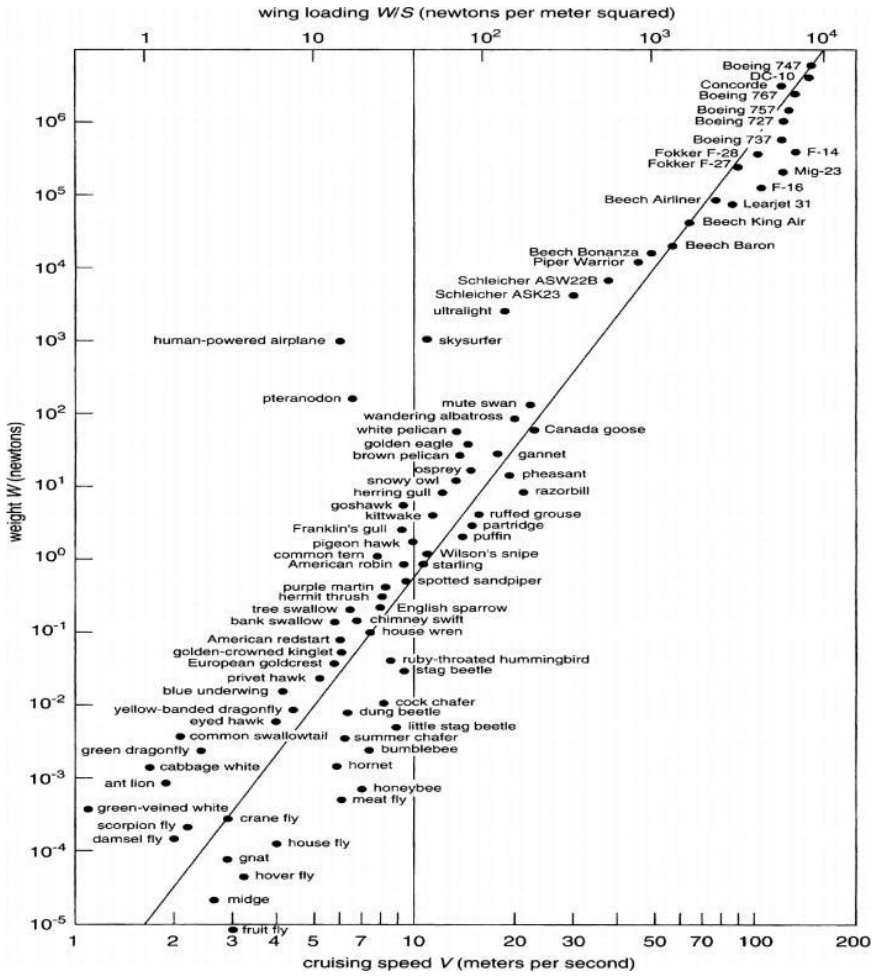

Figure 1.29: The Great Flight diagram. Adapted from Ref. [38]

1.6 Select Prior Studies on Flapping Wings

Many of the challenges of flapping-wing MAV design stem from our general lack of understanding of aerodynamics and aeroelastic phenomena at MAV-scale Reynolds numbers. As a means of overcoming these challenges, a myriad of research activities have been undertaken to further our understanding. Over the past two

decades, hundreds of journal articles have looked at further exploring MAVs including flapping wing MAVs [60]. Figure 1.30 provides plots illustrating the number of MAV related journal articles written as well as a breakdown of the number of articles by MAV type. In an effort to further our understanding, experimental and computational studies have looked at analyzing biological flyers at MAV-scale (small birds and insects) as well as man-made mechanisms designed to emulate certain aspects of flapping wing flight. The following sub-sections discuss relevant prior work as well as some of the major finds from those studies.

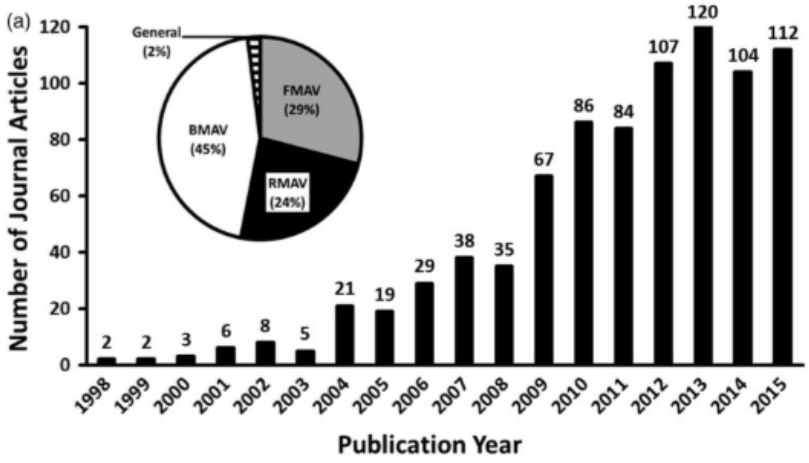

(a) Distribution of MAV journal articles

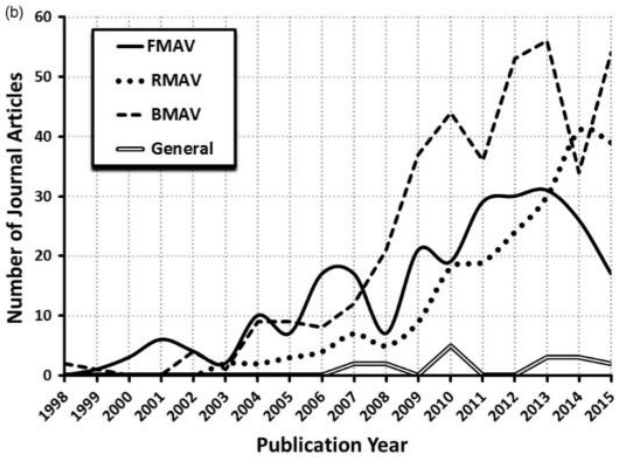

(b) Breakdown of journal articles by MAV type

Figure 1.30: Plot of number of MAV related journal articles by year from Ref. [60]

1.6.1 Live Animal Studies

Researchers have looked at analyzing natural flyers to better understand the physics associated with unsteady flapping wing flight at MAV scales. While some recent work has been conducted by researchers in the engineering field, most of the studies on natural flyers have been performed by researchers in the biological sciences. A few of the notable studies pre-date the current interest in creating man-made flapping wing MAVs. In 1973, Weis-Fogh [61] investigated the aerodynamics of hovering insects. Weis-Fogh noted that for most hovering insects, the wings flap in a horizontal plane and that unsteady aerodynamics play an important role in insect flight especially in those that operate a low Reynolds numbers which range from the order of $10^2 – 10^3$.

The unsteady aerodynamic mechanism discovered by Weis-Fogh is the clap-fling mechanism while analyzing the high-speed video of the chalcid wasp *Encarsia formosa*. Figure 1.31 provides a simple illustration detailing the clap-fling mechanism. The clap-fling mechanism can be thought of in two parts named the “clap” (images A, B and C in Fig. 1.31) and the “fling” (images D, E and F in Fig. 1.31). During the clap, the leading edges of the wings come together at the end of a flap stroke. With the leading edges together, the wings rotate about the leading edges such that the trailing edges begin to approach one another. This pushes the fluid between the wing out of the way resulting in a reactionary force in the thrust direction. During the fling, the wings begin the subsequent flap stroke and the leading edges begin to move away from each other. The motion of the trailing edges lags that of the leading edges such that a high pitch angle is created by the wing. This creates additional circulation about the wing which aides to enhance the lift generated.

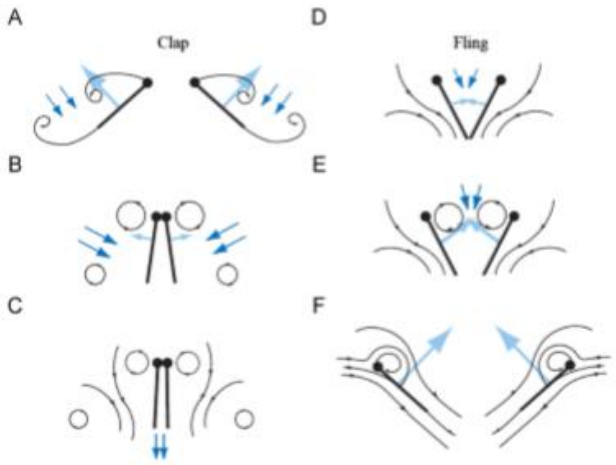

Figure 1.31: Diagram describing the clap-fling mechanism. Adopted from Ref. [39]

In 1984 Ellington described the aerodynamics of hovering insects, their general wing kinematics patterns, possible unsteady aerodynamic mechanisms and a generalized vortex theory to determine the mean lift when unsteady or quasi-steady mechanisms are present [62–67]. In general, wing flapping was found to be similar to simple harmonic motion. The wing moves in a reciprocating motion and can be broken down into a stroke reversal component and a translational component.

During stroke reversal, the wing decelerates as it approaches the end of a flap stroke. A wing eventually reaches zero velocity and begins to accelerate in the opposite direction to begin the subsequent flap stroke. In addition, the wing undergoes a significant rotation about its longitudinal axis to allow for a positive angle of attack favorable for lift production during subsequent flap strokes. During the translational component of the flap cycle, the wing holds a nearly constant pitch angle. Typically, the wing is twisted along its span such that the pitch angle is greater in magnitude toward the wing root in comparison to the wing tip [64]. While little deviation of the wing from the stroke plane was seen, in certain cases, the tip path creates a figure-eight

pattern during the course of the flap cycle. Figure 1.32 illustraes the wing tip kinematics of a hummingbird as a general representation of wing kinematics for hover capable birds and insects.

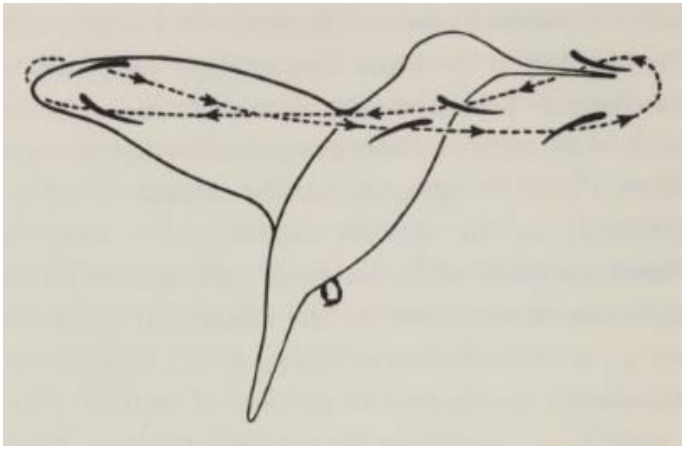

Figure 1.32: Wing tip path of a hummingbird. Adopted from Ref. [62]

At the time unsteady airfoil theory underpredicted the lift forces required for hovering birds and insects to achieve flight. Ellington suggested that the delayed stall phenomenon may play a vital role in enabling flapping wing animals to achieve the lift necessary for flight [65]. However, delayed stall of airfoils is not a newly discovered phenomenon. In 1933, Francis and Cohen [68] investigated the lift produced by airfoils at high incidence angle, which undergo sudden translational motion. Results showed that when airfoils are placed at high pitch angles (i.e. pitch angles greater than that at which steady-state stall occurs), the airfoil is capable of generating large lift forces during the first few chord lengths of travel following the start of translational motion. Results showed that lift increased by 40 – 55% of the steady-state stall value within the first 5 chord lengths of travel after which the lift decreased to steady-state stall values.

Another unsteady mechanism suggested to play a role in flapping wing flight by Ellington is the Kramer effect [69]. Unlike the delayed stall due to a change in translational motion, the Kramer effect occurs due to a change in rotational motion during the pronation and supination parts of the flap cycle. The Kramer effect can be described as a delay in stall when a slight rotational velocity is applied to an airfoil undergoing steady translational motion. The previously mentioned translational and rotational means of delaying stall can be grouped under the phenomenon known as dynamic stall. Dynamic stall is a well-known phenomenon in the field of helicopter aerodynamics and has been widely studied by a number of researchers [70–73]. In general, dynamic stall occurs when an airfoil is subjected to a time-dependent unsteady motion (e.g. pitching, plunging, surging) that increases the effective angle of attack above its normal static stall angle [74]. Figure 1.33 provides a schematic illustration the dynamic stall phenomenon and Fig. 1.34 shows a representative plot describing the change in lift coefficient during dynamic stall in comparison to static stall.

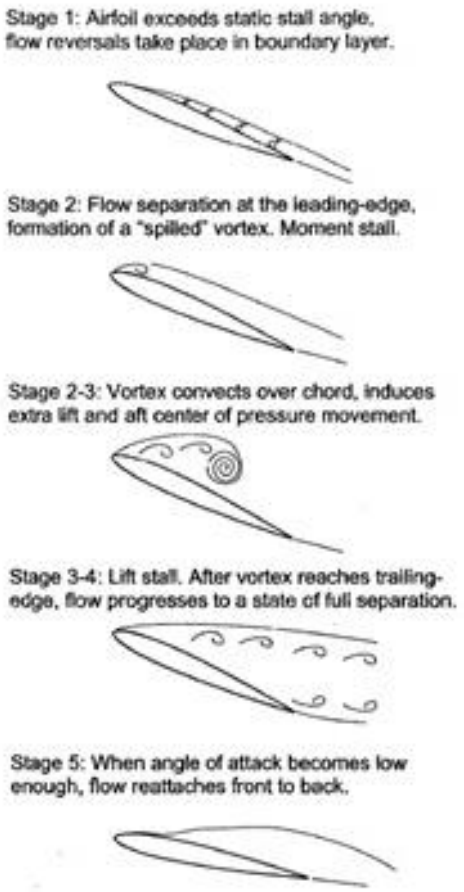

Figure 1.33: Schematic illustrating the dynamic stall phenomenon. Adopted from Ref. [74]

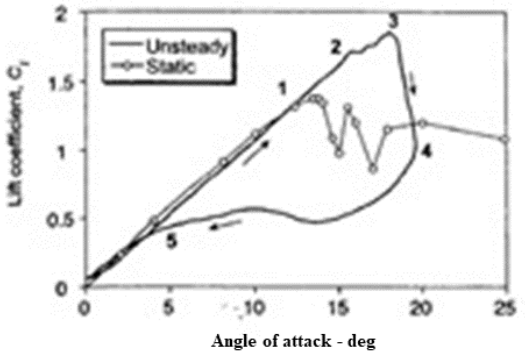

Figure 1.34: Representative plot illustrating the change in lift during dynamic stall in comparison to static stall. Adopted from Ref. [74]

Srygley and Thomas performed studies on red admiral butterflies (*Vanessa atalanta*) in free flight to examine the unsteady flight mechanisms they utilize [75]. Tests were conducted in a wind tunnel and high-resolution flow visualization was used to qualitatively observe the air flow about the wings. Images were taken using high-speed videography. Free-flight, as opposed to tethered flight, was used in this study because the researchers believed that tethering the animals may cause them to alter their flap kinematics. The butterflies were trained to fly between artificial flowers to help ensure they remain in the view area of the high-speed cameras. Analysis of the digital images showed that the butterflies use a variety of unsteady mechanisms and even switch between different unsteady mechanisms in successive flap cycles. The unsteady mechanisms seen include the leading edge vortex, tip vortices, wake capture phenomenon, the clap-fling mechanism and active/inactive upstrokes. The butterflies were able to easily switch between the use of various unsteady mechanisms through a simple change in their wing flap kinematics.

Later studies on natural flyers sought to investigate in detail the previously mentioned kinematics and unsteady aerodynamic mechanisms as well as the importance of wing flexibility in flapping wing flight. Work by Ennos showed the importance of wing flexibility and how allowing for wing twist is necessary to improve performance [76,77]. Ennos also showed the importance of wing mass distribution and how the inertial forces generated by the wing aid in creating wing twist [78].

Combes and Daniel compared the flexural stiffness of a series of insect wings in the spanwise and chordwise directions [79]. Results showed that spanwise stiffness is approximately 1 – 2 orders of magnitude greater in the spanwise direction as opposed

to that in the chordwise direction. This spanwise-chordwise wing stiffness anisotropy is thought to be a character trait of most insect wings and that it is necessary to induce camber due to chordwise bending as well as facilitate wing twist.

Studies on natural flyers helped to provide an initial understanding of flapping wing flight and the expected physics at MAV-scales. These studies have also helped in providing insight and improve quasi-steady and unsteady airfoil theory. However, studies on biological flyers have significant challenges. Animals may be difficult to coax to perform a specific action at the demand of the researcher. Given the small size of many flying animals, obtaining accurate quantitative measurements of the force, power or the flowfield about the wings is difficult with current sensor technology. Flapping wing flight of natural flyers is a complex process involving many interdependent variables. With the goal of enhancing our fundamental understanding of flapping wing flight, it may be extremely challenging or even impossible to isolate certain aspects of flapping wing flight when analyzing biological flyers.

1.6.2 Rigid Wing Studies

Given the complex nature of the flapping wing problem, numerous studies have looked at simplifying various aspects of flapping wing flight and investigating them individually to understand their effect on flapping wing aerodynamics. One such simplification is to make the wing rigid as to eliminate aeroelastic effects due to structural flexibility. Another is to use simplified flap kinematics. Flap kinematics can be broken down into two degrees-of-freedom: a flap degree-of-freedom and a pitching degree-of-freedom. For 2D cases, the flap degree-of-freedom is replaced by a translational plunging of the airfoil.

Dickinson and Götz performed studies on a scaled wing model to investigate the time-dependent forces acting on impulsively moved wings [80]. The model wing was made of aluminum, had a chord of 5 cm, wing span of 15 cm and thickness of 1.0 mm. The leading edge was rounded while the trailing edge was sharply tapered. Test were conducted in a tank filled with a 54% sucrose solution. The wings were moved translationally through the fluid at various constant pitch angles and varied translational velocities. During translation the aerodynamic forces were measured in conjunction with flow visualization. A picture of the experimental setup is shown in Fig. 1.35. This helped to simulate appropriate Reynolds numbers.

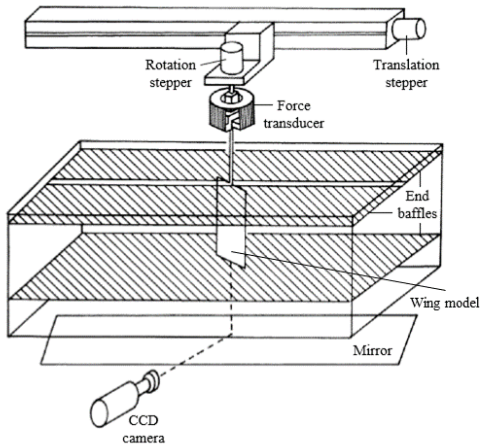

Figure 1.35: Illustration of experimental setup from Ref. [80]

Results showed that at angles of attack greater than 13.5°, a leading-edge vortex (LEV) formed on the wing surface. The LEV remained attached to the wing for the first 2 chord lengths of travel results in an 80% increase in lift compared to the lift measured after 5 chord lengths of travel. The LEV creates a low-pressure region on the suction side of the wing increasing the pressure difference across the wing surface

which in turn enhances the lift generated. After the LEV sheds from the wing, a second vortex of opposite vorticity formed at the trailing edge.

Figure 1.36 provides an illustration of how the LEV enhances lift production using Polhamus' leading-edge suction analogy [81]. Fig. 1.36a depicts the steady-state lift of an airfoil subject to potential flow with the Kutta condition applied at the trailing edge. As the flow attempts to navigate the sharp leading edge by quickly changing velocity, a suction vector ($\mathbf{F_S}$) forms that acts parallel to the wing chord line. The suction vector and normal force vector ($\mathbf{F_N}$) sum to form the lift vector (**L**). With the formation of a LEV, the flow need not rapidly change velocity to navigate the leading edge thus eliminating the suction force parallel to the wing chord. However, a suction force is necessary to allow the LEV to remain attached to the wing surface. This suction force acts in the same direction as the normal force and thereby increases the overall lift produced.

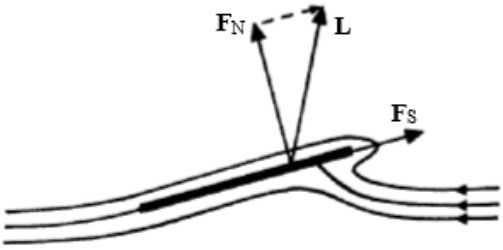

(a) Steady-state lift about a thin airfoil

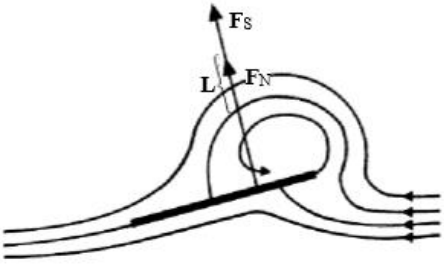

(b) LEV enhanced lift about a thin airfoil

Figure 1.36: Illustration of lift augmentation via a LEV. Adopted from Ref. [80]

Most insect wings operate at high angles of attack and only travel 2 – 4 chord lengths during flapping, which are the same conditions that lead to the formation of a leading-edge vortex. The LEV, which is an artifact of the dynamic stall phenomenon described in Sub-section 1.6.1, was proposed as a mechanism by which insect wings are able to augment their lift during flapping. Follow-up studies have also investigated the LEV for translating, rotating and flapping wing kinematics and have shown how it enhances the magnitude of lift generated by a wing [82–88].

Other notable unsteady flight mechanisms are rapid pitch rotation and wake capture. Rapid pitch rotation occurs at the end of a flap stroke during stroke reversal. As the wing is rotating about the spanwise axis, the timing of the wing pitch rotation can augment the circulation acting on the wing [89]. This behavior utilizes the Kramer effect discussed in the Sub-section 1.6.1. From Ref. [89], if wing rotation is initiated prior to the end of the flap stroke, known as advanced rotation, the lift force generated is increased. Subsequent studies by Sane and Dickinson [90] sought to quantify the effect of rapid pitch rotation. They showed that the rotational forces are proportional to the angular velocity of rotation. The results from the series of experimental studies conducted were used to quantitatively determine the influence of wing rotation on aerodynamic force generation. Rotational force coefficients were applied to a translation-based quasi-steady aerodynamics model to improve the accuracy of predicted instantaneous aerodynamic forces during wing flapping.

In wake capture, depending on the structure of the wake and the wing kinematics, the wing may interact with the shed vorticity from the previous flap stroke after stroke reversal. The resulting interaction can increase fluid velocities about the

wing, which in turn increase the aerodynamic forces generated. Figure 1.37 provides an illustration demonstrating the wake capture mechanism. The wing translates from left-to-right in the image (Fig. 1.37a) and a prominent LEV forms on the wing surface. As the wing undergoes stroke reversal (Figs. 1.37b and 1.37c), vortices are shed from the leading and trailing edges which spin in opposing directions. These vortices impart a velocity in the flow denoted by the dark blue arrows. As the wing is completing stroke reversal and begins translating in the opposite direction (Figs. 1.37d and 1.37e), it interacts with the velocity field imparted by the shed vortices from the previous stroke. The increased velocity imparted on the wing increases the aerodynamic forces produced which are denoted by the light blue arrow emanating from the wing surface. In Fig. 1.37f the wing passes through the previous shed wake and continues through the translational phase of the current stroke.

While rapid pitch rotation and wake capture may result in enhancing the aerodynamic capabilities for a flapping wing, these phenomena only happen for a short duration of the wing stroke and depend heavily on the timing of wing rotation. Therefore, these mechanisms do not contribute much to the time-averaged wing forces. The formation of a LEV is the most prominent unsteady mechanism responsible for augmenting the lift of flapping wings at low Reynolds numbers which is the reason it has garnered so much attention amongst researchers.

Given that the LEV is such an important mechanism in augmenting the lift of flapping wings, it is important to have a thorough understanding of how the wing kinematics affect its generation. Some initial studies sought to analyze the vortex formation on wings undergoing pitching and plunging kinematics using 2D analysis

techniques. The studies by Tuncer and Platzer [91,92] investigated NACA 0012 airfoils undergoing a pure plunging, pure pitching or combined pitching and plunging kinematics in forward flight. Their results showed that thrust producing kinematics were dependent on the plunge amplitude (h_{amp}) and reduced frequency. Reduced frequency is defined as $k = \frac{2\pi f \bar{c}}{2*U_\infty}$ where $\bar{c}$ is the mean chord, f is the oscillating frequency and U_∞ is the freestream flow speed. Thrust is produced when the non-dimensional plunge velocity ($V_h = k * h_{amp}$) exceeds 0.2. In addition, combined pitching and plunging kinematics were shown to produce high propulsive thrusts as well as high propulsive efficiencies.

Kang et al. experimentally and computationally investigated the pitching and plunging of 2D SD7003 airfoils for a range of Reynolds numbers [93]. Overall, the Reynolds number effects were seen to be minimal when tests were conducted in the range of Re = 30,000 – 60,000. For pure plunge kinematics, the LEVs formed at lower Reynolds numbers were larger. However, at higher Reynolds numbers, the flow was seen to be more attached for both pure plunge and combined pitching and plunging kinematics.

Computational studies by Ashraf et al. investigated the effect of thickness and camber on the performance of airfoils undergoing pure plunging and combined pitching and plunging kinematics [94]. The Reynolds number was varied from 200 – 2 million. At a Reynolds number of 20,000, the time-averaged thrust produced by airfoils of various cambers exhibited little difference compared to symmetric airfoils undergoing pure plunge kinematics. Overall thinner airfoils performed better at low Reynolds

numbers for both pure plunging and combined pitching/plunging. Thicker airfoils performed better at higher Reynolds numbers.

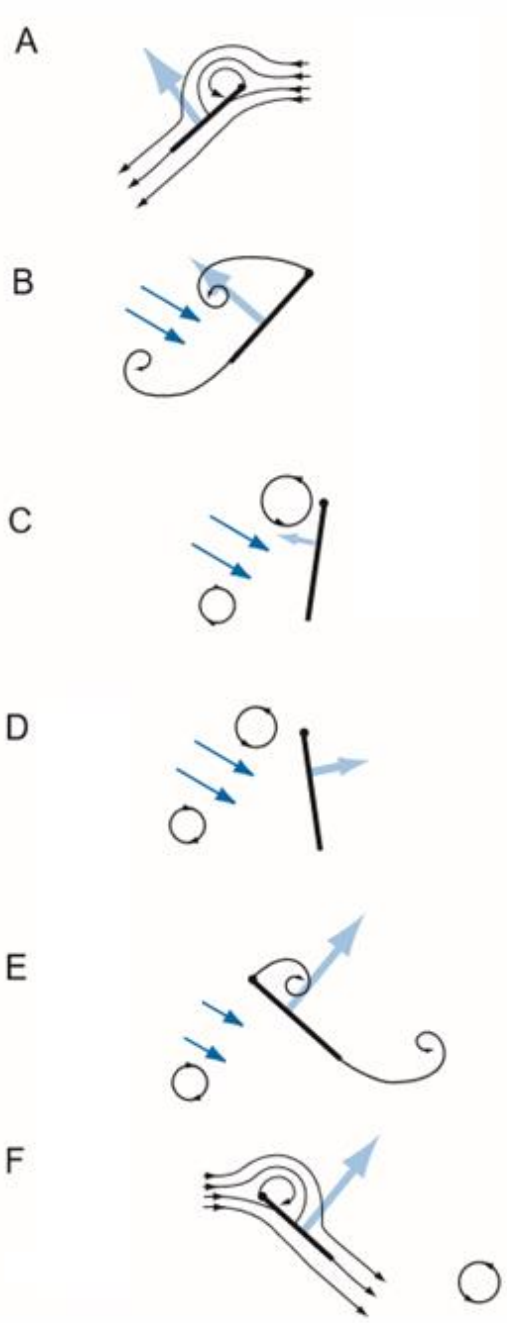

Figure 1.37: Illustration highlighted the wake capture phenomenon. Adopted from Ref. [95]

The main reason behind the variations in performance between thin and thick airfoils is how they influence the formation and movement of the LEV.

While these studies did play an important role in advancing our understanding of how unsteady mechanisms influence the production of aerodynamic force on pitching and plunging airfoils, most focused on forward flight as opposed to the hover flight condition. Yuan et. al. conducted experimental investigations on a 2D pitching and plunging airfoil in hover in accord with 2D numerical analysis [96]. Results showed that shed vortical structures during flapping may remain near the airfoil surface and can potentially interfere with new vortex formation affecting overall aerodynamic performance. Overall, 2D analysis on rigid airfoils has provided some significant insight into the unsteady fluid dynamics of the flapping wing problem. However, the wings of many biological flyers and man-made flapping MAVs have a low aspect ratio (AR<5), thus it is expected that 3D effects could have a significant influence on the aerodynamics about the wing and should be appropriately accounted for within analysis.

Many previous 3D wing experiments were performed on rigid, dynamically-scaled mechanical models in oil or water tanks [80,90,97–100]. In a study by Birch and Dickinson, tests were performed on a dynamically-scaled *Drosophila* wing flapping in mineral oil [97]. The goal was to determine if spanwise flow is responsible for prolonged attachment of the LEV. Results showed that the LEV remained attached even when baffens were used to block spanwise flow. A follow-up study by Lentink and Dickinson [101] showed that rotational accelerations are responsible for prolonging the attachment of the LEV to the wing throughout the flap stroke.

Conducting the experiments in oil or water allows for better matching of the Reynolds numbers associated with natural flyers and MAVs while operating at much lower frequencies. Also, using a lowered operating frequency decreases the generated inertial force and its influence on the total force measured during experimentation. However, when analyzing flapping wings in air, the aerodynamic as well as inertial forces must be considered.

Seshadri et al. [102] performed studies on a rigid, low aspect ratio wing in hover. Flapping kinematics were prescribed using a dual-differential four-bar mechanism-based test rig capable of emulating complex wing kinematics including figure-eight motion. All tests were conducted in air at a constant flap frequency of 3 Hz and force as well as PIV flowfield measurements were recorded. Additionally, a blade element theory analysis was conducted in conjunction with the experimental studies. Results from the study showed that the pure aerodynamic forces can be extracted from the total force measurements subtracting the inertial forces. The formation of a LEV was observed to be the main contributor to the augmented aerodynamic forces generated by the wing.

Conducting experimental measurements on flapping wings can be difficult especially for wings at MAV-scale or flapping at high frequencies. High-fidelity computational studies allow for in-depth analysis of the flowfield and forces produced by flapping wings without the difficulty typically associated with experimental measurements. There have been several notable studies that include 3D simulations and correlation with experiments. Liu and Kawachi [103] published the first 3D Navier-Stokes simulation of insect flapping wings. Their simulation modeled the vortex

structure over a scaled mechanical flapping hawkmoth [82] and showed good qualitative agreement with smoke flow visualization. They also examined the aerodynamic characteristics of the hawkmoth and fruit fly wing shapes, focusing on the spanwise flow inside the core of the LEV [104]. Other notable examples include studies by Sun and Tang [105] and Ramamurti and Sandberg [106] on the *Robofly* wing [89]. The *Robofly* mechanical flapping apparatus has provided a wealth of force data to aid in the validation of 3D computational fluid dynamics (CFD) studies. However, there has not been much comparison of the flowfield.

More recently, studies by Badrya and Baeder [107] investigated the influence of Reynolds number, wing kinematics and aspect ratio on the aerodynamic force and power of a modeled blow fly wing (similar in shape to the *Robofly* wing). Their simulation results showed that Reynolds number and wing pitch angle have a strong effect on peak aerodynamic force production and aerodynamic power. The authors also suggest that when comparing the efficiency of flapping wings, a reasonable metric to use is lift per unit power versus lift.

Zhang et al. [108] also performed CFD studies of wings modeled after the *Robofly* wing. They assessed the influence of five kinematic parameters on lift production: flap frequency, angle of attack at mid-downstroke, angle of attack at mid-upstroke, flap amplitude and the rotation at stroke reversal. Results showed that flap frequency and flap amplitude had the biggest influence on time-averaged lift forces.

Erzincanli and Mehmet conducted CFD simulations on a pair of wings modeled after fruitfly (*Drosophila*) wings. The wing planform was designed to match that of the *Robofly* wing described in the work by Dickinson [89]. The study investigated the

effect of the wing kinematics on the flowfield and aerodynamic forces generated. The CFD solver used is an unstructured finite volume algorithm based on an Arbitrary Lagrangian Eulerian (ALE) formulation. The authors found that advanced pitch kinematics during flapping led to stronger shed vorticity from the leading edge at stroke reversal. Additionally, the root and tip vortices form earlier in the flap cycle and are longer than in the symmetrical pitching case. The root and tip vortices do not form early in the flap cycle when delayed pitch kinematics are used.

Modifications in pitch angle, stroke angle and heave angle were parametrically studied to gain insight into their effect on performance. Maximum pitch amplitude was varied from 0° – 60° and maximum lift was seen at a pitch angle of 50 degrees. Decreasing stroke amplitude reduces translational velocity and leads to weaker LEV strength. Rotational lift during stroke reversal is also reduced with reduced stroke amplitude suggesting that the created rotational lift is related to the translational velocity. For variations in heave angle, the figure-eight pattern and a constant non-zero offset from the stroke plane were seen to significantly affect the magnitude of the aerodynamic forces produced.

Jones and Yamaleev performed computational optimization studies using a 3D unsteady viscous flow solver using a time-dependent discrete adjoint methodology [109]. The study focused on how wing shape and flap kinematic parameters influence thrust and propulsive efficiency. The baseline wing was based on the wing profile of the fruit fly (*Drosophila*). Results from the series of studies conducted showed that the wing planforms are significantly different when solely optimizing the wing planform as opposed to optimizing the wing planform and flap kinematics in conjunction. A

similar statement can be made when solely optimizing the flap kinematics in comparison to optimizing the wing planform and flap kinematics in tandem. Figure 1.38 shows a comparison of the baseline wing planform, the independently optimized wing planform and the wing planform when the kinematics and planform are optimized in tandem. Figure 1.39 show results comparing the baseline flap kinematics, the independently optimized flap kinematics and the flap kinematics when the kinematics and planform are optimized in tandem. When optimizing the wing planform and flap kinematics in tandem, the time-averaged thrust coefficient increased by 70% and 380% over those values obtained by independently optimizing wing planform shape or wing kinematics separately. This suggests that to maximize improvement for a given design, the wing planform and flap kinematics should be optimized together in a coupled fashion.

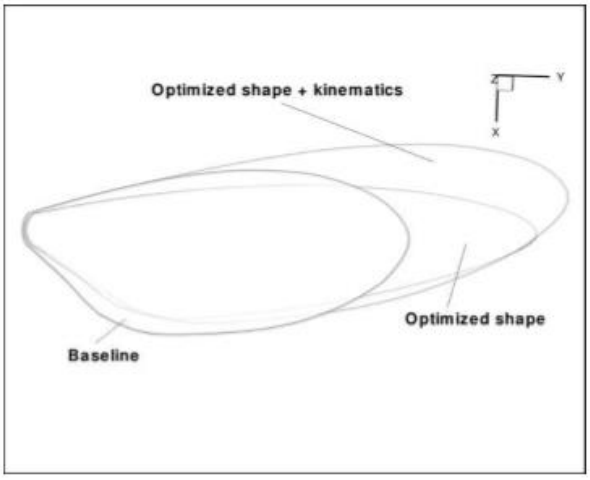

Figure 1.38: Comparison of baseline and optimized wing planforms from Ref. [109]

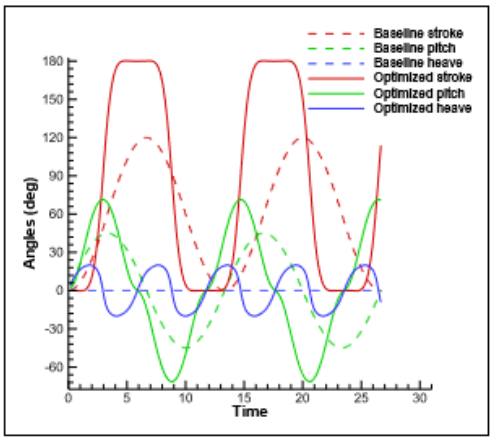

(a) Independently optimized flap kinematics

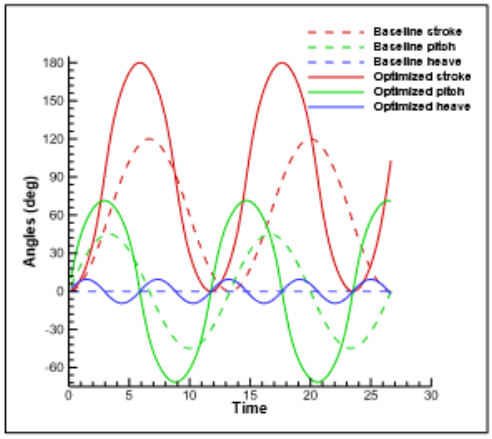

(b) Kinematics when wing planform and flap kinematics optimized in tandem

Figure 1.39: Comparison of baseline and optimized flap kinematics from Ref. [109]

Rigid flapping wing experimental and computational studies have helped to greatly improve our understanding of flapping wing flight. However, many biological and man-made flapping wings are inherently flexible due to their relatively small size and weight. Wing flexibility introduces a coupling between the fluid and structural dynamics allowing for aeroelastic effects to occur. Therefore, it is important to study flexible wings undergoing unsteady kinematics to assess the impact of aeroelastic effects on wing performance.

1.6.3 Flexible Wing Studies

Given the structural compliance of many natural and man-made flapping wings, there is an intrinsic coupling between the wing fluid dynamics and structural dynamics which allow for aeroelastic effects to occur. Aeroelasticity is the study of the interactions between inertial, elastic and aerodynamic forces that are present when an elastic body is exposed to a fluid flow. Figure 1.4 provides a Collar diagram of how the various components of aeroelastic study interact and the resulting fields of study.

Dynamic aeroelasticity comes into play when analyzing flexible flapping wings. Effectively the inertial and aerodynamic forces acting on the wing can cause it to deform which in turn influence the aerodynamic and inertial forces produced. Several experimental and numerical studies have focused on flexible wings and examined whether the wing flexibility provides benefits with respect to wing performance or efficiency.

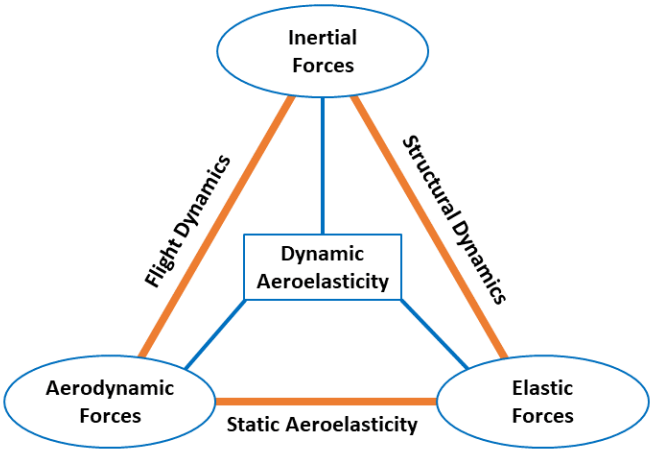

Figure 1.40: Diagram illustrating the components of dynamic aeroelasticity

Heathcote et al. [110] investigated the influence of spanwise flexibility on the performance of a pure plunging wing in forward flight. Three wings were tested which had NACA 0012 profiles and rectangular planforms with an aspect ratio of 3.0. The difference between the wings was their structural stiffness, which were categorized in the experiment as “rigid”, “flexible” and “highly flexible”. Force measurements as well as PIV tests were carried out for a range of Reynolds numbers from 10,000 – 30,000. The wings were compared based on lift and thrust production as well as propulsive efficiency. Figure 1.41 presents the experimental setup and test wings used in the study.

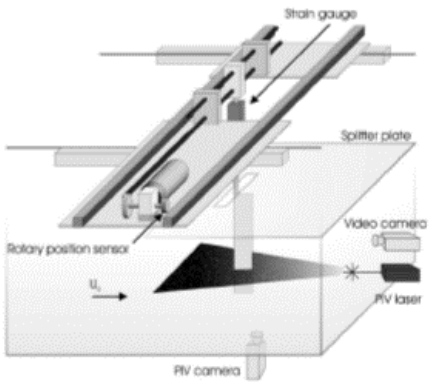

(a) Experimental test setup

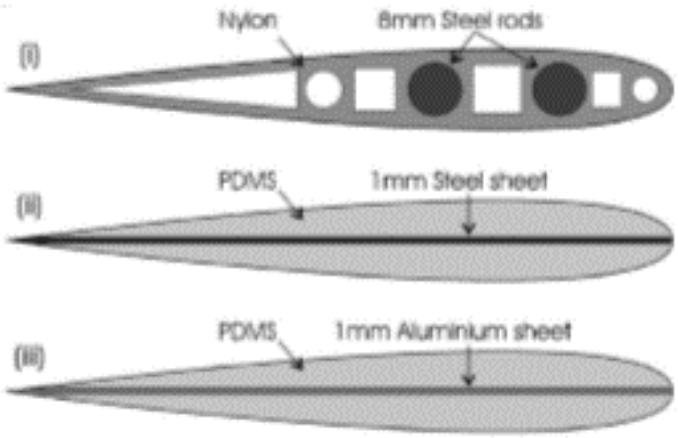

(b) Test wing airfoil cross sections

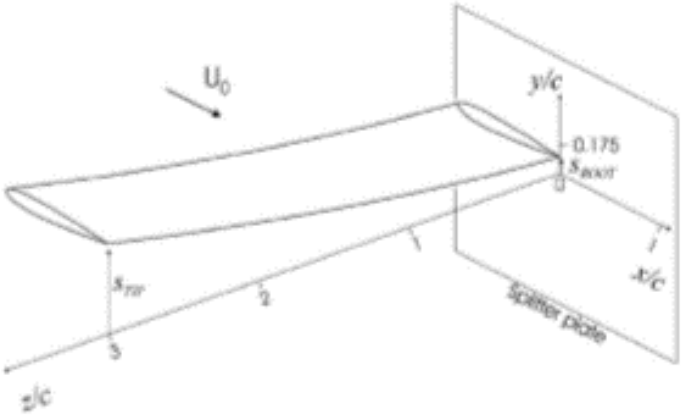

(c) Schematic of flapping wing with coordinate system

Figure 1.41: Images of experimental setup from Ref. [110]

Results showed that including a small degree of flexibility improved wing performance. The “flexible” wing was shown to generate increased thrust and have higher efficiency in comparison to the “rigid” wing. In certain cases, thrust production of the “flexible” wing was up to 50% greater than that of the “rigid” wing. However, too large a degree of flexibility proved to be detrimental to wing performance. The “highly flexible” wing exhibited a significant reduction in thrust and efficiency with respect to the “rigid” and “flexible” wings. This is due to out-of-phase displacement of the wing tip with respect to the wing root plunge motion.

Strouhal number $\left(St = \frac{2\pi fL}{2U}\right)$ is a dimensional value that relates the frequency of oscillation of a flow to the freestream velocity. Note that f is the frequency of oscillation in Hertz, U is the freestream velocity and L is a characteristic length. For Strouhal numbers greater than 0.2, wing flexibility was seen to be beneficial. This finding is in line with the Strouhal numbers of natural flyers which typically lay between 0.2 – 0.4. Later on, computational aeroelastic analysis was performed by Chimakurthi et al. [111], Gordiner et al. [112] and Malhan et al. [113] against the aforementioned study by Heathcote et al. [110] and the computational results compared well to the experimental results.

In the above study, the wings tested had spanwise flexibility. However, measurements by Combes and Daniel [79], which were discussed in Sub-section 1.6.1, showed that spanwise flexural stiffness is 1–2 orders of magnitude greater than chordwise flexural stiffness for various insect wings. This implies that while spanwise flexibility can have a significant influence on force production, chordwise flexibility may play a larger role in the aerodynamic performance of flexible wings.

Experimental and computational studies by Toomey and Eldredge [114] investigated the role of wing flexibility in flapping wings using two rigid elliptical sections connected by a hinge with a damped torsional spring. Experiments on the wing model were conducted in a water tank. The test apparatus allowed for translational as well as rotational movement of the wing. The leading-edge section was actuated under prescribed fruit fly kinematics while the trailing edge section was free to deform passively due to hydrodynamic, inertial and elastic forces. Numerically the fluid dynamics of the problem are modeled using the viscous vortex particle method with coupled fluid-body dynamics. The wing structural dynamics are written in terms of an evolution equation for hinge deflection with a linear spring-damper model.

Overall the numerical results agreed well with the experimental results when comparing lift force and hinge deflection for a variety of applied wing kinematics. The study showed that lifting force and structural deflection are primarily influenced by the nature of the wing's rotation with translational kinematics having little impact on wing deflection or force. Faster wing rotation leads to larger peak deflection and lift generation.

Heathcote et al. [115] examined the effect of chordwise flexibility on the thrust generation of pure plunging airfoils in zero freestream flow (i.e. quiescent flow). The wing has an overall chord of 90 mm and a span of 300 mm. The airfoil profile is composed of 30 mm teardrop shaped rigid airfoil profile with a thin plate of 60 mm at its trailing edge. Figure 1.42 provides a picture of the airfoil profile as well as the experimental setup. The stiffness of the thin plate was varied to create "rigid", "flexible" and "very flexible" wings. Pure plunge kinematics were prescribed to the

wing at plunge amplitudes of 5 – 25 mm and frequencies of 1.0 – 2.5 Hz. Force, PIV flowfield and wing deformation measurements were taken.

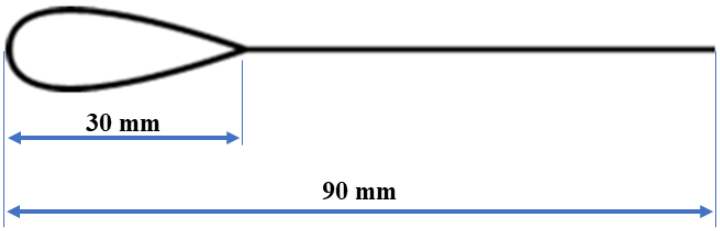

(a) Drawing of airfoil cross section

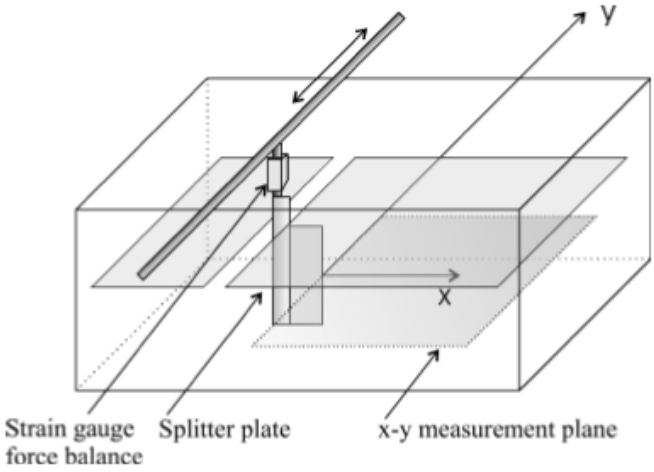

(b) Schematic of experimental setup

Figure 1.42: Illustrations of airfoil cross section and experimental setup adopted from Ref. [115]

Flowfield results showed that the vortical flow varied between the "rigid" and "flexible" cases compared to the "very flexible" case. For the "rigid" and "flexible" cases, vortex pairs were formed. For the "very flexible" case, alternating vortex sheets were formed. The amplitude and phase angle of the trailing edge, relative to the leading edge, was seen to have a significant effect on the strength and spacing of shed vorticity. Results also showed that an airfoil with intermediate stiffness (i.e. the "flexible" wing) produced the greatest thrust and the least stiff airfoil proved to be most effective at lower plunge frequencies. Figure 1.43 shows thrust coefficient versus plunge amplitude

to illustrate the previously stated conclusion. The authors suggest that there can be an optimum airfoil stiffness distribution for maximum thrust generation for a given set of flow conditions, plunge frequency and plunge amplitude.

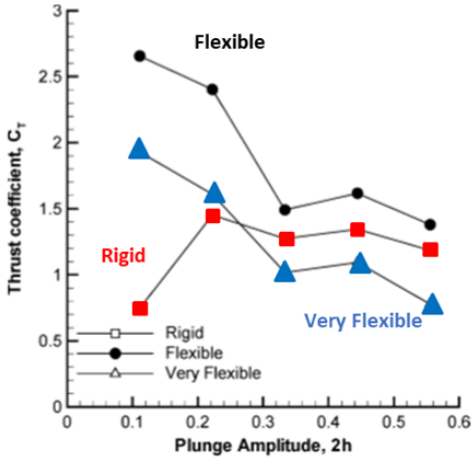

Figure 1.43: Plot of thrust coefficient versus plunge amplitude from Ref. [115]

Conducting 2D numerical analysis of flexible airfoils can provide additional insight into which parameters would improve aerodynamic performance. Work by Yin and Luo sought to investigate 2D flexible flat plate airfoils in hover via numerical analysis [116]. The flow solver used in the study employs the viscous, incompressible Navier-Stokes equations and the wing structure is modeled as a cantilever beam. The airfoil is subjected to pure plunging as well as combined plunging and pitching motion with the pitching occurring at the leading edge. The goal of the study was to investigate the influence of wing inertia and flexural stiffness on lift, drag and power consumption.

The mass ratio (m^*) and frequency ratio (ω^*) were used to parameterize the study. Mass ratio is defined as $\left(m^* = \frac{\rho_s h}{\rho_f c}\right)$ where ρ_s is the surface density of the wing, h is the wing thickness, ρ_f is the density of the air and c is the chord length of the wing. The

frequency ratio is defined as $\left(\omega^* = \frac{2\pi f}{\omega_n}\right)$ where f is the plunge frequency and ω_n is the natural frequency of the flat plate airfoil. Note that the natural frequency of the airfoil is related to its stiffness by $\omega_n = \left(\frac{k_n^2}{c^2}\right)\sqrt{\frac{E_B}{\rho_s h}}$ where E_B is the Young's modulus and k_n is a constant for the first natural frequency, which equals 1.8751. Physically, m^* is the ratio between the inertial force of the wing and aerodynamic pressure and ω^* relates wing rigidity to the frequency of motion.

For cases where there is no active pitching of the wing, wings with a higher mass ratio show peak lift force when flapped near resonance. However, for low mass ratios, peak lift if shown to occur at lower flap frequencies. When analyzing lift-to-drag ratio, lower mass ratios outperform higher mass ratios when rigidity is kept constant. For all mass ratios tested, the best lift-to-power ratio occurs at a frequency ratio of approximately 0.5. When some active pitch rotation of the wing is included along with wing translation, the optimal lift-to-power ratio for the wing occurs near a frequency ratio of 0.4. This suggests that introducing some active pitching reduces the power requirement and improves power efficiency. For near equivalent wing deformations, low mass ratio wings outperform high mass ratio wings when comparing lift-to-drag ratio and lift-to-power ratio. These results suggest that wing deformations dominated by fluid forces (i.e. low mass ratio wings) have aerodynamic advantages over inertial force dominated wing deformations (i.e. high mass ratio wings).

2D numerical aeroelastic studies by Sridhar and Kang [117] found similar conclusions with respect to the frequency ratio for optimum performance. For Reynolds

numbers on the order of 10^3, the highest lift-to-power ratios were found at a frequency ratio of 0.53.

Hua et al. [118] performed similar studies over various heave amplitudes, bending stiffnesses, mass ratios and Reynolds numbers. The propulsive efficiency increases with increased bending stiffness up to an optimal value after which the propulsive efficiency begins to decrease. Flexibility allows for the wing to store elastic potential energy when deformed. A correlation was found between the peak storage of elastic potential energy and peak propulsive efficiency.

The previously discussed studies have provided insight into the effect of chordwise flexibility on flapping wing performance, however most studies only focused on the temporal or spanwise variation of wing deformation. The previous experiments investigating chordwise flexible wings were designed to exhibit the same degree of structural deformation across the entire wing span and the 2D numerical studies would not account for 3D wing deformations. Studies measuring the deformation of a hoverfly wing in free-flight by Walker et al. [119] show that actual flapping wings undergo significant variations in twist and camber along the span during flight.

Wu et al. [120] performed force and structural deformation measurements on a set of flapping wings in hover. The wings were constructed to have a Zimmerman planform with an aspect ratio of 7.62, length of 75 mm and root chord of 25 mm. Note that the Zimmerman planform is composed of two quarter ellipses in which the semi-major axes coincide. The semi-minor axis of the first quarter ellipse makes up the first ¼ chord of the wing and the semi-minor axis of the second quarter ellipse makes up

the remaining ¾ chord. An image of a Zimmerman planform can be seen in Fig. 1.44. Four wings were tested with the structural design of each wing being varied. Wings were actuated using a four-bar mechanism with a flap amplitude of ±35° at flap frequencies of 5 – 35 Hz.

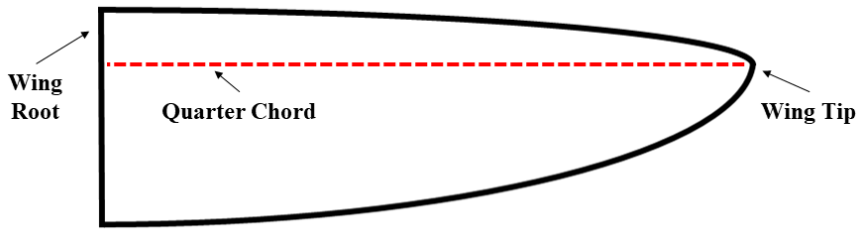

Figure 1.44: Example image of a Zimmerman planform

Results showed that chordwise stiffness needs to be an order of magnitude lower than spanwise stiffness to achieve maximum lift. Wing deformation was dominated by aerodynamic forces during midstroke and inertial forces at stroke reversal. Lift was seen to vary quadratically with flap frequency similar to how lift varies quadratically with velocity in steady-state flight. Stiffer wings tended to produce greater thrust at higher flap frequencies and more flexible wings produced greater thrust at lower flap frequencies. These conclusions were supported by many of the flexible wing studies previously discussed. However, there was no accompanying numerical analysis with the experimental results.

Malhan et al. [121] also performed experimental tests on flapping wings in hover as well as forward flight. Force measurement studies were conducted on a custom four-bar flapping mechanism to determine the time-averaged aerodynamic forces produced. In hover, rigid wings with passive pitch modulation and flexible wings with torsional compliance produced net positive vertical lift. In forward flight, flexible wings with

torsional compliance or rigid wings with asymmetric pitching between the upstroke and downstroke were shown to generate net positive lift in addition to thrust.

Singh and Chopra [122] performed force experiments on a biomimetic flapping mechanism outfitted with several different wing designs. Figure 1.45 shows the flapping mechanism. The device was capable of hover flap kinematics in which the wing orientation would flip at stroke reversal. The wings tested were designed with the planform of insect wings as well as a rectangular planform. In addition, an aeroelastic analysis was created to model flapping wing behavior. In the aeroelastic analysis, structural finite elements are coupled with an unsteady aerodynamics model based on indicial functions.

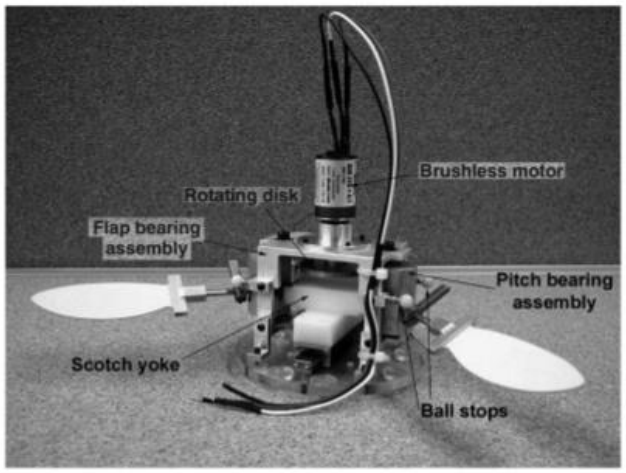

Figure 1.45: Biomimetic flapping mechanism presented in Ref. [122]

Wing flexibility was shown to have a significant effect on performance. The wing with no rigid support at the trailing edge was able to produce the most lift for the range of tested flap frequencies. Further increase of wing flexibility was seen to be detrimental to lift generation. The experimental results were compared to the predicted results from the coupled aeroelastic analysis and showed general correlation. However,

there were some nonlinear effects that weren't adequately captured in the prediction highlighting the need for detailed computational fluid dynamics and structural dynamic analysis when modeling flexible flapping wing flight.

Work by Willis et al. [123] sought out to design a suite of software packages capable of evaluating flapping wing flight performance using models with a range of fidelities. The modeling tools within the software suite included: vortex lattice wake only models (*HallOpt*), lifting line theory-based flight dynamics model coupled with nonlinear beam elements (*ASWING*), a potential flow solver with unsteady boundary elements (*FastAero*) and a Navier-Stokes solver (*3DG*). The authors suggest that lower fidelity tools can be used to more quickly explore the design space of potential flapping wing configurations. While they may not be as accurate as higher fidelity methods, they benefit from having a low computational cost. Higher fidelity methods can then be used to more thoroughly explore a given design and provide additional details at the expense of increased computational cost.

Work by Vanella et al. [124], Fitzgerald et al. [125], Roccia et al. [126] and Preidikman et al. [127] focused on developing and validating a coupled aeroelastic analysis combining an unsteady vortex lattice method (UVLM) with beam element models. In Ref. [125], simulations were run on a segmented airfoil connected by a torsion spring and subjected to prescribed motion. The results from the UVLM based solver are compared to those where the fluid dynamics are solved using direct numerical simulation (DNS). While UVLM is not as high-fidelity as DNS, it has a substantially lower computational cost. The UVLM-based results tended to over-predict the mean lift and drag values in comparison to those predicted using DNS.

However, the UVLM-based solver was able to qualitatively capture most of the flow features predicted using DNS. The lower fidelity UVLM may suffice for capturing the flow physics qualitatively, but higher fidelity methods may be needed to more accurately predict the aerodynamic forces.

Chimakurthi et al. worked to create a high-fidelity, coupled aeroelastic analysis at the University of Michigan [111,128]. Their in-house Navier-Stokes solver (*STREAM*) was coupled with their in-house finite elements solver (*UM/NLABS*). The work describes the formulation of the two solvers independently as well as the means of coupling the solvers together. Special attention was paid to describing the formulation of the co-rotational plate elements used within the structural model. Several validations studies were conducted with the results from the newly developed solver agreeing adequately with previous studies. However, the flexible wing cases against which the solver was validated against only exhibited low to moderate levels of wing deformation and had an isotropic structural makeup. Flapping wing structures in real-world applications typically have anisotropic structural makeups with the structural properties differing at various points along the wing. Man-made flapping wings can be composed of a variety of materials with vastly different stiffnesses, mass distributions, etc.

Malhan et al. [113] worked on creating a coupled aeroelastic solver at the University of Maryland. An in-house, compressible Navier-Stokes solver was combined with an open-source multi-body dynamics solver. Both are discussed in more detail in Chapter 2. Initial validation studies were conducted on the individual solvers

as well as the coupled solver. The goal was to utilize the solver to analyze flapping wings in forward flight.

Studies by Mayo et al. [129,130], also at the University of Maryland, looked at the aerodynamic flowfield produced by rigid and flexible wings undergoing avian-like flapping kinematics in forward flight. By design, the flexible wings tested had anisotropic structural properties. PIV measurements as well as time-averaged force measurements were recorded and compared to predicted results from a high-fidelity coupled aeroelastic analysis. The measured and predicted flowfields showed good correlation for the range of flap frequencies tested. One of the key conclusions from the studies was that chordwise wing flexibility increased aerodynamic performance and, unlike a purely rigid wing at a fixed pitch angle, allowed for simultaneous production of net positive lift force and propulsive thrust for the wing configurations tested.

Past studies on biological flyers as well as experimental flapping wings have shown that the presence of flexibility improves aerodynamic force production and efficiency in comparison to a rigid wing. However, there is still limited understanding of the complex, unsteady flow inherent to flapping wings and how wing flexibility influences the formation of aerodynamic flow and, consequently, force production over time.

1.7 Need for New Experimental Data and Aeroelastic Analysis

Currently flapping wing micro air vehicles (FMAVs) are designed in an ad-hoc, trail-and-error manner. Typically, the wings are designed to match a given thrust

requirement at a specific operating frequency. Incremental changes are made to the designs until the requirements are met with little attention to determining a more optimum design. For example, the Nano Hummingbird, developed by AeroVironment [51], was presented in 2011 and is currently one of the most successful flapping wing MAVs developed to date. A team of engineers worked over the course of 4 years with a program cost of about $4 million dollars toward the design and development of the Nano Hummingbird. Throughout the life of the program, nearly 300 wing designs were experimentally tested for the vehicle. A sample set from the 300 wings tested can be seen in Fig. 1.46.

Figure 1.46: Sample set of test wings from the Nano Hummingbird program [51]

Even with the increased level of flapping wing research since the debut of the Nano Hummingbird, the design approach for flapping wing MAVs has changed very little. In the design and development of the robotic hummingbird flapping-wing MAV from Texas A&M University, over 50 wings were tested before the final design was chosen [52]. Not only is this a time consuming and financial costly process, but it shows our lack of understanding with respect to flapping wing flight.

At this time there are no baseline design principles with regard to flapping wing MAV design. A combination of systematic experimentation and high-fidelity computational analysis can aid in formulating such principles. There is a scarcity of experimental studies on flexible flapping wings which are structurally characterized and undergo significant structural deformations during actuation. Flexible flapping wing studies have been conducted in the past, but most of them examined a limited number of characteristic datasets (i.e. aerodynamic force, flowfield, wing deformation measurements). Others examined wings with low-to-moderate levels of flexibility which would not undergo the large, nonlinear wing deformations seen on natural flyers and current man-made FMAVs. This is mainly due to the difficulty associated with accurately conducting such experiments.

Numerical aeroelastic analysis can provide a wealth of knowledge and understanding that may be difficult to acquire solely through experimentation. A viable flapping wing analysis must accurately predict the expected aeroelastic phenomena that would occur in the real world. To achieve this, both the structural dynamics solver and fluid dynamics solver will need to have adequate fidelity to capture the nonlinear wing deformations and the unsteady, highly vortical 3D flow about the wing. Also, validation against experimental studies on highly flexible flapping wings for a range of datasets is necessary demonstrate the accuracy of predictions. Other aeroelastic solvers have utilized simplified aerodynamic and/or structural models to decrease solver complexity or reduce computational cost. However, the level of accurate predictive capability generally suffers.

Furthermore, the aeroelastic solver must be able to handle a wide-range of aeroelastic flow problems while accurately and reliably facilitating the transfer of information between the structural dynamics and fluid dynamics solvers. Especially when utilizing Navier-Stokes solvers with grids representing the wing, the mesh must be able to deform appropriately and maintain reasonable grid quality. High-fidelity aeroelastic analysis in conjunction with in-depth experimentation can aid in dramatically improving the performance and fundamental understanding of current flapping-wing designs. Insights gained from such work would be vital in the pursuit of designing and developing next-generation FMAVs.

1.8 Research Objectives and Approach

1.8.1 Research Objectives

The goal of this study was to develop a high-fidelity aeroelastic solver capable of modeling flexible flapping wings undergoing significant deformation during flapping. A series of test cases were used to validate the coupled aeroelastic analysis including in-house experimental data and available computational results and test data. New experimental tests were conducted in-house for specific configurations and flight conditions. The wings in the test cases were structurally characterized so that the structural and geometric properties of the wing could be properly represented in the structural model. The coupled solver was validated against multiple data cases including aerodynamic force-time history, flowfield and wing deformation measurements. The focus of the validation studies was to determine how well the

aeroelastic solver predicts the unsteady, aeroelastic phenomena inherent to flexible flapping wing flight. Lastly, the coupled CFD/CSD solver was used to better understand how wing flexibility and structural design influence wing performance.

The objectives of this research are listed below:

1. Develop a high-fidelity coupled CFD/CSD aeroelastic solver capable of modeling MAV-scale, flexible flapping wings in hover
2. Perform systematic experiments on structurally characterized, MAV-scale flexible flapping wings in hover to measure various attributes including flowfield development, aerodynamic force production and wing deformation
3. Validate the coupled CFD/CSD aeroelastic solver against the measured experimental to assess its predictive capability with respect to wing performance and related aeroelastic phenomena
4. Utilize the coupled CFD/CSD aeroelastic solver to study the effect of wing structural design on flapping wing aerodynamic performance

1.8.2 Organization of the Dissertation

This work is focused on modifying and improving an existing coupled CFD/CSD aeroelastic methodology to enable it to model highly flexible flapping wings in hover that may undergo significant structural deformations during flapping. Additionally, in-house experimental tests were performed on various sets of structurally characterized, MAV-scale flexible flapping wings in which aerodynamic forces, velocity fields or wing deformations were measured. The experimental tests provided a series of datasets against which to validate the predictive capability of the coupled solver. Ultimately the goal of this study is to utilize the coupled CFD/CSD solver to better understand the

physics behind flapping wing flight and how wing design influences aerodynamic performance. The hope is that this tool can be used to aid in the design of future MAV concepts. The breakdown of the organization of the dissertation is as follows:

- Chapter 1 provides the motivation as to the importance of further developing MAVs and potential uses of the technology. The current types of MAV configurations are discussed as well as previous experimental and numerical research associated with MAVs.
- Chapter 2 provides a description of the coupled computational methodology. The first section describes the governing equations associated with the aerodynamic portion of the problem and how they are solved. The second section describes the governing equations of the structural dynamics portion of the problem. Efforts also focus on describing the numerical solvers used throughout the study. The third section describes the coupling strategy used to exchange relevant information between the two solvers while the fourth section details the mesh deformation techniques used within the coupled aeroelastic analysis.
- Chapter 3 describes the series of initial validation studies conducted with the computational solver. First the CFD and CSD solvers are validated independently. Next the coupled solver is validated against cases where the wing in question has a degree of structural compliance. In the first flexible wing case, the wing has a low level of wing flexibility. In the second flexible wing case, the wings in question are designed to have moderate to high level of wing flexibility.

- Chapter 4 describes a combined experimental and computational study on a chord-wise flexible flapping wing. The experimental setup and the computational model are discussed. Experimental measurements included PIV velocity field measurements as well as passive wing deformation measurements via a VICON motion capture system. Comparisons are made between the predicted and measured datasets and the computational analysis is used to analyze aerodynamic force production.
- Chapter 5 describes a combined experimental and computational study on a structurally characterized, anisotropic flexible flapping wing. The design of the test wing is based on the wing of a flapping-wing MAV currently under development. The experimental setup and the computational model are discussed. Experimental measurements included aerodynamic force-time history measurements. The inertial force subtraction technique utilized to determine the aerodynamic forces is discussed. Additionally, passive wing deformation measurements via a VICON motion capture system. Comparisons are made between the predicted and measured datasets.
- Chapter 6 discusses the results of a parametric study conducted on the wing in Chapter 5. In the parametric study, the structural stiffness of the various wing components is varied while all other properties are kept the same. The sole influence of wing structural stiffness on aerodynamic performance is assessed. The flowfield and associated wing deformation, which ultimately affect aerodynamic force production, are analyzed to determine how changing wing stiffness affects their development.

- Chapter 7 provides an overall summary of the work as well as major conclusions to be drawn from the studies discussed throughout the dissertation. The major contributions of this work to the field are highlighted and recommendations for future work are provided.

Chapter 2 Coupled Aeroelastic Solver Methodology

This chapter details the fluid dynamics solver, structural dynamics solver and the coupling strategy employed to develop the coupled aeroelastic analysis used throughout this study. This chapter is divided into four sections. The first and second sections describe the governing equations and the numerical solvers used to handle the fluid and structural dynamics. The in-house CFD solver used is OVERTURNS and the CSD solver used is MBDyn. The third section describes the coupling strategy used to run the two solvers in tandem and exchange relevant information between the two solvers at the fluid-structure interface. Lastly, the final section details the mesh deformation techniques used within the coupled aeroelastic analysis. A new mesh deformation technique was implemented in this study to more robustly handle the large wing deformations that are expected to occur in the cases under investigation. The fourth section details how deformations are applied at the wing surface and then propagate throughout the wing mesh.

2.1 Computational Fluid Dynamics Solver: OVERTURNS

2.1.1 Flow Domain of Flapping Wing

The fluid dynamics solver used throughout this study is OVERTURNS, which is an abbreviation for OVERset Transonic Unsteady Reynolds-averaged Navier-Stokes. OVERTURNS is an unsteady, compressible flow solver capable of modeling 3D flow problems using an overset mesh system [131,132]. It was initially developed at the

University of Maryland to solve full-scale rotorcraft problems. It was later modified to simulation MAV-scale rotors and is used to analyze a series of MAV-scale flapping wing systems throughout this study.

Throughout the simulations, a single wing is modeled where the wing surface is treated as a solid wall. The far-field of the domain representing the wing is limited in extent to a few chords lengths in any direction from the wing surface. The flow solution cannot be described continuously throughout the domain but at a finite number of discrete points. In order to accurately model the flow domain, it is decomposed into smaller domains (referred to as cells) via a grid system. The flow solution is made up from the flow variables defined at each grid point and the accuracy of the flow solution is partially determined by the quality of the grid.

It can be difficult or computationally expensive to design a single grid capable of modeling a flapping wing with complex geometry as well as capture prominent flow features away from the wing surface such as shed vorticity. In OVERTURNS, the means of overcoming this difficulty is through the use of a Chimera or overset grid system. Overset grid systems allow for various components of the flow domain to be meshed independently without risk of high levels of mesh distortion [131]. The implementation of Chimera mesh system will be discussed in Section 2.1.2.

2.1.2 Mesh Generation, Connectivity and Grid Motion

The meshes used to represent the wings throughout this study are structured, body-fitted curvilinear meshes constructed using either C-O or O-O topologies. The C-O meshes are created using a hyperbolic mesh generation technique [133] in which 2D C-type meshes are formed around airfoil sections. These sections are then stacked along

the wing span at defined intervals. The C-type meshes near the wing root and wing tip are collapsed using a methodology described in Ref. [134] to create the C-O topology. The O-O meshes are generated using a 3D algebraic mesh generator [132]. The O-O meshes are created by supplying the mesh generator with the surface geometry of the wing. Grid points are then created expanding normal to the wing surface. Figure 2.1 illustrates a C-O topology wing mesh and an O-O topology wing mesh. The background meshes used to capture the shed wake from the wing are created using a Cartesian mesh generator. 2D Cartesian grid are created with the grid spacing, length and height defined by the user. The 2D grid is then replicated and stacked in the spanwise direction for the number of instances defined by the user. Figure 2.2 provides an example of a Cartesian background mesh.

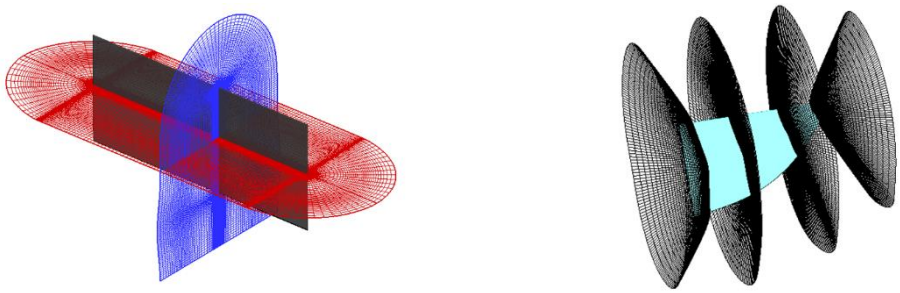

(a) C-O topology mesh (b) O-O topology mesh

Figure 2.1: Examples of C-O and O-O topology meshes

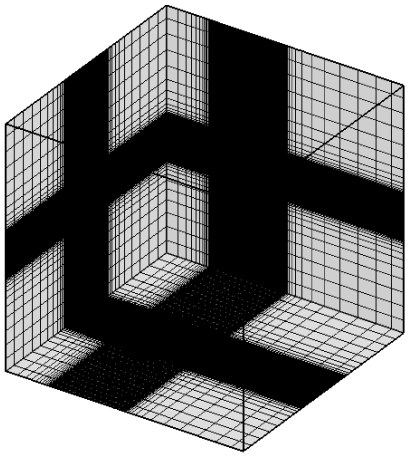

Figure 2.2: Example of Cartesian background mesh

In the simulations carried out in this study, the wing mesh is embedded within the background mesh where the background mesh is used to better capture the shed vorticity from the wing. A Chimera methodology is used to exchange information between the wing and background meshes and can be broken down into three steps: (1) performing “hole cutting”, (2) determine the hole points and chimera boundary points, and (3) finding donor cells and interpolation factors.

A hole-cutting technique is applied to identify grid points which lay inside a “hole” region of a given arbitrary shape (e.g. the geometry of the blade surface). These points are “blanked out” within the flow solver and the flow equations are not solved in this region. If the difference in grid resolutions between the body and background meshes at the fringe of the hole are too large, the hole is expanded and resized to capture points with a more favorable grid resolution. Once the hole points are defined, the hole fringe points are determined. Next, the Chimera points are defined on the body mesh. Chimera points are points on the body mesh that require information from the background mesh and are typically expressed explicitly by the user. After determining

the hole fringe and Chimera points, the donor cells are search for and information is linearly interpolated from the donor cells to the receiver cells.

While the preceding paragraph provides a general, overall description of hole-cutting, the implicit hole cutting (IHC) method described by Lee and Baeder [135] and later modified in Ref. [131] is utilized in this study. The IHC method allows for the solver to determine the optimum sized "hole" to cut from the background mesh. This allows for ease of use because the user does not need to explicitly state the position of the hole to cut. The IHC method also aids in ensuring that the difference in grid resolution between the donor and receiver cells is minimal. A more detailed description of the hole-cutting procedure can be found in Ref. [131].

Insect wing motion is very complex involving wing flapping, pitching as well as deviations out of the stroke plane. Additionally, in the case of highly flexible wings, the wing may significantly twist and deform during flapping. In the CFD solver, wing motion is decomposed into root flapping and wing pitching. Typically, the cases discussed will be explicitly prescribed root flapping or a combination of root flapping and wing pitch kinematics. In the case of flexible wings, the structural deformation at the wing surface determined from the CSD solver are applied to the CFD mesh wing surface using the methods described in Section 2.3.

2.1.3 Navier-Stokes Equations

For each grid point in the flow domain, the flow solution is determined by the solving the flow equations. The flow equations are a mathematical representation of the conservation laws of physics (i.e. conservation of mass, momentum and energy). When defined as a system of partial differential equations (PDEs), the system is

referred to as the Navier-Stokes equations. The flow is assumed to be a compressible, non-reacting, ideal gas. The strong conservative form of the 3D unsteady compressible Navier-Stokes equations, in Cartesian coordinates, are given by:

$$\frac{\partial Q}{\partial t}+\frac{\partial F_i}{\partial x}+\frac{\partial G_i}{\partial y}+\frac{\partial H_i}{\partial z}=\frac{\partial F_v}{\partial x}+\frac{\partial G_v}{\partial y}+\frac{\partial H_v}{\partial z}+S \tag{2.1}$$

where Q is the vector of conserved variables, F_i, G_i, H_i are the inviscid flux vectors and F_v, G_v, H_v are the viscous flux vectors. S represents the vector of source terms that can include body forces as well as centrifugal or Coriolis accelerations if the equations are defined in a non-inertial reference frame. The vector of conserved variables, Q, is given by:

$$Q=\begin{Bmatrix}\rho\\ \rho u\\ \rho v\\ \rho w\\ E\end{Bmatrix} \tag{2.2}$$

where ρ is fluid density, (u, v, w) are the velocity components in x, y and z directions of the Cartesian reference frame. E is the total energy per unit volume and is defined as:

$$E=\rho[e+0.5(u^2+v^2+w^2)] \tag{2.3}$$

where e is the internal energy per unit mass. The inviscid and viscous flux vectors are given by:

$$F_i=\begin{Bmatrix}\rho u\\ \rho u^2+p\\ \rho uv\\ \rho uw\\ (E+p)u\end{Bmatrix} \tag{2.4}$$

$$G_i = \begin{Bmatrix} \rho v \\ \rho vu \\ \rho v^2 + p \\ \rho vw \\ (E + p)v \end{Bmatrix} \tag{2.5}$$

$$H_i = \begin{Bmatrix} \rho w \\ \rho wu \\ \rho wv \\ \rho w^2 + p \\ (E + p)w \end{Bmatrix} \tag{2.6}$$

$$F_v = \begin{Bmatrix} 0 \\ \tau_{xx} \\ \tau_{yx} \\ \tau_{zx} \\ u\tau_{xx} + v\tau_{yx} + w\tau_{zx} - q_x \end{Bmatrix} \tag{2.7}$$

$$G_v = \begin{Bmatrix} 0 \\ \tau_{xy} \\ \tau_{yy} \\ \tau_{zy} \\ u\tau_{xy} + v\tau_{yy} + w\tau_{zy} - q_y \end{Bmatrix} \tag{2.8}$$

$$H_v = \begin{Bmatrix} 0 \\ \tau_{xz} \\ \tau_{yz} \\ \tau_{zz} \\ u\tau_{xz} + v\tau_{yz} + w\tau_{zz} - q_z \end{Bmatrix} \tag{2.9}$$

where q_x, q_y and q_z are the heat conduction terms expressed as a function of temperature (T) and coefficient of thermal conductivity (k) as seen below.

$$q_j = k\frac{\partial T}{\partial x_j} \ (j = x, y, z) \tag{2.10}$$

In Stoke's hypothesis [136], the viscous stress tensor for Newtonian fluids, τ_{ij}, is defined as:

$$\tau_{ij} = \mu\left[\left(\frac{\partial u_i}{\partial x_j} + \frac{\partial u_j}{\partial x_i}\right) - \frac{2}{3}\frac{\partial u_k}{\partial x_k}\,\delta_{ij}\right] \tag{2.11}$$

where the Kronecker delta function, δ_{ij}, equals 1 if i = j and equals 0 if i ≠ j. The coefficient of molecular viscosity is given by Sutherland's formula below:

$$\mu = C_1\frac{T^{1.5}}{T + C_2} \tag{2.12}$$

where $C_1 = 1.458\times10^{-6}$ kg/(m-s-K$^{0.5}$) and $C_2 = 110.4$ K for air at standard temperature and pressure.

2.1.4 Nondimensionalized Navier-Stokes Equations

In formulating OVERTURNS, the Navier-Stokes equations described in Eqs. (2.1)–(2.12) are nondimensionalized to allow for dynamic and energetic similarity between cases with geometric similarity. Characteristic dimensional parameters such as chord length are used to nondimensionalize length while free-stream condition variables are used to nondimensionalize dependent variables. The nondimensionalized variables (denoted with the superscript *) are given as follows:

$$\begin{aligned}
x^* &= \frac{x}{c} & y^* &= \frac{y}{c} & z^* &= \frac{z}{c} \\
u^* &= \frac{u}{a_\infty} & v^* &= \frac{v}{a_\infty} & w^* &= \frac{w}{a_\infty} \\
t^* &= \frac{t a_\infty}{c} & \mu^* &= \frac{\mu}{\mu_\infty} & T^* &= \frac{T}{T_\infty} \\
\rho^* &= \frac{\rho}{\rho_\infty} & p^* &= \frac{p}{\rho_\infty a_\infty^2} & e^* &= \frac{e}{\rho_\infty a_\infty^2}
\end{aligned} \tag{2.13}$$

where c is the chord length of the airfoil, a is the speed of sound and the subscript ∞ denotes free-stream condition variables. Note that the nondimensional parameters Reynolds number (Re), Mach number (M) and Prandtl number (Pr) are defined below as:

$$Re_\infty = \frac{\rho_\infty V_\infty c}{\mu_\infty}$$
$$M_\infty = \frac{V_\infty}{a_\infty}$$
$$Pr = \frac{\mu C_p}{k} \tag{2.14}$$

where V_∞ is the total velocity at free-stream conditions ($V_\infty = \sqrt{u_\infty^2 + v_\infty^2 + w_\infty^2}$), C_p is the fluid's specific heat at constant pressure and Pr is assumed to equal 0.72.

If we ignore the superscript *, the nondimensional form of the Navier-Stokes equations can be represented using Eq. (2.1). The same can be said about the inviscid flux vectors in Eqs. (2.4)–(2.6). However, differences in the terms occur when comparing the dimensional and nondimensional viscous flux vectors, specifically the viscous stress tensor and the thermal conduction terms. These terms now have become functions of the Reynolds number and Prandtl number. The nondimensional viscous stress tensor and thermal conduction terms are shown below.

$$\tau_{ij}^* = \frac{\mu^* M_\infty}{Re_\infty}\left[\left(\frac{\partial u_i^*}{\partial x_j^*} + \frac{\partial u_j^*}{\partial x_i^*}\right) - \frac{2}{3}\frac{\partial u_k^*}{\partial x_k^*}\,\delta_{ij}\right] \tag{2.15}$$

$$q_i^* = -\frac{\mu^* M_\infty}{Re_\infty \mathrm{Pr}(\gamma - 1)}\frac{\partial T^*}{\partial x_i^*} \tag{2.16}$$

OVERTURNS is designed to run structured, body-fitted curvilinear meshes. Thus, it would be convenient to express the Navier-Stokes equations in a generalized

body-fitted curvilinear coordinate system, however, they are not suitable for grids with nonuniform grid spacing. This is overcome by performing a curvilinear coordinate transformation from the nonuniformly spaced physical space (x, y, z) to the computational space, defined by the coordinates ξ, η and ζ, which has uniform spacing. The transform is applied by applying the chain-rule of differentiation to the originally defined Navier-Stokes equations. The transformed equations are as follows:

$$\frac{\partial \hat{Q}}{\partial t} + \frac{\partial \hat{F}}{\partial \xi} + \frac{\partial \hat{G}}{\partial \eta} + \frac{\partial \hat{H}}{\partial \zeta} = \hat{S} \tag{2.17}$$

where,

$$\hat{Q} = \frac{1}{J} Q \tag{2.18}$$

$$\hat{F} = \frac{1}{J} [\xi_t Q + \xi_x (F_i - F_v) + \xi_y (G_i - G_v) + \xi_z (H_i - H_v)] \tag{2.19}$$

$$\hat{G} = \frac{1}{J} [\eta_t Q + \eta_x (F_i - F_v) + \eta_y (G_i - G_v) + \eta_z (H_i - H_v)] \tag{2.20}$$

$$\hat{H} = \frac{1}{J} [\zeta_t Q + \zeta_x (F_i - F_v) + \zeta_y (G_i - G_v) + \zeta_z (H_i - H_v)] \tag{2.21}$$

$$\hat{S} = \frac{1}{J} S \tag{2.22}$$

Note that J is the Jacobian of the coordinate transformation and is defined below.

$$J = \frac{\partial(\xi, \eta, \zeta)}{\partial(x, y, z)} \tag{2.23}$$

2.1.5 Reynolds-Averaged Navier-Stokes Equations

The solution of the Navier-Stokes equations, shown in Eq. (2.17), for inviscid or laminar flows doesn't present any direct challenges. However, most practical engineering flow problems, including those discussed throughout this study, exhibit turbulence. Turbulent flow involves chaotic changes in the fluid motion due to fluctuations in the fluid pressure and velocity. In order to directly simulate turbulent flows, the flow domain requires a high concentration of grid points in order to capture the various length scales of fluid fluctuation inherent to the flow problem. However, a direct, time-dependent simulation of the Navier-Stokes equations, known as Direct Numerical Simulation (DNS), is limited to simple flow conditions at low Reynolds numbers. This is due to the large computational cost associated with running DNS for turbulent flow cases.

For most engineering and physics problems, solving the Reynolds-Averaged Navier-Stokes (RANS) equations provide a means of adequately modeling turbulent flows with a significantly reduced computational cost in comparison to DNS. In the RANS equations, the flow variables are decomposed into a mean component and a fluctuating component. In this sense, any instantaneous flow variable can be written in the form $\phi = \overline{\phi} + \phi'$ where $\overline{\phi}$ is the mean component and ϕ' is the fluctuating component. The reasoning behind this is that for most engineering related problems, we are primarily concerned with the mean component of a given flow variable. For a given flow variable, the mean component is determined via Reynolds averaging which is presented below. Note that $\chi = 1$ if the variable is density or pressure. Otherwise, $\chi = \rho$

for other flow variables such as velocity, internal energy, etc. Also, by definition, the Reynolds average of the fluctuating component of a flow variable is zero.

$$\bar{\phi} = \frac{1}{\bar{\chi}} \lim_{\Delta t \to \infty} \frac{1}{\Delta t} \int_0^{\Delta t} \chi \phi(t) dt \tag{2.24}$$

The decomposed variables can be substituted into the Navier-Stokes equations in Eq. (2.1) and subsequently Reynolds averaged leading to a new set of governing equations. If the overbar representing the mean flow components is ignored, the newly formed set of equations are nearly identical to the ones in Eq. (2.1). However, new terms arise due to the turbulent fluctuating quantities and act as an added stress tensor in Eq. (2.11). The new stress terms are referred to as the Reynolds stress tensor and are described below.

$$\tau_{ij}^R = -\rho \overline{u_i' u_j'} \tag{2.25}$$

However, by Reynolds averaging the Navier-Stokes equations and introducing the Reynolds stress terms, we introduce six additional unknowns into the equations. In order to provide closure of the RANS equations, the Reynolds stress terms must be represented using mean flow variables. Turbulence models can be used to provide closure and details of the turbulence model used throughout this study are described in Sub-section 2.1.8.

2.1.6 Spatial Discretization

OVERTURNS employs a cell-averaged finite volume technique to discretize the terms in Eq. (2.17). In the finite volume approach, a control volume is formulated around a given grid point using the midpoints of the lines joining adjacent grid points

to the current grid point. Fluxes are evaluated at the faces of this control volume and Eq. (2.26) shows a semi-discrete approximation of Eq. (2.17).

$$\frac{\partial \hat{Q}}{\partial t} = -\frac{\hat{F}_{j+\frac{1}{2}} - \hat{F}_{j-\frac{1}{2}}}{\Delta\xi} - \frac{\hat{G}_{k+\frac{1}{2}} - \hat{G}_{k-\frac{1}{2}}}{\Delta\eta} - \frac{\hat{H}_{l+\frac{1}{2}} - \hat{H}_{l-\frac{1}{2}}}{\Delta\zeta} + \hat{S}_{j,k,l} \qquad (2.26)$$

Note that (j, k, l) are the indices which correspond to the curvilinear coordinate directions (ξ, η, ζ) in the computational space. The control volume interfaces, defined by (j ± ½, k ± ½, l ± ½), are the points at which the inviscid and viscous fluxes are calculated. In the spatial discretization, the aforementioned fluxes are calculated at the control volume interface for each grid point in the computational domain. Figure 2.3 provides a 2D representation of a control volume and the control volume faces.

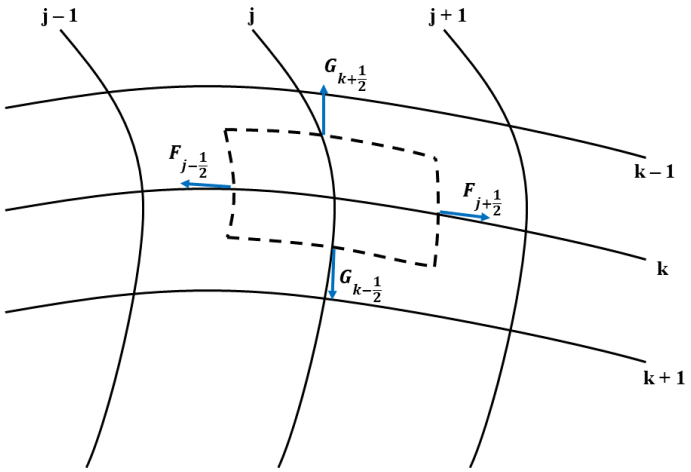

Figure 2.3: 2D illustration of control volume in the computational domain

The inviscid flux terms are calculated using a third-order Monotone Upstream-Centered Scheme for Conservation Laws (MUSCL) scheme [137]. This scheme can be broken down into two steps. In step one, the left state (Eq. (2.27)) and right state (Eq. (2.28)) at each interface are evaluated using the values at the cell center.

$$q^{L}_{i+\frac{1}{2}} = \bar{q} + \phi_i \left[\frac{1}{3}(\bar{q}_{i+1} - \bar{q}_i) + \frac{1}{6}(\bar{q}_i - \bar{q}_{i-1})\right] \tag{2.27}$$

$$q^{R}_{i-\frac{1}{2}} = \bar{q} + \phi_i \left[\frac{1}{3}(\bar{q}_{i+1} - \bar{q}_i) + \frac{1}{6}(\bar{q}_i - \bar{q}_{i-1})\right] \tag{2.28}$$

In Eqs. (2.27) and (2.28), ϕ_i is Koren's differentiable limiter [138] and is used to limit the high order reconstruction so that the scheme is third order accurate in smooth regions and utilizes lower order accuracy in high gradient regions. Koren's limiter is defined below:

$$\phi_i = \frac{3\Delta\bar{q}_i\nabla\bar{q}_i + \varepsilon}{2(\Delta\bar{q}_i - \nabla\bar{q}_i)^2 + 3\Delta\bar{q}_i\nabla\bar{q}_i + \varepsilon} \tag{2.29}$$

where ε is a small number used to prevent division by zero and Δ and ∇ are forward and backward difference operators such that $\Delta\bar{q}_i = (\bar{q}_{i+1} - \bar{q}_i)$ and $\nabla\bar{q} = (\bar{q}_i - \bar{q}_{i-1})$. In step two, the fluxes at the interface are calculated using the Roe flux difference splitting scheme [139] shown below.

$$F(q^L, q^R) = \frac{F(q^L) + F(q^R)}{2} - \left|\hat{A}(q^L, q^R)\right| \frac{q^R - q^L}{2} \tag{2.30}$$

F_L and F_R are the fluxes at the left and right states, respectively, and $\hat{A}$ is the Roe-averaged Jacobian matrix.

The viscous flux terms, in terms of the computational space coordinate system, contain derivatives of the form:

$$\frac{\partial}{\partial\xi}\left(\alpha\frac{\partial\beta}{\partial\eta}\right) \tag{2.31}$$

These terms are evaluated using a second order central differencing scheme which is shown below.

$$\frac{1}{\Delta\xi}\left[\left(\alpha_{j+\frac{1}{2},k}\frac{\beta_{j+\frac{1}{2},k+1}-\beta_{j+\frac{1}{2},k}}{\Delta\eta}\right)-\left(\alpha_{j-\frac{1}{2},k}\frac{\beta_{j-\frac{1}{2},k}-\beta_{j-\frac{1}{2},k-1}}{\Delta\eta}\right)\right] \tag{2.32}$$

$$\alpha_{j\pm\frac{1}{2},k}=\frac{\alpha_{j,k}\pm\alpha_{j\pm1,k}}{2} \tag{2.33}$$

$$\beta_{j\pm\frac{1}{2},k}=\frac{\beta_{j,k}\pm\beta_{j\pm1,k}}{2} \tag{2.34}$$

2.1.7 Time Marching

The spatial discretization of the fluxes on the right-hand side (RHS) of Eq. (2.26) were described in Sub-section 2.1.6. In OVERTURNS, an implicit time marching scheme is utilized due to their improved numerical stability and convergence characteristics over an explicit time marching scheme. A second order accurate backwards in time method, also known as BDF2, is performed on Eq. (2.26) resulting in the equation below:

$$\frac{\partial\hat{Q}^{n+1}}{\partial t}=-\frac{\hat{F}^{n+1}_{j+\frac{1}{2}}-\hat{F}^{n+1}_{j-\frac{1}{2}}}{\Delta\xi}-\frac{\hat{G}^{n+1}_{k+\frac{1}{2}}-\hat{G}^{n+1}_{k-\frac{1}{2}}}{\Delta\eta}-\frac{\hat{H}^{n+1}_{l+\frac{1}{2}}-\hat{H}^{n+1}_{l-\frac{1}{2}}}{\Delta\zeta}+\hat{S}^{n+1}_{j,k,l} \tag{2.35}$$

The left-hand side of the equation is defined below.

$$\frac{\partial\hat{Q}^{n+1}}{\partial t}=-\frac{3\hat{Q}^{n+1}-4\hat{Q}^{n}+\hat{Q}^{n-1}}{2\Delta t} \tag{2.36}$$

In Eqs. (2.35) and (2.36), n+1, n and n-1 represent the given term at the new timestep, current timestep and previous timestep respectively. In Eq. (2.35), all the terms are desired at the new timestep, but due to the implicit nature of the scheme, the fluxes are not known at the new timestep (n+1). Thus, these terms are linearized so that they are expressed by the fluxes and conservative variables at the current timestep (n). The terms are linearized in time about $\hat{Q}^n$ via Taylor series expansion such that:

$$\begin{aligned} \hat{F}^{n+1} &= \hat{F}^n + \hat{A}\Delta\hat{Q} + O(\Delta t^2) \\ \hat{G}^{n+1} &= \hat{G}^n + \hat{B}\Delta\hat{Q} + O(\Delta t^2) \\ \hat{H}^{n+1} &= \hat{H}^n + \hat{C}\Delta\hat{Q} + O(\Delta t^2) \end{aligned} \tag{2.37}$$

where $\hat{A} = \frac{\partial \hat{F}}{\partial \hat{Q}}$, $\hat{B} = \frac{\partial \hat{G}}{\partial \hat{Q}}$, $\hat{C} = \frac{\partial \hat{H}}{\partial \hat{Q}}$ and $\Delta\hat{Q} = \hat{Q}^{n+1} - \hat{Q}^n$. The source terms can be linearized in a similar manner. Given that the linearization is second order accurate, when paired with a second order accurate time marching scheme, the linearization does not degrade the time accuracy. The linearized form of Eq. (2.35) is given below.

$$\left[I + \Delta t(\delta_\xi \hat{A}^n + \delta_\eta \hat{B}^n + \delta_\zeta \hat{C}^n\right]\Delta\hat{Q}^n = -\Delta t\left[\delta_\xi \hat{F}^n + \delta_\eta \hat{G}^n + \delta_\zeta \hat{H}^n - \hat{S}^n\right] \tag{2.38}$$

The equation above can be simplified as

$$LHS\ \Delta\hat{Q}^n = -\Delta t\ RHS \tag{2.39}$$

where the right-hand side (RHS) represents the physics of the flow problem and the left-hand side (LHS) represents the numerical portion of the flow problem which determine the rate of convergence.

The implicit scheme chosen produces an algebraic system of equations which can be formulated in to a large, sparse banded matrix. It is computational expensive to directly invert the LHS matrix to calculate $\hat{Q}^n$. To overcome this, the LHS matrix can

be approximated and the approximation scheme used in OVERTURNS is the Lower-Upper Symmetric Gauss-Seidel (LUSGS) algorithm [140,141]. While there is some loss in the speed of convergence by using the LUSGS algorithm, it reduces the computationally cost of inverting the LHS matrix.

Note that approximation of the LHS leads to factorization errors. To remedy this, a dual time-stepping method with Newton-like sub-iterations is used in time-dependent simulations in which the transient solution needs to be computed [142]. For example, one can think of discretizing Eq. (2.26) in pseudo-time using a backwards Euler time marching method as seen below.

$$\frac{\hat{Q}^{p+1}-\hat{Q}^{p}}{\Delta\tau}+\frac{3\hat{Q}^{p+1}-4\hat{Q}^{n}+\hat{Q}^{n-1}}{2\Delta t}=-\frac{\hat{F}^{p+1}_{j+\frac{1}{2}}-\hat{F}^{p+1}_{j-\frac{1}{2}}}{\Delta\xi}-\frac{\hat{G}^{p+1}_{k+\frac{1}{2}}-\hat{G}^{p+1}_{k-\frac{1}{2}}}{\Delta\eta}-\frac{\hat{H}^{p+1}_{l+\frac{1}{2}}-\hat{H}^{p+1}_{l-\frac{1}{2}}}{\Delta\zeta}+\hat{S}^{n+1}_{j,k,l} \tag{2.40}$$

At each physical time step, n, p number of sub-iterations or pseudo-time steps are performed to march the solution forward to the next physical time step (n+1). At the first pseudo time step (i.e., p = 1), $\hat{Q}^{p}$ is set equal to $\hat{Q}^{n}$. At each pseudo time-step, the RHS is evaluated and the LHS is approximated and inverted using the LUSGS scheme. The progression of the dual time-stepping method can be thought of as solving the steady-state problem for time equals t+Δt using the flow solution at time equals t as the initial condition. Further description of the dual-stepping methodology used in OVERTURNS can be found in [131].

2.1.8 Turbulence Modeling

Throughout this study, the Spalart-Allmaras (SA) turbulence model is used to provide closure to RANS equations. In the SA model, the Reynolds stress tensor (Eq. (2.25)) is related to the mean strain by the isotropic relation, $\overline{u_i' u_j'} = -2\nu_t S_{ij}$, where ν_t is defined as the turbulent eddy viscosity. The SA model is a one equation turbulence model where the turbulent eddy viscosity is found by solving the following partial differential equation for the variable $\bar{\nu}$.

$$\frac{\partial \bar{\nu}}{\partial t} + V \cdot (\nabla \bar{\nu}) = \frac{1}{\sigma}[\nabla \cdot ((\bar{\nu} + \nu)\nabla \bar{\nu}) + c_{b2}(\nabla \nu)^2] + c_{b1}\bar{S}\bar{\nu} - c_{w1} f_w \left(\frac{\bar{\nu}}{d}\right)^2 \quad (2.41)$$

Note that eddy viscosity (ν_t) is related to $\bar{\nu}$ by the relation,

$$\nu_t = \bar{\nu} f_{\nu 1} \quad (2.42)$$

where f_{v1} is a function of $\bar{\nu}$ and the molecular viscosity ν. The variable f_{v1} is defined as:

$$f_{\nu 1} = \frac{\chi^3}{\chi^3 + c_{\nu 1}^3} \quad (2.43)$$

where $\chi = \frac{\bar{\nu}}{\nu}$ and c_{v1} = 7.1. The left-hand side of Eq. (2.41) represents the convection of the working variable at the mean flow velocity *V*. The first, second and third terms on the right-hand side represent the diffusion, production and destruction of eddy viscosity. Additional information on the SA turbulence model and details on the variables $\bar{S}$, d, σ, c_{b1}, c_{b2} c_{w1} and f_w can be found in Ref. [143].

2.1.9 Initial and Boundary Conditions

Within OVERTURNS, the governing equations the solver formulation is based on do not change from one flow problem to the next. To define a new problem,

additional information is required, specifically, initial and boundary conditions. Initial conditions are the specified flow properties (density, velocity, pressure) within the flow domain at the start of the simulation (t = 0). For the hovering flapping wing problems discussed in this study, the flow density and pressure are set to freestream conditions and the flow velocity is equal to zero.

The boundary conditions can be separated into two types: 1) physical boundaries and 2) numerical boundaries. Both types of boundary conditions specify certain conditions at specific spatial locations within the flow domain. Two physical boundary conditions used are the wall boundary condition and the far-field boundary condition. Wall boundaries represent solid surfaces within the flow domain that are exposed to the flow. Wall boundaries impose the physical condition that flow cannot pass through the defined boundary. For viscous fluids flowing pass a wall boundary, the relative velocity between the wall and the fluid in direct contact with the surface is zero which enforces the no-slip boundary condition. Far-field boundary conditions impose prescribed physical flow conditions at the fringes of the flow domain to truncate the physical domain. The far-field boundary condition should fulfill two requirements such that 1) the truncation of the domain should have no notable effect on the flow solution compared to an infinite domain and 2) outgoing disturbances must not be reflected back into the flow domain.

Numerical boundary conditions are not physical in nature but are necessary due to the mesh system or mesh topology used. Examples of numerical boundary conditions used throughout this study are wake cut and periodic boundary conditions. In the C-O and O-O topology meshes grid planes collapse onto one another. The wake cut

boundary condition imposes an explicit average of the flow solution across the collapsed planes. For the O-O mesh topology grids, periodic boundary conditions are used to transfer information between the overlap points used in making up the grid.

2.1.10 Low-Mach Number Pre-conditioning

The MAV-scale flapping wings under investigation in this study operate at low Mach numbers. OVERTURNS was initially designed to solve compressible flows in the subsonic and transonic flow regime. At low Mach numbers, which can be effectively thought of as incompressible flows, convergence of the flow solution is significantly slowed down. This is because the flow solution becomes computationally stiff due to the large differences in the eigenvalues. This difference arises because of the large ratio between the acoustic wave speed and convective wave speed for these low Mach number flows. The preconditioner used within OVERTURNS is based on that discussed by Turkel [144]. Low Mach number preconditioning with dual time-stepping is implemented using the methods discussed by Buelow et al. [145] and Pandya et al. [146].

2.2 Computational Structural Dynamics Solver: MBDyn

Typically, wings at MAV-scale are inherently flexible due to the small size and lightweight of the wings. In performing an aeroelastic analysis on flexible flapping wings, it is imperative that the computational analysis be able to accurately model the unsteady fluid dynamics as well as nonlinear structural dynamics associated with the problem. In this work, the CFD solver described in the Section 2.1 was coupled to a

high-fidelity computational structural dynamics (CSD) solver. Note that the framework through which the CFD and CSD solvers are coupled and the method through which information is exchanged at the fluid-structure interface is discussed in Section 2.3.

The CSD solver used is this study is MBDyn. MBDyn, which is short for Multi-Body Dynamics, is an open-source, general purpose multi-body dynamics solver developed at Politecnico di Milano [147]. MBDyn was chosen for this work because of its capability to model deformable bodies via finite element 1D beams and 2D shell elements. Additionally, MBDyn is designed to couple with external solvers and is capable of exchanging data between non-conformal fluid and structural domains. This section is focused on briefly discussing the formulation behind MBDyn.

2.2.1 Equations of Motion

MBDyn is designed to solve the equations of motion of constrained mechanical system by formulating the generic dynamical problem as a system of implicit Differential-Algebraic Equations (DAEs). The equations of motion are based on Newton's laws of motion, which state that the time rate of change in momentum of a body is proportional to the net applied forces acting on said body. For a given body, the linear momentum (β) and the angular momentum (γ) are described below.

$$\beta = m\dot{x} + \omega \times S \tag{2.44}$$

$$\gamma = S \times \dot{x} + J\omega \tag{2.45}$$

where m is the body mass, J is the mass moment of inertia and x is the position of the body. The variables ẋ, ω and S are, respectively, the velocity of x, angular velocity of x and first-order inertia moment with respect to x. The derivatives of Eqs. (2.44) and

(2.45), shown below, relate inertial forces and moments to the external forces and moments acting on the body.

$$\dot{\beta} = F \tag{2.46}$$

$$\dot{\gamma} + \dot{x} \times \beta = M \tag{2.47}$$

By combining Eqs. (2.44)–(2.47), the dynamics problem can be expressed as a system of ordinary differential equations (ODEs). Equation (2.48) expresses this system of equations in general implicit form.

$$f(y, \dot{y}, t) = 0 \tag{2.48}$$

Note that *y* is an array representing the unknowns and *t* represents time.

2.2.2 Algebraic Constraints

When paired with initial conditions, Eq. (2.48) becomes an initial value problem and the evaluation of such problems is relatively well established. However, for constrained dynamic problems, it may be necessary to implement kinematic constraints between various bodies. These kinematic constraints are represented in the problem using algebraic equations. The algebraic equations contribute to the equilibrium of the system through the algebraic unknowns which represent reaction forces and/or moments. Addition of these algebraic constraints to Eq. (2.48) results in the creation of a system of differential algebraic equations (DAEs) which are more difficult to solve than the previous system of ODEs. Equation (2.49) represents the implicit system of DAEs where *v* represents the algebraic unknowns and *g* represents the algebraic constraint equations.

$$\begin{cases} f(y, \dot{y}, v, t) = 0 \\ g(y, \dot{y}, t) = 0 \end{cases} \tag{2.49}$$

The difficulty in solving a system of DAEs is that differential algebraic equations can be thought of as very stiff differential equations. In order to integrate the system in time, it requires the use of implicit integration schemes that are unconditionally stable. The integration scheme used within MBDyn will be discussed in Sub-section 2.2.4.

2.2.3 Finite Rotations

The handling of finite rotations within the computational framework is key to implementing a multibody dynamics formulation. This is because 3D finite rotations are not additive meaning a given rotation cannot be expressed at the addition of two successive rotations. Instead, rotations need to be expressed as the multiplication of two rotations matrices such that $R_{a\to c} = R_{a\to b} * R_{b\to c}$.

Rotations can be represented using either a three-parameter or four-parameter parameterization. A four-parameter parameterization, such as a quaternion formulation, is appropriate when a total rotation approach is applied, and singularities need to be avoided. However, an updated rotation approach offers ease of implementation. For an updated rotation approach, the use of a four-parameter formulation is computationally more expensive than using a three-parameter formulation. Thus, a three-parameter updated rotation approach is utilized in MBDyn. A three-parameter rotation matrix is defined below:

$$R = I + \sin(\phi)\,\vec{n}\times + (1 - \cos(\phi))\vec{n}\times\vec{n}\times \tag{2.50}$$

where ϕ is the magnitude of the rotation angle, $\vec{n}$ is the vector representing the rotation axis and *I* is an identity matrix. The differentiation matrix and its determinant are given below.

$$G = I + \frac{1-\cos(\phi)}{\phi} n\times + \left(1 - \frac{\sin(\phi)}{\phi}\right) n\times n\times$$
$$\det(G) = \frac{2(1-\cos(\phi))}{\phi} \tag{2.51}$$

One drawback of the above method is that evaluation of the trigonometric terms can be computationally expensive. To increase computational efficiency, the Gibbs-Rodriguez parameters are utilized instead and are shown below.

$$g = 2\tan\left(\frac{\phi}{2}\right) n \tag{2.52}$$

Using the Gibbs-Rodriguez parameter, Eqs. (2.53) and (2.54) can be rewritten as:

$$R = I + \frac{4}{4 + g^T g}\left(g\times + \frac{1}{2} g\times g\times\right) \tag{2.53}$$

$$G = \frac{4}{4 + g^T g}\left(I + \frac{1}{2} g\times\right) \tag{2.54}$$

Note that there are no trigonometric functions present in Eqs. (2.53) and (2.54) which allows for faster computation of the matrices. More details on the rotation parametrization utilized within MBDyn can be found in Ref. [148].

2.2.4 Numerical Integration

When integrating in time an initial value problem composed of a system of DAEs, it's important that the integration scheme be A-stable as well as L-stable. An A-stable scheme is unconditionally stable and is defined as:

$$\lim_{n\to\infty} y_n = 0 \tag{2.55}$$

for all Re(λ) < 0 and a fixed, positive timestep (*h*) when applied to the problem $\dot{y} = \lambda y$. However, the use of just an A-stable scheme may result in high frequency numerical oscillations occurring in the solution which will significantly affect solution accuracy. Thus, an L-stable scheme capable of filtering out those high frequency oscillations is required. An L-stable scheme is A-stable and also satisfies the following:

$$\lim_{Re(\lambda)*h\to-\infty} |y_{n+1}/y_n| = 0 \tag{2.56}$$

Equation (2.56) states that if timestep (*h)* is positive and the system is stable (i.e. Re(λ) < 0), as *h* gets larger such that Re(λ)*h → -∞, the free oscillations within the system approach zero ($|\frac{y_{n+1}}{y_n}| = 0$).

The integration method implemented in MBDyn resembles the class of integration schemes know as implicit Runge-Kutta methods. The second-order accurate integration is a two-step method provided by the trapezoid rule such that:

$$y^{n+1} = y^{n-1} + h\left[\left(\frac{1}{2}+\delta\right)\dot{y}_{n+1} + (1-2\delta)\dot{y}_n + \left(\frac{1}{2}+\delta\right)\dot{y}_{n-1}\right] \tag{2.57}$$

where *h* is the timestep and δ is a tunable variable to adjust the weights in the function. The value of $\dot{y}_n$ is shown below.

$$\dot{y}_{n+1} = -\frac{12}{h} y_n + \frac{12}{h} y_{n-1} + 8\dot{y}_n + 5\dot{y}_{n-1} \tag{2.58}$$

A second-order accurate Crank-Nicholson formula, multiplied by the weight (1-α), is applied over the interval $[t_{n-1},t_n]$.

$$(1-\alpha)\left[y_n - y_{n-1} - \frac{h}{2}(\dot{y}_n + \dot{y}_{n-1})\right] = 0 \tag{2.59}$$

Equation (2.59) is added to the right-hand side of Eq. (2.57) resulting in the formula below.

$$\begin{aligned} y_{n+1} = {} & (1-\alpha)y_n + \alpha y_{n-1} \\ & + h\left[\left(\frac{1}{2}+\delta\right)\dot{y}_{n+1} + \left(\frac{1}{2}(1-\alpha) - 2\delta\right)\dot{y}_n + \left(\frac{\alpha}{2}+\delta\right)\dot{y}_{n-1}\right] \end{aligned} \tag{2.60}$$

The parameters α and δ are tunable and directly related to the asymptotic spectral radius (ρ) which can be defined by the user.

$$\begin{aligned} \alpha &= \frac{4\rho^2 - (1-\rho)^2}{4 - (1-\rho)^2} \\ \delta &= \frac{0.5 * (1-\rho)^2}{4 - (1-\rho)^2} \end{aligned} \tag{2.61}$$

For example, when $\rho = 1$, Eq. (2.60) resembles a Crank-Nicholson type formula.

$$y_{n+1} = y_{n-1} + h(\frac{1}{2}\dot{y}_{n+1} + \dot{y}_n + \frac{1}{2}\dot{y}_{n-1}) \tag{2.62}$$

If $\rho = 0$, Eq. (2.60) resembles a Backwards Differentiation Formula (BDF).

$$y_{n+1} = \frac{4}{3} y_n - \frac{1}{3} y_{n-1} + \frac{2}{3} h\dot{y}_{n+1} \tag{2.63}$$

Further information on the development and formulation of the integration scheme used in MBDyn can be found in Ref. [148].

2.2.5 Beam Element Formulation

Within MBDyn, an original finite volume based geometrically exact beam element is utilized [149,150]. C^0 beams elements are used because they remove the assumption of zero shear strain within the beam. However, when the zero-shear strain assumption is ignored, linear and quadratic finite beam elements can undergo a phenomenon known as shear locking. For a given load case, the shear strain predicted in the beam model can be larger than that present in a physical case. This can cause the element to reach equilibrium under smaller beam displacements, which can make the beam appear stiffer. Beams models formulated using a finite volume approach are intrinsically free of the shear locking phenomenon [149].

The equilibrium equations of the beam can be found below:

$$\begin{cases} T' + p = 0 \\ M' + T + m = 0 \end{cases} \tag{2.64}$$

where p and m are the distributed transverse loads and bending moments respectively. T and M represent the shear force and bending moment, respectively, and the superscript $(\cdot)'$ indicates a derivative with respect to the beam axis. We can think of dividing the beam into non-overlapping segments such that $L = \sum_{i=1}^{n} l_i$ where L is the total length of the beam and l_i is the length of a specified beam segment. Equation (2.64) can then be written as:

$$\begin{cases} \int_a^b w(T' + p)\, dx = 0 \\ \int_a^b w(M' + T + m) dx = 0 \end{cases} \tag{2.65}$$

where a and b represent the bounds of a given beam segment l_i and w is a constant weight function based on a weighted residual formulation. Through integration by parts we Eq. (2.65) becomes:

$$\begin{cases} wT|_a^b + \int_a^b (wp - w'T)\, dx = 0 \\ wM|_a^b + \int_a^b (wT + wm - w'M)\, dx = 0 \end{cases} \tag{2.66}$$

To fully evaluate Eq. (2.66), the following relations are need:

$$\begin{gathered} w(l - \partial l) = 1 \\ w(a^-) = w(b^+) = 0 \\ w(a) = w(b) = \frac{1}{2} \\ w(a^+) = w(b^-) = 1 \\ w' = \frac{1}{2}\delta(x - a) = \frac{1}{2}\delta(x - b) \\ \int_a^b w' f(x)\, dx = \frac{1}{2} f(a) - \frac{1}{2} f(b) \end{gathered} \tag{2.67}$$

where δ is the Dirac delta function and *f(x)* is just some function which is smooth and continuous between the bounds of a and b. After full evaluation, Eq. (2.66) works out to be:

$$\begin{aligned} \int_a^b wT\, dx &= wTx|_a^b - \int_a^b (wT)' x\, dx \\ &= T_b(b - c) - T_a(a - c) + \int_a^b px\, dx \end{aligned} \tag{2.68}$$

and can be rewritten as in the form below.

$$\begin{cases} T_b - T_a + \int_a^b p\, dx = 0 \\ M_b - M_a + T_b(b-c) - T_a(a-c) + \int_a^b (m+px)\, dx = 0 \end{cases} \tag{2.69}$$

Note that c is a reference point on the beam such that $a \leq c \leq b$. Equation (2.69) can be thought of in two parts if the point c is taken to reside at a node. The first part can be considered at the node j and the second part at node $j+1$. From this we get:

$$\begin{cases} T_{b_i} - T_{c_i} + \frac{1}{2}F_i = 0 \\ T_{c_{i+1}} - T_{a_{i+1}} + \frac{1}{2}F_{i+1} = 0 \\ M_{b_i} - M_{c_i} + T_{b_i}(b_i - c_i) + \frac{1}{2}M_i = 0 \\ M_{c_{i+1}} - M_{a_{i+1}} - T_{a_{i+1}}(a_{i+1} - c_{i+1}) + \frac{1}{2}M_{i+1} = 0 \end{cases} \tag{2.70}$$

where $F_i = \int_{c_i}^{b_i} p\, dx$, $F_{i+1} = \int_{b_i}^{c_{i+1}} p\, dx$, $M_i = \int_{c_i}^{b_i} (m+px)\, dx$ and $M_{i+1} = \int_{b_i}^{c_{i+1}} (m+px)\, dx$. Figure 2.4 provides a schematic of the nodes in reference to the finite volume beam element.

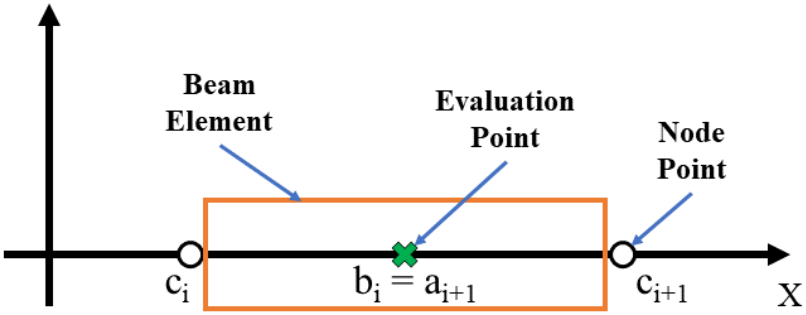

Figure 2.4: Representative schematic of beam element highlight node points and evaluation points for a 2-node beam element

Given that the internal forces and moments at points a_{i+1} and b_i are equal ($T_{a_{i+1}} = T_{b_i} = T$, $M_{a_{i+1}} = M_{b_i} = M$) Eq. (2.70) can be rewritten in matrix form as shown below.

$$\begin{bmatrix} -1 & 0 \\ -(b_i - c_i) & -1 \\ 1 & 0 \\ -(c_{i+1} - a_{i+1}) & 1 \end{bmatrix} \begin{Bmatrix} T \\ M \end{Bmatrix} = \frac{1}{2} \begin{Bmatrix} F_i \\ M_i \\ F_{i+1} \\ M_{i+1} \end{Bmatrix} + \begin{Bmatrix} -T_{c_i} \\ -M_{c_i} \\ T_{c_{i+1}} \\ M_{c_{i+1}} \end{Bmatrix} \tag{2.71}$$

If we consider a coordinate system that would be used in a variational finite element formulation (such as shown in Fig. 2.4) and evaluate the equilibrium relation at a point ξ, Eq. (2.71) assumes the following form:

$$\begin{Bmatrix} F_1 \\ M_1 \\ F_2 \\ M_2 \end{Bmatrix} = \begin{bmatrix} -1 & 0 \\ -\frac{l}{2}(1+\xi) & -1 \\ 1 & 0 \\ -\frac{l}{2}(1-\xi) & 1 \end{bmatrix} \begin{Bmatrix} T \\ M \end{Bmatrix}_{\xi} \tag{2.72}$$

where $\xi = \frac{2x-(c_{i+1}+c_i)}{l}$. Note that l is the length of the beam element and x is a point on the x-axis defining in the coordinate system. Equation (2.72) relates the force and moments acting on the beam element to the shear force (T) and bending moment (M) of the beam element. However, we want to be able to relate the force and moments acting on the beam element to the translational and rotation displacement that would be experienced by said element. We can work toward this relation by using equations from the formulation of beams by finite elements.

$$\begin{Bmatrix} T \\ M \end{Bmatrix} = \begin{bmatrix} GA & 0 \\ 0 & EJ \end{bmatrix} \begin{Bmatrix} \gamma \\ \varphi' \end{Bmatrix} \tag{2.73}$$

$$\delta L_d = \int_0^l \delta \begin{Bmatrix} \gamma \\ \varphi' \end{Bmatrix}^T \begin{bmatrix} GA & 0 \\ 0 & EJ \end{bmatrix} \begin{Bmatrix} \gamma \\ \varphi' \end{Bmatrix} dx \tag{2.74}$$

$$\begin{Bmatrix}\gamma\\ \varphi'\end{Bmatrix} = [H]\begin{Bmatrix}\upsilon\\ \varphi\end{Bmatrix}, \qquad [H] = \begin{bmatrix}1 & 0\\ 0 & 1\end{bmatrix}\frac{\partial}{\partial x} + \begin{bmatrix}0 & -1\\ 0 & 0\end{bmatrix} \tag{2.75}$$

$$\begin{Bmatrix}\upsilon\\ \varphi\end{Bmatrix} = \frac{1}{2}\begin{bmatrix}(1-s) & 0 & (1+s) & 0\\ 0 & (1-s) & 0 & (1+s)\end{bmatrix}\begin{Bmatrix}\upsilon_1\\ \varphi_1\\ \upsilon_2\\ \varphi_2\end{Bmatrix} \tag{2.76}$$

$$\begin{Bmatrix}\gamma\\ \varphi'\end{Bmatrix} = \frac{1}{2}\begin{bmatrix}-\frac{2}{l} & -(1-s) & \frac{2}{l} & -(1+s)\\ 0 & -\frac{2}{l} & 0 & \frac{2}{l}\end{bmatrix}\begin{Bmatrix}\upsilon_1\\ \varphi_1\\ \upsilon_2\\ \varphi_2\end{Bmatrix} \tag{2.77}$$

In Eq. (2.73), *EJ* and *GA* are the flexural and shear stiffness of the beam respectively. The variable φ represents the beam section rotation and γ represents shear deformation. Shear deformation is defined as $\gamma = \upsilon' - \varphi$ where υ is the beam transverse displacement. Equation (2.74) expresses the virtual work associated with deforming the beam while Eq. (2.75) relates shear deformation and the first derivative of beam rotation to the transverse displacement and rotation of the beam. A finite element approximation of beam transverse displacement and rotation for a 2-node beam is shown in Eq. (2.76). Lastly, Eq. (2.77) is formed by applying Eq. (2.75) to Eq. (2.76). Using the relations in Eqs. (2.73)–(2.77), Eq. (2.72) can be expressed as follows:

$$\begin{Bmatrix}F_1\\ M_1\\ F_2\\ M_2\end{Bmatrix} = [K]\begin{Bmatrix}\upsilon_1\\ \varphi_1\\ \upsilon_2\\ \varphi_2\end{Bmatrix} \tag{2.78}$$

where the beam forces and moments are related to the beam deformations and rotations via the stiffness matrix [K] which is expressed below.

$$[K] = \frac{1}{2}\begin{bmatrix} -1 & 0 \\ -\frac{l}{2}(1+\xi) & -1 \\ 1 & 0 \\ -\frac{l}{2}(1-\xi) & 1 \end{bmatrix}\begin{bmatrix} GA & 0 \\ 0 & EJ \end{bmatrix}\begin{bmatrix} -\frac{2}{l} & -(1-\xi) & \frac{2}{l} & -(1-\xi) \\ 0 & -\frac{2}{l} & 0 & \frac{2}{l} \end{bmatrix}$$

$$[K] = \frac{GA}{4l}\begin{bmatrix} 4 & 2l(1-\xi) & -4 & 2l(1+\xi) \\ 2l(1+\xi) & \frac{l^2}{4}\left[(1-\xi^2)+\frac{4}{3}\Phi\right] & -2l(1+\xi) & \frac{l^2}{4}\left[(1+\xi^2)-\frac{4}{3}\Phi\right] \\ -4 & -2l(1-\xi) & 4 & -2l(1+\xi) \\ 2l(1-\xi) & \frac{l^2}{4}\left[(1-\xi^2)-\frac{4}{3}\Phi\right] & -2l(1-\xi) & \frac{l^2}{4}\left[(1-\xi^2)+\frac{4}{3}\Phi\right] \end{bmatrix} \quad (2.79)$$

The term Φ represent the shear factor where $\Phi = \frac{12*EJ}{GA*l^2}$. Further description of the formulation for the finite volume beam element can be found in [149,150].

2.2.6 Shell Element Formulation

A four-node C^0 shell element is implemented in MBDyn to aid in the modeling of 2D structural element. In this work, 2D shell elements are used to model flat plate wings, such as those discussed in Chapter 3, as well as the membrane which makes up the covering of the wing discussed in Chapter 4. The shell element implemented in MBDyn is based on the nonlinear shell element discussed by Witkowski [151], which is developed based on a combination of Enhanced Assumed Strain (EAS) and Assumed Natural Strain (ANS) formulations. An illustration depicting the shell element can be found in Fig. 2.5.

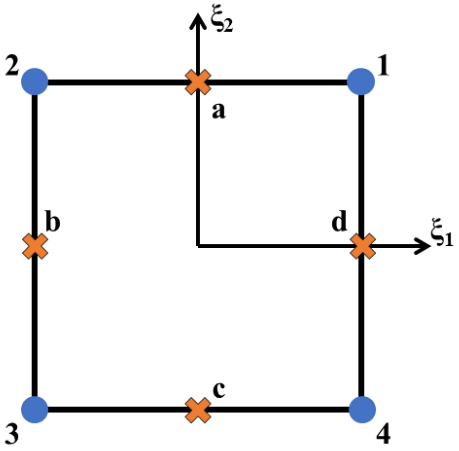

Figure 2.5: Illustration of the four-node shell finite element

In Fig. 2.5, the circles represent the node points which make up the shell element and the x's represent the points at which shear is evaluated within the element. The Biot-like linear deformation vector [152,153] is computed by comparing the deformed and undeformed back-rotated derivatives of the position and is shown below.

$$\vec{\varepsilon}_k = T^T \frac{\partial y}{\partial k} - T_0^T \frac{\partial y_0}{\partial k} \tag{2.80}$$

The variable y represents the position of the shell reference surface and T is a local orthonormal coordinate system- defined on the surface. The variable $\frac{\partial y}{\partial k}$ is the partial derivative of y with respect to the arc length coordinate k where k = 1, 2. Note that the subscript $(\cdot)_0$ represents variables in the undeformed coordinate system. Similarly, the Biot-like angular deformation is defined as:

$$\vec{\kappa}_k = T^T \kappa_k - T_0^T \kappa_{0k} \tag{2.81}$$

where κ_k is the spatial derivative of tensor T with respect to the arc length coordinate k.

The constitutive law of the plate is determined beforehand and relates the generalized stresses to the generalized deformations.

$$\begin{Bmatrix} \vec{n}_1 \\ \vec{n}_2 \\ \vec{m}_1 \\ \vec{m}_2 \end{Bmatrix} = [D] \begin{Bmatrix} \vec{\varepsilon}_1 \\ \vec{\varepsilon}_2 \\ \vec{\kappa}_1 \\ \vec{\kappa}_2 \end{Bmatrix} \tag{2.82}$$

where D is a 12×12 matrix containing the constitutive relations.

$$[D] = \begin{bmatrix} C & 0 & 0 & 0 & \upsilon C & 0 & 0 & 0 & 0 & 0 & 0 & 0 \\ 0 & 2Gh & 0 & 0 & 0 & 0 & 0 & 0 & 0 & 0 & 0 & 0 \\ 0 & 0 & \alpha Gh & 0 & 0 & 0 & 0 & 0 & 0 & 0 & 0 & 0 \\ 0 & 0 & 0 & 2Gh & 0 & 0 & 0 & 0 & 0 & 0 & 0 & 0 \\ \upsilon C & 0 & 0 & 0 & C & 0 & 0 & 0 & 0 & 0 & 0 & 0 \\ 0 & 0 & 0 & 0 & 0 & \alpha Gh & 0 & 0 & 0 & 0 & 0 & 0 \\ 0 & 0 & 0 & 0 & 0 & 0 & 2F & 0 & 0 & 0 & 0 & 0 \\ 0 & 0 & 0 & 0 & 0 & 0 & 0 & P & 0 & -\upsilon P & 0 & 0 \\ 0 & 0 & 0 & 0 & 0 & 0 & 0 & 0 & \beta F & 0 & 0 & 0 \\ 0 & 0 & 0 & 0 & 0 & 0 & 0 & -\upsilon P & 0 & D & 0 & 0 \\ 0 & 0 & 0 & 0 & 0 & 0 & 0 & 0 & 0 & 0 & 2F & 0 \\ 0 & 0 & 0 & 0 & 0 & 0 & 0 & 0 & 0 & 0 & 0 & \beta F \end{bmatrix} \tag{2.83}$$

In the matrix [D], C = E*h/(1-υ^2), P = C*h^2/12, and F = G*h^3/12. The Young's modulus is represented by E, υ is Poisson's ratio and G is the shear modulus. The variables h, α, and β are the shell thickness, shear factor and moment factor respectively. Further details on the formulation and validation of the four-node shell element can be found in Ref. [154].

2.3 Solver Coupling Strategy

A key aspect of developing a computational aeroelastic solver is ensuring it can adequately model both the fluid dynamics and structural dynamics of the problem. In

this study a coupled approach is utilized where two independent solvers (OVERTURNS and MBDyn) are employed to model the fluid and structural dynamics respectively. A major benefit of this approach is that each solver has been specifically designed to model its respective part of the aeroelastic problem with a high level of fidelity. The challenge arises when considering the sharing of information between the two solvers. Assuming the CFD and CSD solvers both appropriately model the problem, the developer must concern themselves with (1) how information is exchanged between the solvers and (2) how that information is interpreted and applied to that particular solver's computational domain. This section addresses how the coupled CFD/CSD solver used throughout this study that overcomes both aforementioned challenges.

2.3.1 Python-based Coupling Framework

Python is an interpreted, object-oriented programming language that is increasingly becoming more widely used in software programming due to the fact it's easy to use, has clear syntax and is open-source. Another feature of Python is that it's capable of easily interfacing with source codes written in different languages. Additionally, it has parallel processing functionality. For these reason, Python was utilized in creating the framework to couple OVERTURNS and MBDyn.

OVERTURNS is written in Fortran while MBDyn is primarily coded in C/C++. These two programming languages are not compatible with one another, but can be interfaced with Python. Fortran and C++ python wrappers were utilized to interface specific subroutines and functions from both solvers with Python. This allowed for a

single python script to initialize and run both solver as well as make function calls to facilitate in the exchange of information between OVERTURNS and MBDyn.

Information at the fluid-structure interface is exchanged between the two solvers. With respect to the flapping wing problems discussed throughout this work, this means that data is exchanged at the points where the wing surface directly interacts with the fluid medium. More specifically, aerodynamic forces are passed from OVERTURNS to MBDyn (i.e. CFD → CSD) and wing deformations are passed from MBDyn to OVERTURNS (i.e. CSD → CFD). Sub-section 2.3.2 discusses how that information is transformed between the domains of the two solvers. In general, the aerodynamic force vectors that are transferred are comprised of the forces acting at a given CFD mesh point in the x, y and z directions where $\vec{f}_{aero} = \langle f_x, f_y, f_z \rangle$. Wing deformations are expressed with respect to the undeformed wing for a given instance within the flap cycle. The deformation vector $\Delta\vec{x}_{deformed} = \langle dx, dy, dz \rangle$ is the change in wing deformation, from one iteration to the next, with respect to the undeformed wing. All forces and wing deformations are expressed in the global reference frame.

Coupling is performed in a tight manner meaning information is passed between the two solvers during each iteration. The time step values in OVERTURNS and MBDyn are set so that the same number of iterations per flap cycle occur for each solver. Note that nondimensional values are utilized in OVERTURNS while MBDyn works with dimensional units. Wing deformations in OVERTURNS are required to be normalized by the reference length (typically the mean chord length) such that $\Delta\vec{x}_{deformed} = \left\langle \frac{dx}{\bar{c}}, \frac{dy}{\bar{c}}, \frac{dz}{\bar{c}} \right\rangle$. Similarly, aerodynamic forces are output as coefficient values from OVERTURNS and must be converted to dimensional values before they

are input into MBDyn. The force vector is modified such that $\vec{f}_{aero} = \frac{1}{2}\rho V^2 c * \langle C_x, C_y, C_z \rangle$ where C_x, C_y and C_z are the aerodynamic force coefficients acting at a given point in the CFD mesh in the *x*, *y* and *z* directions respectively.

2.3.2 Non-conformal Domain Mapping

Ideally, one would desire to have the fluid and structural domains to have the same or similar topologies at the fluid-structure interface (FSI). This would ease the transfer of information between the two solvers by allowing for a one-to-one matching between the CFD mesh points and CSD node points. However, this is typically not feasible or favorable with respect to the maintaining solution accuracy while minimizing computational cost. CFD grids tend to have a much higher concentration of grid points in comparison to the number of nodes used within a structural dynamics model to more accurately resolve flow features at given regions within the flow domain. It's not uncommon for the CFD mesh to have on the order of 10^1–10^2 more points at the FSI compared to the CSD model. An example of this can be seen in Fig. 2.6. Given the potential for a large discrepancy in the number of points between the fluid and structural domains, it's important to have a robust methodology capable of interfacing two non-conformal domain topologies.

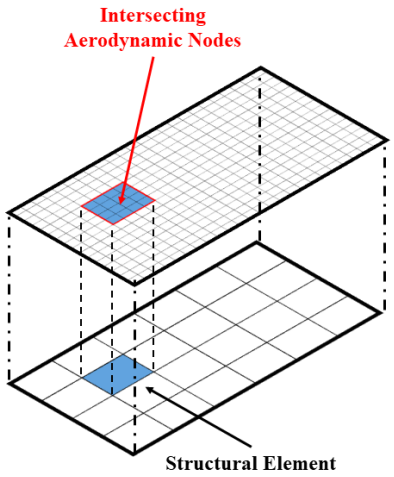

Figure 2.6: Illustration of discrepancy in grid point concentration between fluid domain and structural domain

MBDyn provides that capability through a conservative, mesh-free FSI methodology. The methodology is based on the Moving Least Square (MLS) patches technique used in the field of surface reconstruction from *N* irregularly distributed data points [155]. Not only should the methodology interface the two domains with respect to position, but it should also conserve the exchange of momentum and energy between the fluid and structural domains. This is done by enforcing the coupling conditions through the variation principle of virtual work.

Let's assume that δx_f and δx_s represent virtual displacements in the fluid and structural domains respectively. The subscript $(\cdot)_f$ refers to the fluid domain and likewise the subscript $(\cdot)_s$ refers to the structural domain. The compatibility of the virtual displacements is enforced through the equation below:

$$Tr(\delta x_f)|_\Psi = Tr(\delta x_s)|_\Psi \tag{2.84}$$

where *Tr* is the trace of the virtual displacements onto the virtual interface surface. The virtual interface (Ψ) can be a newly defined virtual interface, the surface of the fluid

domain (Ψ_f) or the surface of the structural domain (Ψ_s). In the following equations, the virtual interface will be assumed to be at the surface of the fluid domain (Ψ_f) unless explicitly stated otherwise. The fluid and structural domain displacements are related as follows:

$$\left(\delta x_f\right)_i = \sum_{j=1}^{j_s} h_{ij} (\delta x_s)_j \tag{2.85}$$

where $(\delta x_f)_i$ are the discrete values of δx_f at the surface of the fluid domain and h_{ij} are coefficients of the displacement interpolation matrix H. The boundary surface virtual displacement is thus defined as:

$$\delta x_f = \sum_{i=1}^{i_f} N_i \sum_{j=1}^{j_s} h_{ij} (\delta x_s)_j \tag{2.86}$$

where N_i are base functions in the approximation space of the fluid domain discretization and i_f is the number of grid points on the virtual interface surface (Ψ_f). The virtual work of the aerodynamic loads acting on the fluid interface and structural interface are shown in Eqs. (2.87) and (2.88) respectively.

$$\begin{aligned} \delta W_f &= \int_{\Psi_f} \left(-p\vec{n} + \sigma_f \cdot \vec{n}\right) \cdot \delta x_f \, dA \\ &= \int_{\Psi_f} \left(-p\vec{n} + \sigma_f \cdot \vec{n}\right) \cdot \sum_{i=1}^{i_f} N_i \sum_{j=1}^{j_s} h_{ij} (\delta x_s)_j \, dA \end{aligned} \tag{2.87}$$

$$\delta W_s = \sum_{j=1}^{j_s} f_j \cdot (\delta x_s)_j \tag{2.88}$$

The variables p and σ_f are the pressure and stresses, respectively, of the fluid and the vector $\vec{n}$ defines the unit vector normal to the surface. The loads applied to the structure are related to the aerodynamic loads in the equation below:

$$f_j = \sum_{i=1}^{i_f} F_i h_{ij} \tag{2.89}$$

where $F_i = \int_{\Psi_f} \left(-p\vec{n} + \sigma_f \cdot \vec{n}\right) N_i \, dA$.

The position and velocity of the points at the FSI as well as the forces acting at the interface can be related through the interpolation matrix (H). The relations are shown below through Eq. (2.90).

$$\begin{gathered} x_{overturns} = H x_{mbdyn} \\ \dot{x}_{overturns} = H \dot{x}_{mbdyn} \\ \delta x_{mbdyn}^T f_{mbdyn} = \delta x_{overturns}^T f_{overturns} = \delta x_{mbdyn}^T H^T f_{overturns} \\ f_{mbdyn} = H^T f_{overturns} \end{gathered} \tag{2.90}$$

The interpolation matrix is composed of the coefficients h_{ij}. Additional details on the formulation and calculation of the interpolation matrix (H) can be found in Ref. [155].

2.4 Inverse Distance Weighting Grid Deformation Scheme

In Section 2.3, the method by which information is exchanged between OVERTURNS and MBDyn as well as how the two non-conformal domains are mapped was discussed. The interpolation matrix (discussed in Sub-section 2.3.2) converts the structural deforms calculated by MBDyn and defines how each grid point on the wing surface must deform in the CFD mesh. However, it is necessary to adjust

the position of the surrounding nodes within the wing mesh otherwise the deformations applied at the wing surface could cause overlapping and negative cell volumes to form.

This section describes how OVERTURNS handles the problem of propagating mesh deformations at the wing surface throughout the wing mesh. The two methods employed in OVERTURNS are a decay function-based scheme and an inverse distance weighting (IDW) scheme. The decay function-based scheme was initially used in OVERTURNS to deform the mesh in aeroelastic rotor blade problems. This scheme benefits from having a relatively low computational cost but is only applicable for relatively small deformations at the surface. For large wing deforms, like those expected in modeling highly flexible flapping wing, this method breaks down resulting in poor mesh quality or the formation of overlapping cells. The newly added IDW scheme is capable of handling large deformations at the wing surface with a relatively low increase in computational cost. Both methods will be discussed in the following sub-sections.

2.4.1 Decay Function-based Mesh Deformation

Decay function-based mesh deformation is a simple and efficient means of prescribing deformations at the wing surface throughout the mesh volume. As described in Sub-section 2.3.1, deformations are applied to the wing surface in delta form where $\Delta\vec{x}_{deformed} = \langle dx, dy, dz \rangle$. The decay functions take the form of:

$$u(x) = \phi(x) * u_j \tag{2.91}$$

where u_j is the known data point and $\phi(x)$ is a radial basis function used to attenuate the magnitude of the known data point based its distance from the point under evaluation.

When applied to the CFD grid, deformations at grid points away from the wing surface are determined using Eq. (2.92).

$$\begin{aligned} dx(\vec{x}) &= \phi(\vec{x}) * dx_j \\ dy(\vec{x}) &= \phi(\vec{x}) * dy_j \\ dz(\vec{x}) &= \phi(\vec{x}) * dz_j \end{aligned} \tag{2.92}$$

The radial basis function used within OVERTURNS takes the form:

$$\phi(\vec{x}) = 1 - \left[0.5 * \left(1 + \cos\left(\pi * \frac{d_{max} - d}{d_{max}}\right)\right)\right]^p \tag{2.93}$$

where $d = \left\|\vec{x} - \vec{x}_j\right\|$ is the distance between the position vector of the known data point and the position vector of the point under evaluation. The variable d_{max} is a constant defined by the user to specify the distance away from the wing surface at when the function approaches zero. The variable p is a power parameter, defined by the user, that controls the shape of the decay function. Figure 2.7 shows how the decay function varies for power parameter values of 1, 2 and 3. Higher values of p increase the distance away from the known data point before significant attenuation of the value begins. However, decay of the value is much steeper for higher p values. Within the scheme utilized in OVERTURNS, d_{max} was set equal to 15 and a power parameter (p) of 3 was used.

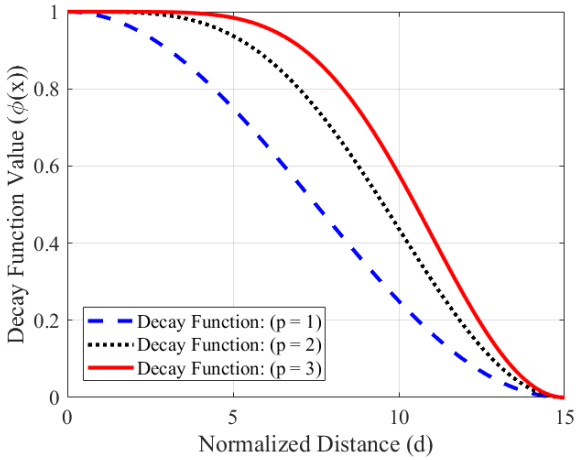

Figure 2.7: Plot of decay function vs distance for various power parameter values

2.4.2 Inverse Distance Weighting Mesh Deformation

Inverse distance weighting (IDW) is an explicit, multivariate interpolation technique applicable to a scattered set of data points. The method was first introduced in 1968 by Shepard [156] as a means of interpolating data in the field of geographical information systems. IDW interpolations assigns the value at unknown points using the weighted average of values at known data points. The weighting function utilized is based on the inverse of the distance from the known points to the unknown point under evaluation. Figure 2.8 provides a 1D example of IDW interpolation.

In Fig. 2.8, the black circles represent the known data points. The red dashed line represents the interpolation function:

$$u(x) = \frac{\sum_{j=1}^{N} w_j(x) * u_j}{\sum_{j=1}^{N} w_j(x)}, \quad w_j(x) = \frac{1}{\left\| x - x_j \right\|^p} \tag{2.94}$$

where N is the total number of known data points, $w_j(x)$ is the weighting function, u_j is the value of the known data point. In the weighting function $w_j(x)$, x is the position of

the point under evaluation, x_j is the position of the known data point, $\|\cdot\|$ represents the Euclidean norm operator and p is the power parameter. The power parameter is typically set so that $p \geq 2$. Greater values of p give greater influence to known points closer in proximity to the interpolated point. For the example shown in Fig. 2.8, p = 2.

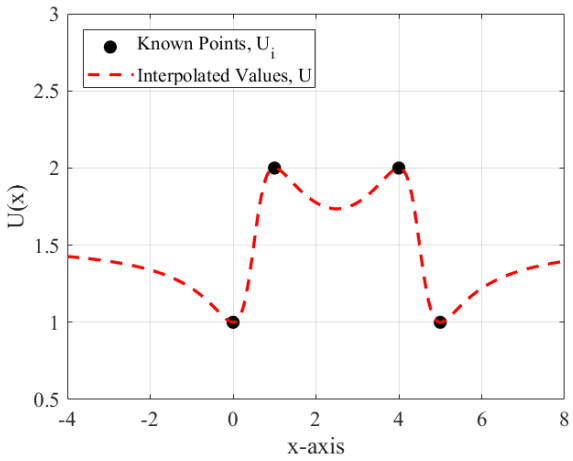

Figure 2.8: 1D example of inverse distance weighting interpolation

While Shepard is credited with first introducing inverse distance weighting interpolation, Witteveen was the first to apply IDW to the problem of CFD mesh deformation [157,158]. In the implementation described by Witteveen, the interpolation function maintains a similar form as in Eq. (2.94), except now the value u_j is replaced by variables representing the change in position of points at the boundary.

$$dx(\vec{x}) = \frac{\sum_{j=1}^{N} w_j(\vec{x}) * dx_j}{\sum_{j=1}^{N} w_j(\vec{x})}$$
$$dy(\vec{x}) = \frac{\sum_{j=1}^{N} w_j(\vec{x}) * dy_j}{\sum_{j=1}^{N} w_j(\vec{x})}$$
$$dz(\vec{x}) = \frac{\sum_{j=1}^{N} w_j(\vec{x}) * dz_j}{\sum_{j=1}^{N} w_j(\vec{x})}$$
$$w_j(\vec{x}) = \frac{1}{\left\|\vec{x} - \vec{x}_j\right\|^p} \tag{2.95}$$

In Eq. (2.95), the variables *dx*, *dy* and *dz* represent the change in the position of the mesh points in the *x*, *y* and *z* respectively. Within the CFD/CSD methodology, these values would be structural deformation data provided by MBDyn at the fluid-structure interface. The variable $\vec{x}$ and $\vec{x}_j$ represent the position vector of the interpolation point and known data point respectively.

A positive attribute of the IDW mesh deformation scheme is that it is an explicit interpolation method. Thus, it has a reduced computational cost in comparison to radial basis function (RBF) methods which require the solution of a system of equations [158]. Another benefit is that IDW is an extremum conserving method meaning that with the implementation of the methodology, points at the boundary of the domain remain at the boundary. However, this is only applicable to cases with pure translation. Instances where rotation is present may cause interior points to move outside of the domain boundary. Other researchers have looked to modify the original IDW to overcome some of its original limitations.

Luke et al. modified the original IDW scheme by applying a displacement field to each boundary node and making improvements to the formulation of the weighting function [159]. The modified weighting function is given as:

$$w_j(\vec{x}) = A_j * \left[\left(\frac{L_{def}}{\|\vec{x} - \vec{x}_j\|} \right)^a + \left(\frac{\alpha L_{def}}{\|\vec{x} - \vec{x}_j\|} \right)^b \right] \tag{2.96}$$

where *a*, and *b* are the 1st and 2nd power parameters, A_j is the area weight, α is an estimated size of the near-body influence region and L_{def} is the estimated length of the region of deformation. The suggested value of these parameters are proposed by Luke et al. in Ref. [159] such that $a = 3$ and $b = 5$. The value of α is varied depending on

whether the boundary is moving or fixed such that α_{moving} = 0.1 and α_{fixed} = 0.0. The variable L_{def} is defined as the maximum distance between any given mesh point and the mesh center such that:

$$L_{def} = \max\left(g - x_j\right), \;\; j = 1, N \tag{2.97}$$

where the mesh center (g) is defined as $g = \frac{1}{N}\sum_{j=1}^{N} x_j$. Note that the variable A_j is set equal to one in this work. The IDW method proposed by Luke et al. does a better job of preserving mesh orthogonality near the surface boundary in comparison to the original IDW scheme and RBF methods [159] due to the inclusion of the second term in the weighting function.

Another drawback of the original IDW scheme is that it does not handle rotation of boundary nodes well. The work by Uyttersprot [160] seeks to modify the IDW scheme to handle both translations and rotations. The proposed methodology by Uyttersprot is detailed in the following paragraphs and was implemented into OVERTURNS.

2.4.3 Calculating the Rotation of Boundary Nodes

For the process of interpolating rotations, quaternions were chosen to represent the rotation at the boundary nodes. Quaternions provide a computational efficient means of representing the rotation without the risk of gimbal lock that which can occur when using Euler angles and a series of rotation matrices to represent rotations. Quaternions can be thought of as a complex number composed of 4 terms such that:

$$Q = q_1 + q_2 i + q_3 j + q_4 k \tag{2.98}$$

where q_1, q_2, q_3 and q_4 are real numbers and i, j and k are imaginary units. The real number (q_1) represents the angle of rotation while the imaginary numbers represent the axis of rotation. In this case, the quaternion can be represented by a scalar value and a vector in Cartesian space:

$$Q = [r, \vec{v}], \;\; r = q_1, \;\; \vec{v} = [q_2 \; q_3 \; q_4]$$
$$r = \cos\frac{\theta}{2}$$
$$\vec{v} = \sin\frac{\theta}{2}\vec{m} \tag{2.99}$$

where θ is the angle of rotation and $\vec{m}$ is the unit axis of rotation. Table 2.1 provides a list of some important mathematical properties pertaining to quaternions which will be utilized throughout the formulation of the proposed mesh deformation method.

Table 2.1**: List of mathematical properties for quaternions**

Property	Mathematical Equation
• Associative:	$(Q_1 \cdot Q_2) \cdot Q_3 = Q_1 \cdot (Q_2 \cdot Q_3)$
• Distributive:	$Q_1 \cdot (Q_2 + Q_3) = Q_1 \cdot Q_2 + Q_1 \cdot Q_3$
• Not commutative:	$Q_1 \cdot Q_2 \neq Q_2 \cdot Q_1$
• Conjugate of a quaternion:	$Q^* = q_1 - q_2 i - q_3 j - q_4 k$
• Magnitude of a quaternion:	$\|Q\| = \sqrt{Q \cdot Q^*} = \sqrt{q_1^2 + q_2^2 + q_3^2 + q_4^2}$
• Inverse of a quaternion:	$Q^{-1} = \frac{Q^*}{Q \cdot Q^*}$
• Unit quaternion:	$\|Q\| = 1$
• For unit quaternions:	$Q^{-1} = Q^*$

Note that the multiplication of two quaternions is defined below.

$$\begin{aligned} Q_1 \cdot Q_2 &= [r_1, \vec{v}_1] \cdot [r_2, \vec{v}_2] \\ &= [r_1 r_2 - \vec{v}_1 \cdot \vec{v}_2, r_1 \vec{v}_2 + r_2 \vec{v}_1 + \vec{v}_1 \times \vec{v}_2] \end{aligned} \tag{2.100}$$

To find the position of some point $\vec{p}$ after a rotation, the point is first defined as a quaternion such that $P = [0 \; \vec{p}]$. The position after rotation (P_{rot}) is found by:

$$P_{rot} = Q \cdot P \cdot Q^{-1} = Q \cdot P \cdot Q^{*} \tag{2.101}$$

To apply Eq. (2.101), the rotation quaternion for the specific point must be known. However, only the position vector ($\vec{x}$) and the boundary displacement vector ($\Delta\vec{x}$) are known for any mesh boundary point. It is necessary to decompose the new position of the boundary point, after the boundary displacements ($\Delta\vec{x}$) are applied, into a translational and rotational component. The new position can be decomposed to the form:

$$X_d = R \cdot X_u \cdot R^{*} + T \tag{2.102}$$

where X, R and T are quaternions representing position, rotation, and translation vectors. X_u and X_d are the position quaternions where the subscripts $(\cdot)_u$ and $(\cdot)_d$ indicate undeformed or deformed. R and T represent the rotation and translation quaternions respectively. Note that $X_u = [0, \vec{x}]$, $X_d = [0, \vec{x} + \Delta\vec{x}]$ and $T = [0, \vec{t}]$. To determine the rotation quaternion (R), information from surrounding boundary points is necessary. The quaternions at the cell centers are determined and then the quaternion values are interpolated onto the boundary nodes as described in Ref. [160].

The rotation quaternions are determined in a three-step process. First, the cell center is calculated for the undeformed and deformed face. The cell center is given by:

$$\vec{c} = \frac{1}{n}\sum_{j=1}^{n} \vec{x}_j \tag{2.103}$$

where n is the total number of face corners. The vertices of the corners are then translated so that the cell centers are at the origin such that:

$$\vec{x}_u' = \vec{x}_u - \vec{c}_u$$
$$\vec{x}_d' = \vec{x}_d - \vec{c}_d \tag{2.104}$$

where x' is the new position of the vertices after the translation is applied. Next, the unit normal of the undeformed and deformed faces are calculated using Eq. (2.105). The face unit normal is computed as an average of the unit normals of two consecutive face corner position vectors.

$$\vec{n} = \frac{1}{n}\sum_{j=1}^{n} \frac{\vec{x}_j \times \vec{x}_{j+1}}{\left\|\vec{x}_j \times \vec{x}_{j+1}\right\|} \tag{2.105}$$

The second step is to align the normal of the undeformed face to that of the deformed face. The angle between the undeformed and deformed unit normal (θ_1) is:

$$\theta_1 = \arccos\left(\frac{\vec{n}_u \cdot \vec{n}_d}{\|\vec{n}_u\| * \|\vec{n}_d\|}\right) \tag{2.106}$$

The cross produced of the undeformed and deformed unit normal defines the axis of rotation ($\vec{m}_1$).

$$\vec{m}_1 = \arccos\left(\frac{\vec{n}_u \cdot \vec{n}_d}{\|\vec{n}_u\| * \|\vec{n}_d\|}\right) \tag{2.107}$$

Equations (2.106) and (2.107) define the angle and axis of rotation for the first rotation quaternion R_1 such that $R_1 = \left[\cos\left(\frac{\theta_1}{2}\right), \sin\left(\frac{\theta_1}{2}\right) * \vec{m}_1\right]$. The rotation is applied to the vertices making up the undeformed face so that they are at a new position defined as:

$$X_u'' = R_1 \cdot X_u' \cdot R_1^* \tag{2.108}$$

where $X_u'' = [0, \vec{x}_u'']$ and $X_u' = [0, \vec{x}_u']$.

The final step involves rotating the undeformed face about its unit normal vector to align its vertices to those of the deformed face. For the second rotation, the axis of rotation is the unit normal of the undeformed face. The angle of rotation is an averaged of the angles between the position vectors at the corresponding corners of the undeformed and deformed faces.

$$\vec{m}_2 = \frac{\vec{n}_d}{\|\vec{n}_d\|} \tag{2.109}$$

$$\theta_2 = \frac{1}{n}\sum_{j=1}^{n} \arccos\left(\frac{\vec{x}_{j,u} \cdot \vec{x}_{j,d}}{\|\vec{x}_{j,u}\| * \|\vec{x}_{j,d}\|}\right) \tag{2.110}$$

The second rotation quaternion R_2 is defined as $R_2 = \left[\cos\left(\frac{\theta_2}{2}\right), \sin\left(\frac{\theta_2}{2}\right) * \vec{m}_2\right]$. The first and second rotation quaternion can be combined to a single quaternion (R) such that $R = R_2 \cdot R_1$. An illustration of the method used to determine the rotation quaternion can be seen in Fig. 2.9.

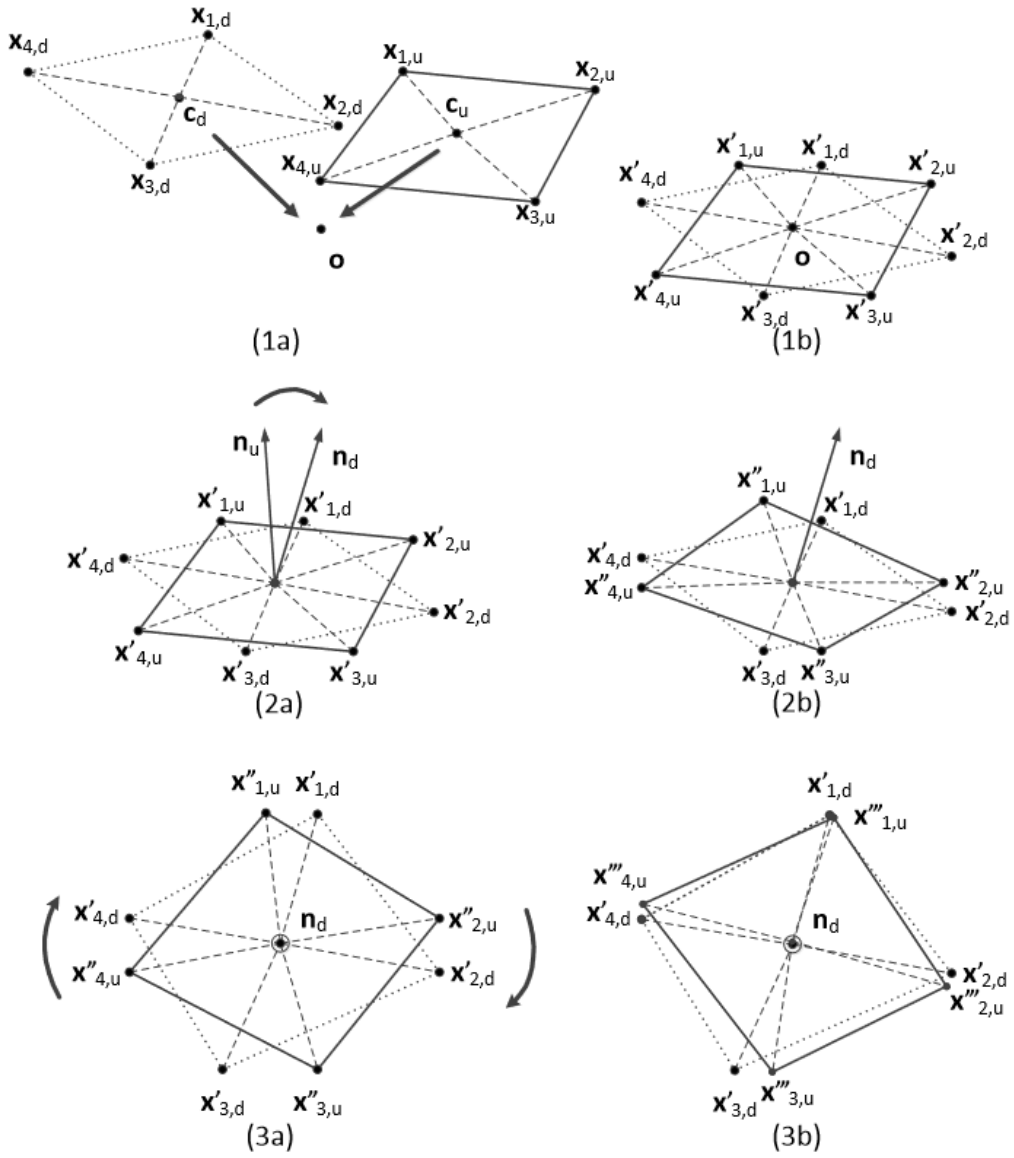

Figure 2.9: Illustration of method to calculate rotation quaternion, Adapted from Ref. [160]

2.4.4 Interpolation of Rotation Quaternions

After the rotation quaternion is calculated for each cell face at the fluid-structure interface boundary of the CFD mesh, those quaternions need to be interpolated onto the boundary nodes. The interpolation of the quaternions onto the boundary nodes is

done using spherical linear interpolation (SLERP) [161]. The spherical linear interpolation of two quaternions is defined as:

$$Q_{SLERP} = \frac{\sin((1-\sigma)\varphi)}{\sin\varphi} Q_1 + \frac{\sin(\sigma * \varphi)}{\sin\varphi} Q_2 \tag{2.111}$$

where σ is a weighting value such that $0 \leq \sigma \leq 1$ and φ is the angle between the two quaternions computed as $\varphi = \arccos(Q_1 \cdot Q_2)$. SLERP can be performed on multiple quaternions using the following formulation:

$$Q_{SLERP_2} = SLERP\left(Q_1, Q_2, \frac{\sigma_2}{\sigma_1 + \sigma_2}\right) \tag{2.112}$$

$$Q_{SLERP_3} = SLERP\left(Q_{SLERP_2}, Q_3, \frac{\sigma_3}{\sigma_1 + \sigma_2 + \sigma_3}\right) \tag{2.113}$$

$$\vdots$$

$$Q_{SLERP_n} = SLERP\left(Q_{SLERP_{n-1}}, Q_n, \frac{\sigma_n}{\sum_{j=1}^{n} \sigma_j}\right) \tag{2.114}$$

When interpolating the rotation quaternion for a boundary node, the rotation quaternions of the *n* faces connected to that node are used. In this instance the weights are set to equal one another ($\sigma_j = \frac{1}{n}$). After the rotation quaternion *R* is determined for each boundary node, Eq. (2.102) can be used to calculate the translation vector ($\vec{t}$) for each boundary node.

Once the translation vector and rotation quaternion are calculated for each boundary node, the deflections at the wing surface need to be propagated throughout the rest of the CFD mesh. This is done by using IDW to interpolate the translation

vector and rotation quaternion at point way from the wing surface. Interpolation of the translation vector is similar to that of Eq. (2.95) such that:

$$\vec{t}(\vec{x}) = \frac{\sum_{j=1}^{n} w_j(\vec{x})\vec{t}_j}{\sum_{j=1}^{n} w_j(\vec{x})} \tag{2.115}$$

where $\vec{t}(\vec{x})$ is the translation vector at some CFD mesh point away from the wing surface at position ($\vec{x}$), n is the total number of boundary points, $\vec{t}_j$ is the translation vector at a specific boundary node and $w_j(\vec{x})$ is the associated weighting function. In this case the weighting function is the one described in Eq. (2.96).

The rotation quaternion can be interpolated using several different methods. In Ref. [160], four interpolation methods are described:

1. Linear Interpolation of Quaternions
2. Spherical Linear Interpolation of Quaternions
3. Linear Interpolation of Logarithm of Quaternions
4. Linear Interpolation of Displacement Field

For brevity, only the first method (Linear Interpolation of Quaternions) will be discussed. This method was utilized in the IDW mesh deformation scheme implemented in OVERTURNS due to its low computational cost and ease of implementation. The linear interpolation of the rotation quaternions follows the same procedure as that used for the translation vector with

$$R(\vec{x}) = \frac{\sum_{j=1}^{n} w_j(\vec{x})R_j}{\sum_{j=1}^{n} w_j(\vec{x})} \tag{2.116}$$

where R_j is the rotation quaternion at a specific boundary node. Note that the interpolated quaternion ($R(\vec{x})$) may not be a unit quaternion and needs to be normalized

before it is applied. The interpolated translation vector ($\vec{t}$) and rotation quaternion (R) are then used to calculate the displacement vector ($\vec{u}$) of a given mesh point at position $\vec{x}$ such that:

$$U(\vec{x}) = \hat{R}(\vec{x})X\hat{R}^{*}(\vec{x}) - X + T(\vec{x}) \tag{2.117}$$

where $U = [0, \vec{u}]$, $X = [0, \vec{x}]$, $T = [0, \vec{t}]$ and $\hat{R}(\vec{x})$ is the normalized rotation quaternion. Equation (2.117) is applied to every grid point in the CFD mesh to calculate its respective displacement vector.

2.4.5 Comparison of Mesh Deformation Schemes

In this section, the resulting meshes after applying the decay function-based scheme and the IDW scheme are compared. Results are compared on a 2D C-type mesh with a NACA 0012 airfoil profile. A rotation is applied about the leading edge to the points at the airfoil surface only. The resulting change in position of the points are interpolated throughout the rest of the wing mesh using the two methods previously described. Cases are conducted for a rotation of 10° (small rotation) and a rotation of 45° (large rotation). Figure 2.10 provides an image of the 2D NACA 0012 C-type mesh in its initial position prior to the rotation being applied.

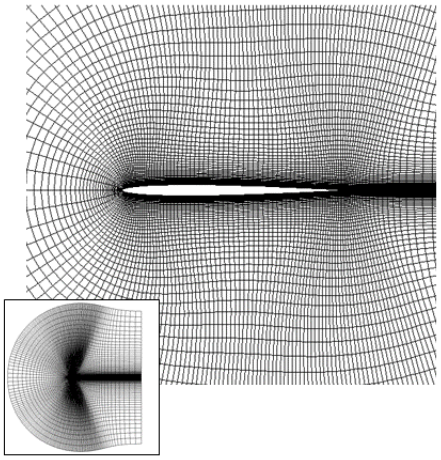

Figure 2.10: NACA 0012 C-type Mesh

Figure 2.11 compares the meshes after a 10° rotation is applied. Fig. 2.11a shows the results using the decay function-based scheme and Fig. 2.11b shows the results using the IDW scheme. For small rotations, the resulting meshes are similar. Given the small magnitude of the rotation, the deformation of the meshes is relatively low. Either scheme is applicable when dealing with relatively low magnitude deformations.

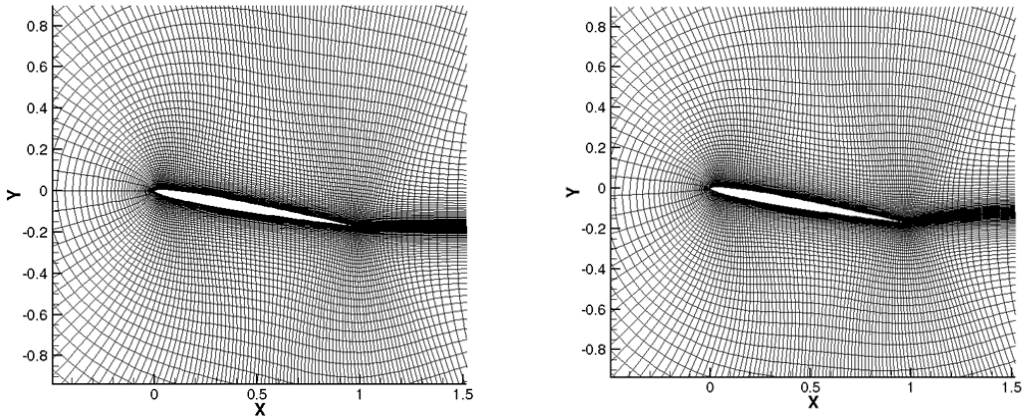

(a) Decay Function-based Scheme (b) IDW Scheme

Figure 2.11: Comparison of mesh interpolation schemes (10° rotation)

Figure 2.12 compares the meshes after a 45° rotation is applied. This large rotation is representative of the large deformations at the wing surface expected during the

flapping wing simulations. There is a significant difference in the mesh quality when comparing the results of the two schemes in Figs. 2.12a and 2.12b. A notable degree of mesh compression and stretching can be seen in Fig. 2.12a while Fig. 2.12b exhibits high mesh quality. When looking more closely at the leading edge (Figs 2.12c and 2.12d) the decay function-based scheme produces a mesh with a high degree of skewing comparing the to IDW scheme. The IDW scheme can better maintain orthogonality near the airfoil surface which serves to increase the accuracy of the simulation results especially for viscous flow solutions.

At the trailing edge (Figs. 2.12e and 2.12f) the decay function-based scheme produces a high amount of cell skewing similar to at the leading edge (Fig. 2.12c). Also, there is a notable discontinuity in the cell directions at the point where the trailing edge meets the grid wake cut region. This is because the decay function-based scheme does not adequately propagate the rotation applied at the wing surface out into the wake cut region. At the trailing edge of the mesh produced using the IDW scheme, the grid points maintain orthogonality at the wing surface. More importantly, the rotation applied at the wing surface is appropriately propagated throughout the mesh especially into the wake cut region. This is because the IDW scheme decomposes deformations into translational and rotational components and is able to interpolate them within the mesh volume. Given its ability to adequately propagate small and large mesh deformations at the wing surface throughout the grid, the IDW scheme is used to handle grid deformation interpolation in OVERTURNS.

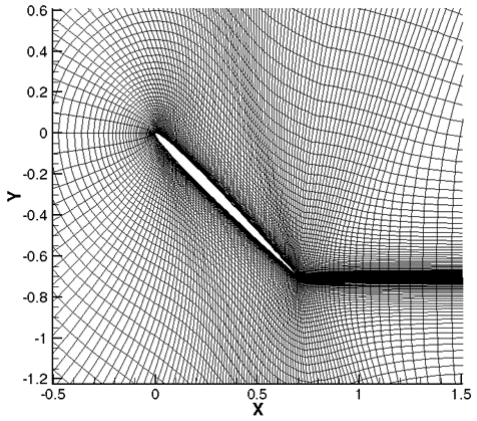

(a) Decay Function-based Scheme

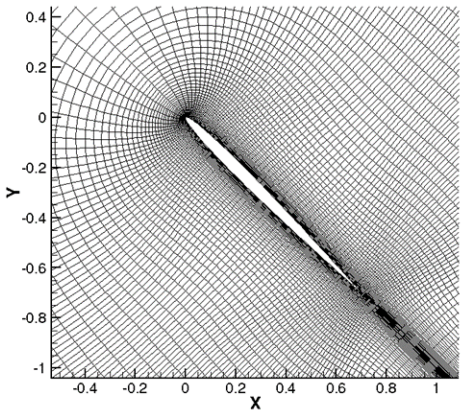

(b) IDW Scheme

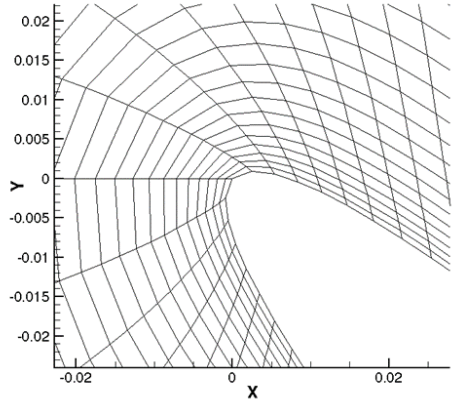

(c) Decay Function-based Scheme (Leading Edge)

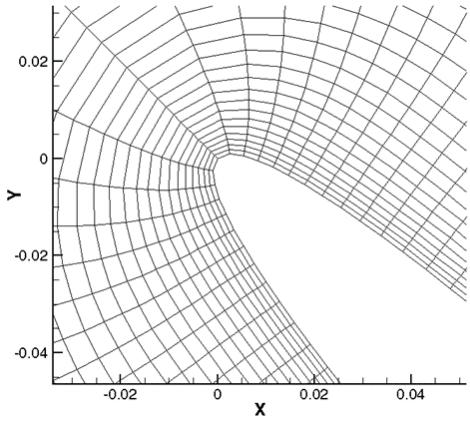

(d) IDW Scheme (Leading Edge)

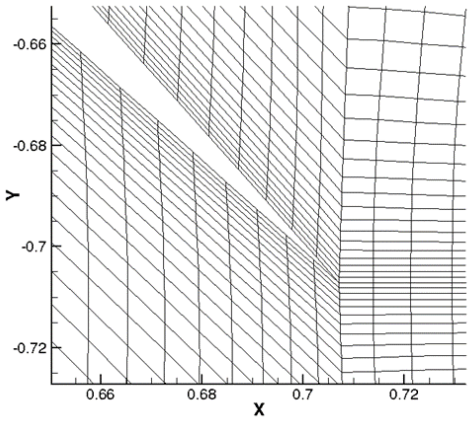

(e) Decay Function-based Scheme (Trailing Edge)

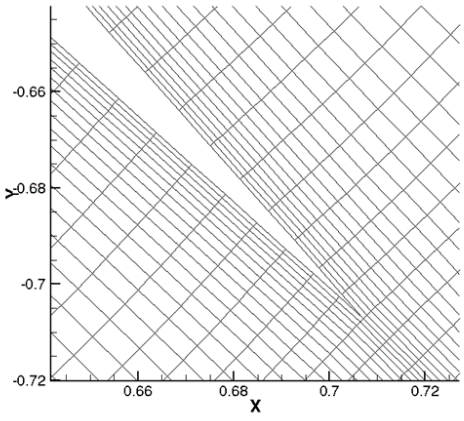

(f) IDW Scheme (Trailing Edge)

Figure 2.12: Comparison of mesh interpolation schemes (45° rotation)

Chapter 3 Coupled Aeroelastic Solver Validation Studies

This chapter focuses on the validation of the coupled CFD/CSD aeroelastic solver to assess and assure the predictive capability of the aeroelastic analysis. The flapping wing problem involves wings operating at low Reynolds numbers, undergoing unsteady kinematics producing highly vortical flow structures. Additionally, flexible wing structures may experience large, nonlinear deformations which can significantly affect the aerodynamics of the wing. Thus, the validation cases are chosen to highlight the aforementioned characteristics of the flapping wing problem and are intended to explore the predictive range of the aeroelastic analysis.

First, the CFD and CSD solvers are tested individually. Later validation studies focused on the coupled CFD/CSD aeroelastic solver. The specific cases discussed are as follows:

i. Rigid bio-inspired wing with passive wing pitch in hover (CFD)
ii. Flat plate undergoing single degree-of-freedom flap motion (CSD)
iii. Zimmerman planform wing with structural compliance (CFD/CSD)
iv. Flexible isotropic rectangular planform wing in hover (CFD/CSD)

3.1 Rigid Bio-inspired Wing with Passive Wing Pitch

3.1.1 Experimental Setup

The present validation study is based on the results of experimental tests performed by Benedict et al. [162]. The wing used throughout the experiment, depicted in Fig. 3.1, consists of a stiff carbon fiber frame covered by a thin Mylar membrane

film resulting in a total wing weight of 3.0 grams. The wing length and thickness are 15.24 cm and 1.6 mm respectively. The wing has a straight leading edge from root to tip with a tapered trailing edge defined by the following equation:

$$c(r) = a_1 r^3 + a_2 r^2 + a_3 r + a_4 \tag{3.1}$$

where a_1 = -0.5764 cm^{-2}, a_2 = 0.1503 cm^{-1}, a_3 = -0.9443, a_4 = 9.1091 cm, c is the local wing chord in centimeters and r is the spanwise location from the wing root in centimeters. The wing has a planform area (S) of approximately 97.85 cm^2 with an aspect ratio (AR) of 2.38 and a mean aerodynamic chord ($\bar{c}$) of 6.42 cm. Note that there is an 8.89 cm offset between the flapping axis of rotation and the wing root and the pitching axis of rotation is 1.016 cm behind the leading edge. All the experimental tests were carried out at an operating flap frequency of 5 Hz and a flapping stroke amplitude of 107°. The mean chord Reynolds number (Re) for all tests was approximately 25,000 based on an average wing maximum tip speed (V_{tip}) of 6.3 m/s.

While the wing flapping was performed by a four-bar mechanism, actuated via an inrunner electric motor, the wing pitching was passive and occurred due to the aerodynamic and inertial forces acting on the wing. The physical passive pitching mechanism is shown in Fig. 3.1 and Fig. 3.2 provides a schematic of the passive pitching mechanism. In Fig. 3.2, the wing is free to rotate about the pitching axis. Stoppers were used to limit the amount of rotation allowed about the pitching axis. Magnets were placed on the stoppers and the wing to hold the wing in place during the translational phases of the flap cycle. At stroke reversal, the inertial and aerodynamic forces act to disengage the wing from the magnets on the stop and cause it to rotate

about the pitching axis. Rotation continues until the wing engages with the other stopper, at which point the magnets hold the set wing pitch for the duration of the subsequent flap stroke. Tests were conducted at three separate translational pitch angles of 40°, 50° and 60°. The flap angle was measured using a USA Digital MA3 shaft encoder. The pitch angle was measured using a USA Digital MA3 shaft encoder with high viscous damping. Each shaft encoder has a measurement uncertainty of ±0.5 deg. Figures 3.3a and 3.3b show the variation of the pitch kinematics when tests were conducted in vacuum and air respectively. The flap kinematics in air and vacuum followed a cosine variation with a flap amplitude of ±53.5°.

During the experimental tests, instantaneous aerodynamic force data was recorded using an ATI Nano-17 six-axis force transducer. The Nano-17 force transducer has an experimental uncertainty of ±0.4 grams. It was placed at the wing root on the pitching axis to measure the total wing forces and moments produced by the wing. Additionally, flowfield measurements were recorded via particle image velocimetry (PIV). Flowfield measurements were taken using time-resolved, two-component PIV with a double-pulsed Nd-YLF laser (Litron LDY304, 30mJ/pulse, 10 kHz max). The laser sheet was set to illuminate the region of interest at the 25%, 50%, and 75% span locations, measured from the wing root, at various azimuthal positions within the flap cycle. The estimated uncertainty of the measured velocity within the experimental flowfield measurements is 0.667%. A more detailed description of the experimental set-up and procedure can be found in Ref. [162].

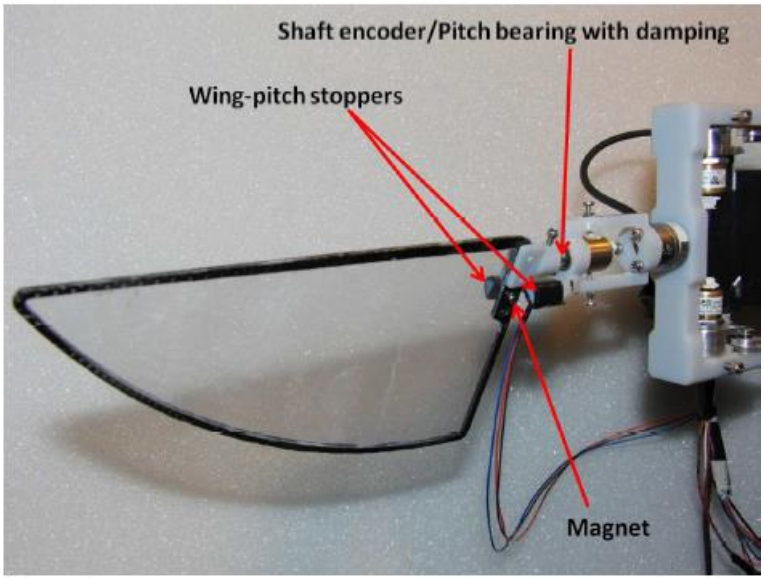

Figure 3.1: Test wing with passive pitching mechanism, as given in Ref. [162]

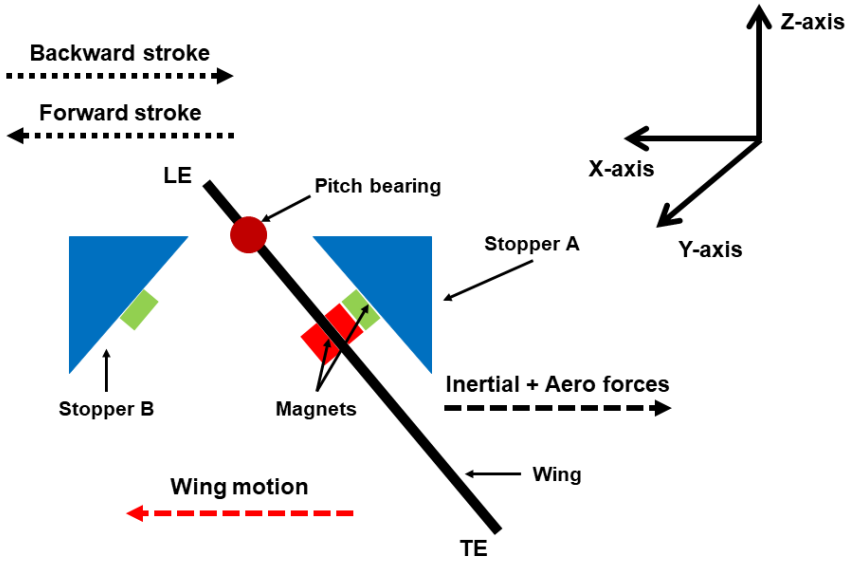

Figure 3.2: Schematic of the passive pitching mechanism

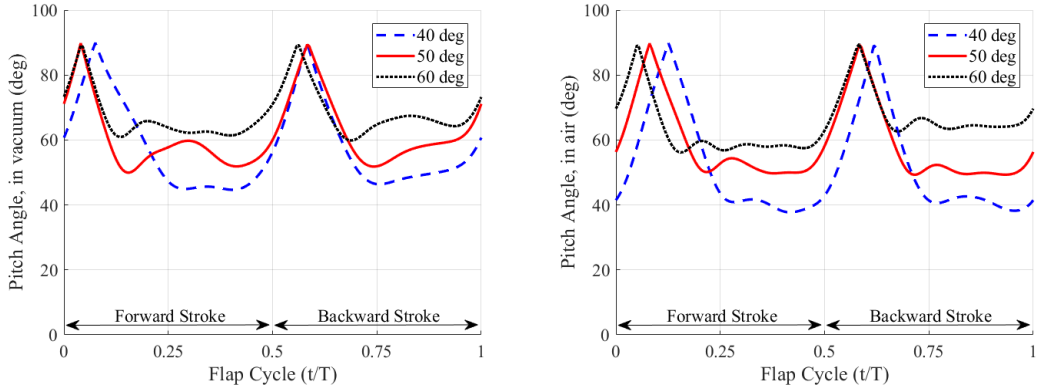

(a) Wing kinematic variation in vacuum (b) Wing kinematics variation in air

Figure 3.3: Variation of wing pitch for the 40°, 50° and 60° translational pitch cases

3.1.2 Computational Setup

Given that the experimental wing in the validation case was rigid, only the CFD solver (OVERTURNS) was utilized when modelling the wing. The flapping wing case was modelled using an overset mesh system with a structured mesh, representing the wing, set inside a cartesian background mesh. Pictures of the overset mesh system are shown in Fig. 3.4. The wing was represented using a structured, curvilinear, body-fitted mesh with an O-O topology (Fig. 3.4a–c). The wing mesh was made up of approximately 4.76 million grid points with 231×161×128 nodes in the wrap-around, spanwise and normal directions respectively. The planform of the wing mesh was made to match that of the experimental test wing. The wing mesh has a thickness-to-chord ratio of 2.5% and was offset from the flapping axis by $1.38\bar{c}$ and the pitching axis by $0.16\bar{c}$, where $\bar{c}$ is the mean chord length, to match that of the experimental setup. A spacing of 1.0×10^{-4} is used for the first node points from the wing surface in the normal direction. This was to satisfy the y-plus dimensionless wall distance criteria as well as provide a fine clustering of mesh points near the wing surface to more accurately

capture the flow separation and formation of voritcal flow structures expected near the wing surface.

To capture the highly vortical flow in the wake, a Cartesian background mesh, seen in Fig. 3.4d, was implemented with 252×252×92 nodes in the x, y and z directions respectively. The background mesh was made up of approximately 6 million nodes with farfield boundary conditions applied 10 chord lengths away from the wing surface. All simulations were run for 4 consecutive flap cycles using 2880 timesteps per flap cycle. A constant dual time step was used with 8 sub-iterations to minimize factorization errors and improve the unsteady computational solution accuracy. The flap kinematics were set to vary sinusoidally, as in the experiment, with the flap amplitude set to ±53.5°. Given the nature of the experiment, the measured pitch kinematics in air, shown in Fig. 3.3b, were prescribed directly into the simulation to correctly account for the pitch angle variation over the flap cycle for the nominal 40°, 50° and 60° pitch cases studied.

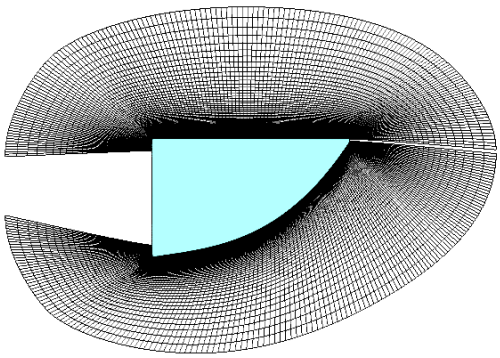

(a) Wing mesh – planform view

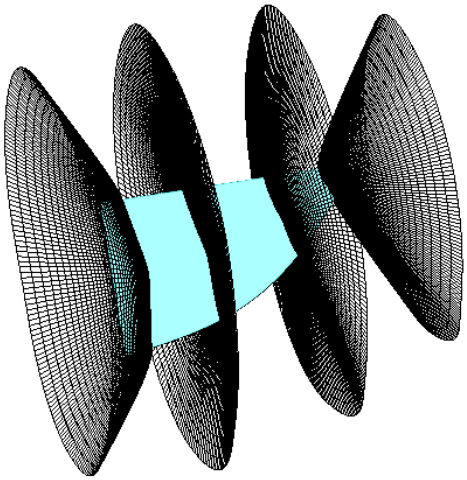

(b) Wing mesh – spanwise slices view

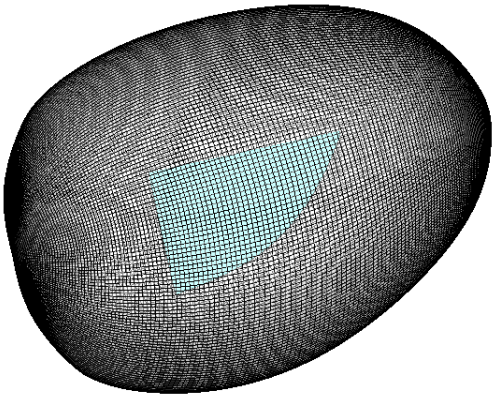

(c) Wing mesh – outer boundary view

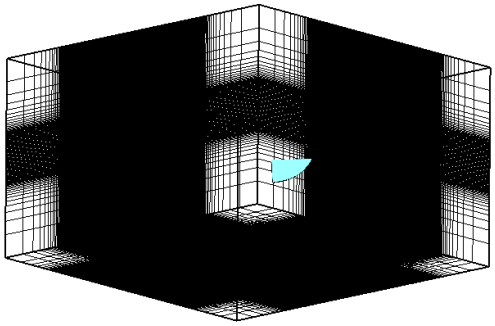

(d) Cartesian background mesh with wing

Figure 3.4: Structured, body-fitted wing mesh and Cartesian background mesh

3.1.3 Aerodynamic Force and Power Time History Comparison

This sub-section focuses on the comparison of the aerodynamic force-time histories and aerodynamic power acquired from the experimental tests and CFD simulations. The experimental force measurement data is used to validate the predictive capability of the unsteady CFD simulations. The experimental aerodynamic forces are determined via inertial force subtraction were the wing is flapped in air and in vacuum. The inertial wing forces measured in vacuum are subtracted from the total wing force,

which is a combination of aerodynamic and inertial forces, measured in air. Ideally, the wing would need to be undergoing the same kinematics in air as in vacuum with the subtraction of forces and moments occurring when the wing is at the same flap angular position in both cases. The experimental setup, described by the authors in Ref. [162], was designed to produce similar flap and pitch kinematics in air and vacuum.

Figure 3.5 provides an illustration of the flapping wing coordinate system that will be referred to through this section. Flapping occurs about the flapping axis which coincides with the z-axis. With respect to the right-hand rule, a forward stroke is a negative rotation about the z-axis while a backward stroke is a positive rotation about the z-axis. While the x-axis and y-axis are a part of the inertial frame, the x′-axis and y′-axis make up the body frame and rotate with the wing while it's flapping. The pitching axis coincides with the y′-axis. Positive aerodynamic lift produced by the wing is said to act along the positive z-axis while aerodynamic drag acts in opposition to the wing motion along the x′-axis.

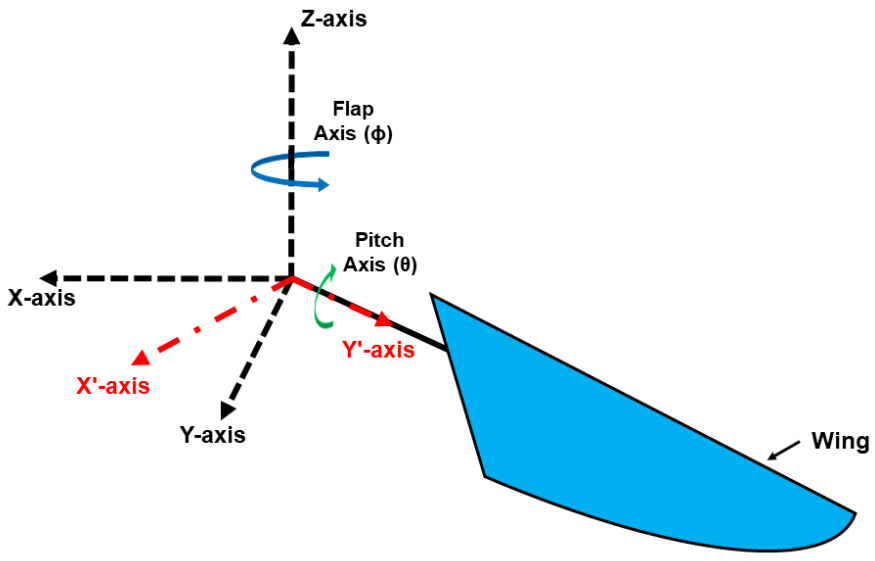

Figure 3.5: Illustration of flapping wing reference coordinate system

Figure 3.6 contains plots comparing the measured and predicted aerodynamic lift and drag force-time histories acquired from the experiment and CFD analysis for the 40°, 50° and 60° translational pitch cases respectively. The experimental force trends shown consist of an average of 10 trials where each trial is an average of 90 flap cycles. The shaded region encompassing the experimental force trend represents the standard deviation from the average of the 10 trials. The average is shown as a black line. In all the plots shown in Fig. 3.6, the horizontal axis represents the time over one flap cycle nondimensionalized by the flap period (T). Figures 3.6a, 3.6c and 3.6e show the variation of lift, in grams, over the course of a flap cycle for the 40°, 50° and 60° translational pitch cases respectively. The lifting force remains positive throughout a majority of the forward and backward strokes, but some negative lift was produced at stroke reversal (t/T = 0.0, 0.5 and 1.0). This behavior in the lift force trend, described in Refs. [90,163], is expected because of the delayed rotation kinematics inherent to the passive pitching mechanism used. Nevertheless, the overall variation in lift predicted by the CFD model agrees well with the measured force trend for all three translational pitch cases tested. There is a slight phase difference between the experimental and computational force-time histories for the 50 and 60 translational pitch cases (Figs. 3.6c and 3.6e). However, the predicted instantaneous peak force magnitudes are similar to those of the experiment and fall within the bounds of uncertainty from the experimental results.

Figures. 3.6b, 3.6d and 3.6f show the variation of drag, in grams, over the course of a flap cycle for the 40°, 50° and 60° translational pitch cases respectively. Note that the sign value of the instantaneous drag designates the direction in which drag force

vector acts. Positive or negative values of drag indicate that the drag force acted in the positive or negative x′-direction, respectively. Throughout the flap cycle, drag is said to oppose the wing flapping motion. Overall, there is adequate correlation between the predicted and measured instantaneous drag results for all three cases. For the 40° pitch case (Fig. 3.6b), there is a notable phase shift between the predicted and measured results. However, the peaks in drag force from the simulation are similar in magnitude to the mean value measured in the experiment. For the 50° and 60° translational pitch cases (Figs. 3.6d and 3.6f), the predicted peaks in instantaneous drag force tended to be greater in magnitude than the experimental mean value for their respective cases. Focusing on the 50° case (Fig. 3.6d), during the flap cycle there was a slight difference between the measured and predicted drag force values in the instance at which maximum instantaneous drag occurred. The peak magnitudes of the CFD drag force-time history occur at mid-forward stroke and mid-backward stroke ($t/T = 0.25$ and 0.75). Peak magnitude in the experimentally measured drag values occurred slightly after and slightly before mid-forward stroke and mid-backward stroke, respectively. However, it is important to note that the standard deviation in the experimental data becomes quite large near the peak values of drag in comparison to that near the end of a stroke.

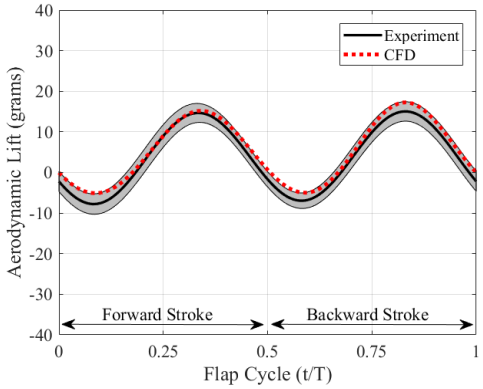

(a) Lift force time history (40° case)

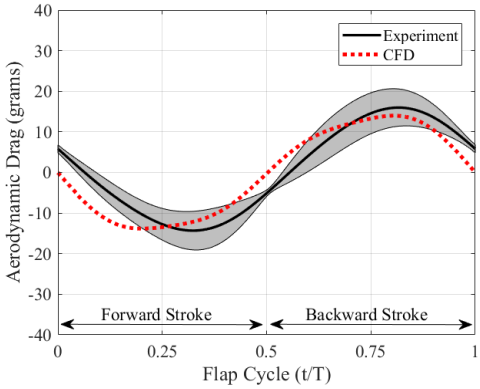

(b) Drag force time history (40° case)

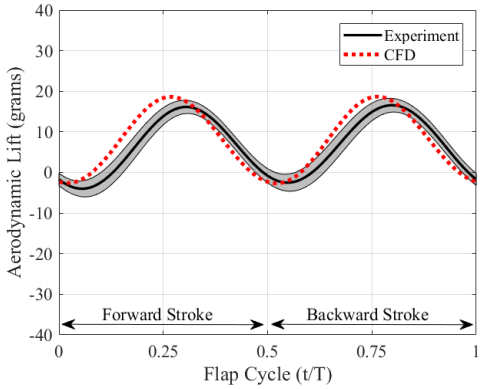

(c) Lift force time history (50° case)

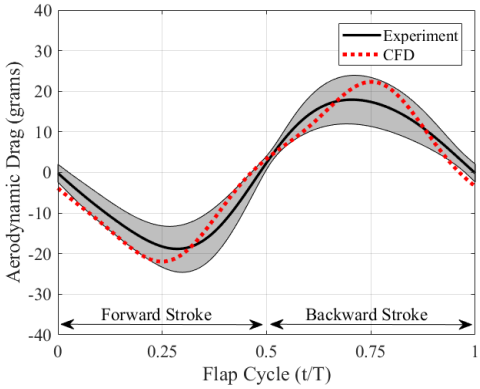

(d) Drag force time history (50° case)

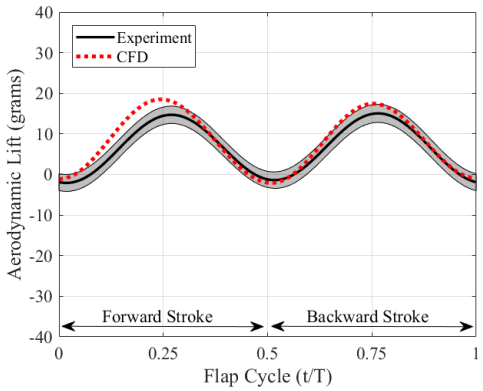

(e) Lift force time history (60° case)

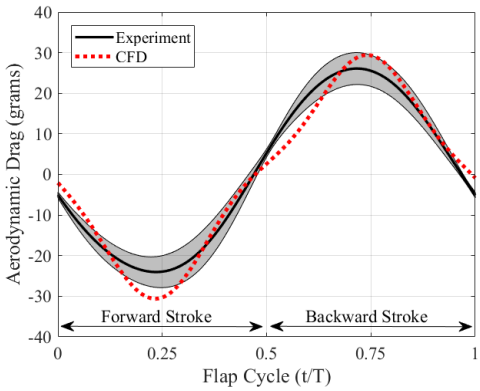

(f) Drag force time history (60° case)

Figure 3.6: Experimental and CFD aerodynamic force-time histories for the 40°, 50° and 60° translational pitch cases

The large deviation in the drag force peak magnitude is due to the challenge of separating the large inertial loads in the flap plane from the aerodynamic loads generated by the wing. Nevertheless, the predicted drag force-time histories from the

CFD lay within or near the experimental bounds of uncertainty for all the cases. Overall, the variation in drag predicted by the CFD model correlates well with the measured force trend. This gives confidence in the accuracy and feasibility of using vacuum force subtraction techniques to experimentally measure instantaneous aerodynamic forces in air, especially when the inertial forces dominate the total force measurements.

As the design and development of future MAV concepts progresses, it is important to assess not only the aerodynamic performance, but also the aerodynamic efficiency of a particular design. In conventional aircraft design, typical measures of aerodynamic efficiency include power (P), the lift-to-drag ratio (L/D) and power loading (L/P). Note that throughout this sub-section, references to power infer aerodynamic power. The inertial power of the flapping mechanism was not investigated in this study.

Aerodynamic power is calculated by summing the dot product of the local aerodynamic force vector with the local velocity vector along the span of the wing. Figure 3.7 shows the variation of instantaneous power over a flap cycle for the 40°, 50° and 60° translational pitch cases. As expected, the peak magnitude of aerodynamic power increases with increased translational pitch angle and approaches a magnitude of zero during stroke reversal. Slight differences in the peak magnitude and variation of the instantaneous power trend line occur between the forward and backward strokes for all of the translational pitch cases. This is because of fluctuations in the measured wing pitch angles, which were discussed previously. If perfectly symmetric pitch

kinematics were used, as opposed to the experimentally measured values, it is expected that the results of the forward and backward strokes would be symmetric.

From Ref. [162], lift per unit power (L/P) was a metric utilized to determine the aerodynamic efficiency of the wing kinematics used in this study. In the study, only the translational phases of the forward stroke and backward stroke (t/T = 0.1—0.4 and 0.6—0.9) were accounted for when analyzing the instantaneous variation of L/P. The instances of the flap cycle where stroke reversal occurred were ignored because the wing produced negative lift at those times and was said not to be operating at its highest possible efficiency.

The power loading variation over the translational phase of the flap cycle for the forward stroke and backward stroke is shown in Fig. 3.8. Figure 3.8a also contains experimental data for instantaneous lift-to-power ratio presented in Ref. [162]. Note that the available experimental data is only for the forward stroke from approximately t/T = 0.2—0.4 which omits regions of negative lift in the lift-to-power ratio trends. From Fig. 3.8, there is little difference between the computational trends predicted in the forward stroke in comparison to the backward stroke. Thus, all subsequent discussion on the CFD instantaneous L/P trend will refer to Fig. 3.8a. However, the same analysis applies to the CFD trends in Fig. 3.8b.

The CFD 50° and 60° cases have a relatively constant L/P during the translational phase similar to the experimental data for those two cases. However, the computational trend lines initially under-predict the magnitude of L/P (especially for the 50° case) and then over-predict L/P toward the end of the translational phase. For the 40° case, the CFD L/P curve is monotonically increasing while it is relatively

constant for the respective experimental L/P curve. Initially, the instantaneous L/P for the computational 40° case is negative because of the negative lift produced at the beginning of the specified segment of the flap cycle. However, toward the end of the translational phase, the magnitude of the lift-to-power ratio for the 40° case far exceeds that of the other two cases.

In general, the CFD model predicts a similar trend in lift-to-power ratio in comparison to the 50° and 60° cases. However, it tends to under-predict the magnitude of L/P compared to the experiment. There is a noticeable discrepancy between the experimental and CFD predicted L/P trends for the 40° case and needs further investigation. It is believed that due to the larger variation in pitch angle for the 40° case, the CFD model may be prolonging the diffusion of the LEV and consequently over-predicting the lift-to-power ratio toward the end of the flap stroke.

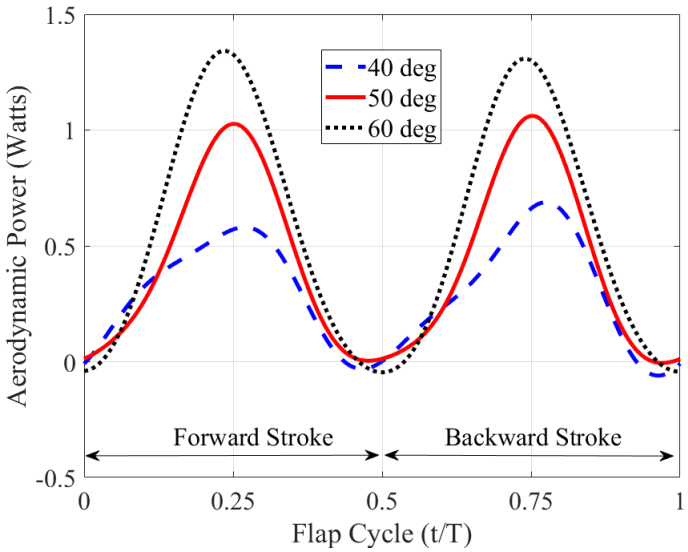

Figure 3.7: Variation of instantaneous aerodynamic power over a flap cycle (40°, 50° and 60° translational pitch cases)

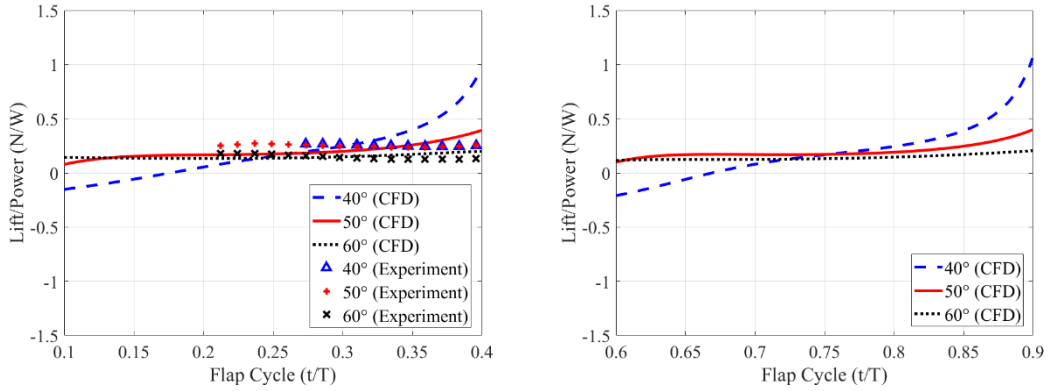

(a) Translational phase: forward stroke (b) Translational phase: backward stroke

Figure 3.8: Lift per unit power during the translational phase of the forward and backward stroke (40°, 50° and 60° translational pitch cases)

3.1.4 Measured and Predicted Flowfield Comparison

To compare the PIV and CFD flowfields, the vorticity field was used. Vorticity is defined as the curl of the velocity field via the following equation:

$$\omega = \nabla \times \vec{V} \tag{3.2}$$

where ω is vorticity, ∇ is the del operator and $\vec{V}$ represents the velocity vector. The gradients of the velocity field were calculated using a second order accurate least squares differencing method. While force measurement tests were carried out for all three translational pitch cases, PIV flowfield studies were only conducted at the 50° translational pitch angle. In the vorticity contour plots, overlaid velocity vectors are plotted with every other velocity vector displayed for clarity. In addition, the magnitude of vorticity is normalized by the maximum tip velocity experienced by the wing (V_{tip}) and the mean aerodynamic chord ($\bar{c}$).

Figure 3.9 provides a comparison of the measured PIV and computed CFD vorticity field near the leading edge of the wing for the 50° translational pitch case. Figures 3.9a–c and 3.9d–f are the results at the 25%, 50% and 75% span locations, for the PIV and CFD respectively, at the mid-forward stroke (t/T = 0.25). This comparison displays the capability of the CFD model to predict the spatial variation of the vorticity within the LEV. The mid-forward stroke position (t/T = 0.25) was selected because at this instance in the flap cycle, the wing experiences the highest rotational velocity and vortex strength was expected to be near its greatest magnitude. Note that for this case spanwise position is measured with respect to the wing root. For example, at the wing root r/b equals 0.0 and at the wing tip r/b equals 1.0.

The LEV near the wing root in Figs. 3.9a and 3.9d is tightly formed and attached to the wing. The CFD solver was able to accurately model the LEV size and location in comparison to the PIV results. In Fig. 3.9b, the LEV has burst, becoming more diffused and begins to separate from the wing surface. Again, the CFD solver is able to capture this behavior, shown in Fig. 3.9e, displaying a larger, more diffused LEV. For the PIV (Fig. 3.9c), at the 75% span location, the LEV has decreased in size and is clearly not attached to the wing. The separated LEV remains in relatively close proximity to the wing surface and a smaller secondary LEV has begun to form at the leading edge. While the CFD results at the 75% span location in Fig. 3.9f also predict a decrease in leading edge vortex size and separation from the wing surface, there are noticeable differences between the PIV and CFD. Mainly, the CFD solver over-predicts the degree by which the LEV has separated from the wing surface. Also, the general formation of the predicted LEV differs from that measured by the PIV. Qualitatively,

the LEV from CFD is less diffused and has a more oblong shape in comparison the LEV from PIV. Largely, there is good correlation between the PIV and CFD results and many of the vortical flow variations in the LEV were predicted by the CFD model. There is some deviation between the PIV and CFD vorticity fields at the more outboard sections, but the salient flow features are still predicted.

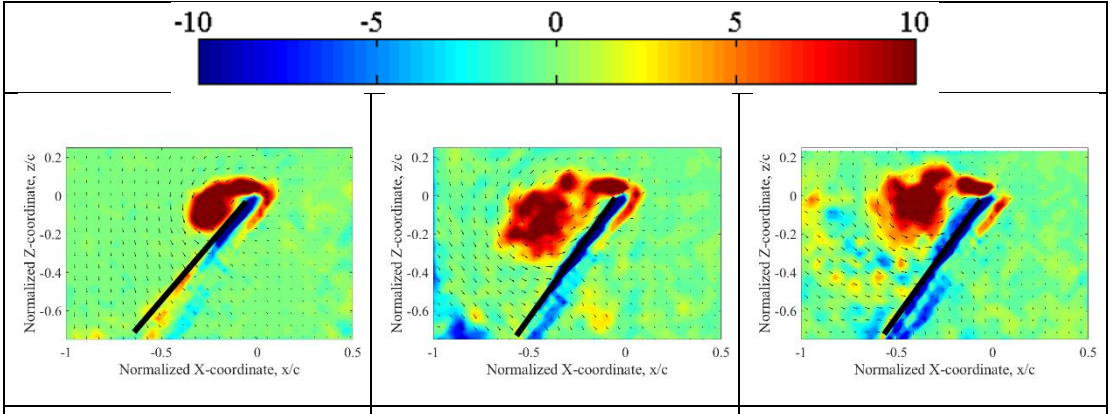

(a) PIV, r/b = 25% (b) PIV, r/b = 50% (c) PIV, r/b = 75%

(d) CFD, r/b = 25% (e) CFD, r/b = 50% (f) CFD, r/b = 75%

Figure 3.9: Spatial variation of PIV and CFD vorticity contours at t/T = 0.25 (50° translational pitch case)

Figures 3.10a–c and 3.10d–f show the results at the t = 0.15T, 0.25T and 0.35T time instances of the flap cycle, for the PIV and CFD respectively, at the 50% span location of the wing. The contours in Fig. 3.10 validate the temporal evolution of the LEV predicted by the CFD against that measured during the experiment. In Fig. 3.10a, the LEV has formed, and rotation of the flow is visible via the overlaid velocity vectors.

In Fig. 3.10b, the LEV begins to form, but clear rotation of the flow has not yet begun. Figures 3.10b and 3.10e show that the LEV has burst, become more diffused and then begins to separate from the wing surface. From the PIV data in Fig. 3.10c, the flow has become highly separated with a small amount of vorticity generated at the leading edge. Also, there is a small region of counter-rotating vorticity located below the region of separation. The CFD results shown in Fig. 3.10f, exhibit largely separated flow but the concentration of vorticity is not as diffused as that seen in Fig. 3.10c. The CFD model is also predicting a small region of counter-rotating vortical flow similar to the PIV. However, the location of the counter-rotating vorticity is much closer to the leading edge in comparison to that seen in Fig. 3.10c. Overall the CFD solver has demonstrated an acceptable capability to model the temporal evolution of the LEV and predict the salient variations of the LEV over time seen in the PIV.

The PIV and CFD vorticity contours provided a qualitative comparison of the LEV from the measured and predicted results. In addition, the velocity field can be used to quantitatively compare the estimated LEV circulation strength in both the CFD and PIV.

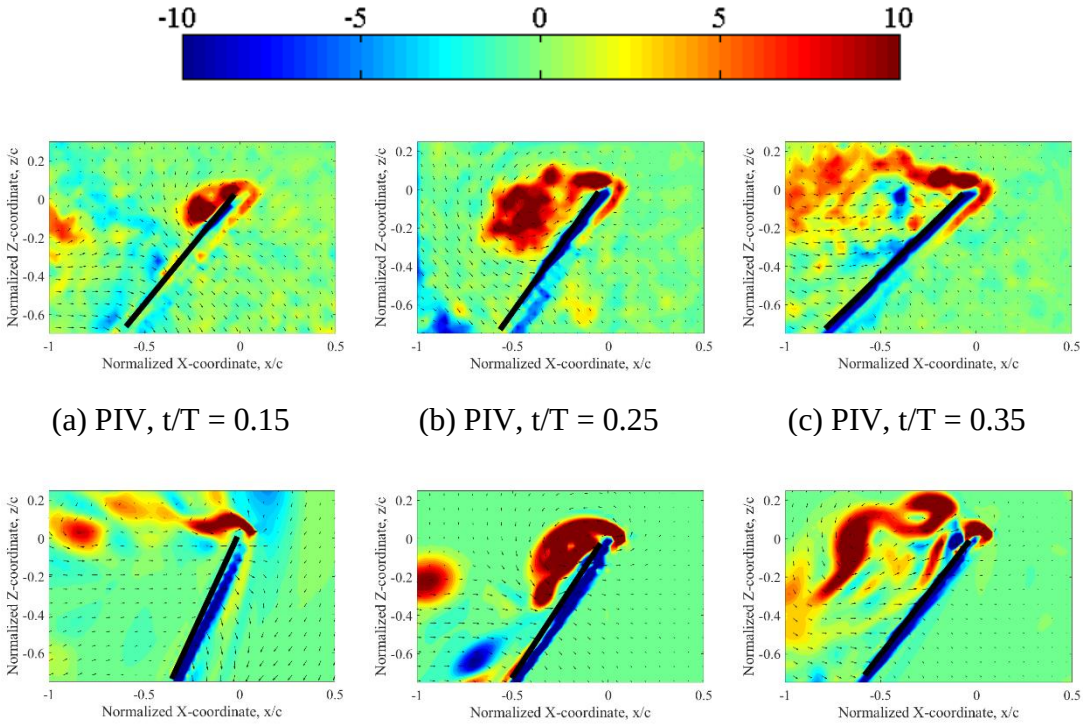

(a) PIV, t/T = 0.15 (b) PIV, t/T = 0.25 (c) PIV, t/T = 0.35

(d) CFD, t/T = 0.15 (e) CFD, t/T = 0.25 (f) CFD, t/T = 0.35

Figure 3.10: Temporal variation of the PIV and CFD vorticity contours at the 50% span location (50° translational pitch case)

The circulation is obtained by choosing a suitable integration contour (i.e. around the LEV in this case) and numerically evaluating the closed-loop velocity integral. This loop must completely enclose the LEV, but obviously without intersecting any other extraneous circulation. The equation for circulation is given below as:

$$\Gamma = -\oint \vec{V} \bullet \overrightarrow{ds} = -\iint_A (\nabla \times \vec{V}) \bullet \overrightarrow{dS} \tag{3.3}$$

where $\vec{V}$ is the velocity vector, $\overrightarrow{ds}$ is the directed line segment at a point on a predefined contour, $\nabla \times \vec{V}$ is the curl of the velocity vector and $\overrightarrow{dS}$ is the area enclosed by a curve. For this analysis, a vorticity threshold was set ($-400 < \omega < 400$) so that low magnitude extraneous vorticity would not be included in the integration contour that was used to

enclose the LEV. Next, the vorticity field is scanned in order to locate pockets of vorticity of a certain size (3×3 grid square) within that threshold. These regions are then stored as grid locations. Line contours are drawn around these concentrations of vorticity so that an area integral of vorticity can be assessed to obtain the circulation for the vortices in the PIV experiment flowfield and those generated by the CFD solver.

Figure 3.11a provides an illustration of how the circulation is computed using a representative phase-averaged vorticity field for the 50° translational pitch case. The white dots represent the calculated center of vorticity for a given region of vorticity while the black boxes represent the discretized vorticity field. By summing the area integral of vorticity within the vorticity field, the circulation strength of the LEV can be determined. The circulation strength of the LEV is found using the following equation:

$$\Gamma = \sum_{i=1}^{n} \Gamma_i = \sum_{i=1}^{n} \iint_A (\nabla \times \vec{V}) \bullet \overrightarrow{dS_i} \tag{3.4}$$

where Γ_i is the incremental circulation within the incremental surface area $\overrightarrow{dS_i}$ and n is the total number of incremental surface areas within the discretized vorticity field.

Figure 3.11b shows the circulation values for the shedding process at the 50% span location for the 50° translational pitch case. From the PIV analysis, it can be seen that the circulation of the LEV at the 50% span location increases up to the midstroke location (t/T = 0.25) and then drops. However, for the CFD, the circulation increases past the midstroke location to about t/T = 0.30 and then begins to decrease. Also, the decrease in circulation after midstroke can be correlated to the LEV burst within the vorticity contours (see Figs. 3.9 and 3.10).

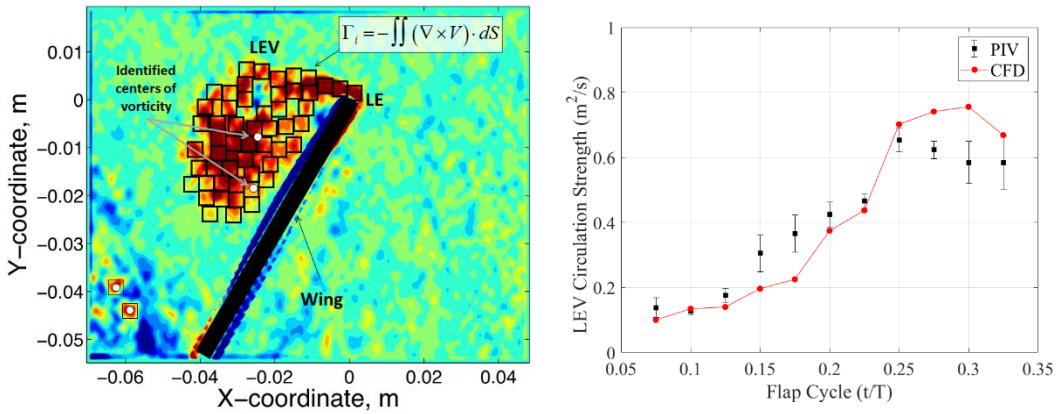

(a) Representative illustration of circulation summation method

(b) PIV and CFD LEV circulation strength variation over time

Figure 3.11: Illustration of circulation summation method and plot of LEV circulation strength variation

3.2 Flat plate undergoing single degree-of-freedom flapping motion

3.2.1 Computational Setup

The present validation study is based on a case presented in Ref. [128]. In the study, an aluminum flat plate wing with a rectangular planform is modeled undergoing prescribed flap kinematics. A schematic of the wing used throughout the test case can be seen in Fig. 3.12. The wing has a length of 80 mm, chord length of 27 mm and thickness of 0.2 mm. Note that Ref. [128] erroneously reports the thickness to be 2.0 mm. The flap axis, which coincides with the x-axis, runs parallel to the wing chord at the root of the wing. At the start of the simulation, the wing lays within the xy-plane with the wing leading edge coinciding with the y-axis. The prescribed flap kinematics are sinusoidal in nature and are described by the function:

$$\phi(t) = \phi_{amp}[1 - \cos(2\pi f t)] \tag{3.5}$$

where the flap amplitude (ϕ_{amp}) equals 17° with the flap frequency (f) varied between 5 Hz, 10 Hz and 30 Hz. Starting at the leading edge of the wing root, there is a 5 mm × 5 mm region in which the wing deformation is constrained in all degrees of freedom. This is to represent the area on the wing which would typically be attached to a flapping mechanism and is highlighted in red in Fig. 3.12. The wing is assumed to be made of aluminum alloy with a Young's modulus (E) of 70 GPa, Poisson ratio (ν) of 0.3 and a material density of 2700 kg/m^3. Table 3.1 contains a list of the pertinent structural and kinematic properties used in the MBDyn model of the wing. For each simulation, a residual tolerance of 1.0×10^{-1} was used with a maximum number of 100 iterations for convergence testing. For each flap frequency tested, the time step was changed to have 2880 iterations per flap cycle.

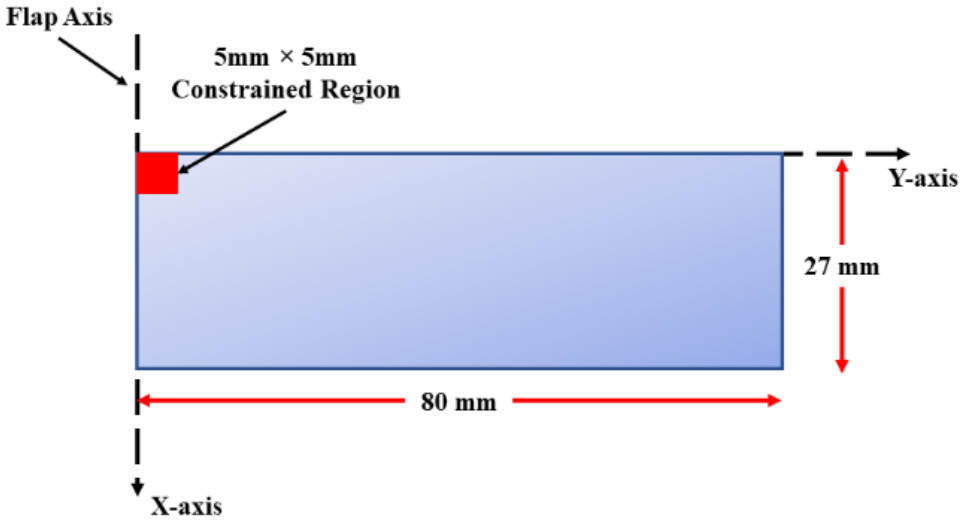

Figure 3.12: Schematic of flat plate wing with dimensions

Table 3.1: Flat plate wing structural and geometric properties

Property	Value
Length	80 mm
Width	27 mm
Thickness	0.2 mm
Density	2700 kg/m^3
Young's Modulus	70 GPa
Poisson's Ratio	0.3
Flap Frequency	5, 10 and 30 Hz
Flap Amplitude	17°

3.2.2 Results Comparison – Element Sensitivity Study

Initial studies sought to compare the predicted results from the simulation for a varied number of plate elements. In the study, three cases were explored where the number of plate elements were varied in groupings of 10×10, 10×18 and 10×26. The number of plate elements in the chordwise direction is kept constant with only the number of plate elements in the spanwise direction varying. This is because most of the deformation for the case in consideration is due to spanwise bending of the wing.

Figures 3.13a–c show the variation in normalized vertical displacement of the wing tip over several flap cycles for the 5 Hz, 10 Hz and 30 Hz cases respectively. The vertical displacement being compared is the z-displacement of the leading edge at the wing tip. Vertical displacement is normalized by the length of the wing span and time is normalized by the flap period (T) for the flap frequency in consideration.

In Fig. 3.13a, there is minimal variation in the normalized vertical displacement time history between the three structural grids tested with the results from the 10×18 and 10×26 being nearly identical. When comparing the results at f = 10 Hz in Fig. 3.13b, all three cases appear to be nearly identical for the first and second flap cycles. However, during the third and fourth flap cycles there is a noticeable deviation in the

vertical deflection between the 10×10 case and the other two cases with a greater number of plate elements. The vertical displacement time histories for the 10×18 and 10×26 cases in Fig. 3.13b fall on top of one another similar to the results at f = 5 Hz.

At a flap frequency of 30 Hz (Fig. 3.13c), significant differences are seen between the three different structural grids shortly after the first flap cycle. There is a significant phase difference in the variation of vertical displacement when comparing the results from the 10×10 case to the 10×18 and 10×26 cases. In comparing the 10×18 and 10×26 cases, the time-histories are more in-phase with one another but there are distinct differences in the magnitudes between the two cases. This is due to the high flap frequency which causes significant geometry nonlinearities and large inertial forces which act on the wing. For the high flap frequencies, the output of the structural model is highly sensitive to the number of plate elements used. However, for the flap frequencies of interest ($f \leq$ 10 Hz), using 10×18 plate elements will suffice. In the following validation study, the structural model made up of 10×26 plate elements will be utilized.

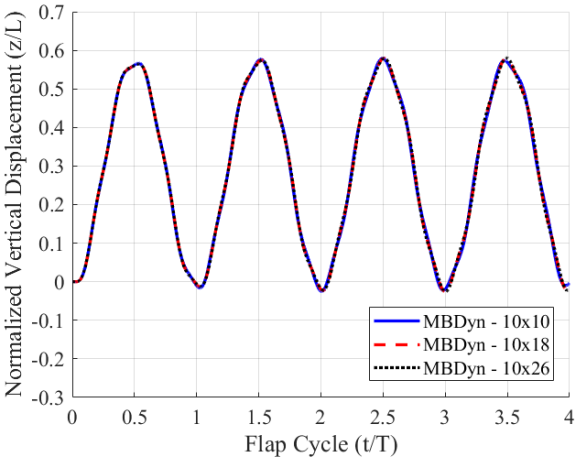

(a) Normalized vertical displacement vs time, f = 5 Hz

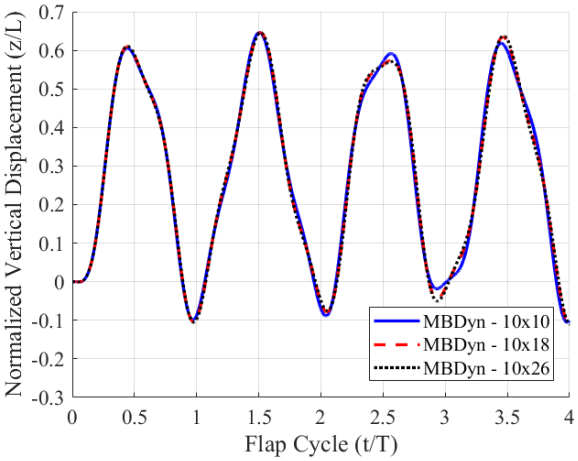

(b) Normalized vertical displacement vs time, f = 10 Hz

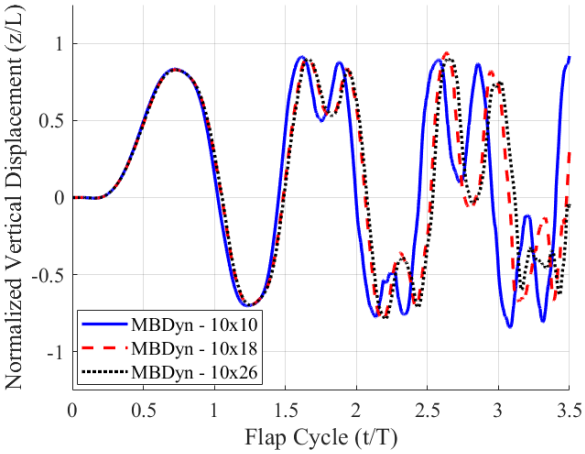

(c) Normalized vertical displacement vs time, f = 30 Hz

Figure 3.13: Normalized vertical displacement vs flap cycle for varied numbers of plate elements (f = 5, 10 and 30 Hz)

3.2.3 Results Comparison – Validation Comparison

The results in the previous sub-section for the case of 10×26 plate elements are compared to the results from two different computational structural dynamics solvers described in Ref. [128]. The two solvers against which the current results are compared were MSC Marc and UM/NLAMS. Marc is a commercial, general purpose, nonlinear finite element analysis solver developed by MSC Software capable of modeling structural as well as multi-physics problems. UM/NLAMS is University of Michigan's Nonlinear Membrane Shell Solver. UM/NLAMS is a multi-body dynamics-based finite element analysis which utilizes a body-fixed floating frame of reference to describe the rigid body motion with a co-rotational framework to handle the geometric nonlinearities. The co-rotational framework is favorable for problem which have small strains but large rotations.

As described in Ref. [128], the wing is modeled using the bilinear thin-triangular shell element no. 138 within MSC Marc. For the 5 Hz and 10 Hz cases, a non-dissipative form of the Newmark time-integration scheme is used. For the 30 Hz case, the generalized- method was utilized with a spectral radius of 0.4. The time step used is 1.5×10^{-4} s for the 5 and 10 Hz cases and 1.0×10^{-5} s for the 30 Hz case. For all three cases, a convergence criterion tolerance of 1.0×10^{-4} is imposed.

Figure 3.14 shows the variation in normalized vertical displacement of the wing tip over several flap cycles between the different structural solver. Figures 3.14a, 3.14b and 3.14c correspond to flap frequencies of 5, 10 and 30 Hz respectively. In Fig. 3.14a, the results from MSC Marc and UM/NLAMS lay on top of one another and the current results from MBDyn show good agreement with respect to the variation in normalized

vertical displacement. For the 10 Hz case (Fig. 3.14b) the results from MBDyn and MSC Marc lay on top of one another. The results from UM/NLAMS slightly deviate from the MBDyn and MSC Marc results near the peaks in tip displacement but maintain good correlation throughout other portions of the flap cycles. Lastly, for the 30 Hz case (Fig. 3.14c), there is significant difference between the results of all three models. The variation in normalized vertical displacement for the three solvers agree well for the first flap cycle. However, after the first flap cycle, the trends deviate significantly due to the large inertial forces and geometric nonlinearities present at such a high flap frequency for this wing. Figure 3.15 shows images of the wing flapping in the MBDyn case at various times in the simulation to illustrate the extent of wing bending and twisting that occurs at the 30 Hz flap frequency.

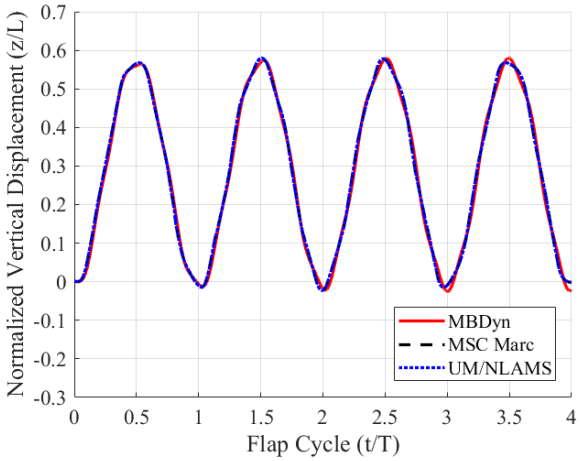

(a) Normalized vertical displacement vs time, f = 5 Hz

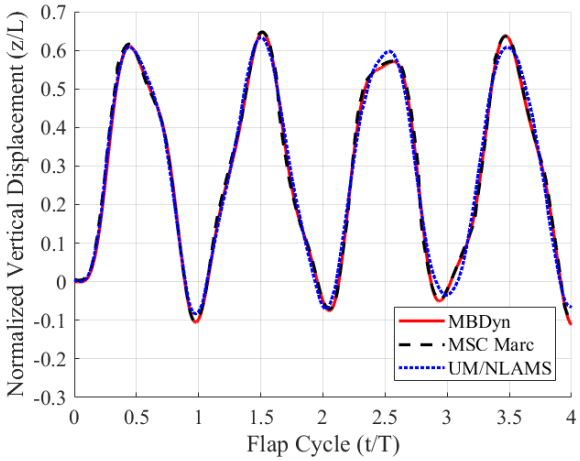

(b) Normalized vertical displacement vs time, f = 10 Hz

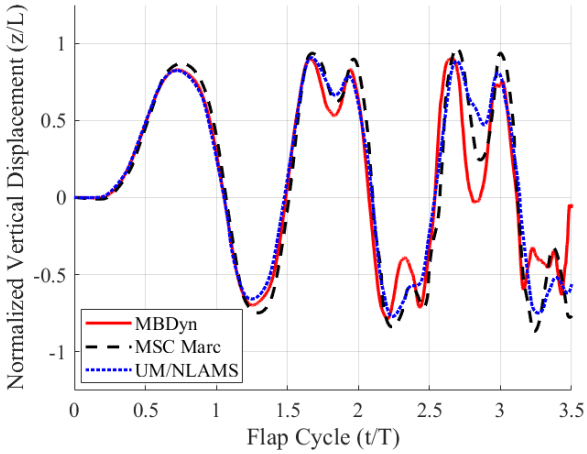

(c) Normalized vertical displacement vs time, f = 30 Hz

Figure 3.14: Normalized vertical displacement vs flap cycle for different structural solvers (f = 5, 10 and 30 Hz)

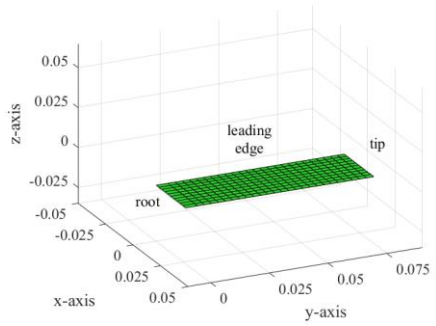

(a) t/T = 0.0

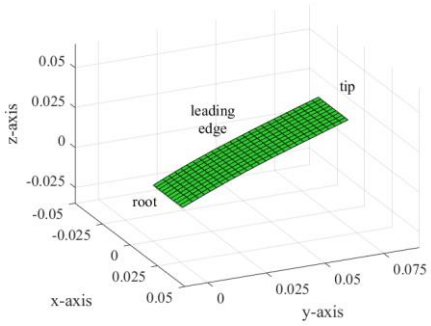

(b) t/T = 0.5

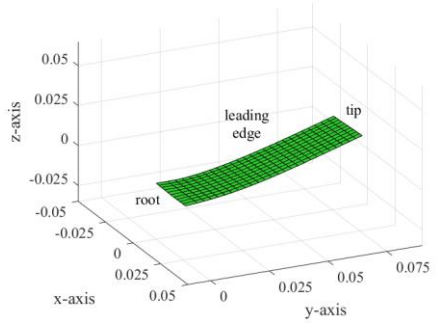

(c) t/T = 1.0

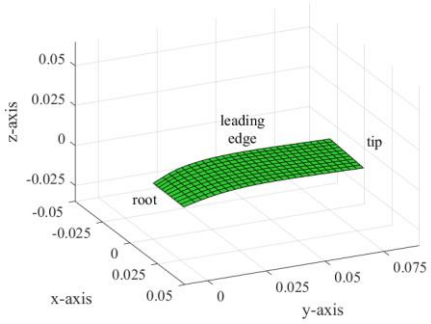

(d) t/T = 1.5

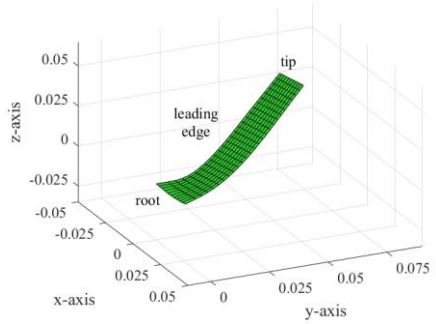

(e) t/T = 2.0

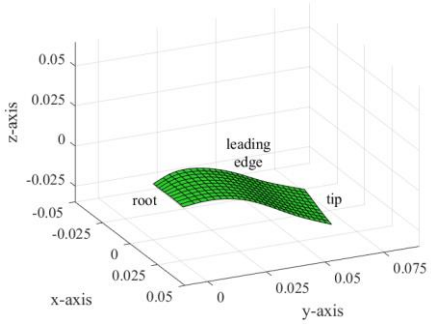

(f) t/T = 2.5

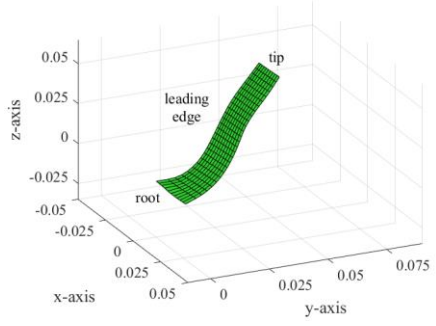

(g) t/T = 3.0

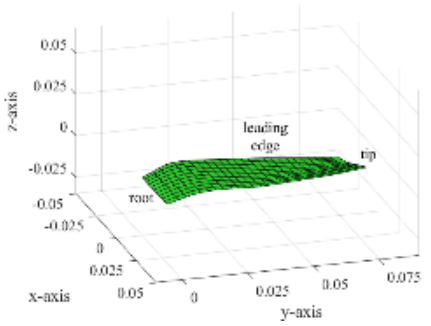

(h) t/T = 3.5

Figure 3.15: Images of the wing deformation for the f = 30 Hz case at various time instances of the simulation

3.3 Zimmerman Planform Wing with Structural Compliance

3.3.1 Description of Experimental and Computational Test Case

The validation case presented in this section is based on the combined experimental and computational study discussed Aono et al. in Ref. [164]. In this study, PIV flowfield measurements and digital image correlation (DIC) wing deformation measurements are performed on a custom-built flapping wing setup. DIC is a non-contact, visual-based measurement technique that is capable of measuring the 3D, full-field displacements and strains of an object's surface via stereo triangulation. A picture of the flapping mechanism from Ref. [164] can be seen in Fig. 3.16. Note that the wings in the Fig. 3.16 are different from those tested and are there solely for illustrative purposes. The wings tested have a Zimmerman planform which is constructed from a quarter section of two ellipses whose semi-major axes join at the quarter-chord location of the wing root and whose semi-minor axes lay at the wing root. Figure 3.17 provides a schematic of the wing geometry with dimensions. The root chord length is 25 mm while the wing has an overall mean chord length ($\bar{c}$) of 19.6 mm. The radial location of the reference mean chord position is 46.4 mm from the wing root. The wing length and planform area are 75 mm and 0.0014726 m^2 respectively, resulting in a wing aspect ratio of 3.82.

The wings are constructed out of a solid aluminum sheet with a thickness of 0.4 mm and is assumed to have a Young's modulus (E) of 70.0 GPa, Poisson ratio (ν) of 0.3 and a material density of 2700.0 kg/m^3. Given that the wing has some degree of structural compliance, it's important to assess how the wing flexibility may influence

the aeroelastic phenomena producing by the wing. The scaling parameter (Π_1) is the ratio of elastic forces to aerodynamic forces and is defined as:

$$\Pi_1 = \frac{D_{plate}}{\rho_{ref} V_{ref}^2 c_{ref}^3} \tag{3.6}$$

where D is the bending stiffness of an isotropic plate, ρ_{ref} is the reference fluid density, V_{ref} is the reference velocity and c_{ref} is the reference length dimension. Note that $D_{plate} = \frac{Eh^3}{12(1-\nu^2)}$ where E is the Young's modulus, h is the plate thickness and ν is the Poisson's ratio.

The linkage lengths of the flapping mechanism were chosen to emulate a sinusoidal variation in wing flap angle with a flap amplitude of ±21°. All tests were conducted at a flap frequency of 10 Hz. Additional information on the design of the flapping mechanism can be found in Ref. [164]

Figure 3.16: Flapping wing mechanism from Ref. [164]

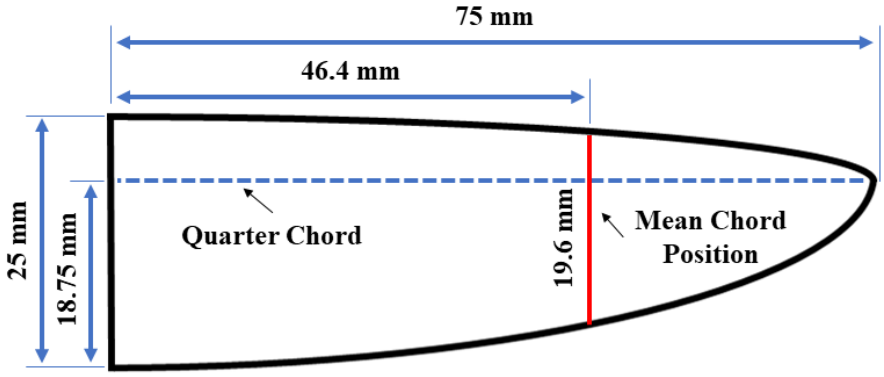

Figure 3.17: Schematic of the Zimmerman wing planform with dimensions

In addition to the experimental tests, the study presented in Ref. [164] included a high-fidelity numerical analysis of the flapping wing problem using a coupled CFD/CSD framework. To solve the fluid dynamics of the problem, the CFD solver

(STREAM) is employed. STREAM is an unsteady, incompressible 3D Navier-Stokes solver. The convection terms are discretized using a second-order upwind scheme while the pressure and viscous terms are discretized using a second order central scheme. An implicit Euler scheme is used for time integration. A master-slave moving grid technique is employed to facilitate re-meshing of the CFD grid due to deformations applied at the fluid-structure interface.

The structural dynamics of the problem are solved using UM/NLAM University of Michigan's Nonlinear Membrane Shell Solver (UM/NLAMS). UM/NLAMS is a multi-body dynamics-based finite element analysis, which utilizes a body-fixed floating frame of reference to describe the rigid body motion with a co-rotational framework to handle the geometric nonlinearities. The shell element used with the structural solver is a superposition of the optimal membrane element and a discrete Kirchhoff triangle plate bending element. More information on the STREAM, UM/NLAMS and the development of the authors' aeroelastic analysis can be found in Ref. [111,128].

The authors utilized an O-type structured, multi-block grid to represent the Zimmerman wing within the CFD solver. The CFD mesh was generated with approximately 0.7 million cells and a time step size of 1.5×10^{-3} s was implemented. In the structural model, a total of 480 triangular plate elements were utilized. The structural and geometry properties of the aeroelastic model were made to match those described in the experimental setup. Table 3.2 contains a list of the relevant structural parameters and flow conditions for this case.

Table 3.2: Zimmerman wing structural and flow condition properties

Property	Value
Wing Span, b	0.075 m
Root Chord Length, c_{root}	0.025 m
Mean Chord Length, $\bar{c}$	0.0196 m
Span Location (at mean chord), b_{ref}	0.0464 m
Wing Thickness, h	0.4 mm
Wing Planform Area, S	0.0014726 m^2
Material Density, ρ	2700 kg/m^3
Young's Modulus, E	70.0 GPa
Poisson's Ratio, v	0.3
Aspect Ratio, AR	3.83
Flap Frequency, f	10 Hz
Flap Amplitude, ϕ_{amp}	21°
Maximum Tip Velocity, V_{tip}	1.73 $m\text{-}s^{-1}$
Maximum Velocity (at mean chord span location), V_{ref}	1.07 $m\text{-}s^{-1}$
Reduced Frequency ($\frac{2\pi f\bar{c}}{2V_{tip}}$)	0.357
Air Density, ρ_{air}	1.209 $kg\text{-}m^{-3}$
Reynolds Number ($\frac{\rho_{air}V_{tip}\bar{c}}{\mu}$)	4092
Π_1 ($\frac{D_{plate}}{\rho_{air}V_{tip}^2\bar{c}^3}$)	3.8×10^4

3.3.2 Computational Setup

For this validation case, a flexible wing was studied, thus, the coupled CFD/CSD aeroelastic analysis was utilized when modelling the wing. In the CFD model, the case was modelled using an overset mesh system where a C-O topology, structured body-fitted mesh was used to represent the wing and a Cartesian background mesh was used to model the surrounding wake. The wing shape was designed to match that of the test wing schematic shown in Fig. 3.17. In the CFD wing mesh, all dimensions are normalized by the mean chord. The wing mesh was approximately comprised of 1.9 million grid points with 227×91×93 grid points in the wrap-around, spanwise and normal directions respectively. Note that of the 227 points in the wrap-

around direction, 147 lay on the wing body while the remaining points make up the wakecut region of the wing mesh. Grid points on the wing mesh were clustered along the leading and trailing edges as well as the wing root and tip to better capture the vortices that are expected to form in those respective regions. The background cartesian mesh is composed of 128×153×103 nodes in the x, y and z directions respectively. The outer boundary of the wake mesh is 20 mean chord lengths from the origin in each direction with a clustering of grid points in the immediate vicinity of the wing to more accurately capture the shed vorticity. A picture of the wing and background meshes can be seen in Figs. 3.18a and 3.18b.

The structural model was made up of plate elements with 11 elements in the spanwise direction and 8 elements in the chordwise direction. A picture of the node points making up the wing structural model can be seen in Fig. 3.18c. Structural parameters from the experiment (Table 3.2) were implemented in the structural model. Given that the wing has no defined root cutout, at the start of the simulation, the wing root lays along the positive x-axis. The wing span lays along the positive y-axis with the leading edge of the wing root positioned at the origin. The sinusoidal flapping motion was prescribed at the leading edge of the wing root about the x-axis resulting in the wing flapping in the yz-plane. Note that the simulation was set to start at the middle of the downstroke to match the results of the validation computation.

Overall, the simulation was run for 4 flap cycles with 2880 iterations per flap cycle resulting in a timestep size of 3.47×10^{-5} s used in the structural model. The timestep in the CFD model was set so that the positional change in the wings match between the CFD and structural models. A total of 8 sub-iterations were used in the

CFD solver to minimize factorization errors and improve solution accuracy. In the CSD solver, MBDyn's original A/L stable linear multistep algorithm was used with a spectral radius of 0.6. The residual tolerance was set to 1.0×10^{-2}.

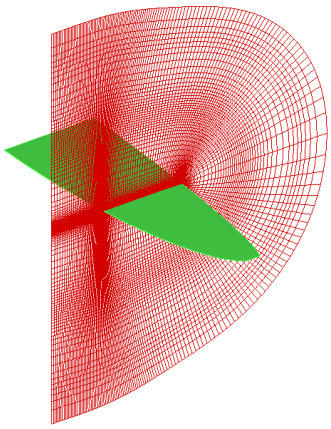

(a) CFD mesh of Zimmerman profile wing

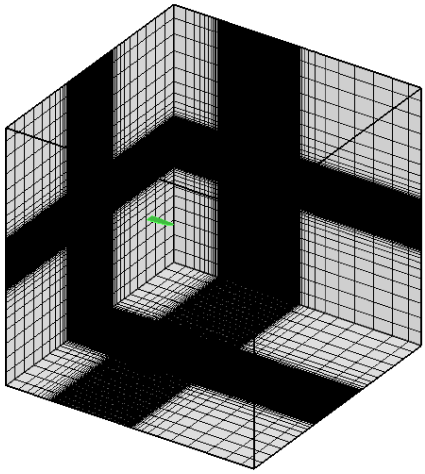

(b) CFD background mesh with embedded wing mesh (Depicted in green)

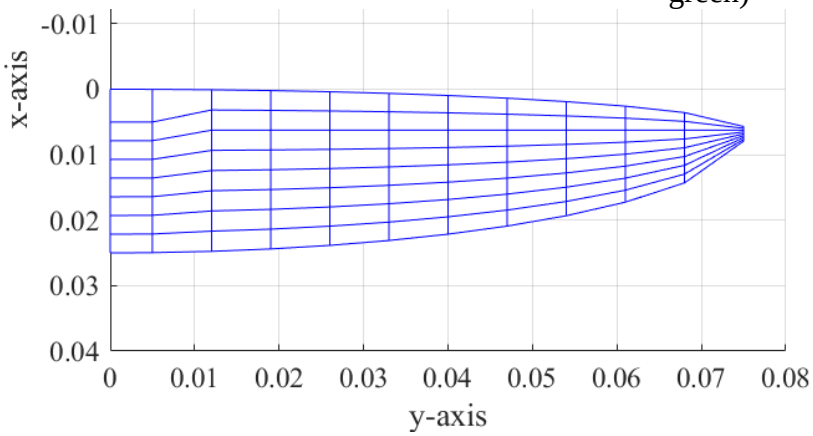

(c) Structural model node points

Figure 3.18: Images of overset mesh system (Wing and background meshes) and structural model node points

3.3.3 Results Comparison

In this section we will be comparing the experimental and computational results from Ref. [164] to those predicted using the current aeroelastic analysis for a variety of

datasets. Data to be compared include wing tip deflection, instantaneous lift force coefficient time history, vorticity and velocity field contours and velocity profiles at select positions of the wing span.

Figure 3.19 is a plot comparing the vertical displacement at the wing tip over the course of a flap cycle. Note that the wing position is compared at the leading edge of the wing tip. Also, in Fig. 3.19, the vertical displacement is normalized by the wing span. The results using the current CFD/CSD solver match well to the computational results from Aono with the two graphs laying on top of one another. The current CFD/CSD solver results also exhibit a similar trend to that of the experimental data with respect to peak tip displacement as well as phase in the variation of tip displacement over time. Figure 3.20 compares the computationally predicted lift coefficient time histories. To calculate the lift coefficient, the lift force generated by the wing is normalized by $0.5\rho_{air}(V_{ref})^2 S$. The variation in predicted instantaneous lift coefficient from Aono and the current CFD/CSD solver agree well. However, the peaks in lift coefficient predicted by the current CFD/CSD solver are slightly greater in magnitude than the results predicted by Aono.

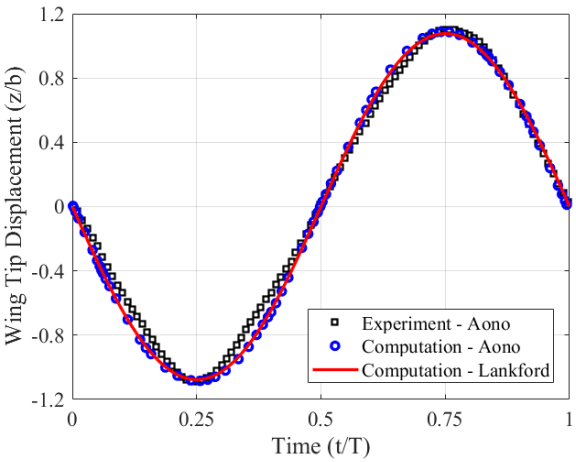

Figure 3.19: Comparison of wing tip deflections from Ref. [164] and current CFD/CSD solver

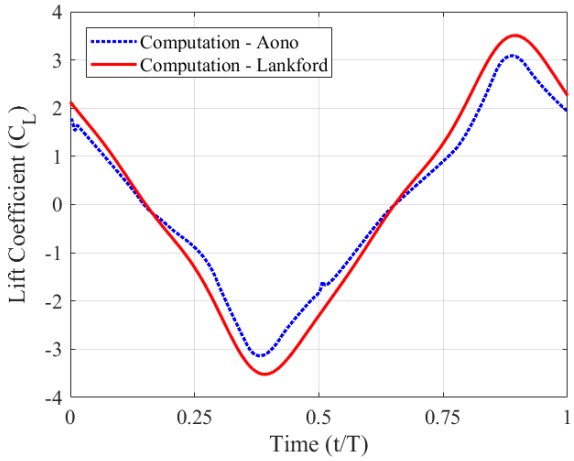

Figure 3.20: Comparison of computational C_L time-history from Ref. [164] and current CFD/CSD solver

In addition to comparing the wing tip deflection and lift coefficient variation, comparisons of vorticity and velocity fields were conducted. Figures 3.21 and 3.22 show vorticity and velocity magnitude contours, respectively, from the experimental and computational studies performed in Ref. [164] and the predicted results from the current CFD/CSD solver. The vorticity and velocity magnitude contours in Figs. 3.21 and 3.22 are at t/T = 0.30. At this time in the flap cycle, the wing is in the early stages of the upstroke. The flowfields in the plots are taken along the wing span at the quarter chord location of the wing root. In Ref. [164], the authors present the computational flowfield results in two ways. The first uses the flowfield data during the 6th flap cycle and the second is a phase-average of the data at the 3rd, 4th, 5th and 6th flap cycles. The results from the current CFD/CSD solver a from the last flap cycle only. Note that the

vorticity contours constructed using the results from current CFD/CSD solver were calculated in the same manner as those in Sub-section 3.1.4.

Overall, there is adequate agreement between the vorticity contours shown by Aono et al. (Figs. 3.21a–c) and those predicted by the current CFD/CSD solver (Fig. 3.21d). There is a significant level of incoherent vortical structures present in Fig. 3.21d due to the separation occurring at the wing tip. A high degree of separated, vortical flow is apparent in the computational results from Aono (Figs. 3.21b and 3.21c). In the experimental results (Fig. 3.21a), the vorticity is weaker and more diffused especially at points in the flow that are not in immediate proximity of the wing tip. Similarly, the velocity magnitude contour plots in Fig. 3.22 exhibit adequate agreement. The velocity magnitudes toward the wing root are lower in the results from the current CFD/CSD solver (Fig. 3.22d) compared to the computational results from Aono (Figs. 3.22b and 3.22c). The velocity magnitude below the wing in Fig. 3.22d is relatively low and resembles the experimental velocity magnitude contours (Fig. 3.22a) in that region more so than the computational results from Aono.

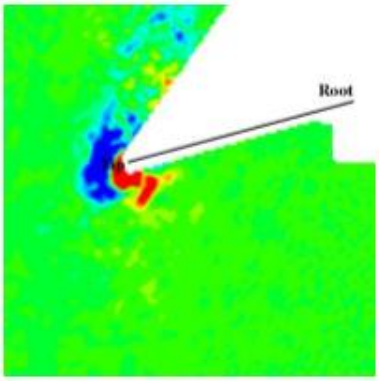

(a) Experiment (Phase averaged) – Aono

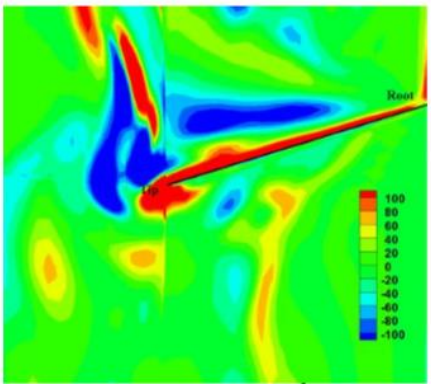

(b) Computation (6th cycle) – Aono

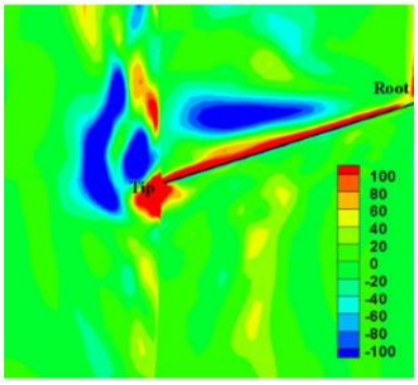

(c) Computation (Phase averaged) – Aono

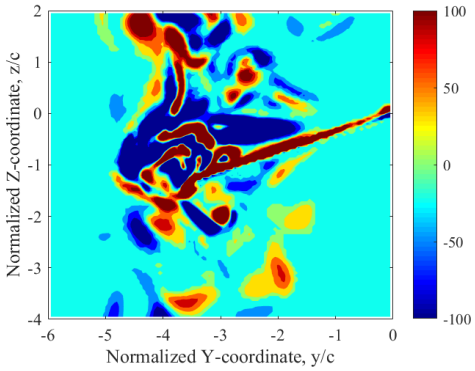

(d) Computation (Last cycle) – Lankford

Figure 3.21: Vorticity contour plots at t/T = 0.30 for the experimental and computational results

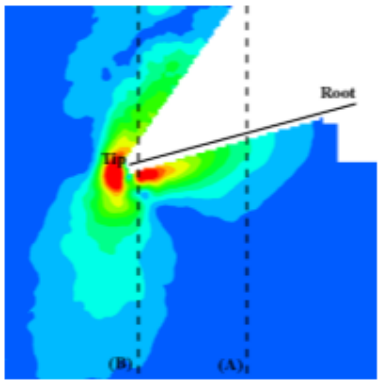

(a) Experiment (Phase averaged) – Aono

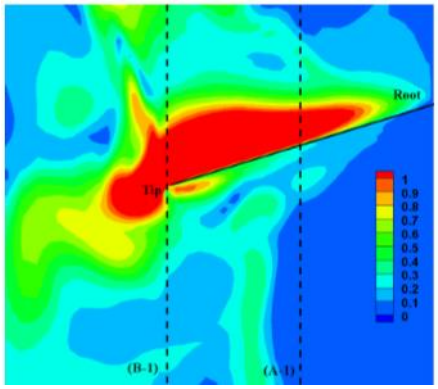

(b) Computation (6^{th} cycle) – Aono

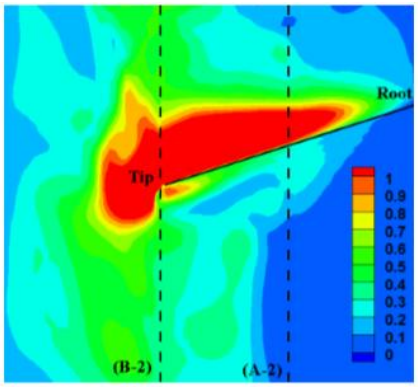

(c) Computation (Phase averaged) – Aono

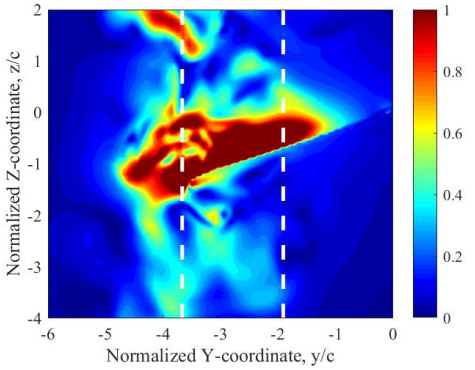

(d) Computation (Last cycle) – Lankford

Figure 3.22: Velocity magnitude contour plots at t/T = 0.30 for the experimental and computational results

Figures 3.23 and 3.24 show vorticity and velocity magnitude contours, respectively at t/T = 0.48. At this time in the flap cycle, the wing is approximately half way through the upstroke and is also half way through the flap cycle. Again, there is overall adequate agreement between the vorticity contours shown by Aono (Figs. 3.23a–c) and those predicted by the current CFD/CSD solver (Fig. 3.23d). Most of the vorticity is focused on the underside of the wing as the tip vortex continues to develop and evolve throughout the upstroke. The location and general size of the tip vortex is similar between the experimental results (Fig. 3.23a), those predicted by Aono (Figs. 3.23b and 3.23c) and those predicted using the current CFD/CSD solver (Fig. 3.23d).

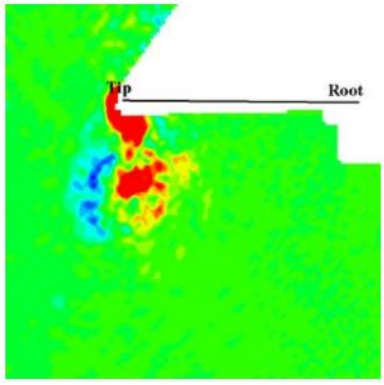

(a) Experiment (Phase averaged) – Aono

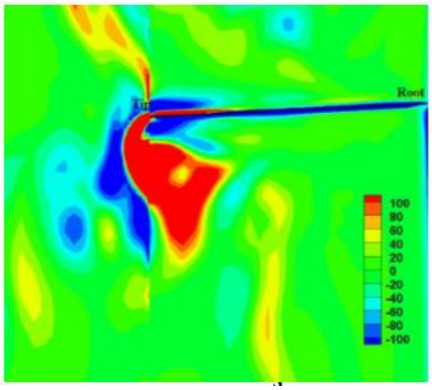

(b) Computation (6th cycle) – Aono

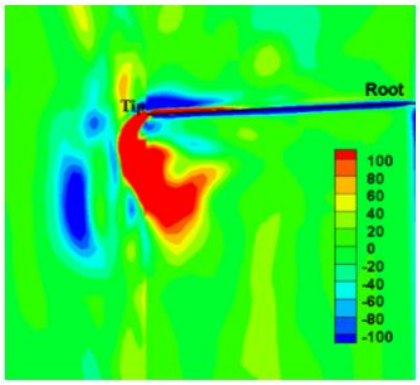

(c) Computation (Phase averaged) – Aono

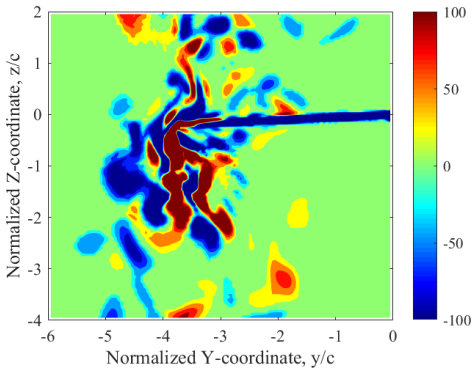

(d) Computation (Last cycle) – Lankford

Figure 3.23: Vorticity contour plots at t/T = 0.48 for the experimental and computational results

Likewise, the velocity magnitude contour plots in Fig. 3.24 exhibit adequate agreement. The velocity magnitude contours of the experiment (Fig. 3.24a) and the current CFD/CSD solver agree well with respect to shape and magnitude of the region of high velocity magnitude ($|V| \geq 1.0$). The velocity magnitude predicted by Aono (Figs. 3.24b and 3.24c) tended to over-predict the size of the region below the wing with increased velocity magnitudes.

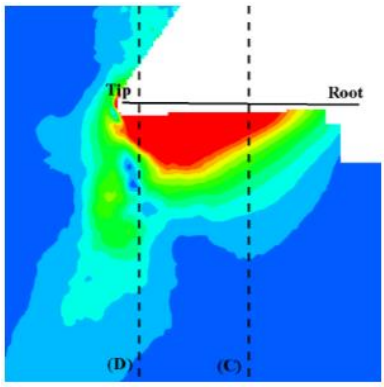

(a) Experiment (Phase averaged) – Aono

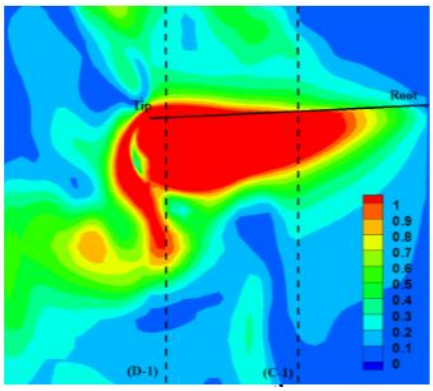

(b) Computation (6^{th} cycle) – Aono

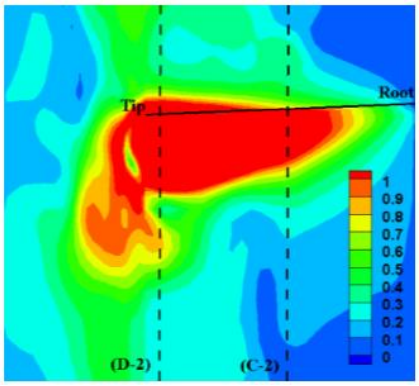

(c) Computation (Phase averaged) – Aono

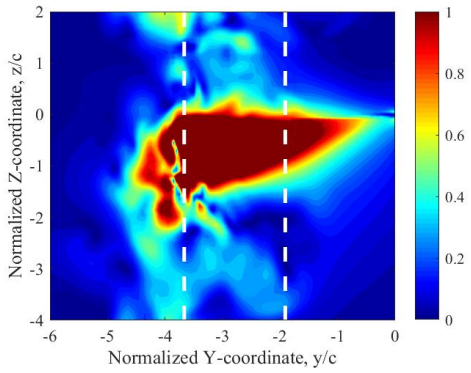

(d) Computation (Last cycle) – Lankford

Figure 3.24: Velocity magnitude contour plots at t/T = 0.48 for the experimental and computational results

In order to provide a quantitative comparison of the flowfield, comparisons of the velocity profiles were performed. Figure 3.25 shows the velocity profiles from the

experimental and computational results of Aono as well as the results generated from the current CFD/CSD solver. Velocity cuts were taken in the vertical direction from the flowfield data presented in Figs. 3.22 and 3.24 at location near midspan and the wing tip. The dashed vertical lines in Figs. 3.22 and 3.24 depict the location of the velocity cuts within the flowfield. Figures 3.25a and 3.25b were taken at t/T = 0.30 and Figs. 3.25c and 3.25d were taken at t/T = 0.48.

In comparing the velocity profiles, there are some notable differences in the variation of velocity over the cut for all the cases presented. However, in general, there is agreement between the experimental peak velocity magnitudes and those predicted by the current CFD/CSD solver. There is better agreement between the experimental and computational velocity profiles at the midspan location (Figs. 3.25a and 3.25c) as opposed to the wing tip (Figs. 3.25b and 3.25d). This is most likely due to the lower degree of highly separated flow at the midspan location in comparison to the wing tip. Notably, in Fig. 3.25b, the computational results tend to over-predict the peak velocity magnitude.

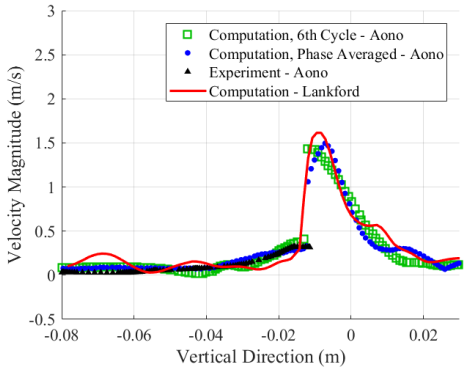

(a) Slice at midspan, t/T = 0.30

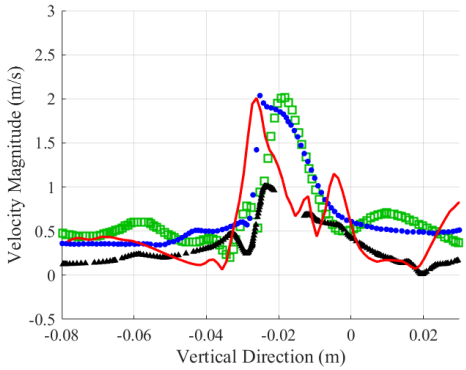

(b) Slice at the wing tip, t/T = 0.30

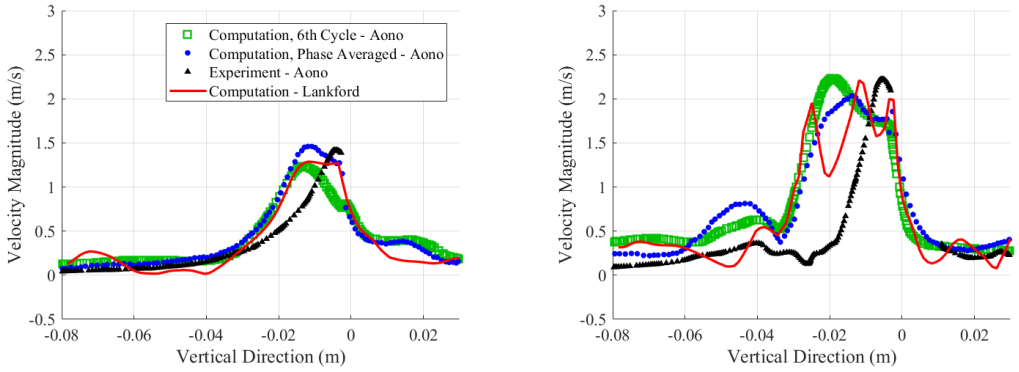

(c) Slice at midspan, t/T = 0.48 (d) Slice at the wing tip, t/T = 0.48

Figure 3.25: Comparison of experimental and computational velocity magnitude profiles at t/T = 0.30 and 0.48

3.4 Flexible Isotropic Rectangular Planform Wing in Hover

3.4.1 Experimental Setup

The present validation study is based on the results of in-house experimental tests performed on a custom built flapping mechanism and set of flat plate-like wings. The wings used throughout the experiment consisted of a thin plastic rectangular plate secured within a stiff aluminum leading edge spar. The wing length and chord were 6.0 inches and 3.0 inches respectively resulting in an aspect ratio of 2.0. Three wing thicknesses (h) of 0.015 in (15 mil), 0.010 in (10 mil) and 0.0075 in (7.5 mil) were tested. Note that the 10 mil and 7.5 mil wings were made of polyester plastic while the 15 mil wing was made of polyethylene terephthalate glycol (PETG). The leading edge spar is constructed out of aluminum and is composed of two halves which sandwich the plastic plate and are fastened together via four screws. Each half of the leading edge spar has a length of 6 inches, width of 0.2 inches and thickness of 0.1 inches. When the

wing is fully assembled, the total leading edge spar thickness is 0.2 inches. A picture of the 10 mil thick wing can be seen in Fig. 3.26.

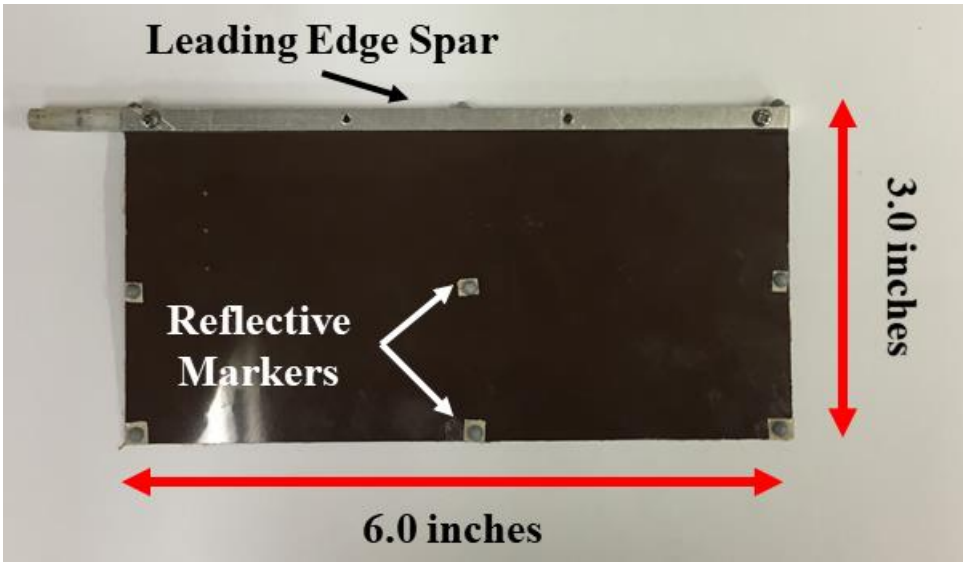

Figure 3.26: 10 mil isotropic flat plate wing with reflective markers

The wing in the experimental tests was actuated using a custom made four-bar crank-rocker mechanism. The mechanism was designed to emulate one degree-of-freedom sinusoidal flapping motion with a flap amplitude of ±40°. A kinematic analysis described in Ref. [165] was applied in order to correctly size the mechanism linkages to minimize variation in angular acceleration, and consequently the variation in angular velocity and angular position, between the forward and backward strokes. Figure 3.27 provides a schematic of the four-bar linkage system as well as a CAD photo of the flapping mechanism.

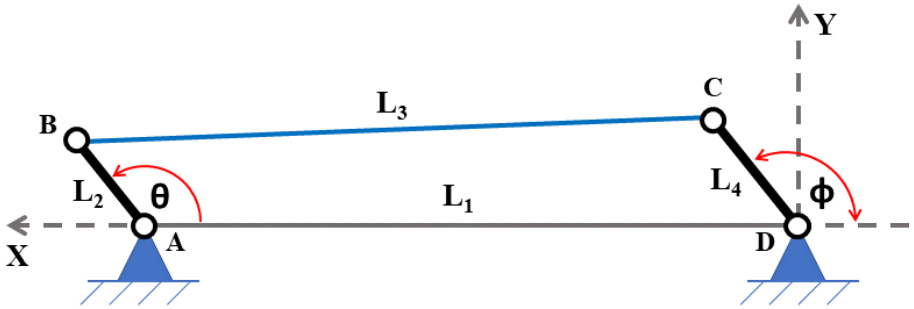

(a) Schematic of four-bar mechanism linkages

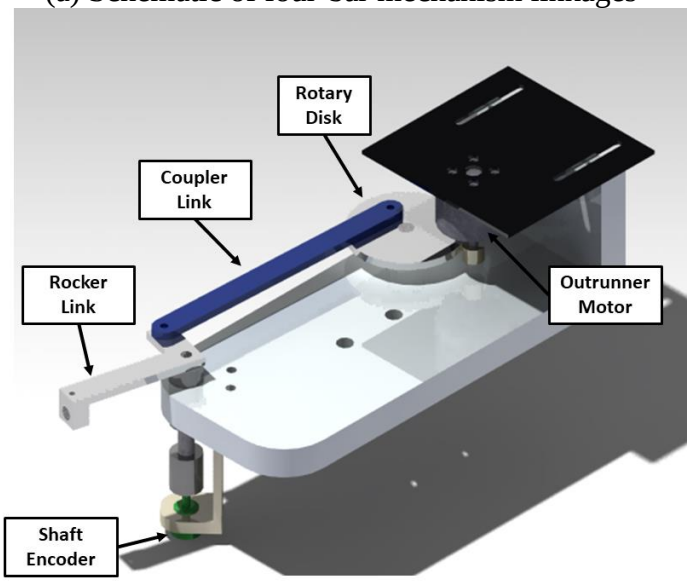

(b) CAD image depicting flapping mechanism setup

Figure 3.27: Schematic of four-bar mechanism linkages and CAD of flapping mechanism

From Fig. 3.27a, the presented terms are defined below:

$$B_x = L_1 - L_2 * \cos(\theta) \tag{3.7}$$

$$B_y = L_2 * \sin(\theta) \tag{3.8}$$

$$\alpha = \arctan(-B_y/B_x) \tag{3.9}$$

$$\beta = \arccos\left(\frac{L_3^2 - L_4^2 - (B_x^2 + B_y^2)}{-2 * L_4\sqrt{B_x^2 + B_y^2}}\right) \tag{3.10}$$

$$\phi = \alpha + \beta \tag{3.11}$$

where L_1, L_2, L_3 and L_4 are the lengths of the fixed link, crank link, coupler link and rocker link respectively. In Fig. 3.27a, the vertices A, B, C and D represent the connection point of two linkages. The angle between L_1 and L_2 is θ and the flap angle ϕ is the angle between L_4 and a reference line coincident with L_1. The linkage lengths, determined via the kinematic analysis [165], are such that L_1 = 4.506 in, L_2 = 0.403 in, L_3 = 4.43 in and L_4 = 0.63 in. Figure 3.28 provides a plot of the expected flap angle variation over time based on Eqs. (3.7) – (3.11). A cosine function is included in the plot to provide reference. Note that in Fig. 3.28, the flap angle variation calculated by Eq. (3.11) is normalized about its mean value so that the minimum and maximum flap angles are of equal magnitude. The crank link is driven by an eRC BL300 DC brushless motor through a two-gear drive train with a gear ratio of 5.3:1 to increase the input torque of the crank link. A US Digital MA3 miniature shaft encoder was attached to the rocker link to measure the flap angle over time during actuation. The shaft encoder has resolution of ±0.5°. The wings were tested at flap frequencies of 2 Hz – 4 Hz resulting in tip-based Reynolds number ranging from 8,400 to 16,850. Note that when attached to the four-bar mechanism, the wing is offset from the flap axis by 2.0 inches.

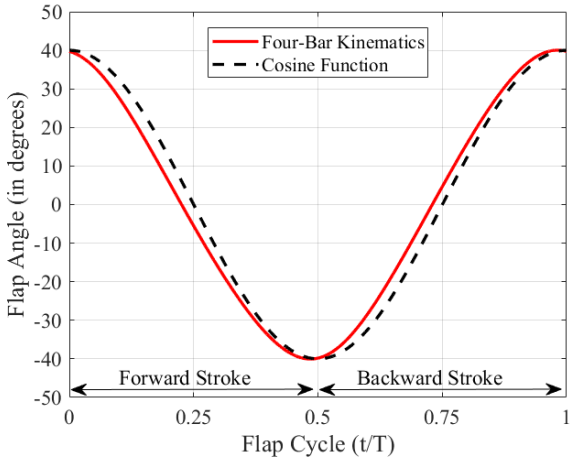

Figure 3.28: Expected four-bar mechanism flap kinematics over time (from Eq. (3.11))

To determine the Young's modulus of the plastic flat plate wings, tensile tests were conducted on a series of test samples. Tensile tests were conducted using an Instron 8841 machine attached to an Instron 8800 controller. The WaveMaker software package was used to run the tests and collect the measured data. Data was collected at a sample rate of 1000 Hz. Given the nature of the material, the protocols outlined in ASTM D638-14 [166] were followed which were designed for testing thin plastic materials. Dogbone specimens were created according to the dimensions outlined in Ref. [166]. Figure 3.29 provides a CAD drawing illustrating the dogbone specimen as well as picture of the specimen in the Instron machine. Four dogbone test samples were created using the material at the three different thicknesses. All tensile tests were conducted at a pull speed of 0.2 inches per minute for a total of 5 minutes or until material failure was reached.

Figure 3.30 shows the stress versus strain curves for the three different thicknesses of material tested. In order to calculate the Young's modulus for a

particular case, the data in the range of 0.0 mm/mm 0.015 mm was linearized for each trial. The Young's modulus is assumed to be the slope of the linearized fit to the data in that range. An average of the data from the four trials is used to calculate the Young's modulus used through the computational analysis for each case. Table 3.3 provides a list of the relevant material properties and flow conditions of the test wing including the average Young's modulus for each material thickness as well as the standard deviation between the four trials.

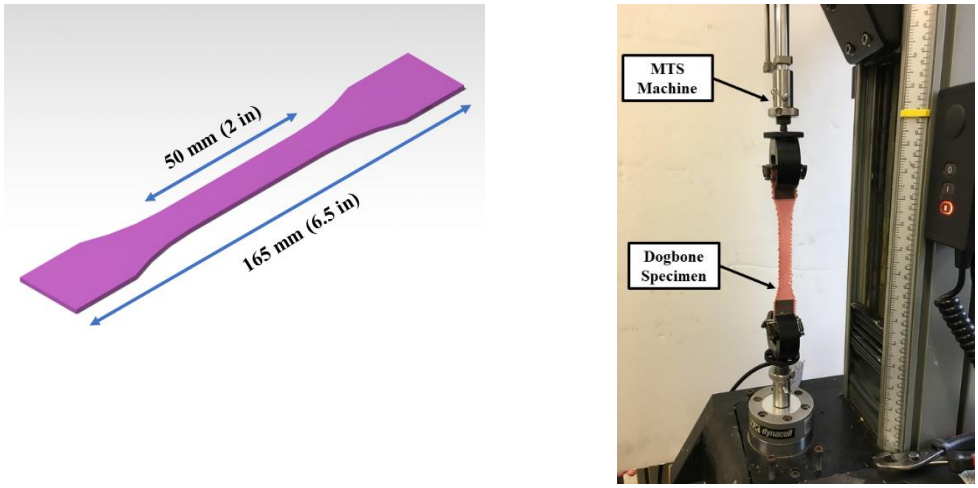

(a) CAD drawing of dogbone specimen

(b) Picture of dogbone specimen during testing (h = 15 mil)

Figure 3.29: CAD drawing of dogbone specimen and picture of specimen during tensile testing

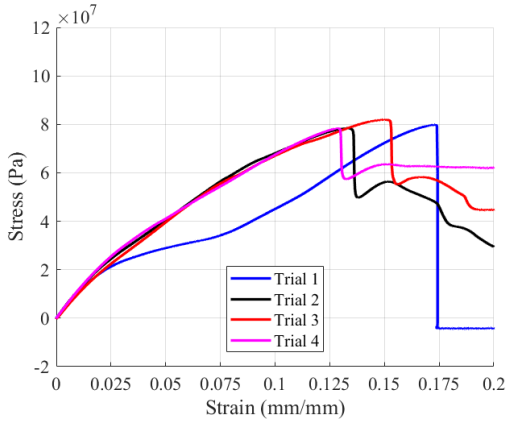

(a) h = 15 mil

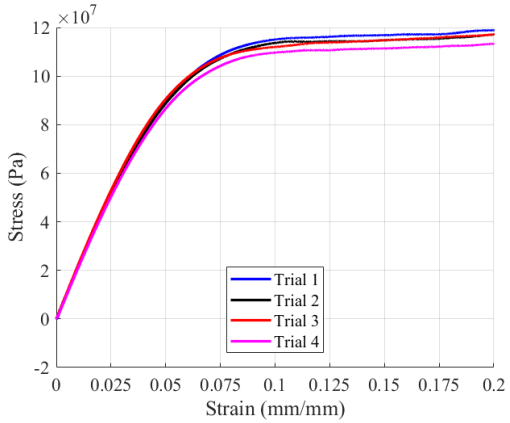

(b) h = 10 mil

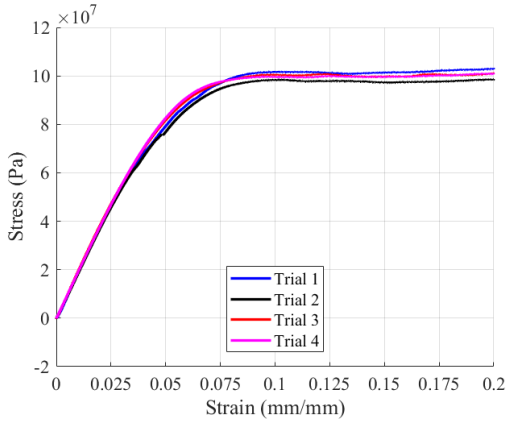

(c) h = 7.5 mil

Figure 3.30: Stress versus strain curves for the plastic flat plate wing material (thickness = 15 mil, 10 mil and 7.5 mil)

Table 3.3: Isotropic flat plate wing structural and flow properties

Property	Value, h = 15 mil	Value, h = 10 mil	Value, h = 7.5 mil
Wing Span, *b*	0.1524 m (6.0 in)	0.1524 m (6.0 in)	0.1524 m (6.0 in)
Chord Length, *c*	0.0762 m (3.0 in)	0.0762 m (3.0 in)	0.0762 m (3.0 in)
Wing Thickness, *h*	0.381 mm (15 mil)	0.254 mm (10 mil)	0.1905 mm (7.5 mil)
Wing Planform Area, *S*	0.0116 m^2 (18 in^2)	0.0116 m^2 (18 in^2)	0.0116 m^2 (18 in^2)
Aspect Ratio, *AR*	2.0	2.0	2.0
Material Density, ρ_{plate}	1450 kg-m^{-3}	1400 kg-m^{-3}	1400 kg-m^{-3}
Young's Modulus, E_{plate}	3.18 ± 0.16 GPa	3.69 ± 0.07 GPa	7.25 ± 0.16 GPa
Poisson's Ratio, ν_{plate}	0.35	0.35	0.35
Material Density, $\rho_{leading\ edge}$	2700 kg-m^{-3}	2700 kg-m^{-3}	2700 kg-m^{-3}
Young's Modulus, $E_{leading\ edge}$	70.0 GPa	70.0 GPa	70.0 GPa
Poisson's Ratio, $\nu_{leading\ edge}$	0.3	0.3	0.3
Flap Frequency, *f*	2 – 4 Hz	2 – 4 Hz	2 – 4 Hz
Flap Amplitude, ϕ_{amp}	40°	40°	40°
Maximum Tip Velocity, V_{tip}	1.78 – 3.57 m-s^{-1}	1.78 – 3.57 m-s^{-1}	1.78 – 3.57 m-s^{-1}
Reduced Frequency ($\frac{2\pi f c}{2V_{tip}}$)	0.269	0.269	0.269
Air Density, ρ_{air}	1.23 kg-m^{-3}	1.23 kg-m^{-3}	1.23 kg-m^{-3}
Reynolds Number ($\frac{\rho_{air} V_{tip} \bar{c}}{\mu}$)	8400 – 16850	8400 – 16850	8400 – 16850
Π_1 ($\frac{D_{plate}}{\rho_{air} V_{tip}^2 \bar{c}^3}$)	2.41 – 9.69	0.8279 – 3.33	0.686 – 2.76

To measure the static wing deflection under point loads as well as the passive wing deformations due to inertial and aerodynamic forces, a VICON motion capture system was utilized. VICON motion capture systems utilize a passive optical motion capture technique in which retroreflective markers are tracked in space. The retroreflective markers reflect infrared light that is recorded using a set of high-precision infrared cameras. The motion capture images were acquired using VICON T40-S cameras which have a 4 Megapixel resolution with a maximum frame rate of 500 Hz at full resolution. Both static and dynamic test experiments were conducted. When performing the motion capture testing, six T40-S cameras were run at a frame rate of 400 frames per second (fps) to accurately capture the wing deformation. Figure 3.31 provides a picture of the VICON motion capture test setup. Reflective markers were placed at the wing root, midspan and wing tip along the leading edge, mid-chord and trailing edge of the wing. The placement of the reflective markers can be seen in Fig. 3.26. The cameras were arranged to ensure at least two cameras are able to view a particular reflective marker at any point in the flap stroke. Motion capture data was recorded and post-processed using VICON Nexus 1.8.5.

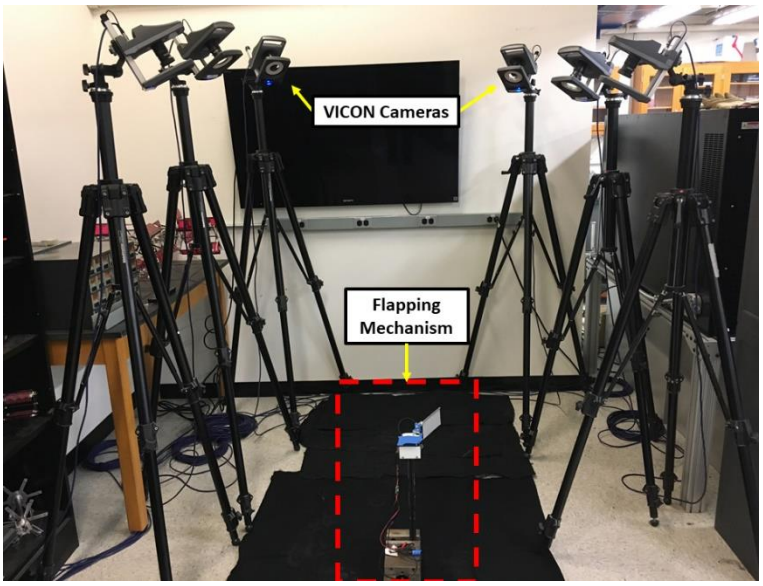

Figure 3.31: VICON motion capture setup with flapping mechanism

3.4.2 Computational Setup

The flexible flat plate wing studied in this validation case was modelled using the coupled CFD/CSD aeroelastic analysis. An overset mesh system was utilized to model the wing geometry and flow environment within the CFD solver. A C-O topology, structured body-fitted mesh was used to represent the wing and a Cartesian background mesh was used to model the surrounding wake. The wing geometry was designed to have a rectangular planform with an aspect ratio and thickness-to-chord ratio to match that of the test wing in Fig. 3.26. The wing mesh was approximately comprised of 3.2 million grid points with 267×141×85 grid points in the wrap-around, spanwise and normal directions respectively. Note that of the 267 points in the wrap-around direction, 187 lay over the wing surface while the remaining points make up the wakecut region of the wing mesh. Grid points were clustered near the leading edge, trailing edge, wing root and wing tip. These regions of the wing are where vortical or highly separated flow is expected to form. The background cartesian mesh is composed

of 128×98×148 nodes in the x, y and z directions respectively. The outer boundary of the wake mesh is 20 chord lengths from the origin in each direction with a clustering of grid points in the immediate vicinity of the wing to more accurately capture the shed vorticity. A picture of the wing and background meshes can be seen in Fig. 3.32.

The structural model was made up of 100 plate elements and 10 beam elements with 10 elements in the spanwise direction and 10 elements in the chordwise direction. A picture of the node points making up the wing structural model can be seen in Fig. 3.33. Note that in Fig. 3.33 the black, solid line represents that leading edge of the wing. The structural parameters from the experiment, shown in Table 3.30, were implemented in the structural model.

When the wing is placed within the flapping mechanism, the wing root is offset from the flapping axis by 2.0 inches (0.0508 m) and this offset is properly represented within the simulation. The flap angle measured during experimentation is prescribed to the aeroelastic model during the simulation. At the start of the simulation, the wing is at a 90° pitch angle such that the wing chord line is parallel to the z-axis. The wing starts at the beginning of the forward stroke with the flap motion being prescribed about the flap axis such that wing flapping occurs in the xy-plane.

Overall, the simulation was run for 3 flap cycles with 2880 iterations per flap cycle resulting in a timestep size of $1.74\times10^{-4} - 8.68\times10^{-5}$ s used in the structural model. The range of the timestep depends on the flap frequency being tested ranging from 2 Hz to 4 Hz. The timestep in the CFD model was set so that the positional change in the wings match between the CFD and structural models. A total of 8 Newton sub-iterations were used in the CFD solver to minimize factorization errors and improve

solution accuracy. In the CSD solver, MBDyn's original A/L stable linear multistep algorithm was used with a spectral radius of 0.6 and the residual tolerance was set to 1.0×10^{-3}.

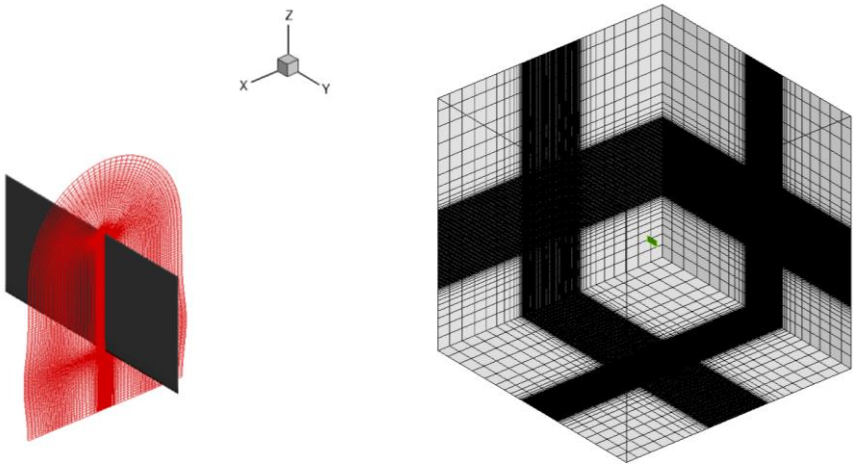

(a) C-O wing mesh

(b) Background mesh (wing mesh depicted in green)

Figure 3.32: Pictures of CFD C-O wing mesh and Cartesian background mesh

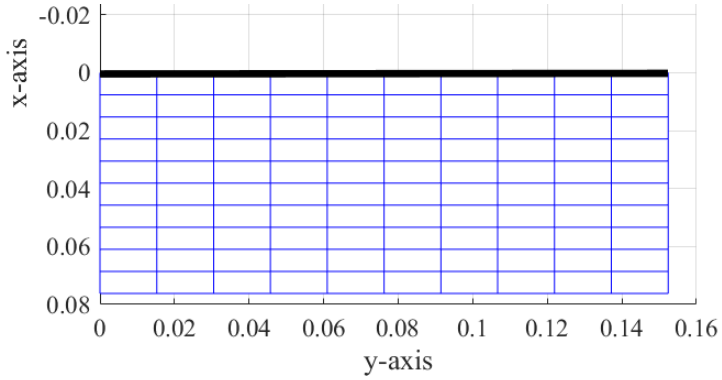

Figure 3.33: Graph depicting the node points used within the structural model

3.4.3 Static Wing Deflection Comparison

The VICON system described in the previous sub-section was used to measure the static deflections of the wing under various point loads. Comparisons were made between the experimentally measured results and those predicted by the computational

analysis. For the static deflection cases, only the CSD solver was used in predicting the wing deformation under load. During the static deflection experiments, the wing was clamped at the root of the leading edge. Two load cases were explored: 1) loads applied at the trailing edge of the wing root and 2) loads applied at the trailing edge of midspan. The load magnitudes were varied from 0.0 to 20.0 grams in 5.0 gram increments. Static load tests were conducted on the 15 mil, 10 mil and 7.5 mil wings. Figure 3.34 provides pictures of the 10 mil thick wing during the static loads tests under no load (Fig. 3.34a), maximum load applied at the wing root (Fig. 3.34b) and maximum load applied at midspan (Fig. 3.34c). The same loads and boundary conditions were applied to the CSD model to emulate the experimental tests.

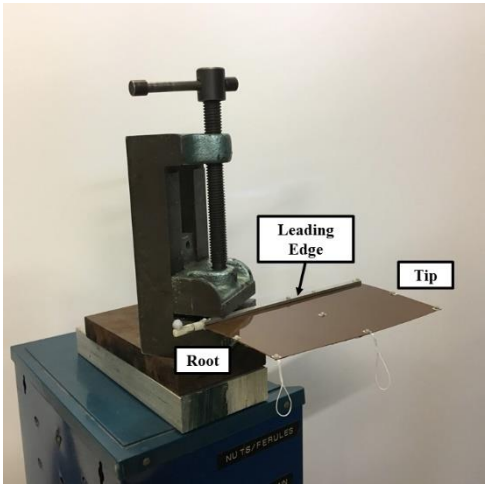

(a) Wing under no load

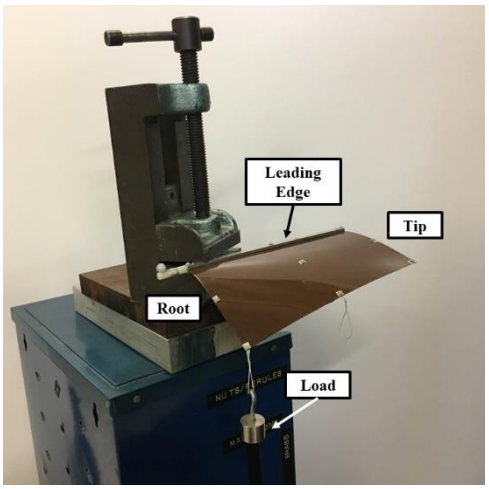

(b) 20 gram load applied at trailing edge, wing root

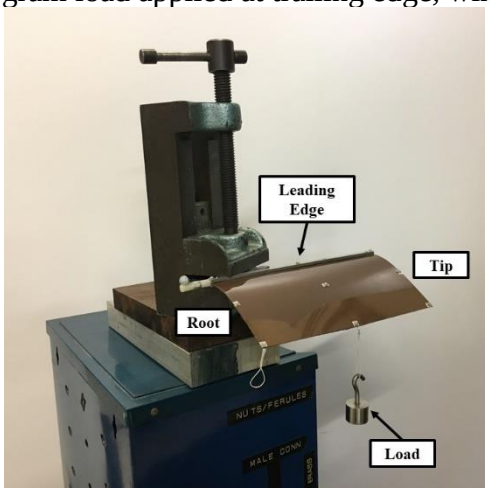

(c) 20 gram load applied at trailing edge, midspan

Figure 3.34: Pictures of the 10 mil test wing under static loads

Figure 3.35 provides deflection vs load plots for the three test wings under the different load cases. The data presented represents the vertical displacement of the nodes at the wing root, midspan and tip along the trailing edge. Displacement of the wing while loaded is measured with respect to the wing position in the unloaded condition. The symbols represent the experimental data while the computational results are shown via the dashed lines. Overall, there is good agreement between the experimental and computational deflection versus load curves for the three wings

tested. To provide a more complete picture of the agreement in the computational and measured wing deflections, Fig. 3.36 shows the full wing deformation measured using VICON and predicted using MBDyn. The experimental data is represented by the red markers and blue polygons and the computational data is presented by the green gridded rectangles. In the plots, the maximum 20 gram load is applied on each of the test wings for the case where the trailing edge of the wing root is loaded (Fig. 3.36a,c,e) as well as the trailing edge of wing midspan is loaded (Fig. 3.36b,d,f). Again, qualitatively there is good agreement between the predicted and measured data.

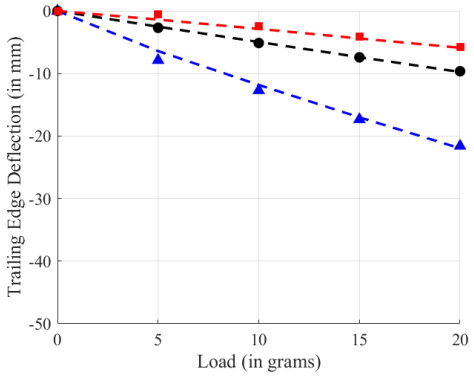

(a) 15 mil wing, wing root loaded

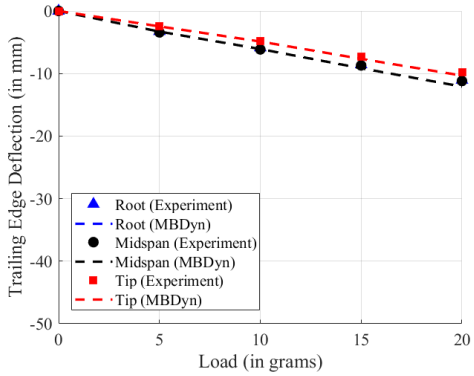

(b) 15 mil wing, midspan loaded

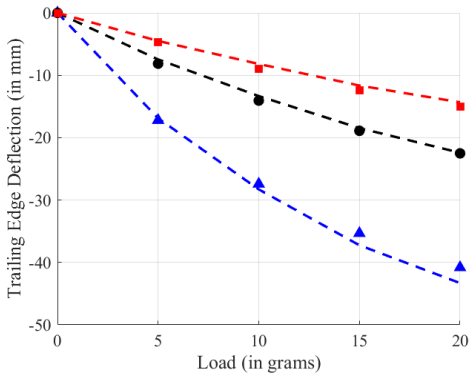

(c) 10 mil wing, wing root loaded

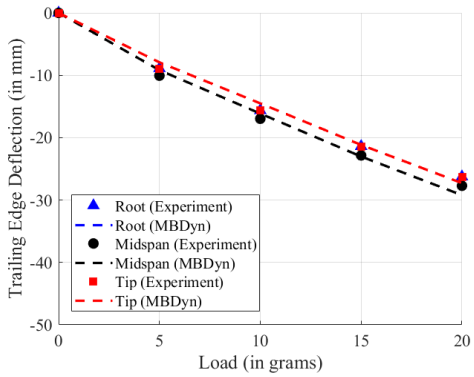

(d) 10 mil wing, midspan loaded

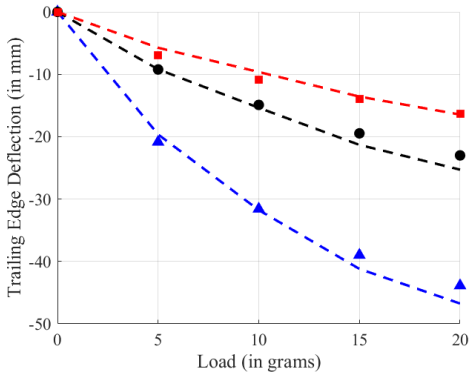

(e) 7.5 mil wing, wing root loaded

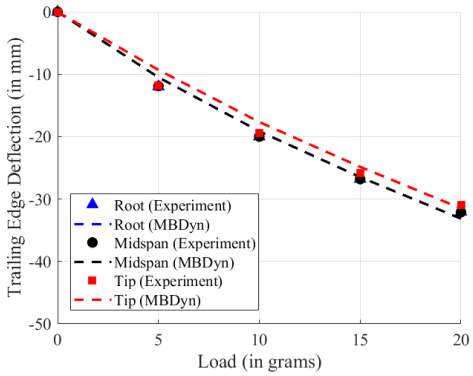

(f) 7.5 mil wing, midspan loaded

Figure 3.35: Deflection vs load curves of the wing trailing edge under static load (thickness = 15 mil, 10 mil and 7.5 mil)

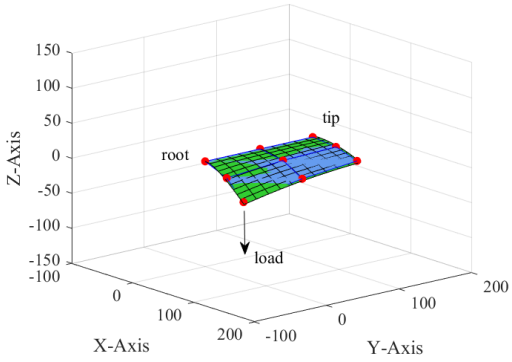

(a) 15 mil wing, wing root loaded

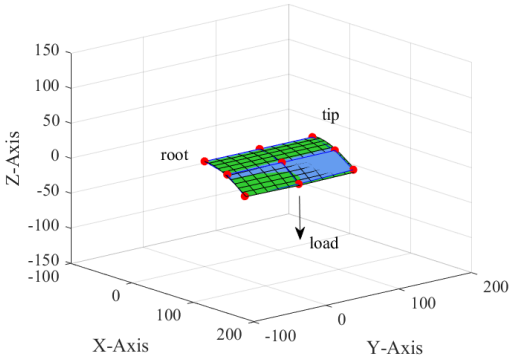

(b) 15 mil wing, midspan loaded

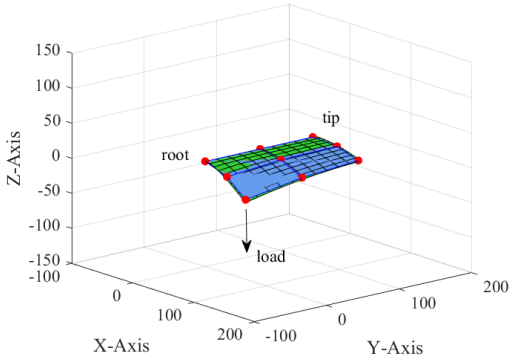

(c) 10 mil wing, wing root loaded

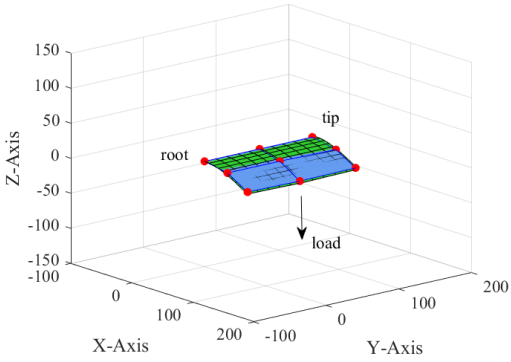

(d) 10 mil wing, midspan loaded

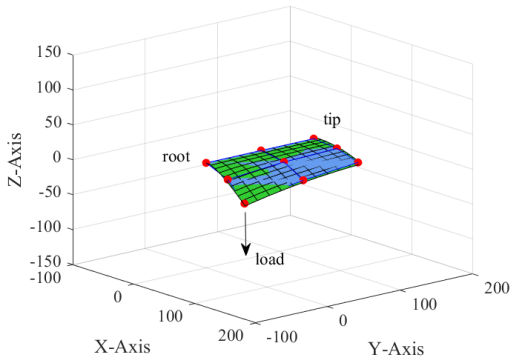

(e) 7.5 mil wing, wing root loaded

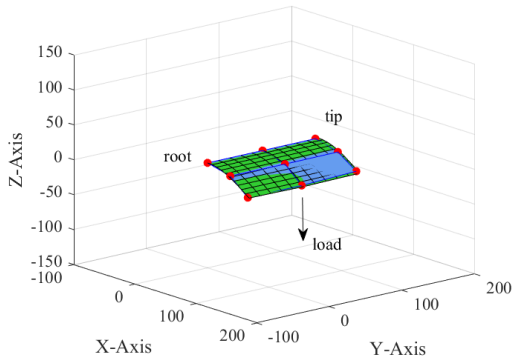

(f) 7.5 mil wing, midspan loaded

Figure 3.36: Comparison of predicted and measured full wing deformation under static load (Load = 20 grams, h = 15 mil, 10 mil and 7.5 mil)

3.4.4 Dynamic Wing Deflection Comparison

In addition to static wing deflection comparisons, dynamic wing deflections were compared. Dynamic wing deformations are due to the aerodynamic and inertial forces acting on the wing as the flapping mechanism is actuated. Before discussing the dynamic deflection results, it's important to review the reference coordinate system used throughout the study as well as how particular terms are defined. Figure 3.37 provides an illustration of the flapping wing coordinate system. Flapping occurs about the flapping axis which coincides with the z-axis. With respect to the right-hand rule, a forward stroke is a negative rotation about the z-axis while a backward stroke is a positive rotation about the z-axis. While the x-axis and y-axis are a part of the inertial frame, the x′-axis and y′-axis make up the body frame and rotate with the wing while it's flapping. Throughout the flapping motion, the pitch angle at a particular spanwise

location is defined as the angle between the local chord line and a reference plane parallel to the x′y′-plane.

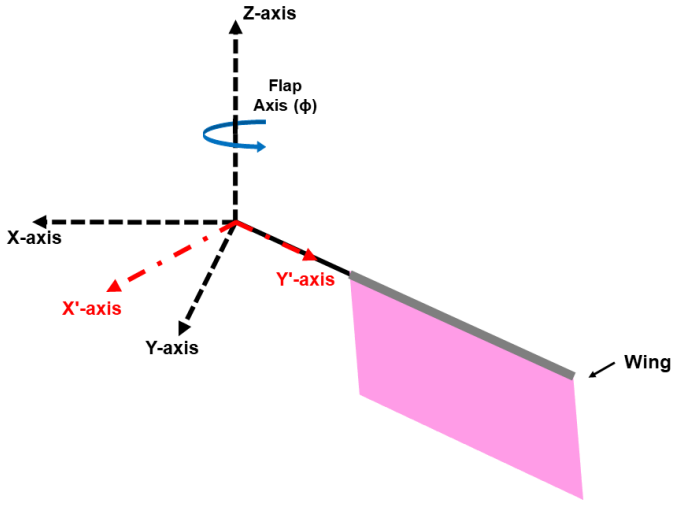

Figure 3.37: Reference coordinate system used in isotropic flat plate wing study

Figure 3.38 shows the variation of the wing trailing edge position from the experimental and computational results for the three test wings at flap frequencies of 2 Hz (Fig. 3.38a–c), 3 Hz (Fig. 3.38d–f) and 4 Hz (Fig. 3.38g–i). Comparisons are made at the trailing edge of the wing root, midspan and wing tip over the course of a flap cycle. The data shown is the x-component of the position vector, with respect to the inertial reference frame shown in Fig. 3.37, at the aforementioned points along the trailing edge. The experimental results are an average of the data captured over 40 flap cycles while the computational results are from the last flap cycle of the simulation. Note that flap cycle time is nondimensionalized by the flap period (T). For all the cases shown in Fig. 3.38, the computational results compare well against the experimental data with respect to the peak displacement magnitude and temporal variation of position over time. At the 2 Hz flap frequency, the trailing edge position variation

strongly follows the sinusoidal nature for the flap angle variation. However, at the higher flap frequencies there is notable higher harmonic content present in the experiment and computational data especially for the thinner wings.

Figure 3.39 shows the instantaneous pitch angle variation over time at the wing root, midspan and wing tip at flap frequencies of 2 Hz (Fig. 3.39a–c), 3 Hz (Fig. 3.39d–f) and 4 Hz (Fig. 3.39g–i). The computational data is shown by the dashed lines while the experiment data is shown in solid lines. At a flap frequency of 2 Hz, the variation in pitch angle is minimal for all the wings tested. Wing deformation is dominated by the inertial forces with the largest change in pitch angle occurring after stroke reversal. But there is still minimal deviation from the initial 90° pitch angle of the wing. The discrepancies between the experimental and computational data is due to the wing vibrating after stroke reversal about the initial 90° wing pitch angle.

For the 3 Hz and 4 Hz flap frequency cases, the inertial forces acting on the wings during stroke reversal are larger in magnitude and the aerodynamic forces begin to play a more significant role in the passive wing deformations over time. At 4 Hz (Fig. 3.39g–i), the instantaneous pitch angle variations are of the highest magnitudes between all the cases performed. While there is some discrepancy between the predicted and measured instantaneous pitch angles, especially at the peaks in pitch magnitude, there is good correlation with respect to the temporal variation of wing pitch over the course of a flap cycle.

To provide a more comprehensive, qualitative comparison of the wing deformations, Fig. 3.40 shows experimental and computational full wing deformations for the 10 mil thick wing at a flap frequency of 4 Hz. Figure 3.40 provides snapshots

of the wing at different instances of the flap cycle to highlight how the passive wing deformations vary over time. As stated in the previous sub-section, the experimental data is represented by the red markers and blue polygons and the computational data is presented by the green gridded rectangles. A solid, black standalone marker signifies the position of the origin. The flap axis passes through the origin and coincides with the z-axis. In general, the measured and predicted results exhibit good agreement throughout the flap cycle.

Overall, the trailing edge position and pitch angle variations between the experimental and computational results show good agreement demonstrating that the coupled CFD/CSD aeroelastic analysis is capable of modeling wings undergoing large, nonlinear deformations.

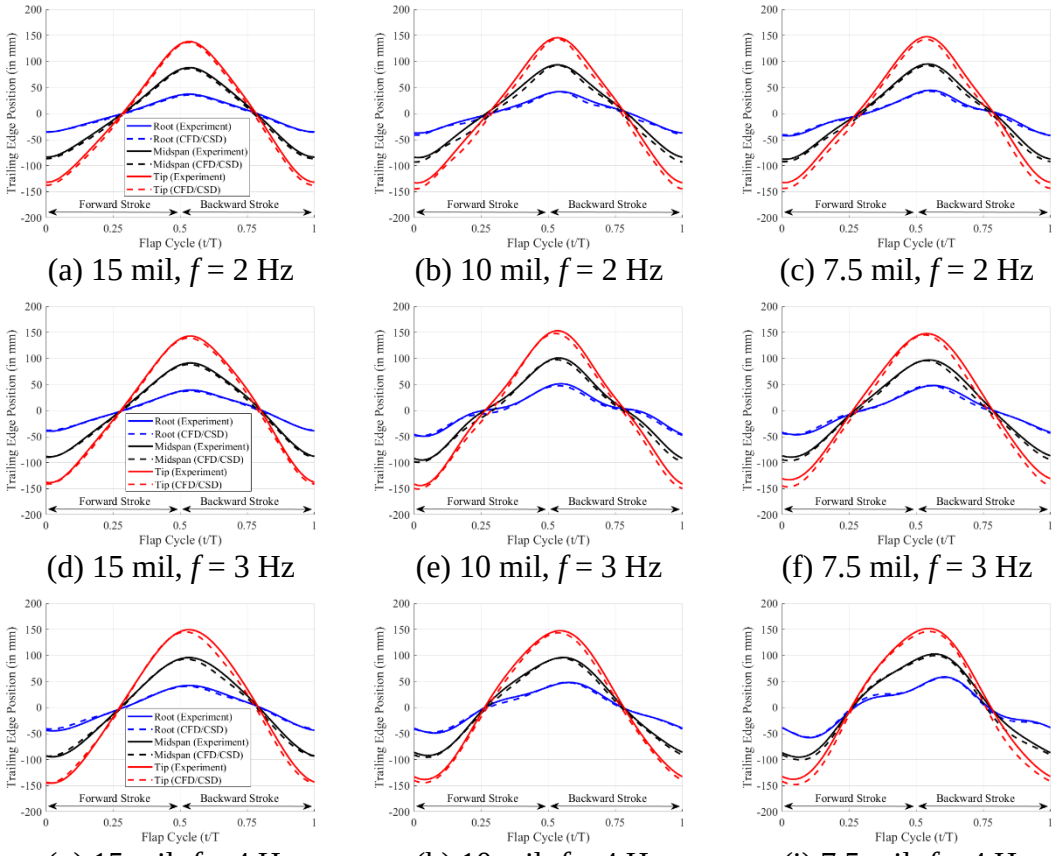

(a) 15 mil, f = 2 Hz (b) 10 mil, f = 2 Hz (c) 7.5 mil, f = 2 Hz

(d) 15 mil, f = 3 Hz (e) 10 mil, f = 3 Hz (f) 7.5 mil, f = 3 Hz

(g) 15 mil, f = 4 Hz (h) 10 mil, f = 4 Hz (i) 7.5 mil, f = 4 Hz

Figure 3.38: Comparison of experimental and computational passive trailing edge deformations (thickness = 15 mil, 10 mil and 7.5 mil)

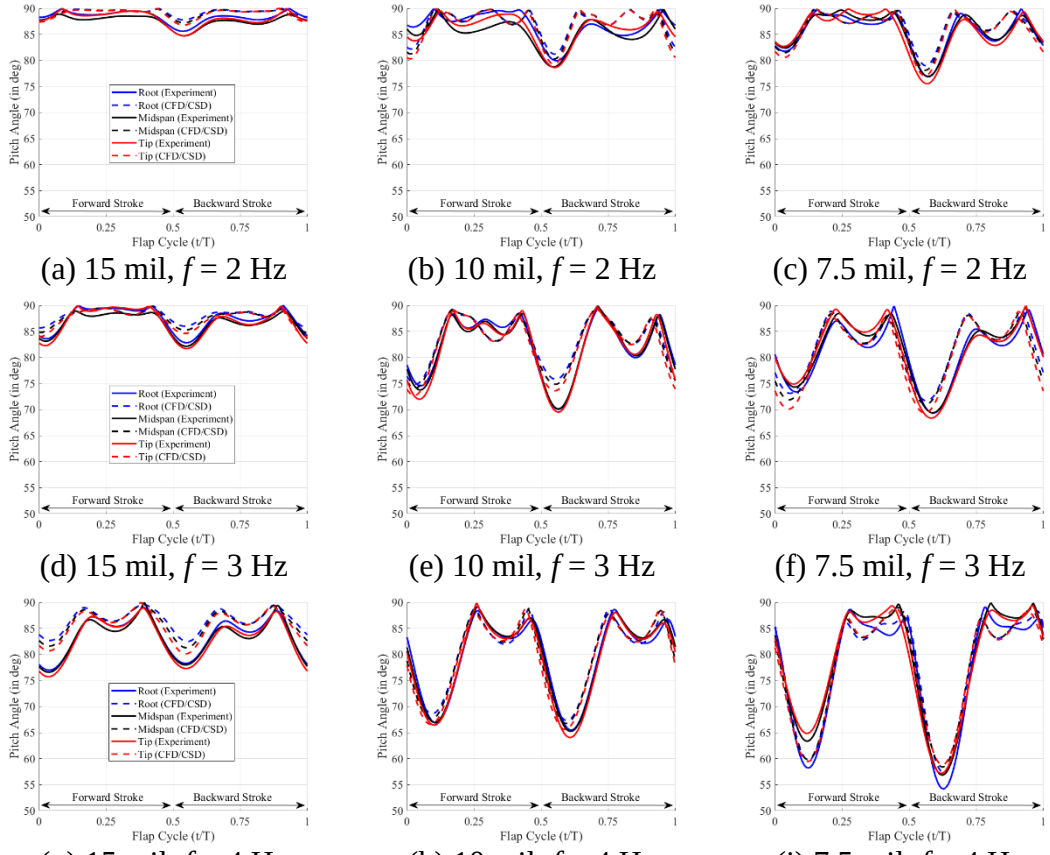

(a) 15 mil, f = 2 Hz (b) 10 mil, f = 2 Hz (c) 7.5 mil, f = 2 Hz

(d) 15 mil, f = 3 Hz (e) 10 mil, f = 3 Hz (f) 7.5 mil, f = 3 Hz

(g) 15 mil, f = 4 Hz (h) 10 mil, f = 4 Hz (i) 7.5 mil, f = 4 Hz

Figure 3.39: Comparison of experimental and computational instantaneous pitch angle variation (thickness = 15 mil, 10 mil and 7.5 mil)

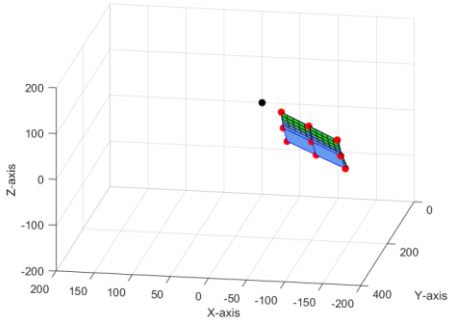

(a) t/T = 0.0

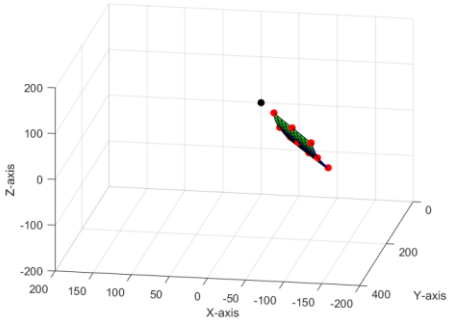

(b) t/T = 0.125

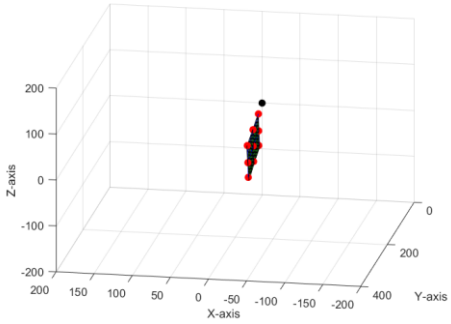

(c) t/T = 0.25

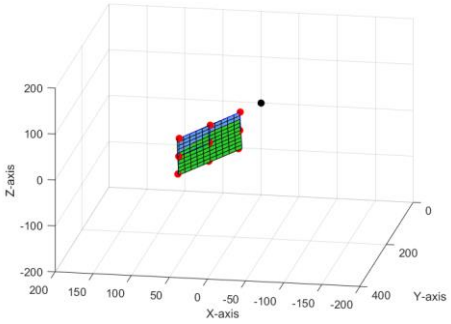

(d) t/T = 0.375

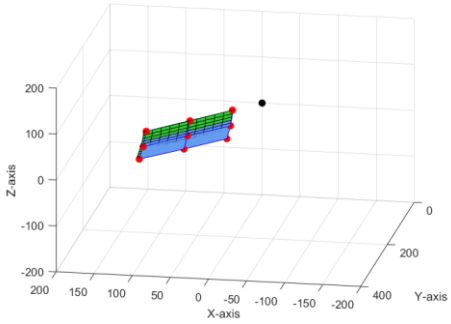

(e) t/T = 0.50

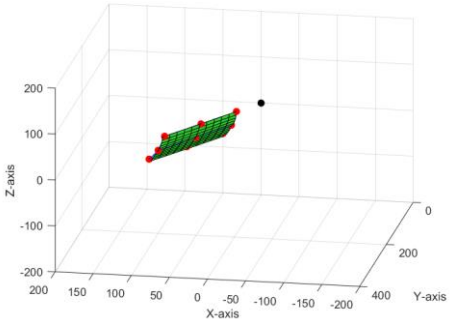

(f) t/T = 0.625

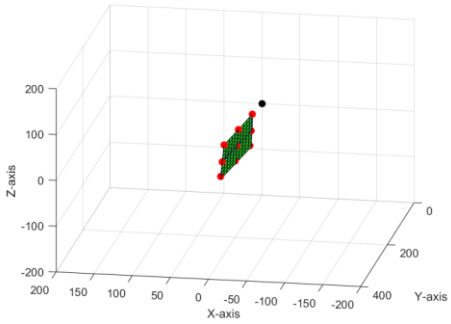

(g) t/T = 0.75

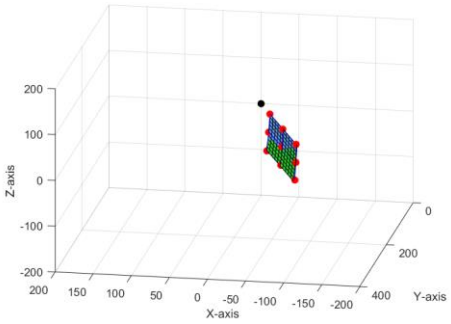

(h) t/T = 0.875

Figure 3.40: Comparison of measured and predicted full wing deformations over a flap cycle (h = 10 mil, f = 4 Hz)

3.4.5 Influence of Kinematics on Predicted Results

Throughout this validation study, the experimentally measured flap angle time histories from each case were prescribed into the aeroelastic analysis to ensure a one-to-one match between the experimental and computational kinematics. However, when analyzing the data, it was apparent that the experimentally measured flap kinematics deviated from those analytically calculated using Eqs. (3.7)–(3.11). There were differences in the measured flap kinematics between the three test wings and even discrepancies in the flap angle time histories for the same test wing depending on the flap frequency. This was found to be due to the wing aerodynamic and inertial forces acting on the flapping mechanism during actuation.

A similar phenomenon was also seen in a flapping wing study performed by Stanford et al. [167]. Given the relatively small size of the flapping mechanism in comparison to the wing, the aerodynamic and inertial forces generated by the wing feedback into the mechanism causing its kinematic pattern to deviate from what is expected. The authors in Ref. [167] recommend that future computational studies on MAV-scale flapping wings may need to model the entire flapping wing system (power source, actuation mechanism, wings) to improve the validation process. However, this would add a much higher degree of complication and may increase the computational cost of performing numerical studies.

Many previous studies assume the flap kinematics to be sinusoidal in nature and prescribe a sine or cosine function with a given flap amplitude and flap frequency. In

this sub-section, computational tests were performed to assess the influence of the input flap kinematics on the wing deformation over time. Comparative studies were carried out using the structural and flow condition properties of the 10 mil thick wing at a flap frequency of 4 Hz. Figure 3.41 shows the flap angular position, angular velocity and angular acceleration for three input flap kinematics: (1) experimentally measured values, (2) analytically calculated four-bar kinematics, and (3) cosine function with appropriate flap amplitude. The flap amplitude prescribed to the cosine function is 40°. In Fig. 3.41a, we see that there is slight but noticeable deviation between the experimental, analytical and cosine function kinematics. However, when examining the flap angular velocity and angular acceleration (Figs. 3.41b and 3.41c), the slight variations between the flap angular position trends lead to significant and distinct deviations in the angular velocity and angular acceleration time histories. These differences are expected to have influence on the aerodynamic and inertial forces that act on the wing affecting the overall wing deformation during flapping.

To compare the difference in wing deformation associated with the input flap kinematics, Fig. 3.42 compares the variation in the wing trailing edge position at the wing root, midspan and tip for the three different input kinematics tested. In Fig. 3.42, the peak trailing edge displacements are of similar magnitudes. For the cosine function input kinematics (Fig. 3.42c), the trailing edge position variation is nearly symmetric between the forward and backward strokes. However, for the experimentally measured and analytical four-bar kinematics (Fig. 3.42a and 3.42b) the peak in trailing edge position occurs slightly after the end of a flap stroke.

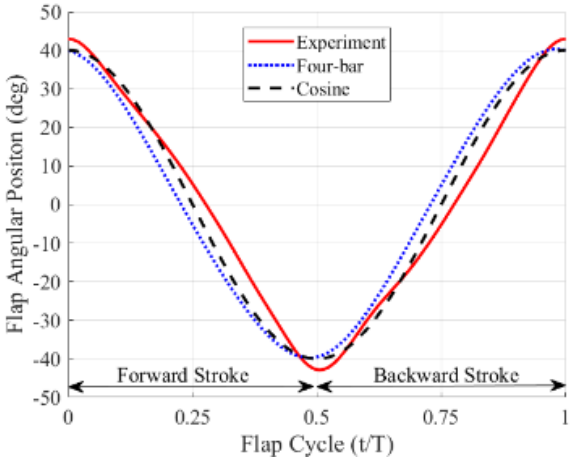

(a) Flap angular position versus time

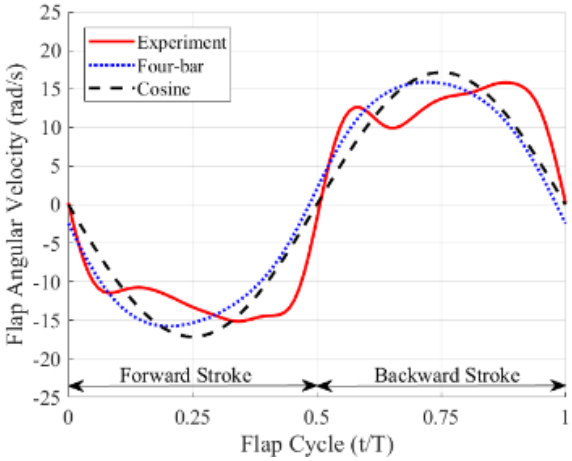

(b) Flap angular velocity versus time

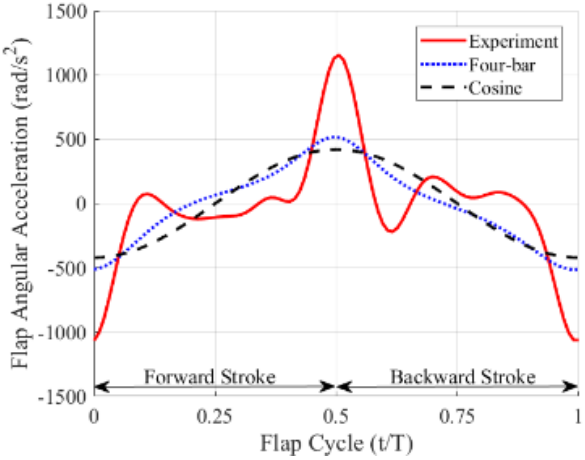

(c) Flap angular acceleration versus time

Figure 3.41: Comparison of experimental, analytical four-bar and cosine function flap kinematics

Similarly, Fig. 3.43 compares the instantaneous pitch angle variation at the wing root, midspan and tip for the three different input kinematics tested. There are distinct differences in the instantaneous pitch angle time histories between the different flap kinematics studies. The magnitude of the peak pitch variation is of greater magnitude when using the experimental kinematics (Fig. 3.43a) in comparison to those using the idealized kinematics (Fig. 3.43b and 3.43c). Higher harmonic content is also present in the pitch angle variation using the experimental kinematics. However, the temporal variations in pitch angle for the idealized kinematics more closely follow that of the input flap kinematics. This is mostly due to the greater variations in angular velocity and angular acceleration seen in the experimental kinematics compared to the analytical and cosine function kinematics.

It's also important to note that the curves in Fig. 3.43a nearly overlap each other suggesting that the pitch angle is almost uniform along the wing span. In Fig. 3.43b and 3.43c, there is notable spacing between the pitch angle curves suggest that there is a wing twist present with the wing tip exhibit a greater change in wing pitch compared to the wing root. Comparing the analytical and cosine function flap kinematic cases, while the peak pitch angle magnitudes are of similar value, there is a distinct difference in the variation of pitch angle between the two cases. In the analytical case (Fig. 3.43b), there is a gradual change in peak wing pitch followed by a steep return to the initial 90° pitch angle. For the cosine function kinematics (Fig. 3.43c), the change in wing pitch is more symmetric about the points of maximum and minimum pitch angle. Overall, idealized flap kinematics may suffice for preliminary design analysis or for parametric trade studies of a flapping wing system. But for validation studies, it is necessary to use

the experimentally measured kinematics, if possible, to more accurately predict the passive wing deformations.

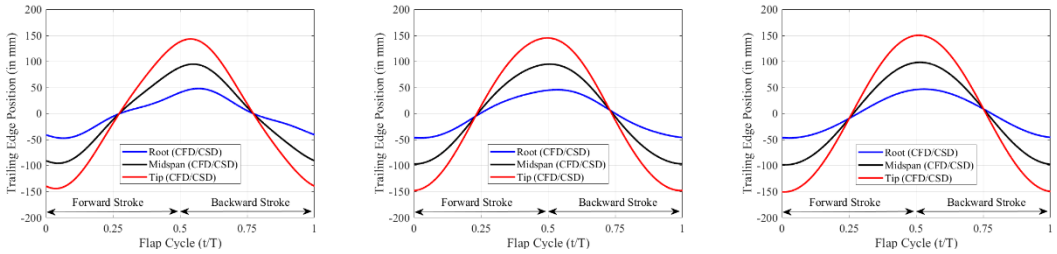

(a) Experimental kinematics (b) Analytical four-bar kinematics (c) Cosine function kinematics

Figure 3.42: Comparison of computational trailing edge position variation for varied input flap kinematics (h = 10 mil, f = 4 Hz)

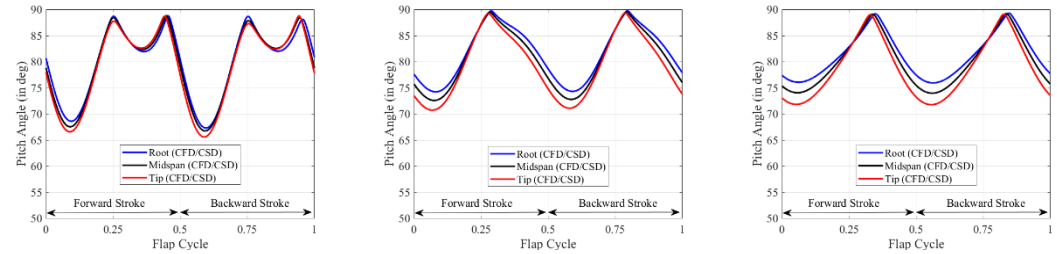

(a) Experimental kinematics (b) Analytical four-bar kinematics (c) Cosine function kinematics

Figure 3.43: Comparison of computational pitch angle variation for varied input flap kinematics (h = 10 mil, f = 4 Hz)

3.5 Summary

This chapter has focused on validating the coupled CFD/CSD aeroelastic analysis against a series of experimental and computational case studies. The predictive capability of the CFD solver (OVERTURNS) and CSD solver (MBDyn) were assessed individually. Additionally, the coupled aeroelastic analysis was validated against two different flexible wing studies. The overall summary and conclusions are as follows:

i. Rigid bio-inspired wing in hover: The aerodynamic force-time histories predicted by the CFD solver correlate well with the experimental force-time histories for the translational pitch angles tested. The CFD solver was able to predict the salient flow features measured in the experimental PIV tests both spatially and temporally. Quantitatively, the CFD model was able to adequately capture the trend in LEV circulation strength over time measured during experimentation.

ii. Flat plate undergoing single degree-of-freedom flap motion: The CSD solver demonstrated the capability to model the large deformation of a thin flat plate subject to flapping motion prescribed at the root. The flat plate tip displacement time history agreed well with the computational results from other CSD solvers for the 5 Hz and 10 Hz flap frequencies. At a flap frequency of 30 Hz, the results tended to deviate from one another over time. This is mainly due to the highly nonlinear and chaotic wing deformations that occur at such a high flap frequency for this particular case.

iii. Zimmerman planform wing with structural compliance: The results predicted using the coupled CFD/CSD aeroelastic solver agreed well with the experimental and computational validation results for a wing with a small degree of structural compliance. There was excellent agreement between the current CFD/CSD solver and the validation CFD/CSD solver predicted wing tip displacement time history. Similarly, good agreement was seen with respect to the lift coefficient time history. Additionally, there was satisfactory agreement between the results from the current CFD/CSD study and the

experimental and computational validation data when comparing the vorticity field, velocity field and velocity profiles.

iv. Flexible isotropic rectangular wing in hover: Static and dynamic wing deformations predicted using the computational analysis correlated well with the experimental results for a set of wings with a significant level of structural compliance. The CFD/CSD solver was able to satisfactorily predict the trailing edge displacement of the wing as well as the instantaneous pitch angle variation over time. Computational studies show that using idealized kinematics may suffice for preliminary analysis. However, the measured experimental kinematics should be prescribed in the computational model to most accurately predict the deformation of the wing during flapping.

Chapter 4 Chord-wise Flexible, Rectangular Wing Study

The validation studies presented in Chapter 3 focused on assessing the predictive capability of the individual CFD and CSD solvers as well as the coupled CFD/CSD aeroelastic analysis against experimental and/or computational data. With respect to flexible wings, the case discussed in Section 3.4 focused on an isotropic flat plate wing due to the relatively simple structural composition of the wing. Comparisons of the experimental and computational data solely focused on wing deformations under static loading as well as dynamic flapping conditions. Realistic MAV-scale wings tend to have a much more complex structural make-up typically being composed of a wing frame with a membrane covering. Also, given the complicated nature of the flapping wing problem, predictive capability should be assessed by comparing different characteristic datasets. (i.e. wing deformation, aerodynamic loading, flowfield evolution, etc.).

The work presented in this chapter seeks to analyze the aerodynamic flowfield and passive structural deformation of a MAV-scale flapping wing in hover using flowfield and motion capture experiments. The predictive capability of the coupled CFD/CSD model is assessed against PIV flowfield measurements and wing deformation measurements using a motion tracking system on a structurally characterized, highly flexible flapping wing. Focus is on investigating the temporal and spatial development of the velocity field and vortical flow structures about the wing as well as passive wing deformation over time.

4.1 Experimental Setup

4.1.1 Test Wing and Flapping Mechanism

A four-bar mechanism was used to provide the one degree-of-freedom flapping motion during experimentation. A picture of the experimental flapping mechanism as well as a schematic of the four-bar linkages can be seen in Figs. 4.1a and 4.1b respectively. The lengths of the flapping mechanism linkages are L_1 = 6.41 cm, L_2 = 0.42 cm, L_3 = 5.52 cm, and L_4 = 1.6 cm. The linkage lengths were chosen to reproduce harmonic sinusoidal motion with a flap stroke amplitude of 80°. The flap angle produced by the flapping mechanism can be determined by applying Eqs. (3.7)– (3.11) from Sub-section 3.4.1 the values associated with Fig. 4.1b. The flapping mechanism is driven by an AXI 2217 brushless outrunner motor manufactured by Model Motors. The AXI 2217 is connected to a 3:1 planetary gear box to generate the input torque required to actuate the mechanism.

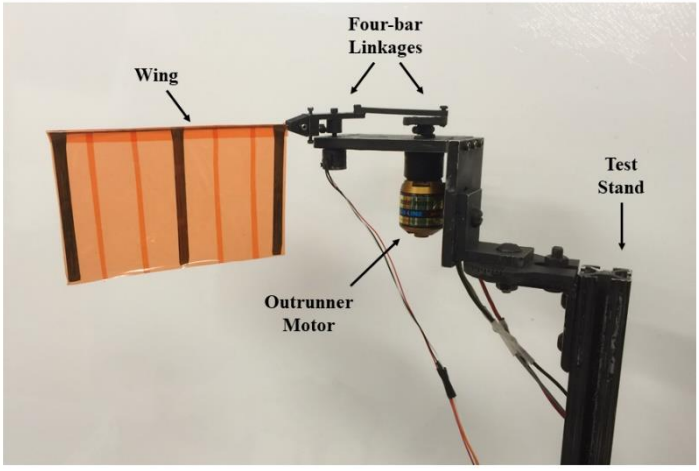

a) Test wing and flapping mechanism

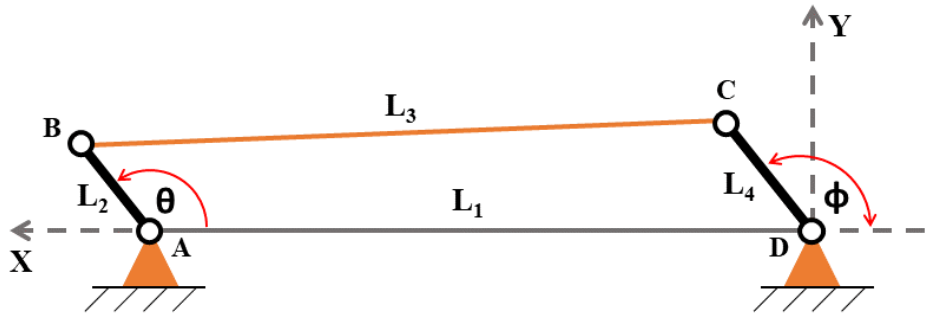

b) Schematic of four-bar linkages

Figure 4.1: Photo of test wing with mechanism and schematic of four-bar linkages

Figure 4.2 presents the flexible flapping wing used throughout experimentation. A solid titanium rod with a diameter of 1.5875 mm was used to fabricate the leading edge spar. The ribs are made out of a single layer of unidirectional carbon fiber. Each rib has a measured width of 6.80 mm and a thickness of 0.30 mm. The wing was designed to have a rectangular planform with a wing span (*b*) of 12.7 cm and a wing chord (*c*) of 7.62 cm resulting in a wing aspect ratio (*AR*) of 1.67. The root cutout region, defined as the distance from the flapping axis of rotation to the root rib, is 4.35 cm in length. A thin, heat resistant film, with a thickness (*h*) of 0.06 mm, was used to cover the wing to prevent laser burn during the PIV tests. Additionally, the wing was coated with a layer of flat black paint to reduce reflections from the laser.

To characterize the structural properties of the test wing, static deflection and dynamic shaker tests were conducted. The structural properties of each structural member were obtained experimentally through bending and torsion tests. Deflection measurements of the wing ribs and spar were taken using a VICON motion capture system. The general motion capture system is described in Section 3.4. The specific camera configuration and recording settings will be discussed in Sub-section 4.1.3.

Manufacturer properties were used for the Mylar film and were later verified via structural tension tests. The mass of each structural member was taken during the wing fabrication process. Note that the mass of a particular component of the wing is assumed to be distributed uniformly over that component. The dimensional characteristics of the wing, as well as the structural stiffness and mass properties are mentioned in Table 4.1.

When determining the ratio of elastic to aerodynamic forces acting on the wing, the aeroelastic scaling parameter (Π_1) discussed in sub-section 3.3 is not directly applicable because the test wing is not isotropic. A modification to the scaling parameter is presented to allow for use with anisotropic wing structures. From the definition of the scaling parameter (Π_1), the variable D_{plate} is related to the natural frequency of the wing through the following relation:

$$\omega_n = \frac{K_n}{c^2}\sqrt{\frac{D_{plate}}{\rho h}} \tag{4.1}$$

where ω_n is the natural frequency of the chordwise bending mode of the wing, ρ is the density of the wing structure and K_n is a constant determined by the geometric boundary conditions of the wing structure. From Eq. (4.1), the isotropic plate bending coefficient is proportional to the natural frequency and structural geometry of the wing such that:

$$D_{plate} \propto \omega_n^2 * m * \frac{c^3}{b} \tag{4.2}$$

where m is the total mass of the wing. Using Eq. (4.2), a modified aeroelastic scaling parameter is defined below:

$$\pi_1 = \frac{\omega_n^2 * m * \frac{c^3}{b}}{\rho_{ref} V_{ref}^2 c^3} = \frac{\omega_n^2 * m}{\rho_{ref} V_{ref}^2 b} \tag{4.3}$$

While the geometric and structural properties of the wing can be directly measured, the natural frequency of the first chordwise bending mode is determined using an eigen-analysis of the structural model using MBDyn [168]. Details of the structural model are discussed in sub-section 4.2. The calculated natural frequency of the first chordwise bending mode for the wing is 97.4 rad/s.

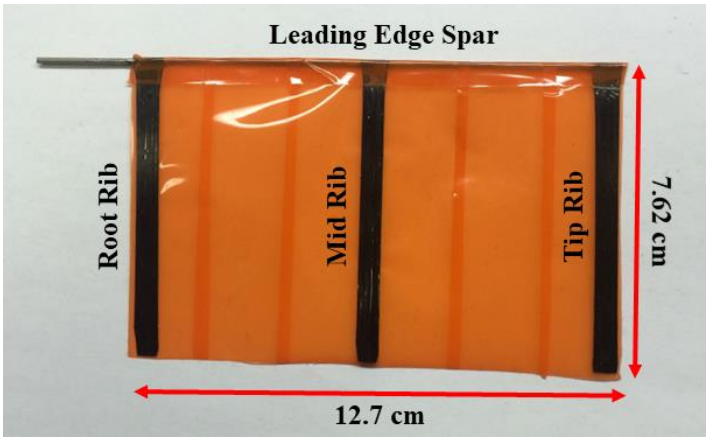

Figure 4.2: Flexible carbon fiber wing with film covering

Table 4.1**: Chord-wise flexible rectangular wing structural properties**

Wing length, *b*	12.7 cm
Wing chord, *c*	7.62 cm
Membrane thickness, *h*	0.06 mm
$EI_{root\ rib}$	1.7142×10^{-4} N-m^2
$EI_{mid\ rib}$	2.2316×10^{-4} N-m^2
$EI_{tip\ rib}$	2.7014×10^{-4} N-m^2
EI_{spar}	2.9104×10^{-2} N-m^2
GJ_{spar}	1.60×10^{-2} N-m^2
$E_{membrane}$	4.016×10^{9} N-m^{-2}
$\nu_{membrane}$	0.45
Root rib mass	0.1383 grams
Mid rib mass	0.1492 grams
Tip rib mass	0.1492 grams
Spar mass	1.136 grams
Membrane mass	1.03 grams

4.1.2 Particle Image Velocimetry Experimental Setup

Time-resolved, two-component PIV tests were conducted to measure the instantaneous velocity field about the wing during flapping. A double-pulsed Nd-YLF laser (Litron LDY304, 30mJ/pulse, 10 kHz max) was used to illuminate the region of interest during testing. Images were acquired with a Phantom v311 camera, which has a 4 Megapixel CMOS sensor and a 3.25 kHz frame rate at maximum resolution. The viewing axis of the camera was set orthogonally to the plane of the laser sheet with the pulse rate of the Nd-YLF laser and frame rate of the CMOS camera set to capture 725 frames per second in double frame mode. The quiescent flow was seeded using vaporized mineral oil. The seeding density was adjusted to provide at least 10 particles in each interrogation window and obtain a more optimal spatial resolution in the region of interest. Post-processing of the PIV image data was performed in DaVis v8.3. Particle cross-correlation was conducted using square and circular multi-pass

interrogation windows of 64×64 pixels with 50% overlap and 48×48 pixels with 75% overlap respectively. Any outliers in the data were removed using a median filter. For each test trial, a minimum of fifteen flowfield images were taken to be used for averaging. A schematic of the PIV test setup and the reference coordinate system used during experimentation are shown in Fig. 4.3a and Fig. 4.3b respectively.

From Fig. 4.3b, the flapping axis of rotation coincides with the z-axis and the inertial x-axis and y-axis make up the flapping plane. A positive rotation about the z-axis, (as defined by the right-hand rule), designates a forward stroke while a negative rotation designates a backward stroke. At midstroke, the wing span is in-line with the y-axis. Axes labeled with a $(\cdot)'$ mark a body frame coordinate system where the x'-axis and y'-axis rotate with the wing during flapping. Note, the z'-axis coincides with the z-axis and thus only the z-axis is labeled. The y'-axis is always along the wing span and the x'-axis is perpendicular to the $y'z$-plane.

The laser sheet was set to illuminate chordwise planes along the wing at the 25%, 50%, and 75% span locations (highlighted in Fig. 4.3b), as measured from the wing root. Measurements were taken at various azimuthal positions to capture the temporal evolution of the flowfield throughout the flap cycle. A summary of the flow and test parameters are shown in Table 4.2.

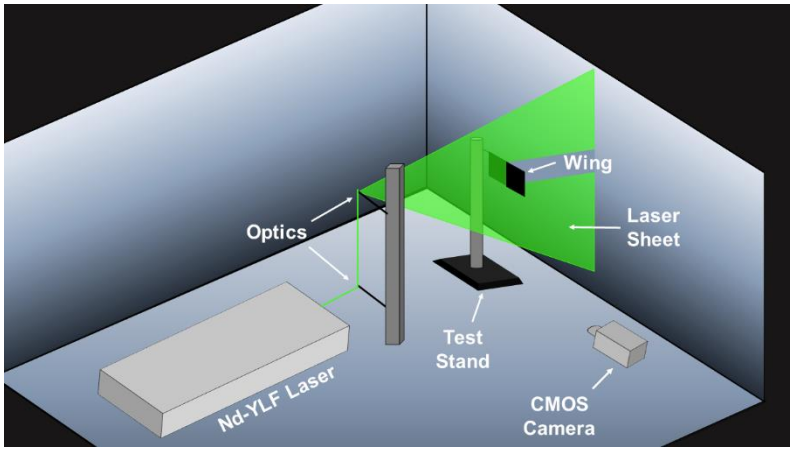

(a) Schematic of PIV experimental setup

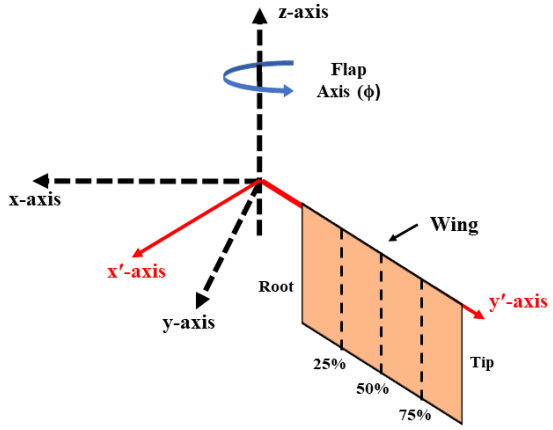

(b) Sketch of reference coordinate system

Figure 4.3: Schematic of PIV experimental setup and flapping wing reference coordinate system

Table 4.2: PIV experimental flow and test parameters

Parameter	Value
Flap frequency, $\boldsymbol{f}$	4 – 8 Hz
Flap amplitude, ϕ_{amp}	40°
Reduced Frequency, $\left(\boldsymbol{k} = \frac{\boldsymbol{\omega c}}{\boldsymbol{2 * V_{tip}}}\right)$	0.341
Reynolds number, $\left(\boldsymbol{Re} = \frac{\boldsymbol{\rho V_{tip} c}}{\boldsymbol{\nu}}\right)$	14,200 – 34,000
Scaling parameter, $(\pi_1 = \frac{\boldsymbol{\omega_n^2 * m}}{\boldsymbol{\rho V_{tip}^2 b}})$	5.0 – 20.0
Flap angle, ϕ	8° – 56°, $\Delta\phi$= 16°
Span location	25%, 50%, 75%

4.1.3 VICON Motion Capture Experimental Setup

A VICON motion capture system was utilized to determine the structural properties of the various wing components as well as measure the passive wing deformations, due to inertial and aerodynamic loading, during flapping. The motion capture images were acquired using VICON T40-S cameras (4 Megapixel resolution with a maximum frame rate of 500 Hz at full resolution). The motion capture test setup consisted of 6 cameras operating at 100 frames per second (fps) when performing static wing deformation tests to calculate the wing structural stiffness. However, for dynamic flapping wing tests, the six cameras were run at 400 fps to accurately capture the wing deformation over time. Figure 4.4 provides a picture of the VICON motion capture test setup. Reflective markers were placed at the leading edge, mid-chord and trailing edge of each rib at the wing root, midspan and wing tip to track the motion of those locations on the wing. Figure 4.5 presents the experimental test wing with the reflective markers in place. The cameras were arranged to ensure that at least two cameras are able to view the reflective markers at any point in the flap stroke. Data recorded during the motion capture tests was post-processed using VICON Nexus 1.8.

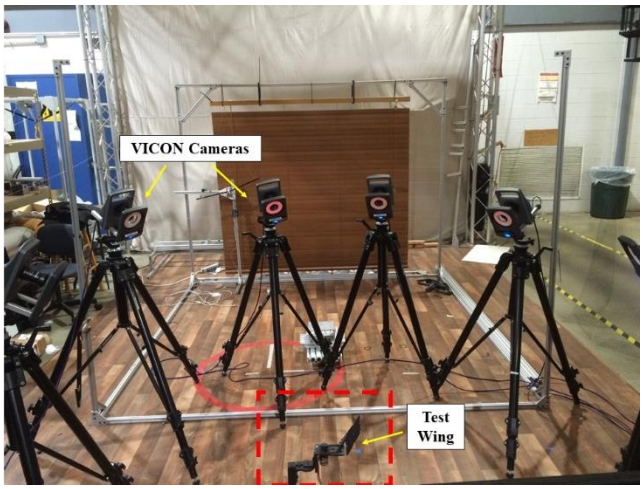

Figure 4.4: VICON motion capture setup

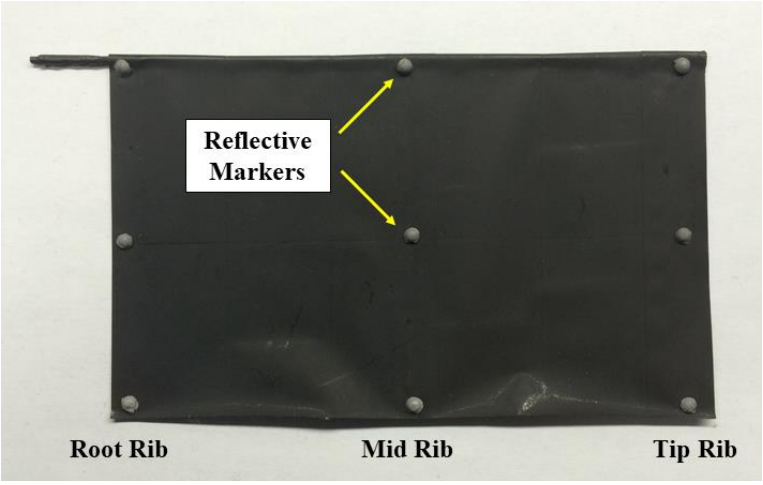

Figure 4.5: Experimental test wing with reflective markers

4.2 Computational Setup

The chord-wise flexible rectangular wing was modelled using the coupled CFD/CSD aeroelastic analysis. An overset mesh system was utilized to model the wing geometry and flow environment within the CFD solver. A C-O topology, structured body-fitted mesh was used to represent the wing and a Cartesian background mesh was used to model the surrounding wake. The wing geometry was designed to have a

rectangular planform with an aspect ratio of 1.67 to match that of the test wing in Fig. 4.2. Note that a thickness-to-chord ratio (*h/c*) of 1.0% was used. The wing mesh was approximately comprised of 3.2 million grid points with 267×141×85 grid points in the wrap-around, spanwise and normal directions respectively. Note that of the 267 points in the wrap-around direction, 187 lay over the wing surface while the remaining points make up the wakecut region of the wing mesh. Grid points were clustered near the leading edge, trailing edge, wing root and wing tip. These regions of the wing are where vortical or highly separated flow is expected to form. The background cartesian mesh is composed of 127×195×162 nodes in the x, y and z directions respectively. Farfield boundary conditions are applied 10 chord lengths away from the origin of the background mesh. Grid points are clustered with the initial 2.5*c* of the origin in all directions to improve spatial resolution of the shed wake. The flow parameters from Table 4.2 were utilized in the CFD simulation. A picture of the wing and background meshes can be seen in Fig. 4.6.

The structural model was made up of 64 plate elements with 8 by 8 elements in the spanwise and chordwise directions respectively. A total of 32 beam elements are used to model the wing leading edge spar and the three chordwise ribs. A picture of the node points making up the wing structural model can be seen in Fig. 4.7. Note that in Fig. 4.7 the black solid lines represent the leading edge and ribs of the wing. The measured structural parameters, shown in Table 4.1, were implemented in the structural model.

When the wing is placed within the flapping mechanism, the wing root is offset from the flapping axis by 4.35 cm (0.57*c*) and this offset is properly represented within

the CFD and CSD models. The flap angle measured during experimentation is prescribed to the aeroelastic model during the simulation. At the start of the simulation, the wing is at a 90° pitch angle such that the wing chord line is parallel to the z-axis. The wing starts at the beginning of the forward stroke with the flap motion being prescribed about the flap axis such that wing flapping occurs in the xy-plane.

Overall, the simulation was run for 3 flap cycles with 2880 iterations per flap cycle resulting in a timestep size of $8.68\times10^{-5} - 4.34\times10^{-5}$ seconds used in the structural model. The value of the timestep is dependent on the flap frequency being tested ranging from 4 Hz to 8 Hz. The timestep in the CFD model was set so that the positional change in the wings match between the CFD and structural models. A total of 8 Newton sub-iterations were used in the CFD solver to minimize factorization errors and improve solution accuracy. In the CSD solver, MBDyn's original A/L stable linear multistep algorithm was used with a spectral radius of 0.6 and the residual tolerance was set to 1.0×10^{-3}.

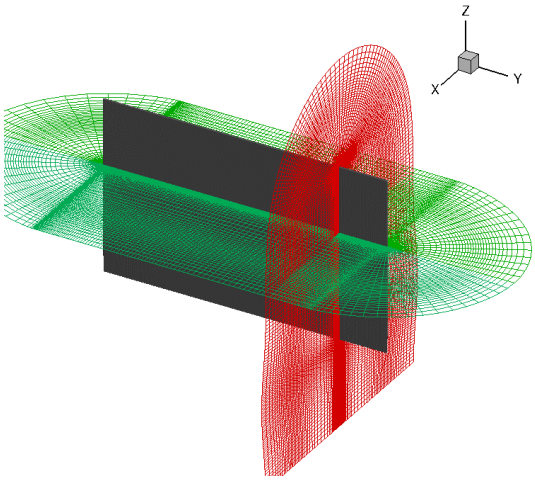

(a) C-O topology wing mesh

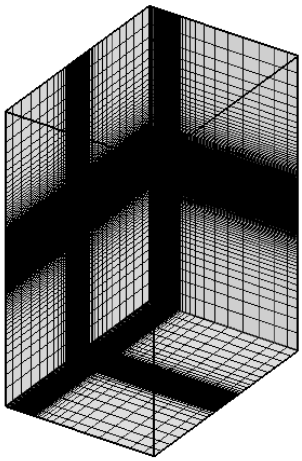

(b) Cartesian background mesh

Figure 4.6: CFD overset mesh system for chord-wise flexible wing

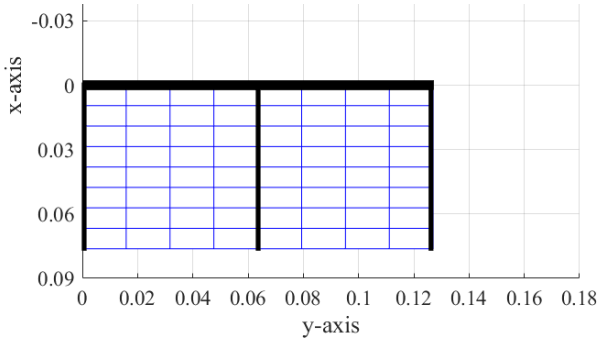

Figure 4.7: Illustration of CSD model nodes

4.3 Results Comparison

4.3.1 Flowfield Comparison

Given the highly unsteady nature of the aerodynamic regime about the wing, the vorticity field is used to compare the measured and predicted flowfields. Vorticity ($\vec{\omega}$) is equal to $\vec{\nabla} \times \vec{V}$ with the velocity gradients from the velocity field being calculated using a second order accurate "Least Squares" differencing method. It should be noted that the velocity fields from the coupled CFD/CSD results were interpolated onto a

Cartesian grid with grid spacing equal to that of the PIV results for comparison purposes. Figures 4.8, 4.9 and 4.10 show the experimental and computational vorticity contour plots for the 4 Hz flap frequency case at flap angles of 24°, 40° and 56° respectively. Similarly, Figs. 4.11 – 4.13 and Figs. 4.14 – 4.16 show vorticity contours for the 6 Hz and 8 Hz flap frequencies, respectively, at flap angles of 24°, 40° and 56°. Flap angles of 24°, 40° and 56° corresponds to times during the flap cycle of t/T = 0.18, 0.25 and 0.32 respectively.

The PIV vorticity contours at the 25%, 50% and 75% span locations (relative to the wing root) are shown in sub-Figs. (·)a, (·)b and (·)c respectively were (·) corresponds to a figure in the range of 4.8 – 4.16. Likewise, sub-Figs. (·)d, (·)e and (·)f are the CFD/CSD vorticity contours at the 25%, 50% and 75% span locations. Note that overlaid velocity vectors are plotted within the vorticity contour plots with every 5th velocity vector displayed for clarity. Additionally, the vorticity magnitude is normalized by the maximum tip velocity of the wing (V_{tip}) and the wing chord (c) for the given flap frequency case.

In general, the computational results exhibit good agreement with the experimental results. In Figs. 4.8a and Fig. 4.8d, a well-formed LEV and counter-rotating trailing edge vortex (TEV) can be seen attached to the wing surface. The leading and trailing edge vortices at the 25% span location remain attached to the wing surface at flap angles of 40° and 56° in Figs. 4.9a and 4.9d and Figs. 4.10a and 4.10d respectively. In Figs. 4.8b and 4.8e, the LEV is of greater size but is still within close proximity of the wing surface. The trailing edge vortex has shed from the wing and a noticeable shear layer has formed at the trailing edge. Moving forward in the flap cycle

(Figs. 4.9 and 4.10) at the 50% span location, the LEV has slightly increasee in size but remains in close proximity to the wing surface and is coherent in its form. However, the TEV has become more diffused and is significantly separated from the wing surface.

At the 75% span location in Figs. 4.8c and 4.8f, the LEV has begun to slightly separate from the wing surface and the TEV is completely detached from the wing surface. At a flap angle of 40° (Figs. 4.9c and 4.9f), the LEV has significantly grown in size, becoming more diffused and is starting to breakdown. The trailing edge vortex is no longer coherent and is only partly visible in the region of interest about the wing. In Figs. 4.10c and 4.10f, the breakdown of the LEV is more visible and a shear layer has formed from the trailing edge. The velocity vectors show flow moving down and to the right on the low-pressure side of the wing due to the influence of the LEV.

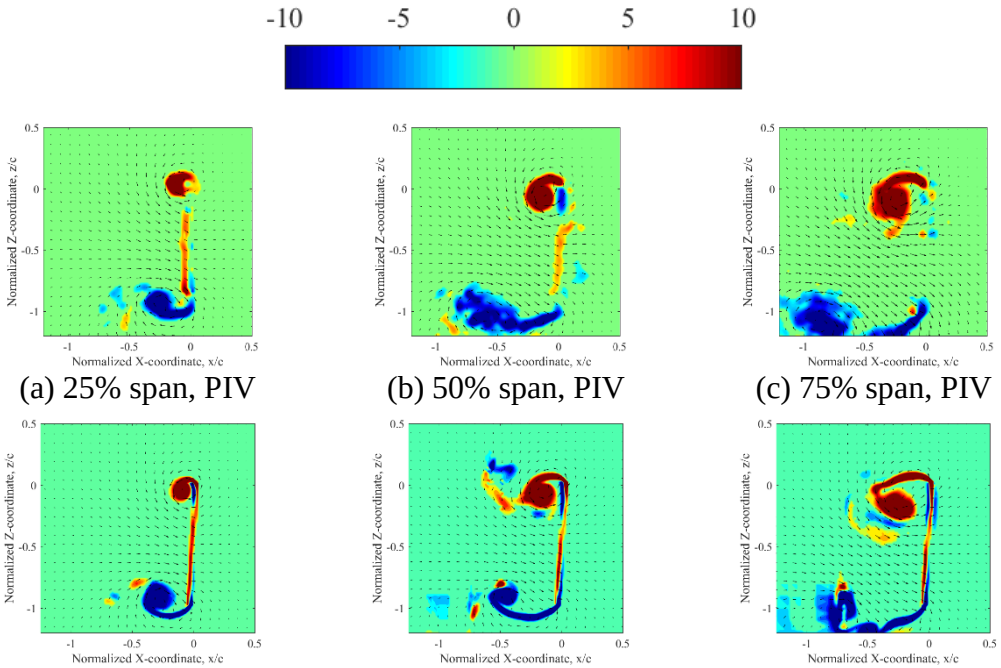

(a) 25% span, PIV (b) 50% span, PIV (c) 75% span, PIV

(d) 25% span, CFD/CSD (e) 50% span, CFD/CSD (f) 75% span, CFD/CSD

Figure 4.8: Spanwise variation of PIV and CFD/CSD vorticity contours at f = 4 Hz, ϕ = 24°

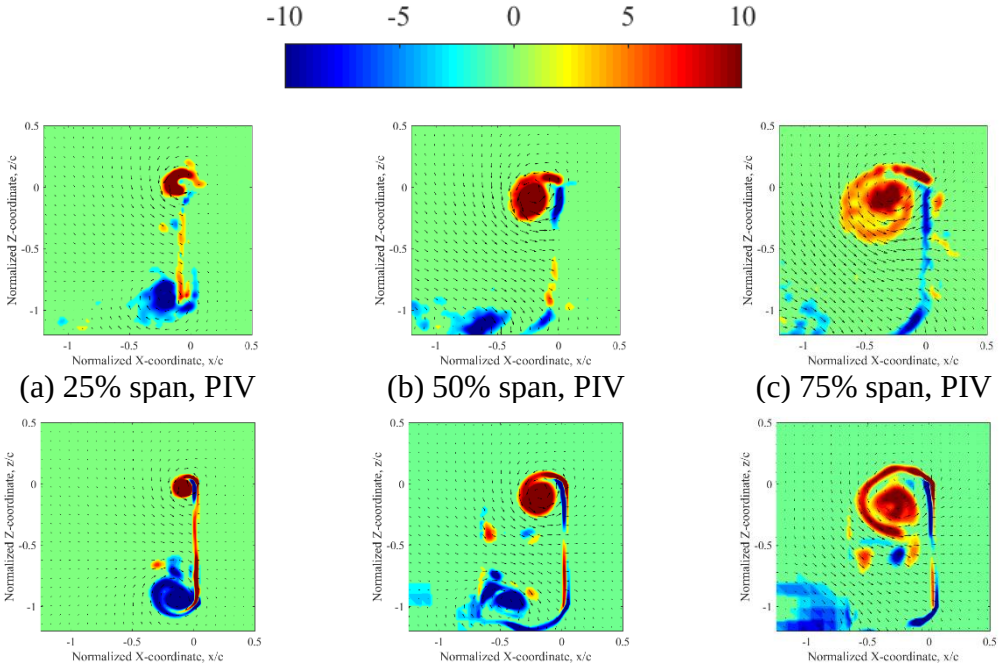

(a) 25% span, PIV (b) 50% span, PIV (c) 75% span, PIV

(d) 25% span, CFD/CSD (e) 50% span, CFD/CSD (f) 75% span, CFD/CSD

Figure 4.9: Spanwise variation of PIV and CFD/CSD vorticity contours at f = 4 Hz, ϕ = 40°

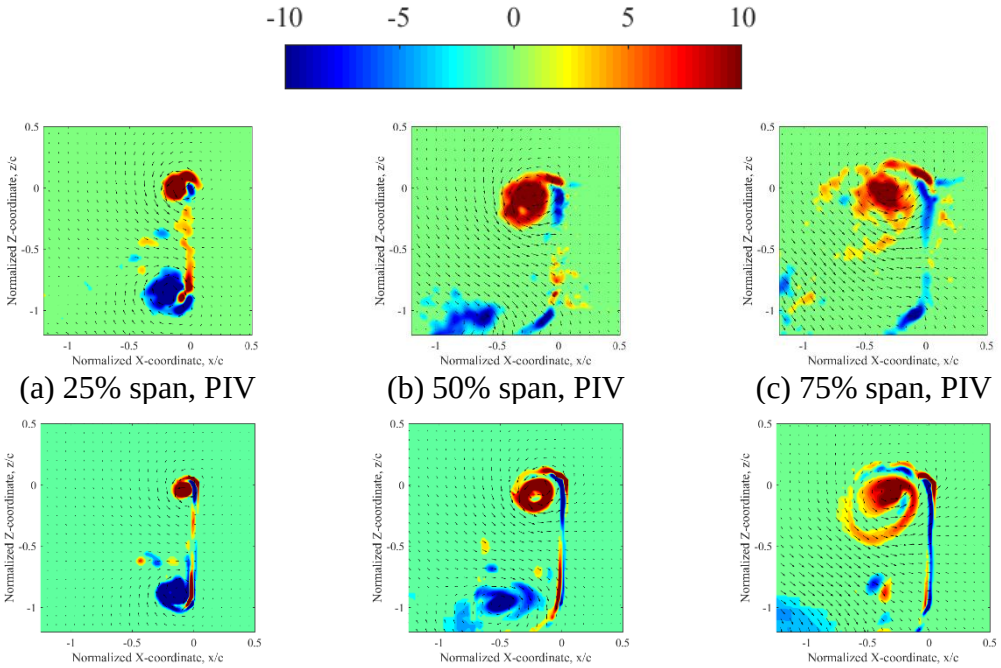

(a) 25% span, PIV (b) 50% span, PIV (c) 75% span, PIV

(d) 25% span, CFD/CSD (e) 50% span, CFD/CSD (f) 75% span, CFD/CSD

Figure 4.10: Spanwise variation of PIV and CFD/CSD vorticity contours at f = 4 Hz, ϕ = 56°

While the computational results exhibited good correlation to the experimental data for the 4 Hz flapping case, it is important to assess the predictive capability of the coupled aeroelastic solver at higher flap frequencies. Figures 4.11 – 4.13 show the experimental and computational vorticity contour plots for the 6 Hz flap frequency case. Comparing Figs. 4.11a and Fig. 4.11d, the wing is deformed and a leading edge vortex is beginning to form on the wing surface. Similar behavior is seen at 50% span (Figs. 4.11b and 4.11e) and 75% span (Figs. 4.11c and 4.11f) however the size of the leading edge vortex increases as one moves further outboard along the wingspan. The TEV has shed from the wing and a notable shear layer has formed at all spanwise stations analyzed.

At midstroke (Figs. 4.12a and 4.12d), the wing is approximately at a 90° pitch angle. The LEV is still attached to the wing and remains the same in size. At 50% span (Figs. 4.12b and 4.12e) and 75% span (Figs. 4.12c and 4.12f) the LEV has increased in size in comparison to the corresponding LEVs at $\phi = 24°$. At the 75% span location, the predicted LEV is shown to be more diffused compared to the experimentally measured LEV. Trailing edge shear layers have formed in all the vorticity contours in Fig. 4.12. However, there are some slight discrepancies in the trajectory of the trailing edge shear layers between the experimental and computational results.

After midstroke ($\phi = 56°$), the LEVs are still in close proximity to the wing surface. At the 75% span location (Figs. 4.13c and 4.13f) the LEV is beginning to become more diffused and breakdown. There are some discrepancies in the level of shed vorticity toward the trailing edge when comparing the measured and predicted

results. However, in both cases, the vorticity near the trailing edge is highly separated and incoherent.

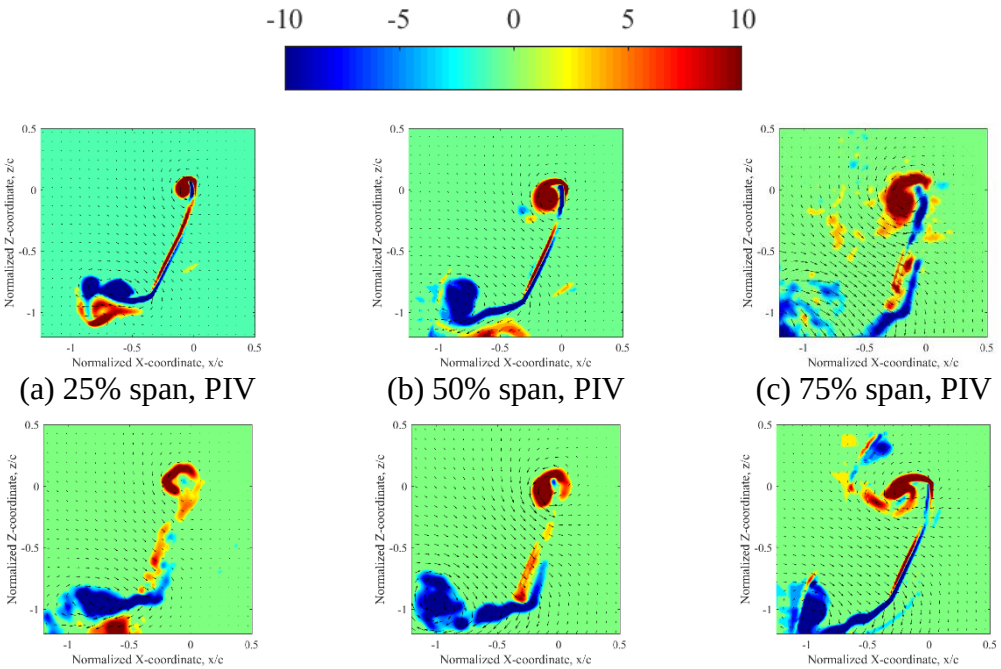

(a) 25% span, PIV (b) 50% span, PIV (c) 75% span, PIV

(d) 25% span, CFD/CSD (e) 50% span, CFD/CSD (f) 75% span, CFD/CSD

Figure 4.11: Spanwise variation of PIV and CFD/CSD vorticity contours at f = 6 Hz, ϕ = 24°

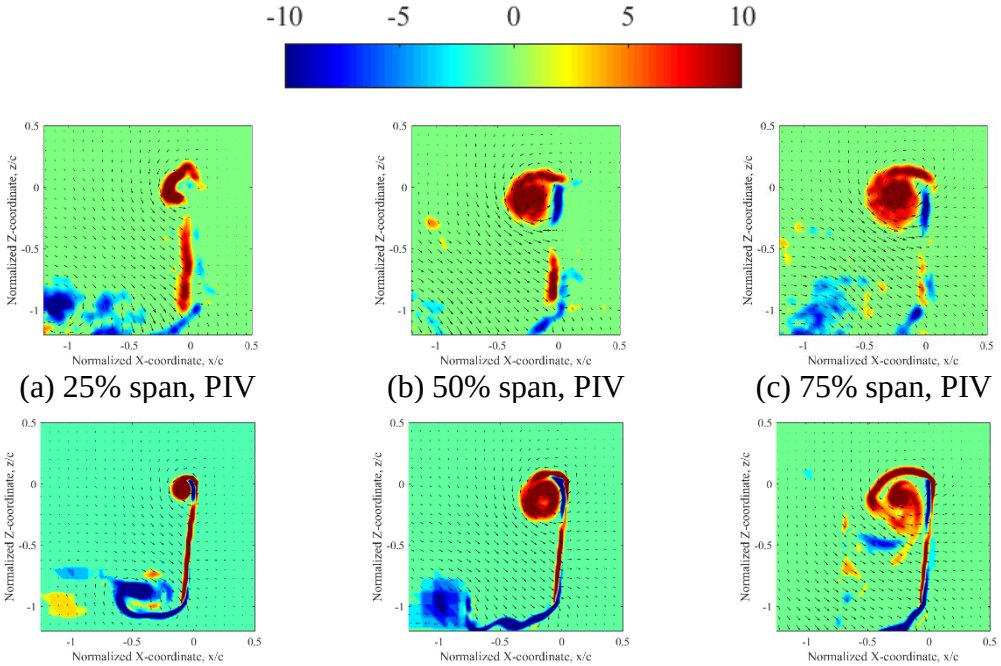

(a) 25% span, PIV (b) 50% span, PIV (c) 75% span, PIV

(d) 25% span, CFD/CSD (e) 50% span, CFD/CSD (f) 75% span, CFD/CSD

Figure 4.12: Spanwise variation of PIV and CFD/CSD vorticity contours at f = 6 Hz, ϕ = 40°

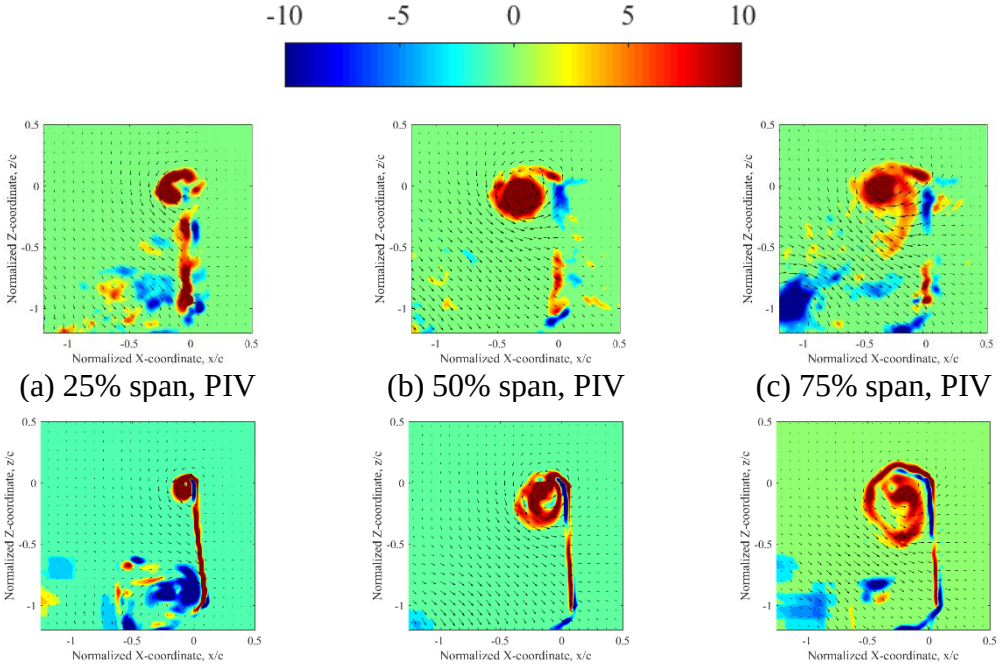

(a) 25% span, PIV (b) 50% span, PIV (c) 75% span, PIV

(d) 25% span, CFD/CSD (e) 50% span, CFD/CSD (f) 75% span, CFD/CSD

Figure 4.13: Spanwise variation of PIV and CFD/CSD vorticity contours at f = 6 Hz, ϕ = 56°

Figures 4.14 – 4.16 shows the experimental and computational vorticity contour plots for the 8 Hz flap frequency case. Early in the flap stroke (ϕ = 24°), when comparing Fig. 4.14a and Fig. 4.14d, the wing is highly deformed and a leading edge vortex is beginning to form on the wing surface. The trailing edge vortex has shed from the wing and a notable shear layer has formed. Similar behavior is seen at 50% span (Figs. 4.14b and 4.14e) and 75% span (Figs. 4.14c and 4.14f). Note that the size of the LEV increases when analyzing regions further outboard on the wing.

At midstroke (Figs. 4.15a and 4.15d), the LEV remains at approximately the same size and location with respect to the wing. At 50% span (Figs. 4.15b and 4.15e) and 75% span (Figs. 4.15c and 4.15f) the LEV has increased in size in comparison to the corresponding LEVs at ϕ = 24°. Prominent trailing edge shear layers can be seen in all the vorticity contours plots in Fig. 4.15. Note that in the experiment (Fig. 4.15a), the TEV has detached from wing and is no longer in view of the region of interest. However, in the computational vorticity contour (Fig. 4.15d), the shed trailing edge vortex has not shed as far from the wing as in the experiment and is still visible in the image.

After midstroke at a flap angle of 56° (Fig. 4.16), the wing is nearly at 90° and the LEV is still attached to the wing. There are some discrepancies in the level of shed vorticity toward the trailing edge when comparing the measured and predicted results. However, in both cases, the vorticity near the trailing edge is highly separated and incoherent.

Overall, there is good correlation between the PIV and CFD/CSD results. There is some discrepancy between the experimental and computational results regarding the

size and progression of the shed TEV or trailing edge shear layer, but the evolution of the LEV is well resolved. Qualitatively, the coupled aeroelastic analysis is capable of predicting the salient aerodynamic features within the flowfield.

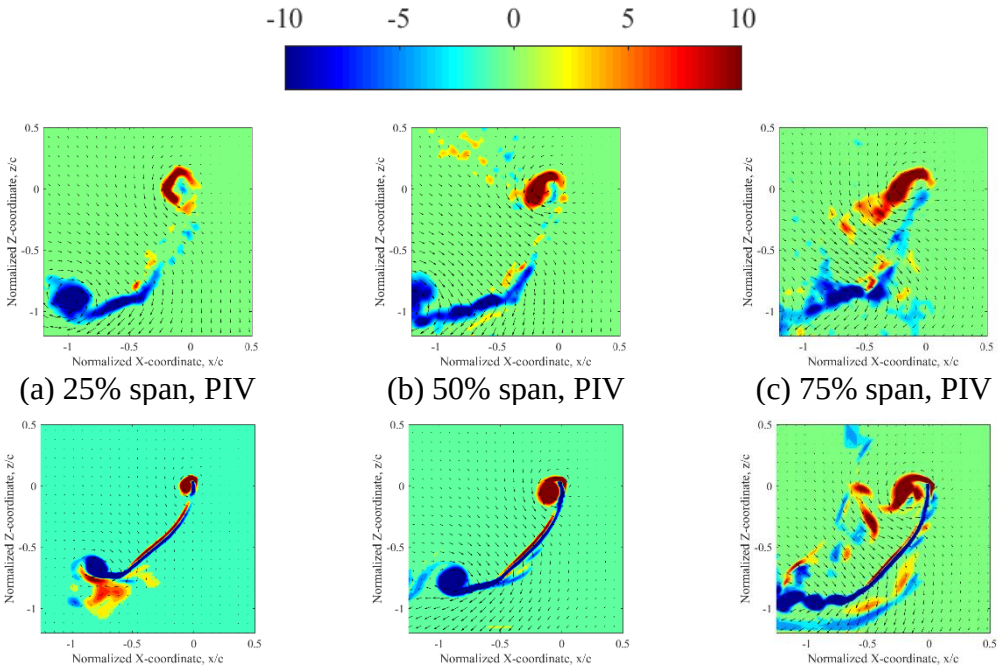

(a) 25% span, PIV (b) 50% span, PIV (c) 75% span, PIV

(d) 25% span, CFD/CSD (e) 50% span, CFD/CSD (f) 75% span, CFD/CSD

Figure 4.14: Spanwise variation of PIV and CFD/CSD vorticity contours at f = 8 Hz, ϕ = 24°

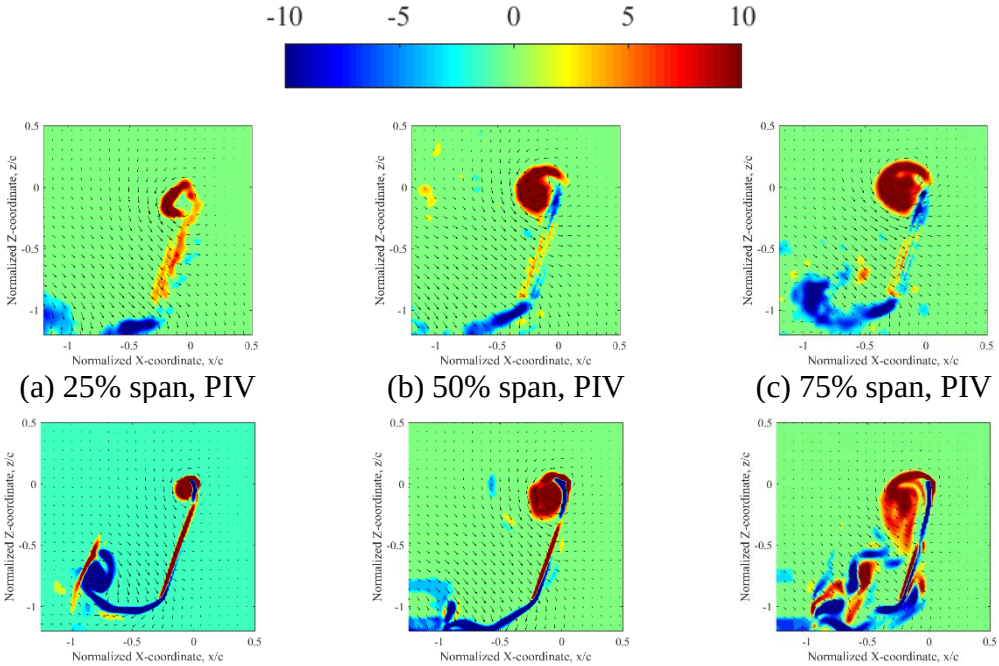

(a) 25% span, PIV (b) 50% span, PIV (c) 75% span, PIV

(d) 25% span, CFD/CSD (e) 50% span, CFD/CSD (f) 75% span, CFD/CSD

Figure 4.15: Spanwise variation of PIV and CFD/CSD vorticity contours at f = 8 Hz, ϕ = 40°

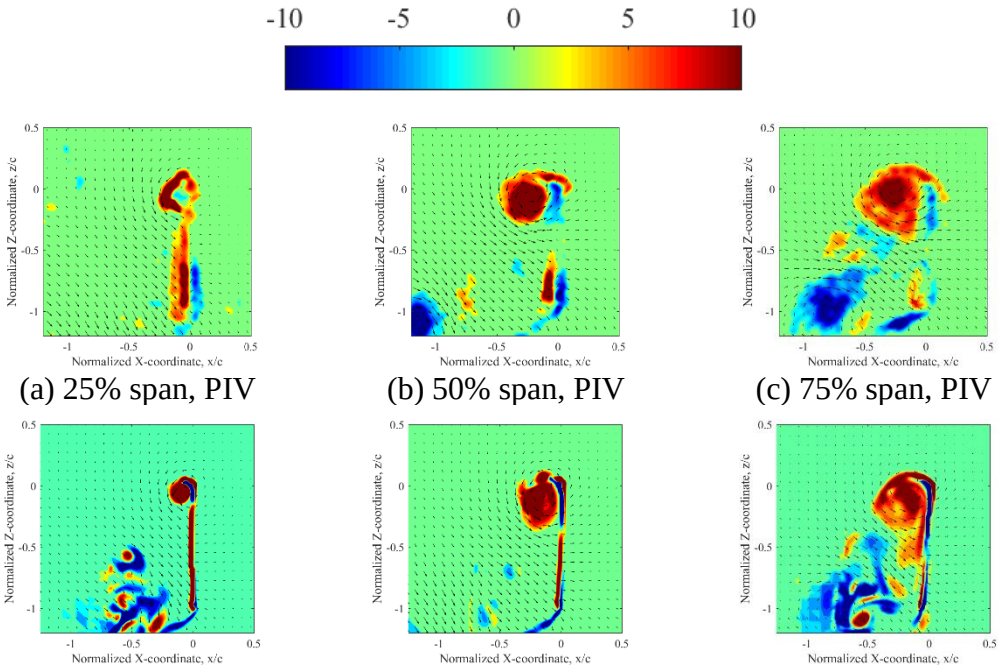

(a) 25% span, PIV (b) 50% span, PIV (c) 75% span, PIV

(d) 25% span, CFD/CSD (e) 50% span, CFD/CSD (f) 75% span, CFD/CSD

Figure 4.16: Spanwise variation of PIV and CFD/CSD vorticity contours at f = 8 Hz, ϕ = 56°

4.3.2 Wing Deformation Comparison

In addition to the flowfield comparisons, efforts were made to compare the predicted passive wing deformations to those measured experimentally. Figure 4.17 shows the variation of the wing trailing edge position from the experimental and computational results at f = 4 Hz (Fig. 4.17a), f = 6 Hz (Fig. 4.17b) and f = 8 Hz (Fig. 4.17c). Comparisons are made at the trailing edge of the root, mid and tip ribs over the course of a flap cycle. The curves shown are the x-component of the trailing edge position vector expressed in the global reference frame from Fig. 4.3b. The time over the course of a flap cycle is nondimensionalized by the flap period (T). The displayed experimental results are an average of 40 flap cycles while computational results are taken from the last flap cycle of the simulation.

For the 4 Hz flapping case (Fig. 4.17a), the computational results compare well against the experimental data with respect to peak displacement magnitude and phasing. During the forward stroke, the curves from the predicted results lay on top of the measured results. However, there is slight deviation between the predicted and measured curves during the backward stroke. The 6 Hz (Fig. 4.17b) and 8 Hz (Fig. 4.17c) cases are similar to the 4 Hz case in that the computational results agree well with the experimental results. Predicted and measured peak magnitudes as well as the overall temporal variation in the trailing edge position exhibit good agreement. Similar to Fig. 4.17a, the measured and predicted results match more closely during the forward stroke with a slight deviation in results during the backward stroke.

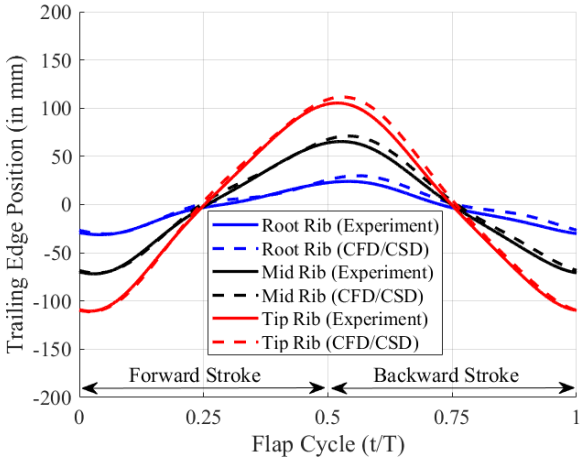

(a) f = 4 Hz

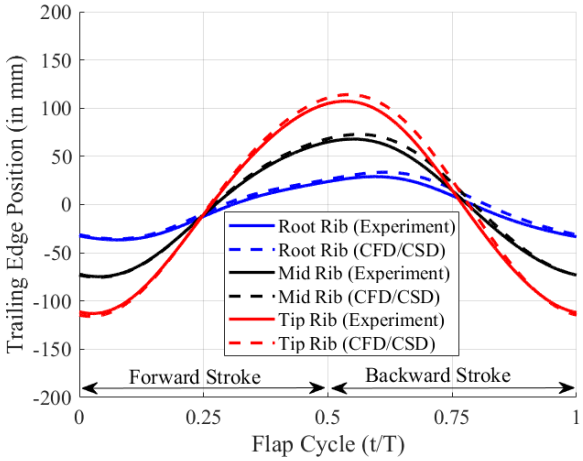

(b) f = 6 Hz

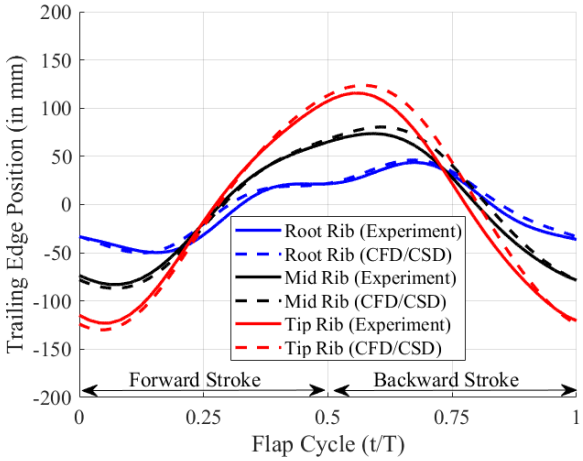

(c) f = 8 Hz

Figure 4.17: Comparison of experimental and CFD/CSD passive trailing edge wing deformations

Note that as flap frequency is increased, there is a notable degree of higher harmonic content present which is especially visible in the root rib trailing edge position curves. Additionally, with increased flap frequency, there is a phase shift in the peak trailing edge deflection such that it occurs later in time of a given forward or backward stroke.

Figure 4.18 shows the instantaneous pitch angle variation for the 4 Hz, 6 Hz and 8 Hz cases. Pitch angles are compared at the root, mid and tip ribs which correspond to the 0% span, 50% and 100% span locations respectively. Figures 4.18a, 4.18b and 4.18c show the instantaneous pitch angle variation over time for the 4 Hz, 6 Hz and 8 Hz cases respectively. At the 4 Hz flap frequency, the pitch angle variation is minimal. The highest change in pitch angle magnitude occurs during stroke reversal due to the inertial forces acting on the wing.

For the 6 Hz and 8 Hz flap frequency cases, the pitch angle variations are larger in magnitude and the aerodynamic forces begin to play a more significant role in the passive wing deformations over time. At a flap frequency of 6 Hz (Fig. 4.18b), the pitch angle variation follows a nearly sinusoidal trend. There is relatively good agreement between the experimental and computational results with some discrepancy between the trends for the root rib pitch angle. The magnitude of variation is similar between the root, mid and tip ribs with a peak magnitude of approximately 70°. As expected, the instantaneous pitch angle variations are at their highest magnitudes for the 8 Hz (Fig. 4.18c) flap frequency case. The measured and predicted results agree well with respect to the peak pitch magnitude.

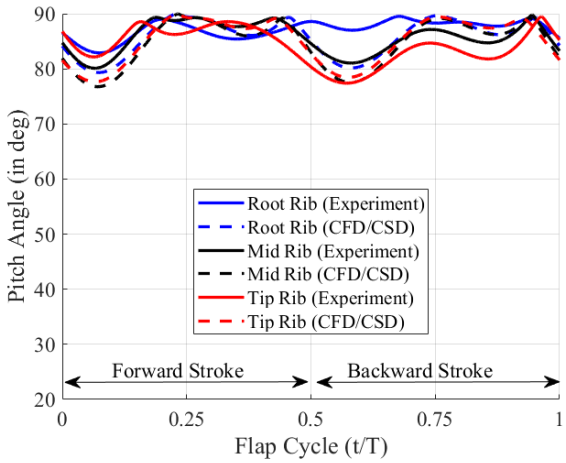

(a) f = 4 Hz

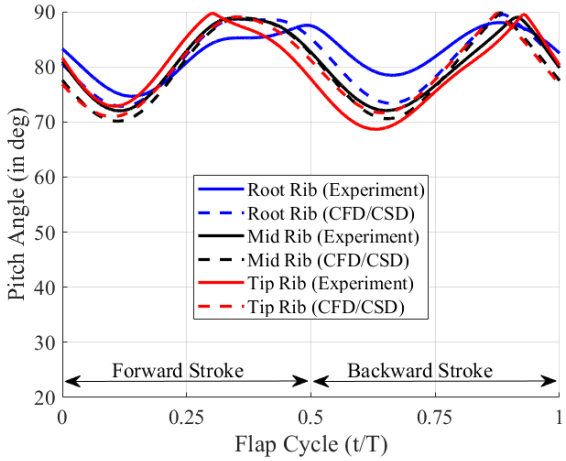

(b) f = 6 Hz

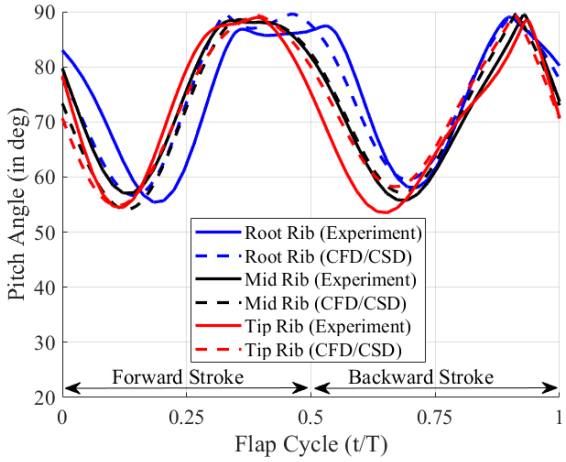

(c) f = 8 Hz

Figure 4.18: Comparison of experimental and CFD/CSD instantaneous pitch angles

For all three ribs, peak pitch angle magnitude is approximately 55° for the experimental and computational results. However, there are notable differences in the variation of wing pitch over time especially for the results at the root rib. Overall, the aeroelastic analysis is capable of capturing the general temporal variation in wing pitch over the course of a flap cycle.

In general, the coupled CFD/CSD analysis is capable of adequately predicting the passive wing deformations and instantaneous pitch angle variation over the course of a flap cycle. There are some noticeable differences between the measured and predicted wing deflections especially when comparing the instantaneous pitch angle variation or higher harmonic oscillations present in the trailing edge position data. However, the aeroelastic analysis is capable of predicting the overall wing deformation during flapping.

4.3.3 CFD/CSD Force-time Histories

The coupled CFD/CSD results are used to further investigate the difference in aerodynamic force production for the various flapping frequency cases studied. Figures 4.19 and 4.20 illustrate the variation in instantaneous lift coefficient and drag coefficient for the 4 Hz, 6 Hz and 8 Hz flap frequency cases. Note that lift is defined as positive when acting in the positive z-direction (see coordinate system in Fig. 4.3b) and drag is said to act in opposition to wing motion. Negative drag coefficient values do not represent propulsive thrust, but instead a change in direction of the drag force vector due to a change in the flap motion direction.

In Fig. 4.19, as anticipated, the magnitude of the peak lift coefficient (C_L) increases with increased flap frequency. However, while the maximum velocities

experienced by the wing occur at midstroke (t/T = 0.25 and 0.75), peak lift occurs slightly before midstroke for all flap cases. When comparing the drag force-time histories (Fig. 4.2), there is little variation in peak drag coefficient (C_D) magnitude between the 6 Hz and 8 Hz cases. The 4 Hz case shows a significantly different drag coefficient trend in comparison to the higher frequency cases. There is a noticeable phase shift in the drag coefficient variation trend with increased flap frequency. Unlike the lift coefficient force-time histories in Fig. 4.19, peak drag coefficient magnitude occurs near midstroke where the induced flapping velocities are at their highest.

Figure 4.21 shows the time history of the aerodynamic power coefficient for the 4 Hz, 6 Hz and 8 Hz flap frequencies. All three cases exhibit a peak aerodynamic power coefficient of approximately 1.25. However, the variation of aerodynamic power varies between the three cases. The 4 Hz case exhibits a double peak behavior where a secondary peak in aerodynamic power occurs after midstroke but before the start of the next flap stroke. At flap frequencies of 6 Hz and 8 Hz, there is a single peak in aerodynamic power during each flap stroke at approximately midstroke. The decrease in aerodynamic power after the peak is steeper for f = 6 Hz in comparison to f = 8 Hz.

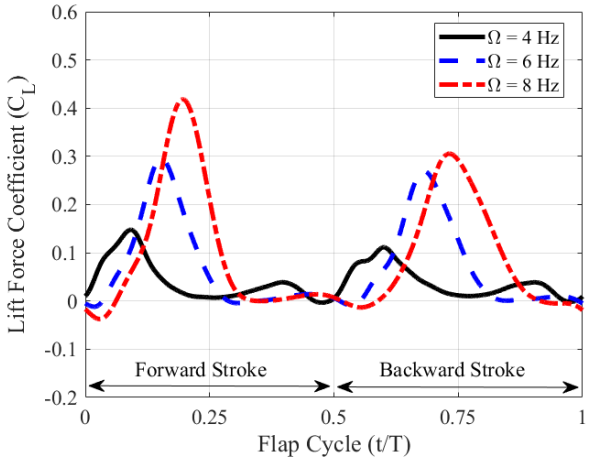

Figure 4.19: Lift coefficient time history over a flap cycle

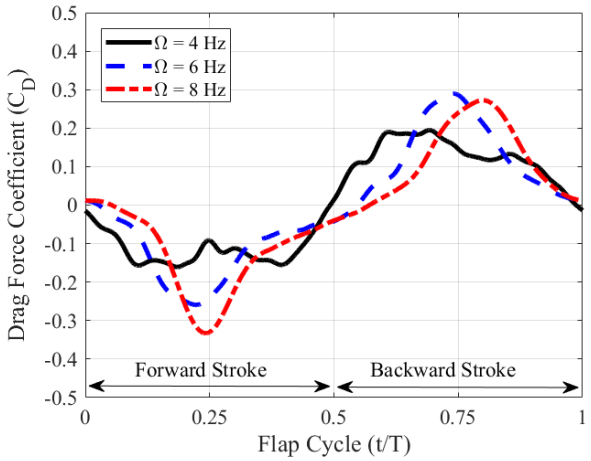

Figure 4.20: Drag coefficient time history over a flap cycle

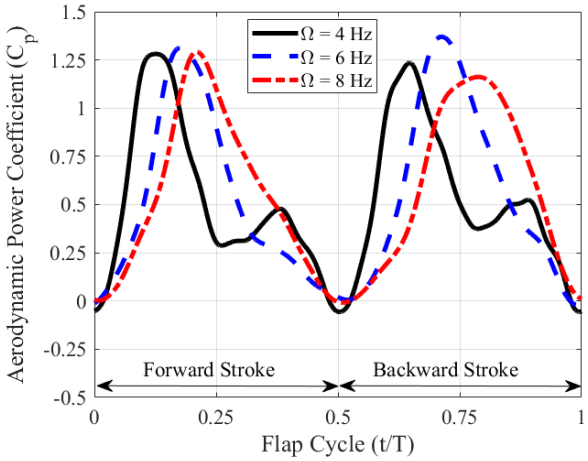

Figure 4.21: Aerodynamic power coefficient time history over a flap cycle

4.4 Summary

The goal of the present study was to validate the predictive capability of the coupled CFD/CSD solver for the case of a chord-wise flexible flapping wing in hover. Experiments were conducted on a flexible flapping wing at flap frequencies of 4 Hz, 6 Hz and 8 Hz. PIV experiments were conducted to investigate the flowfield in the immediate vicinity of the wing's surface at particular span locations and instances of the flap cycle. VICON motion tracking experiments were performed to measure passive wing deformation throughout a flap cycle. The model analyzed by the coupled aeroelastic solver was constructed to replicate the kinematics, geometry and structure of the wing used during experimentation. Results from the experiments were utilized in validating the coupled CFD/CSD analysis by comparing the aerodynamic velocity and vorticity fields, wing trailing edge deflections over time and instantaneous pitch angle variation over time. The overall conclusions are as follows:

i. The coupled CFD/CSD model was able to predict the prominent aerodynamic flow features for the flexible flapping wing cases analyzed. The aeroelastic analysis is able to predict the general size, location and temporal evolution of the LEV for the various spanwise locations analyzed. There were some discrepancies in the trajectory and coherence of the shed trailing edge vortex or trailing edge shear layer between the PIV and computational results. Overall, the coupled CFD/CSD results showed good agreement with the experimental PIV data.

ii. The coupled aeroelastic analysis was able to adequately predict the passive wing deformations due to aerodynamic and inertial forces. High frequency oscillations present in the experimental results were adequately captured in the computational results. At higher flap frequencies, there is a notable phase shift between the flapping motion and trailing edge deflection response. Additionally, there is a slight discrepancy in trailing edge deflection that is more noticeable during the backward stroke as opposed to the forward stroke. Instantaneous pitch angle variation results match well between the measured and predicted values. As expected, peak pitch angle magnitude increased with increased flap frequency. For a given flap frequency, the wing pitch angle variation was nearly uniform across the span of the wing throughout the flap cycle.

iii. The computational analysis was used to compare the lift, drag and aerodynamic power coefficient time histories for the flap frequencies tested. Peak lift coefficient values increased with increased flap frequency. Peak lift coefficient

values occur slightly before midstroke while peak drag coefficient values occur at approximately midstroke. Peak aerodynamic power coefficients are nearly the same for all flap frequencies tested, however, the temporal variation differs between the cases tested. The 4 Hz case exhibits a double peak behavior while the 6 Hz and 8 Hz cases exhibit a single peak behavior within a given flap stroke.

Chapter 5 Anisotropic Flexible Wing – Validation Study

The work presented in this chapter seeks to analyze the aerodynamic force-time histories and passive structural deformation of an anisotropic MAV-scale flapping wing in hover via force and motion capture experiments. In this case, an anisotropic wing is one where the wing properties (mass distribution, structural stiffness, material composition, etc.) vary throughout the wing due to its structural design. The predictive capability of the coupled CFD/CSD model is assessed against instantaneous aerodynamic force and power measurements in addition to wing deformation measurements using a motion tracking system on a structurally characterized, highly flexible flapping wing. Focus is on investigating the lift, drag and aerodynamic power of the wing as well as passive wing deformations over time.

5.1 Experimental Setup

5.1.1 Test Wing and Flapping Mechanism

The wing in the experimental tests was actuated using a custom made four-bar crank-rocker mechanism. The mechanism was designed to produce a near sinusoidal, one degree of freedom flapping motion. A kinematic analysis described in Ref. [165] was applied correctly size the mechanism linkages. This same mechanism was described in Section 3.4 and is referred to for descriptions of the mechanism linkage lengths as well as the expected flap kinematics. One major change in the flap mechanism from the studies discussed in Section 3.4 and the mechanism used in this study is in the rocker link. The rocker link needed to be modified to allow for the

attachment of a force transducer. Figure 5.1 provides a CAD drawing illustrating the flap mechanism used throughout this study.

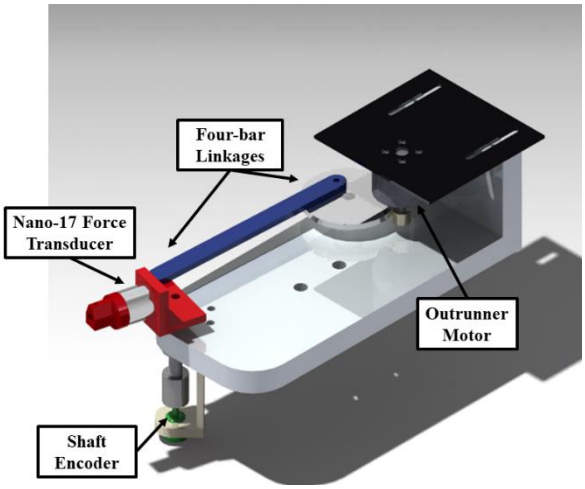

Figure 5.1: CAD image of custom-built four-bar flapping mechanism

A picture of the flexible wing tested can be seen in Fig. 5.2a. The geometry and structural design of the test wing is inspired by the flapping wing MAV developed by Coleman et al. [52]. However, for the tests conducted, the wing was uniformly scaled, increasing the dimensions of the wing geometry by 50%. The test wing is composed of two carbon fiber spars with one running along the wing leading edge (leading edge spar) and the other across the wing plane (cross spar). The leading-edge spar has a diameter of 1.6 mm (0.063 in) and the cross spar has a diameter of 0.5 mm (0.0197 in). A third spar, composed of plastic shim stock, supports the wing root (root spar) and has a length of 7.70 cm (3.03 in), a width of 5.0 mm (0.197 in) and a thickness of 0.762 mm (0.030 in). The leading edge, cross and root spars make up the wing frame which is covered with a foam mesh fabric with a thickness of 0.8 mm (0.0315 in). This lightweight, flexible, low aspect ratio wing has a length of 19.05 cm (7.5 in), a mean chord length of 5.26 cm (2.07 in), a wing area of 100.13 cm^2 (15.52 in^2) and an aspect

ratio of 3.62. The wing has a maximum thickness of 1.6 mm (0.063 in) due to the thickness of the leading-edge spar. The wing has a bilinear taper with the taper ratio transition point at 14.71 cm (5.79 in) along the length of the wing. The chord length values at the wing root, transition point and wing tip are 7.70 cm (3.03 in), 4.55 cm (1.79 in) and 0.28 cm (0.11 in) respectively. A schematic of the flapping wing with dimension can be seen in Fig. 5.2b. There is a 5.08 cm (2.0 in) offset between the flapping axis of rotation and the wing root. All tests were carried out at a constant flap stroke amplitude of 80° at various flap frequencies. Since the tests were conducted in hover, this results in a reduced frequency (k) of 0.156 for all cases. Note that reduced frequency is defined as $k = \frac{2\pi f \bar{c}}{2V_{tip}}$ where f is the flap frequency, $\bar{c}$ is the mean chord length and V_{tip} is the maximum tip velocity of the wing.

The structural properties of the various wing components were determined using static deflection and torsion tests. The mass of the wing components was measured and recorded during fabrication. Note that it is assumed that the mass of a particular structural component is assumed to be distributed uniformly over that component. A list of the relevant wing geometric and structural properties can be found in Table 5.1.

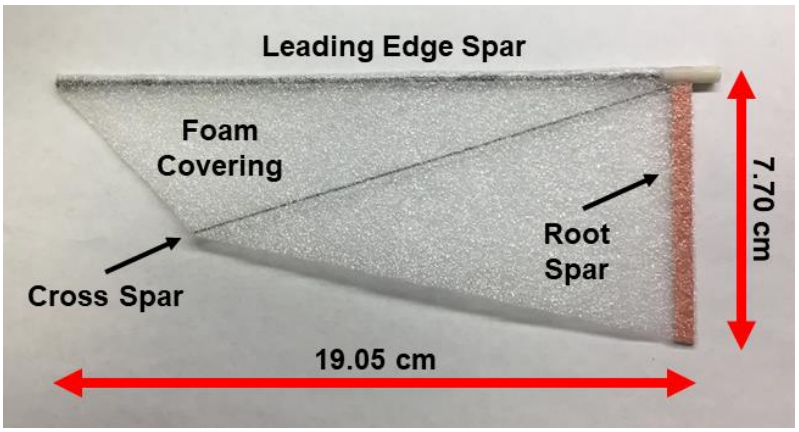

(a) Experimental test wing

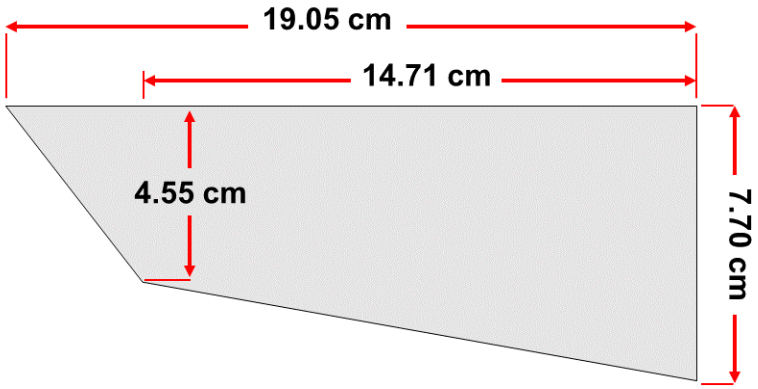

(b) Schematic of wing dimensions

Figure 5.2: Picture of experimental test wing and schematic depicting wing dimensions

Table 5.1: Experimental wing structural properties

Wing span, *b*	19.05 cm
Mean wing chord, $\bar{c}$	5.26 cm
Membrane thickness, *h*	0.80 mm
$EI_{root\ spar}$	6.24×10^{-4} N-m^2
$GJ_{root\ spar}$	8.27×10^{-4} N-m^2
$EI_{cross\ spar}$	3.27×10^{-4} N-m^2
$GJ_{cross\ spar}$	2.42×10^{-4} N-m^2
$EI_{leading\ edge\ spar}$	4.33×10^{-2} N-m^2
$GJ_{leading\ edge\ spar}$	3.21×10^{-2} N-m^2
$E_{foam\ sheet}$	1.83×10^{6} N-m^{-2}
$\nu_{foam\ sheet}$	0.3
$\rho_{carbon\ fiber}$	1433.0 kg-m^{-3}
$\rho_{plastic}$	1505.0 kg-m^{-3}
$\rho_{foam\ sheet}$	34.0 kg-m^{-3}

5.1.2 Force Measurement Setup and Test Procedure

Figure 5.3 provides a picture showing the test wing attached to the flapping mechanism. The forces and moments produced by the wing during actuation were measured using an ATI Nano-17 force/torque sensor. The ATI Nano-17 is a miniature six-component balance with a resolution of ±0.318 gram-force and a resonant frequency of 7200 Hz. The force balance is mounted at the wing root to capture the total forces and moments produced by the wing. The flap angle at a given instance of the flap cycle is measured using a US Digital MA3 miniature absolute magnetic shaft encoder with a resolution of ±0.7°. The measurements from the Nano-17 are output to an interface power supply (IFPS) box which is connected to a National Instruments USB DAQ system (NI USB-6251). All measurements were recorded at a sample frequency of 1000 Hz. The voltage signals from the force transducer are recorded and written to file in LabVIEW 2016. The voltages are converted to the six forces and moments using a calibration matrix provided by the manufacturer in MATLAB.

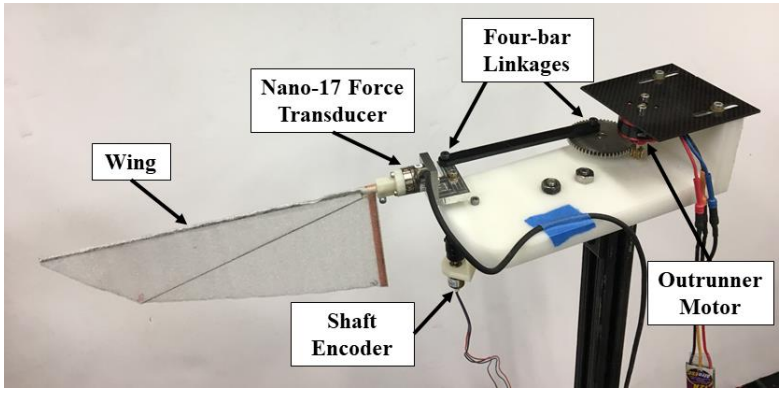

Figure 5.3: Test wing and flapping mechanism with Nano-17 force transducer

The goal of the force studies was to measure the instantaneous aerodynamic forces and moments generated by the wing over the course of a flap cycle. However,

when the wing is flapped in air, both aerodynamic and inertial forces are generated. In certain instances, the magnitude of inertial forces may be equal to or exceed that of the aerodynamic forces and can significantly contaminate the results. Inertial force subtraction is a technique that can help to isolate the aerodynamic forces from the total force measurements conducted in air.

The force measurement procedure can be thought of in three parts. First, the wing is flapped in air and the resulting force and moments are measured. In air, the forces are composed of both aerodynamic and inertial loads such that:

$$F_{air} = F_{aero,wing} + F_{inertial,wing} + F_{aero,balance} + F_{inertial,balance}$$
$$F_{air,balance} = F_{aero,balance} - F_{inertial,balance} \quad (5.1)$$

where F_{air} is the force measured by the force transducer and $F_{aero,wing}$ and $F_{inertial,wing}$ are the aerodynamic and inertial forces produced by the wing respectively. Since the force balance is actuated along with the wing, it also contributes to the forces measured. $F_{aero,balance}$ and $F_{inertial,balance}$ are the aerodynamic and inertial forces produced by the force balance. Separate tests were conducted without the wing attached to isolate the forces produced by the balance. During the tests, the flap angle is measured in addition to the forces and moments. Several flap cycles are measured during a given test and are averaged representing the results of 1 trial. An example of such averaging can be seen in Fig. 5.4. Each trial is composed of an average of 40 flap cycles.

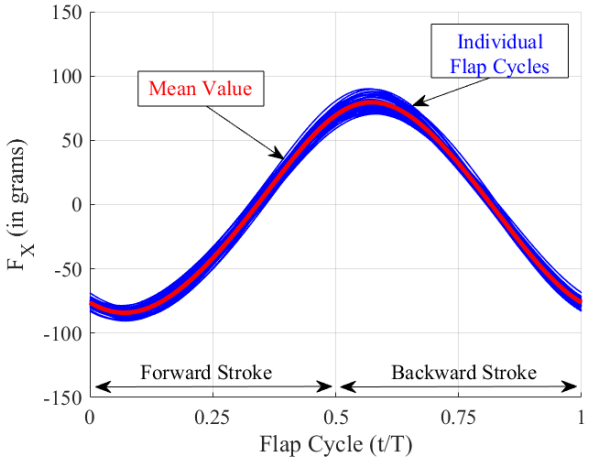

Figure 5.4: Example of averaging flapping wing forces over multiple flap cycles

Second, the flapping wing force tests are repeated in vacuum to remove aerodynamic forces. The measured force is said to be solely composed of inertial forces such that:

$$F_{vacuum} = F_{inertial,wing} + F_{inertial,balance}$$
$$F_{vacuum,balance} = F_{inertial,balance} \quad (5.2)$$

Note that separate tests were conducted in vacuum without the wing attached to measure the inertial forces produced by the balance. Ideally, for the inertial forces measured in vacuum to match those measured in air, the wing needs to undergo the same flap kinematics and deformations in air and vacuum. This isn't entirely possible for a flexible wing subject to passive wing deformations due to inertial and aerodynamic forces. However, studies by Combes and Daniel [169] found that aerodynamic forcing may contribute little to the wing deformations of a flexible flapping wing. In their work, hawkmoth wings were flapped in air as well as in helium which is 15% as dense as air. Results showed that there was only a slight difference in the wing deformation patterns even though there was an 85% reduction in aerodynamic

forcing when the wings were flapped in helium as opposed to air. Thus, even with the absence of the aerodynamic forces, the inertial loads should produce wing deformations similar to those experienced by the wing in air.

Like in the first part, the flap angle is measured and a total of 40 flap cycles are averaged for a given trial. Tests were conducted in a custom built vacuum chamber shown in Fig. 5.5a. Figure 5.5b provides an image of the flapping wing setup in the vacuum chamber. During testing, the air pressure in the chamber was brought down to 0.15 psi which results in approximately 99% vacuum.

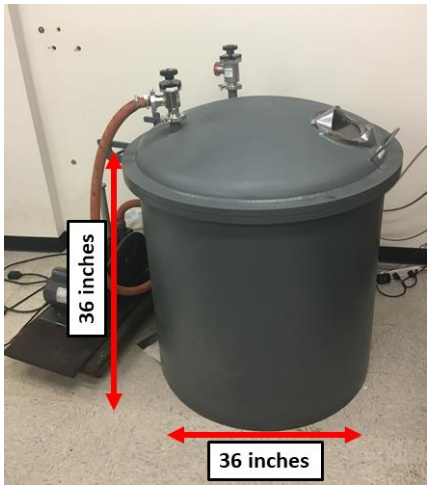

(a) Vacuum chamber used during testing

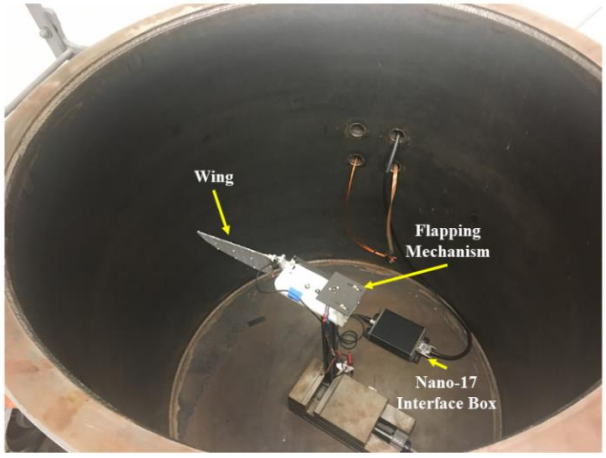

(b) Flapping mechanism inside vacuum chamber

Figure 5.5: Images of flapping wing setup in the vacuum chamber

In the third part, the inertial forces measured in vacuum are subtracted from the total forces measured in air to isolate the aerodynamic forces. The aerodynamic forces produced by the wing are isolated via the follow relation:

$$F_{aero,wing} = F_{air} - F_{vacuum} - \left(F_{air,balance} - F_{inertial,balance}\right) \qquad (5.3)$$

To accurately calculate the instantaneous aerodynamic forces and moments, the data measured in air and vacuum was synchronized such that the wing is at the position within the flap stroke between the air and vacuum tests. The plots in Fig. 5.6 demonstrate how the aerodynamic force-time histories are calculated for a given trial. Four different flap frequencies were tested between 2 – 8 Hz in increments of 2 Hz. The aerodynamic force and moment time history results presented for a given flap frequency are an average of 10 separate trials where each trial is composed of data averaged over 40 flap cycles. Table 5.2 provides a list of the relevant in test parameters and flow conditions during testing. Note that when determing the modified aeroelastic scaling parameter, the calculated natural frequency of the first chordwise bending mode is 162.4 rad/s. Figure 5.7 shows plots of the measured flap angle over time in air for the flap frequencies tested.

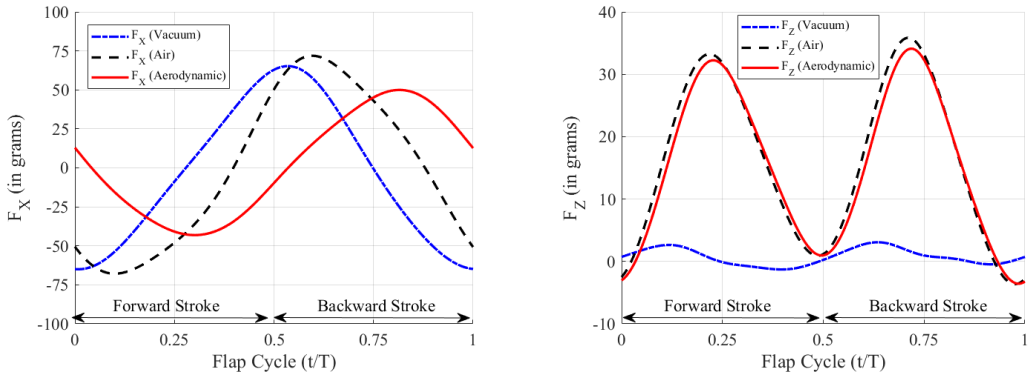

(a) F_X force time history (b) F_Z force time history

Figure 5.6: Example of inertial force subtraction for instantaneous forces

Table 5.2: List of test parameters and flow conditions

Parameters	Value
Flap frequency, f	2 – 8 Hz, Δf = 2 Hz
Flap amplitude, ϕ_{amp}	40°
Maximum Tip Velocity, (V_{tip})	2.11 – 8.47 m-s^{-1}
Reduced Frequency, $\left(\boldsymbol{k = \frac{2\pi\Omega\bar{c}}{2*V_{tip}}}\right)$	0.156
Fluid density, ρ_{air}	1.23 kg-m^{-3}
Reynolds number, $\left(\boldsymbol{Re = \frac{\rho V_{tip}\bar{c}}{\nu}}\right)$	6,900 – 27,600
Scaling parameter, $\left(\boldsymbol{\pi_1 = \frac{\omega_n^2 * m}{\rho * V_{tip}^2 * b}}\right)$	2.05 – 33.01

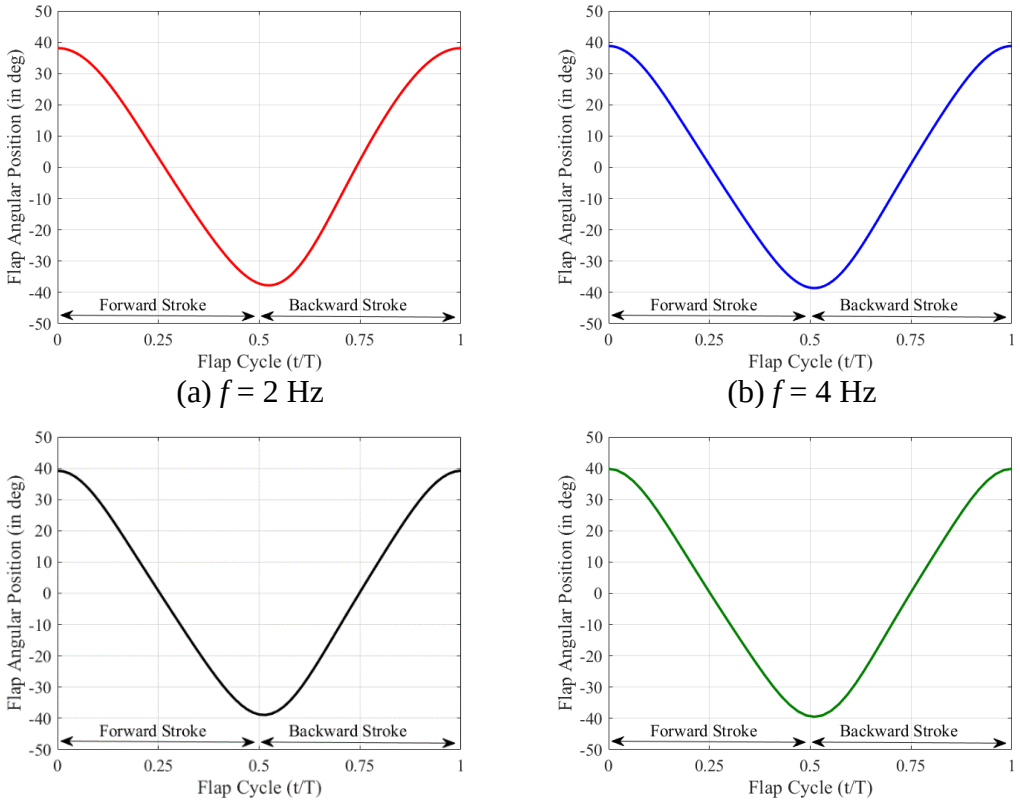

(a) f = 2 Hz (b) f = 4 Hz

(c) f = 6 Hz (d) f = 8 Hz

Figure 5.7: Plot of measured flap angle over time for the flap frequencies tested

5.1.3 VICON Motion Capture Setup

VICON motion capture was utilized to determine the structural properties of the wing, conduct static deflection tests as well as measure the passive wing deformations due to inertial and aerodynamic loading during flapping. The motion capture images were acquired using VICON T40-S cameras which have a 4 Megapixel resolution with a maximum frame rate of 500 Hz at full resolution. When performing the static and dynamic flapping wing tests, the six cameras were run at 400 frames per second (fps) to accurately capture the wing deformation over the course of a flap cycle. Figure 5.8a provides a picture of the VICON motion capture test setup. Reflective markers were placed along the wing chord line at 0%, 25%, 50% and 75% span to capture the motion

and determine the deflection along the wing trailing edge and wing spars. Additionally, a reflective marker was placed at the wing tip to track the motion at that location on the wing. Figure 5.8b depicts the experimental test wing with the reflective markers in place. The cameras were arranged to ensure that at least two cameras are able to view the reflective markers at any point in the flap stroke. Similar to the force measurement experiments, tests were carried out at flap frequencies of 2, 4, 6 and 8 Hz. The measurements recorded during the motion capture tests were post-processed using VICON Nexus 1.8.5.

(a) VICON motion capture setup

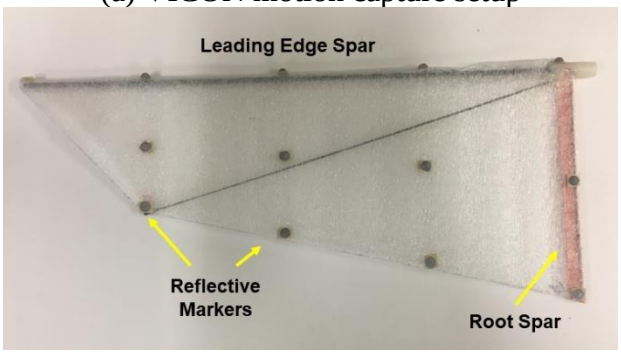

(b) Flapping wing with reflective markers

Figure 5.8: VICON motion capture setup and flapping wing with reflective markers

5.2 Computational Setup

The coupled CFD/CSD aeroelastic analysis was used to numerically model the flapper wing. An overset mesh system was utilized to model the wing geometry and flow environment within the CFD solver. A C-O topology, structured body-fitted mesh was used to represent the wing and a Cartesian background mesh was used to model the surrounding wake. The wing geometry of the CFD mesh was designed match that of the test wing shown in Fig. 5.2. Overall, the wing aspect ratio was set to 3.62 (same as in the experiment) and a thickness-to-chord ratio of 3.0% was used. The wing mesh was made up of approximately 1.28 million grid points with 128×91×75 grid points in the wrap-around, spanwise and normal directions respectively. Of the 187 points in the wrap-around direction, 147 are used to form the wing surface and the remaining points make up the wakecut region of the wing mesh.

Grid points were clustered near the leading edge, trailing edge, wing root and wing tip to more highly resolve regions of the wing where vortical or highly separated flow is expected to develop. The background cartesian mesh is composed of 128×98×148 nodes in the x, y and z directions respectively. Farfield boundary conditions are applied 20 chord lengths away from the origin of the background mesh. The background mesh grid points are clustered with the immediate vicinity swept out by the wing to improve spatial resolution of the shed wake. A picture of the wing and background meshes can be seen in Fig. 5.9a and Fig. 5.9b respectively.

The structural model is made up of 12 × 7 elements in the spanwise and chordwise directions respectively resulting in a total of 84 shell elements within the model. A total of 26 beam elements are used to model the wing spars (leading-edge,

root and cross spars. Note that 12 beam elements are used in modeling the leading-edge spar while 7 beam elements are used to model the root spar and cross spar. A picture of the node points making up the wing structural model can be seen in Fig. 5.9c. Black solid lines are used in Fig. 5.9c to represent the wing spars. The structural parameters from the experiment, shown in Table 5.1, were implemented in the structural model were applicable.

When the wing is placed within the flapping mechanism, the wing root is offset from the flapping axis by 5.08 cm ($0.97\bar{c}$) and this offset is properly represented within the CFD and CSD models. The flap angle measured during experimentation is prescribed to the aeroelastic model during the simulation. At the start of the simulation, the wing is at a 90° pitch angle such that the wing chord line is parallel to the z-axis. The wing starts at the beginning of the forward stroke with the flap motion being prescribed about the flap axis such that wing flapping occurs in the xy-plane.

Overall, the simulation was run for 3 flap cycles with 2880 iterations per flap cycle resulting in a timestep size of $4.34\times10^{-5} - 1.74\times10^{-4}$ s used in the structural model. The value of the timestep is dependent on the flap frequency being tested ranging from 2 Hz to 8 Hz. The timestep in the CFD model was set so that the positional change in the wings match between the CFD and structural models. A total of 8 Newton sub-iterations were used in the CFD solver to minimize factorization errors and improve solution accuracy. In the CSD solver, MBDyn's original A/L stable linear multistep algorithm was used with a spectral radius of 0.6 and the residual tolerance was set to 1.0×10^{-3}.

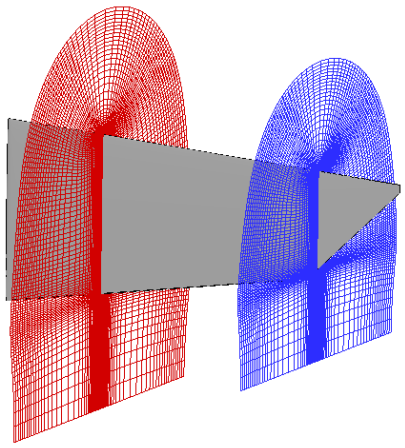

(a) C-O topology CFD mesh of test wing

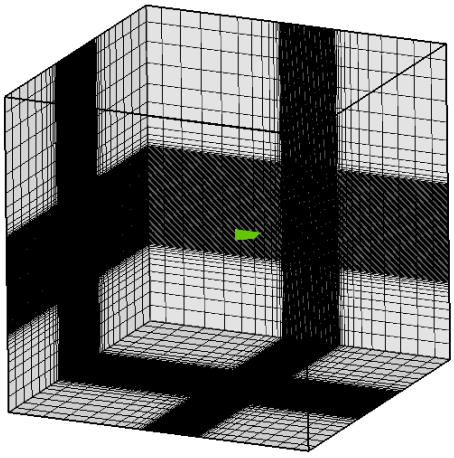

(b) Cartesian background mesh

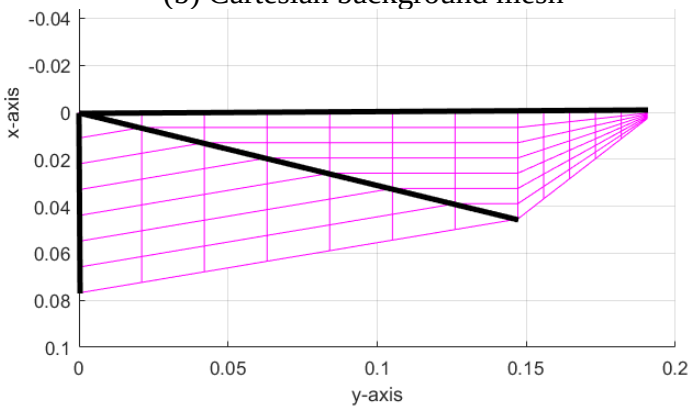

(c) Grid of CSD model node points

Figure 5.9: Images of CFD mesh system and CSD model used in aeroelastic analysis

5.3 Results Comparison

5.3.1 Static Wing Deflection Comparison

The computational model was first validated with experimental data through a series of static deflection tests. The VICON motion capture system described in the Section 5.1 was used to measure the static deflections of the wing under various point loads. During experimentation, the wing was clamped at the root of the leading edge. Loads were applied at the trailing edge of the 0% span location and the 75% span location. Note that the trailing edge of the 0% and 75% span locations correspond to the end of the root spar and cross spar respectively. Loads applied to the root spar were varied from 0.0 – 10.0 grams and loads applied to the cross spar were varied from 0.0 – 5.0 grams.

Computationally, only the CSD solver (MBDyn) was used in predicting the wing deflections with the wing model being under the same load and boundary conditions as in the experiment. Comparisons were made between the experimentally measured results and those predicted by the MBDyn. Images from the static deflection tests can be seen in Figure 5.1.

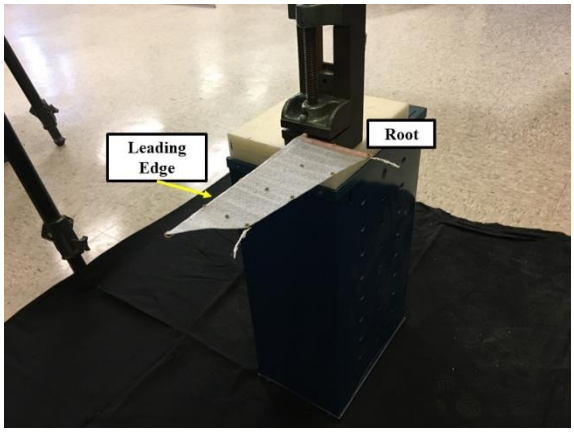

(a) Test wing under no load

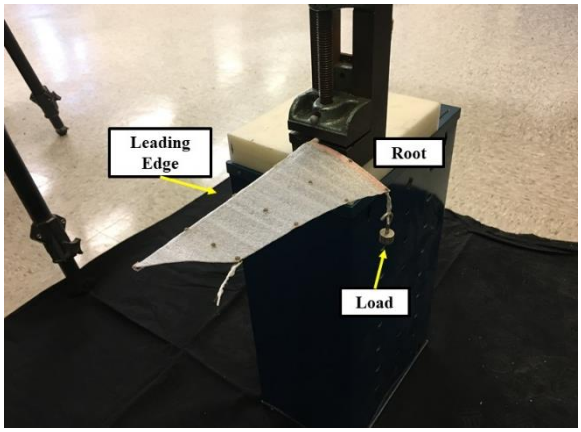

(b) Root spar loaded, 10 gram load

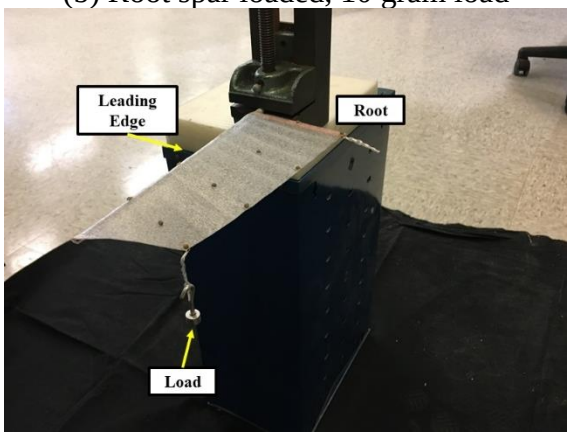

(c) Cross spar loaded, 5 gram load

Figure 5.10: Images of experimental static deflection tests

Figure 5.11 provides deflection vs load plots comparing the experimental and computational results for the test wing. The data presented represents the vertical displacement of the nodes along the wing trailing edge at 0%, 50% and 75% span with respect to the unloaded condition The data in Fig. 5.11a is from the root spar loaded case and the data in Fig. 5.11b is from the cross spar loaded case. The symbols represent the experimental data while the computational results are shown via the dashed lines. Overall, there is good agreement between the experimental and computational deflection versus load curves.

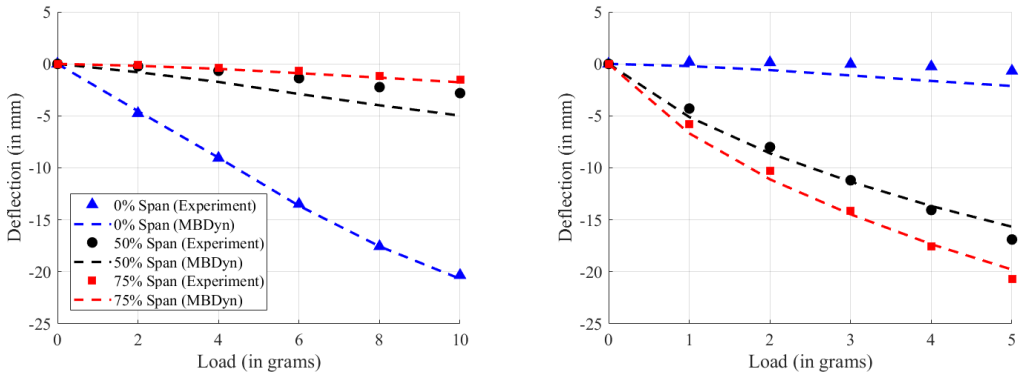

(a) Root spar load case (b) Cross spar load case

Figure 5.11: Experimental and computational deflection vs load curves

Figure 5.12 shows the full wing deformation under static loading for both the measured and predicted results. The experimental data is represented by the red markers and blue polygons and the computational data is presented by the green gridded quadrilaterals. Each plot shows the maximum applied load for the root spar loaded case (Fig. 5.12a) and the cross spar loaded case (Fig. 5.12b). Qualitatively, there is good agreement between the predicted and measured data.

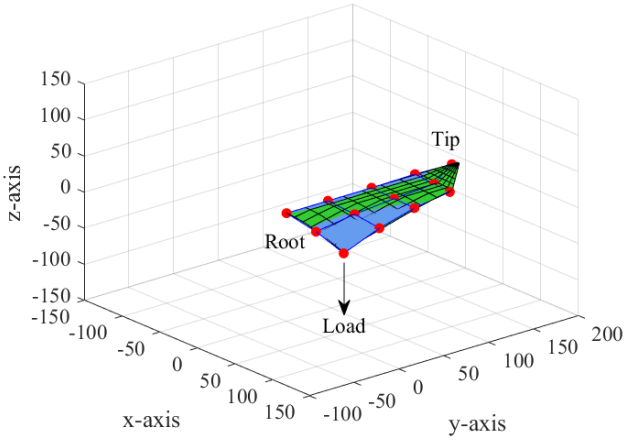

(a) Root spar loaded case

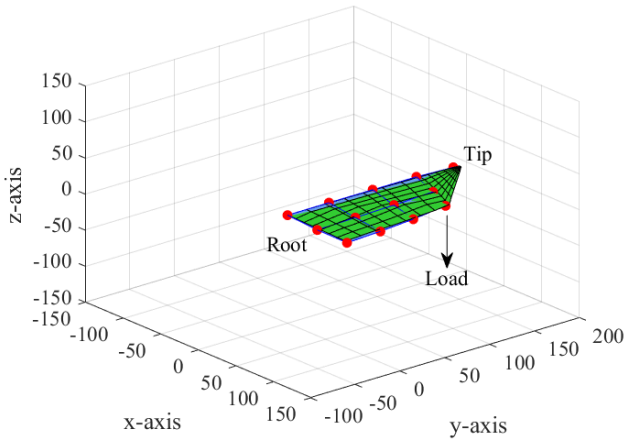

(b) Cross spar loaded case

Figure 5.12: Full wing deformation comparison under static load

5.3.2 Aerodynamic Force and Power Time History Comparison

This section focuses on comparing the measured and predicted aerodynamic forces produced by the wing. The experimentally measured time-averaged as well as instantaneous lift force values over the course of a flap cycle are compared with the predicted results from the coupled aeroelastic analysis. Before discussing the results, it is important to present the reference frame in which the data is to be presented. Figure 5.13 provides a schematic of the coordinate reference frames to be used throughout this study. The fixed, right-handed global reference frame is defined by the x, y and z-axes with the flap axis coinciding with the z-axis. A body reference frame, denoted by the x′-axis and y′-axis, rotates with the flapping wing. Note that the z′-axis coincides with the z-axis and is not labeled for clarity. The body reference frame moves with the wing such that the y′-axis remains along the wing span of the undeformed wing as depicted in Fig. 5.13. The forward stroke is defined as the portion of the flap cycle during which

negative rotation about the z-axis (i.e. flap axis) occurs, while the backward stroke is when positive rotation about the z-axis occurs.

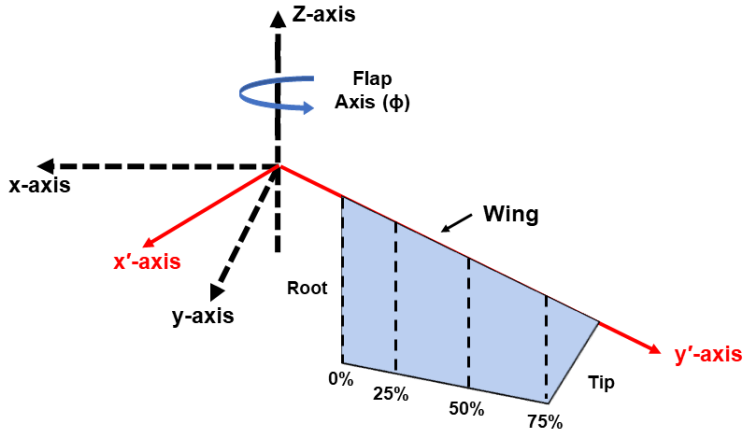

Figure 5.13: Reference coordinate system of the test wing

Figures 5.14 – 5.17 contains plots comparing the measured and predicted aerodynamic lift and drag force-time histories acquired from the experiment and CFD/CSD analysis. Figures 5.14, 5.15, 5.16, and 5.17 correspond to the 2, 4, 6 and 8 Hz cases respectively. Note that in each of those cases, Fig. (·)a is the lift force-time history and Fig. (·)b is the drag force time history. The horizontal axis represents the time over one flap cycle nondimensionalized by the flap period (T). Positive lift is said to act in the positive z-direction. Drag force acts in opposition to wing motion. Negative drag force does not denote thrust but instead signals a change in the direction of the drag vector due to a change in direction of wing flapping.

For the 2 Hz case, the lift generated by the wing (Fig. 5.14a) is nearly negligible with a peak lift force of approximately 0.5 grams. The predicted lift force-time history matches well with that measured during the experiment despite the relatively low magnitude of lift generated. The drag force variation (Fig. 5.14b) is nearly sinusoidal

with the peak drag during the backward stroke being slightly greater than the peak drag during the forward stroke. The magnitude of the predicted drag force trend is slightly less than that of the experimentally measured drag force trend.

At a flap frequency of 4 Hz, the magnitude of lift and drag produced increases as expected. In Fig. 5.15a, measured lift time history exhibits a more distinct double peak behavior which is predicted by the CFD/CSD solver. The measured and predicted trends match well over the course of the forward stroke with the peaks in lift matching very closely. However, the predicted peak in lift during the backward stroke is slightly lower in magnitude compared to experimental results. Similar to the 2 Hz case, the drag force trend (5.15b) is sinusoidal and the peak magnitude is underpredicted by the coupled CFD/CSD analysis.

The instantaneous aerodynamic force time histories at 6 Hz (Fig. 5.16) and 8 Hz (Fig. 5.17) exhibit similar trends as in the 4 Hz case. Both the lift and drag trends predicted by the coupled CFD/CSD solver match well with the experimental results. However, the peak magnitude in lift and drag are underpredicted. Note that the difference in underprediction is greater for the drag results in comparison to the lift results. This is due to the large inertial loads acting in the in-plane direction as opposed to the out-of-plane direction. Note that the referred plane is the flap plane. Lift is the primary force acting out-of-plane with negligible inertial loads acting in that direction. However, inertial loading is high in the in-plane which can contaminate the drag results. Even with inertial force subtraction, eliminating all of the inertial loads in the in-plane direction proves difficult.

Aside from the 2 Hz case, the lift force trends show a double peak lift behavior. During the first half of a flap stroke, there is a steep linear increase in lift up to a peak which typically occurs at approximately t/T = 0.1 when analyzing the forward stroke and t/T = 0.6 for the backward stroke. After the peak in lift force, there is a steady, more shallow decrease in lift until the end of the flap stroke (i.e. t/T = 0.5 or 1.0). For all cases, the peak in instantaneous aerodynamic loading is higher during the backward stroke than the forward stroke. This was found to be due to the nature of the flap kinematics in which the flap angular velocity and acceleration was slightly higher during the backward stroke in comparison to the forward stroke.

Figure 5.18 provides plots of mean lift and drag versus flap frequency. There is a good agreement in the trend of mean lift versus flap frequency. As expected, the mean lift force varies quadratically with flap frequency. Mean drag is underpredicted by coupled CFD/CSD analysis.

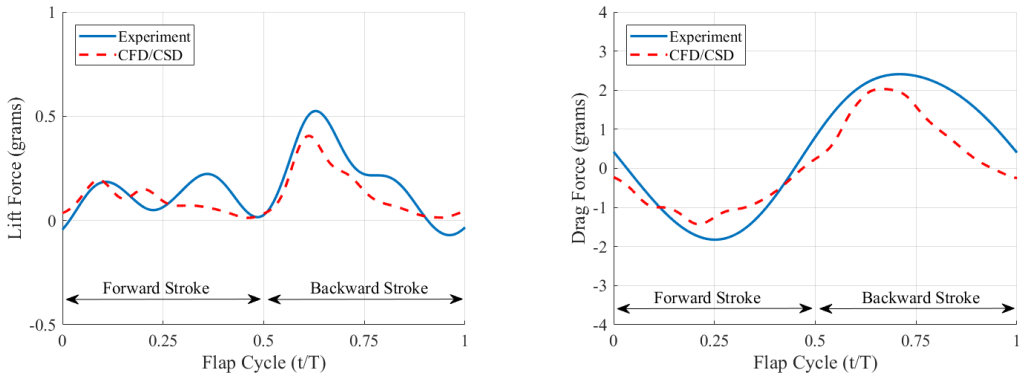

(a) Lift force vs time (b) Drag force vs time

Figure 5.14: Comparison of experimental and CFD/CSD force-time histories (f = 2 Hz)

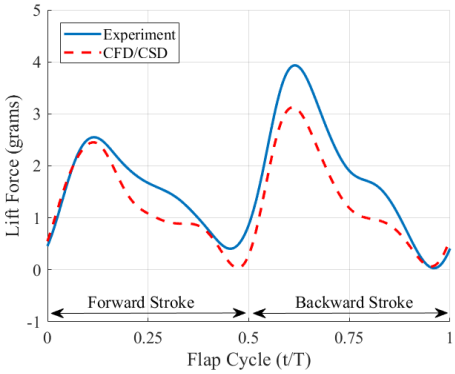

(a) Lift force vs time

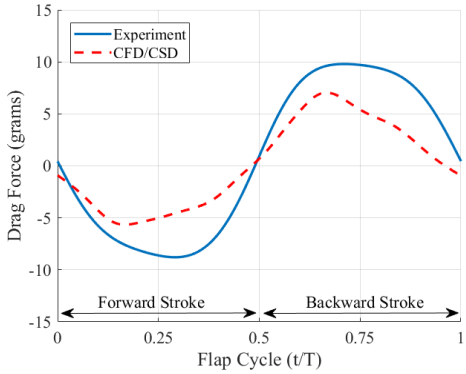

(b) Drag force vs time

Figure 5.15: Comparison of experimental and CFD/CSD force-time histories (f = 4 Hz)

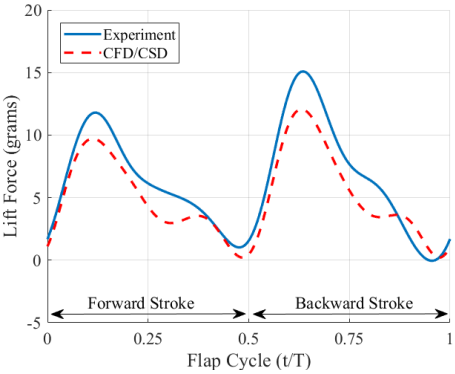

(a) Lift force vs time

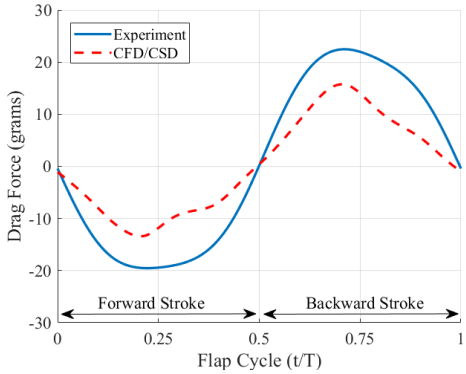

(b) Drag force vs time

Figure 5.16: Comparison of experimental and CFD/CSD force-time histories (f = 6 Hz)

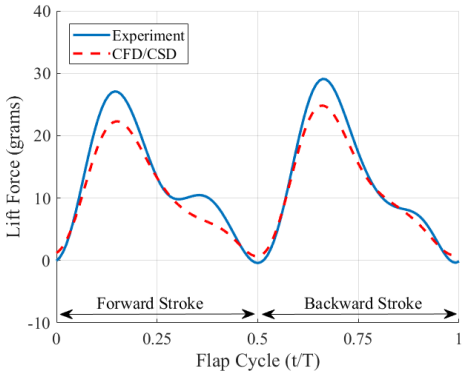

(a) Lift force vs time

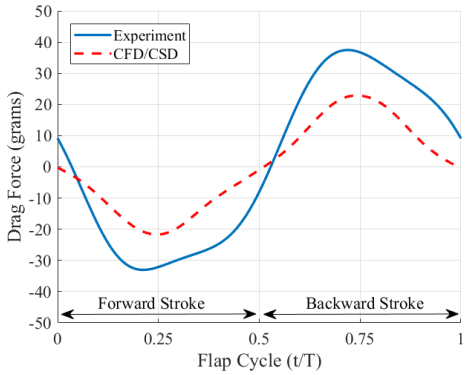

(b) Drag force vs time

Figure 5.17: Comparison of experimental and CFD/CSD force-time histories (f = 8 Hz)

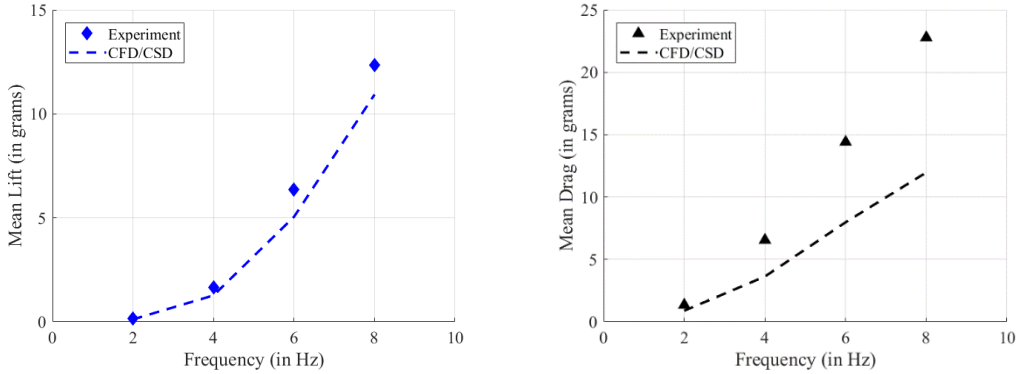

(a) Mean lift vs flap frequency (b) Mean drag vs flap frequency

Figure 5.18: Comparison of experiment and CFD/CSD mean aerodynamic force vs flap frequency

Using the force and moment data measured during the force experiments, the aerodynamic power could be calculated. From the experimental data, aerodynamic power is calculated using the following equation:

$$P(t) = T_Z(t) * \dot{\phi}(t)$$
$$T_Z(t) = M_Z(t) + r_{offset} * D(t) \quad (5.4)$$

where P(t) is the aerodynamic power, $T_Z(t)$ is the torque acting about the flap axis and $\dot{\phi}(t)$ is the flap angular velocity. The torque is composed of the aerodynamic moment $M_Z(t)$ and the moment due to the drag force D(t) with a moment arm of r_{offset}. The value of r_{offset} is the distance between the wing root and the flap axis which in this case is the flap axis offset value of 5.08 cm (2 in). To calculate aerodynamic power within the aeroelastic analysis, the dot product of the local aerodynamic force vector with the local velocity vector is summed for every grid point on the wing surface.

Figure 5.19 provides plots of instantaneous aerodynamic power over a flap cycle. Overall, there is good agreement between the measured and predicted peaks in aerodynamic power. However, there are some discrepancies in the variation of

aerodynamic power especially at lower flap frequencies. This is most likely due to the low aerodynamic forces acting on the wing at low flap frequencies. Thus, the inertial forces play a more significant role in contaminating the experimental results. At higher flap frequencies, the experimental and computational variations in aerodynamic power exhibit better agreement in temporal variation as well as peak magnitude.

When comparing the results at 6 Hz and 8 Hz, there is a notable change in the instantaneous aerodynamic power trends. During the 6 Hz case, the aerodynamic power reaches a peak early in the flap stroke. After that peak, aerodynamic power begins to decrease. However, after mid-flap stroke ($t/T = 0.25$ or $t/T = 0.75$), there is secondary peak in aerodynamic power before the value descends to zero at the end of the flap stroke. This behavior is approximately captured by the coupled CFD/CSD analysis as a plateau in aerodynamic power as opposed to a distinct secondary peak. This secondary peak is not seen at 8 Hz with the variation in aerodynamic power exhibiting a single peak for a given flap stroke. Further investigation in required to determine a possible mechanism response for this behavior.

For all flap frequencies, the peak in aerodynamic power is greater during the backward stroke as opposed to the forward stroke. This is thought to be due to slight differences in the flap kinematics between the forward and backward strokes that were discussed when analyzing the force-time history trends.

Figure 5.2 a provides plots of the mean aerodynamic power versus flap frequency. In addition, a plot of lift-to-power ratio versus flap frequency is shown in Fig. 5.2 b. In calculating lift-to-power ratio, the lift values were acquired from the data in Fig. 5.18a. There is good agreement between measured and predicted mean

aerodynamic power versus flap frequency. When analyzing lift-to-power ratio, there is significant discrepancy between the experimental and computational results at 2 Hz. This is possibly due the low aerodynamic lift and power at that flap frequency. For higher flap frequencies, the predicted results are slightly lower in magnitude than those measured experimentally. In both the experiment and CFD/CSD analysis, the lift-to-power ratio appears to plateau for the 6 Hz and 8 Hz flap frequencies.

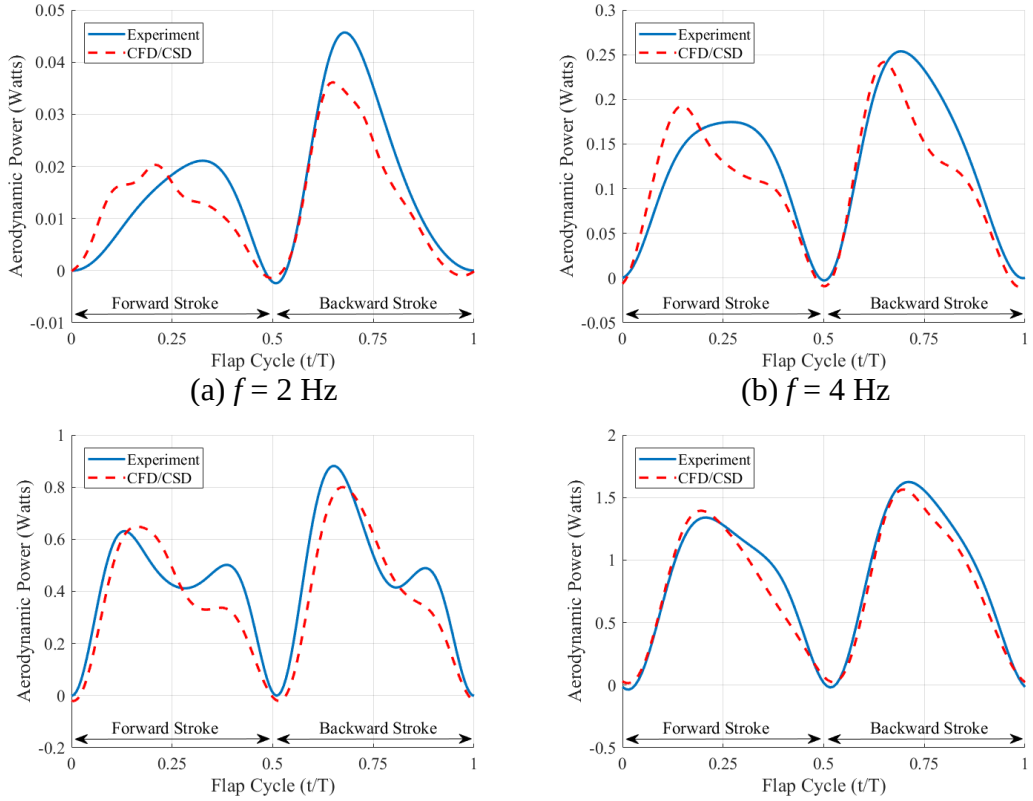

(a) f = 2 Hz (b) f = 4 Hz

(c) f = 6 Hz (d) f = 8 Hz

Figure 5.19: Aerodynamic power versus time (All flap frequencies)

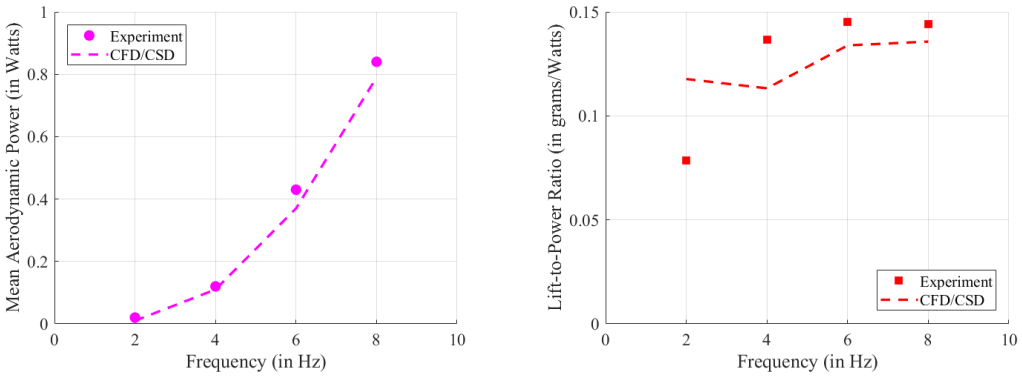

(a) Mean aerodynamic power vs flap frequency

(b) Lift-to-power ratio vs flap frequency

Figure 5.20: Mean aerodynamic power and lift-to-power ratio vs flap frequency

5.3.3 Wing Deformation Comparison

Figure 5.21 compares the experimental and computational wing trailing edge (TE) deformations for the 2 Hz (Fig. 5.21a), 4 Hz (Fig. 5.21b), 6 Hz (Fig. 5.21c) and 8 Hz (Fig. 5.21d) flap frequency cases. Comparisons of the passive wing deformations are made at the wing's trailing edge because that part of the wing experiences the greatest deformation over the flap cycle. The results shown are for 0%, 25%, 50% and 75% span. The percent span locations are with respect to the wing root. The curves in the plots represent the x-position of the specific point on the trailing edge with respect to the global reference frame shown in Fig. 5.13. Note that the experimental results are an average of 40 flap cycles for the particular flap frequency presented, while the computational results are taken from the last flap cycle of the coupled aeroelastic simulation.

The overall trend in trailing edge displacement is captured well by the aeroelastic analysis. For the 2 Hz and 4 Hz flap frequency cases, the measured and predicted temporal variations in trailing edge position nearly lay on top of one another

at all four spanwise locations of the wing. However, at these lower flap frequencies, the magnitude of wing deformation is relatively low.

At the higher flap frequencies tested (6 Hz and 8 Hz), the wing deformations are larger to the increased inertial and aerodynamic forces acting on the wing. The CFD/CSD aeroelastic analysis tends to slightly overpredict the peak TE displacement further outboard along the span. However, the predicted peak in displacement throughout the flap cycle matches that measured from the experiment. There are some higher harmonic fluctuations in the experimental results that aren't directly captured in the predicted results. This is most noticeable for the 8 Hz case at the 0% span location.

One notable feature is the temporal shift in peak TE displacement with increased flap frequency. At a flap frequency of 2 Hz, the variation in TE displacement in nearly symmetrical about t/T = 0.5 with the peak occurring slightly after the end of a given flap stroke. With increased flap frequency, the peak in TE displacement occurs later in the stroke with the phase shift being most notable for the curves at 0% span.

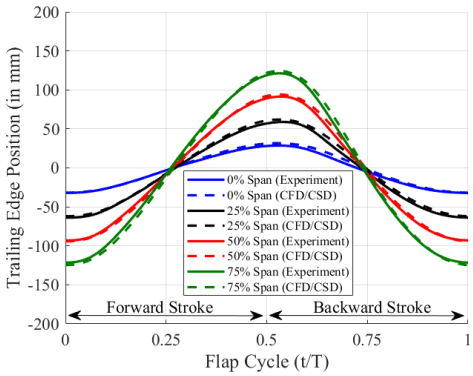

(a) f = 2 Hz

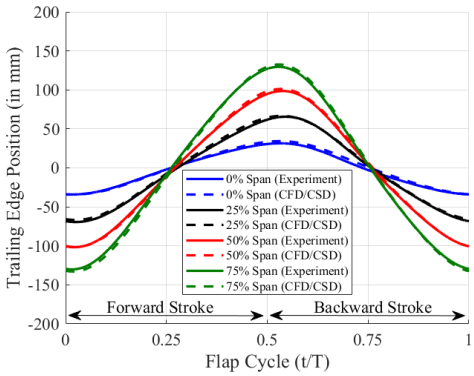

(b) f = 4 Hz

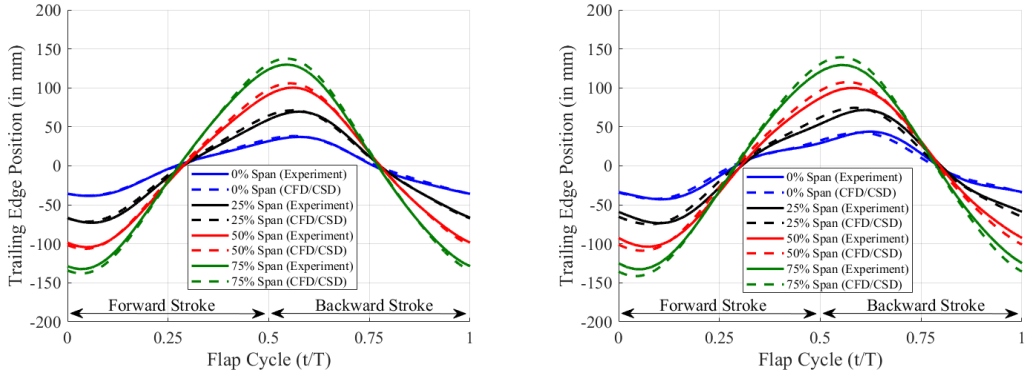

(c) f = 6 Hz (d) f = 8 Hz

Figure 5.21: Comparison of experimental and CFD/CSD trailing edge deflection vs time

Figure 5.22 shows the instantaneous pitch angle variation for the different flap frequencies tested. The instantaneous pitch angle variations are computed at 0%, 25%, 50% and 75% span. Figures 5.22a, 5.22b, 5.22c and 5.22d show the instantaneous pitch angle variation over time for the 2Hz, 4 Hz, 6 Hz and 8 Hz cases respectively. At the 2 Hz flap frequency (5.22a) the pitch angle variation is minimal denoting that wing deformation is low at this flap frequency. There is a slight increase in pitch angle toward the start of the backward stroke. This peak in pitch angle corresponds with the peak in lift force seen in the corresponding lift time history plot (Fig. 5.14a) at the same instance in the flap cycle. This wing deformation is mainly due to the inertial forces act on the wing during stroke reversal.

At 4 Hz (Fig. 5.22b), there is a more distinct variation in the pitch angle. At the wing root, the pitch angle remains relatively constant at 90°. However, due to wing twisting, the magnitude of wing pitch angle varies outboard of the wing root. The temporal variation in wing pitch is similar between the forward and backward strokes. During the start of a particular flap stroke, there is a steep change in pitch angle that peaks at approximately t/T = 0.1 for the forward stroke and t/T = 0.6 for the backward

stroke. For the remainder of the flap stroke, the wing pitch angle gradually approaches the initial wing pitch angle of 90°. The variation in wing pitch is similar to the variation in lift force seen in Fig. 5.15a suggesting that the temporal variation in wing deformation directly influences the variation in aerodynamic lift.

For the 6 Hz and 8 Hz flap frequency cases, the pitch angle variations are larger in magnitude and the aerodynamic forces begin to play a more significant role in the passive wing deformations over time. At a flap frequency of 6 Hz (Fig. 5.22c), the pitch angle variation follows a similar trend to that of 4 Hz. There is relatively good agreement between the experimental and computational results in terms of the variation in wing pitch. However, the aeroelastic analysis tended to slightly underpredict the pitch magnitude especially at 25%, 50% and 75% span. The wing root (0% span) is undergoing more notable wing deformations with it reach a peak pitch value reaching approximately 80°. At the 75% span location, the experimental peak pitch values are approximately 52° and 49° during the forward and backward strokes respectively. The CFD/CSD results differ slightly with peak pitch values of approximately 56° and 54° during the forward and backward strokes respectively.

As expected, the instantaneous pitch angle variations are at their highest magnitudes for the 8 Hz (Fig. 5.22d) flap frequency case. The measured and predicted results agree well with respect to the variation in wing pitch, but the peak pitch magnitudes are slightly underpredicted. Variation of the wing root pitch angle is significant with a peak pitch value of approximately 75°. This results in a maximum difference of 15° with respect to the initial 90° pitch angle. The change in pitch angle over the time is nearly symmetric between the forward and backward strokes at all span

locations analyzed. Peak pitch value at 75% span is approximately 40° resulting in a maximum wing twist, between the wing root and 75% span, of approximately 35°. Note that in both the 6 Hz and 8 Hz cases, the temporal variation in wing pitch correlates well with the temporal variation in instantaneous lift force over the course of a flap cycle. This again suggests that wing deformation patterns strongly influence the variation lift force production.

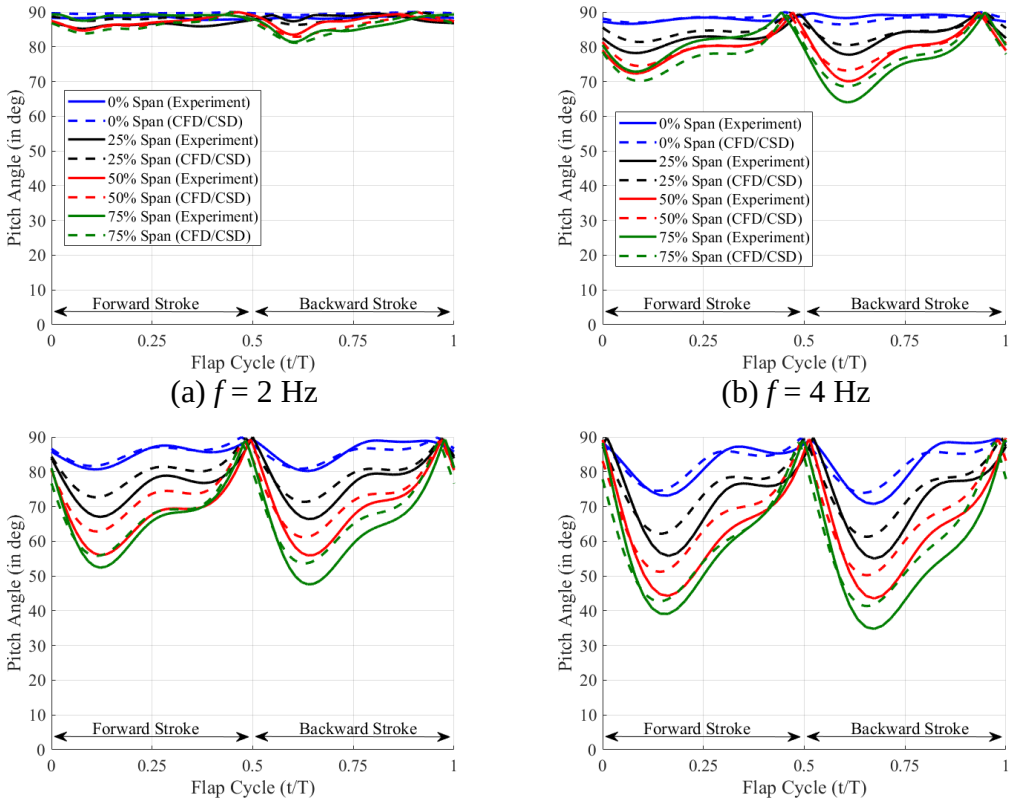

(a) f = 2 Hz (b) f = 4 Hz

(c) f = 6 Hz (d) f = 8 Hz

Figure 5.22: Comparison of experimental and CFD/CSD instantaneous pitch angle variation vs time

For illustrative purposes, Fig. 5.23 shows images comparing the full wing deformation between the VICON and coupled CFD/CSD results at various instances of the flap cycle. The experimental data is represented with red markers and blue polygons while the computational data is represented by the green quadrilaterals. Note

that the lone black mark highlights the origin of the coordinate system. The case shown is for the 8 Hz flap frequency because the largest wing deformations were experienced at that flap frequency. Overall there is good qualitative agreement between the measured and predicted passive wing deformations. This demonstrates that even for large, nonlinear deformations, the coupled CFD/CSD analysis is able to accurately predict the aeroelastic behavior of the wing.

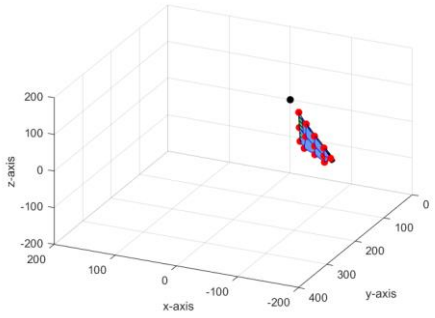

(a) t/T = 0.0

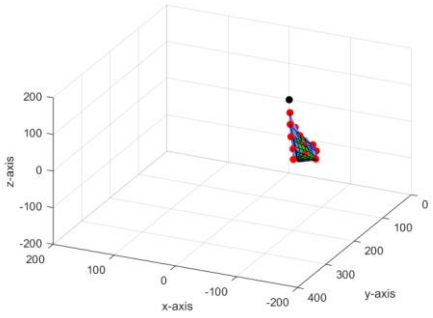

(b) t/T = 0.125

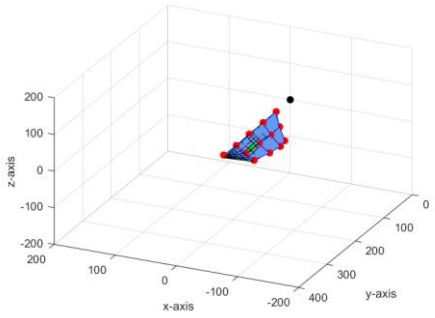

(c) t/T = 0.25

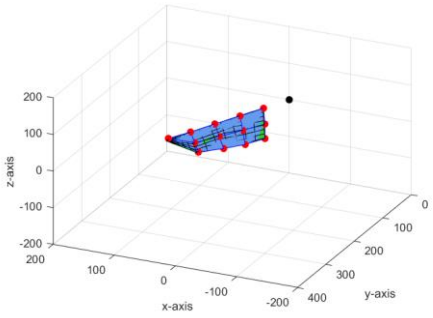

(d) t/T = 0.375

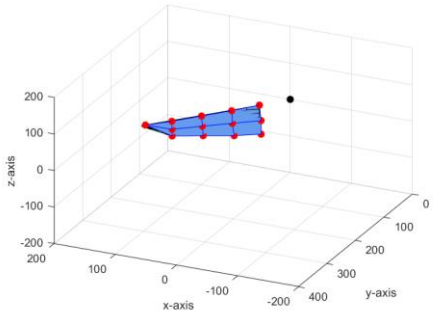

(e) t/T = 0.5

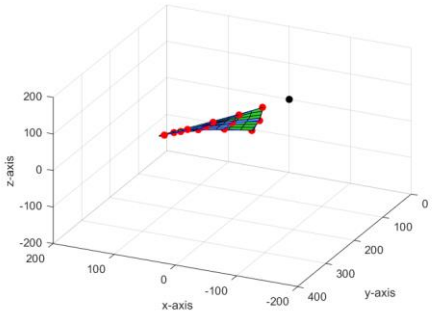

(f) t/T = 0.625

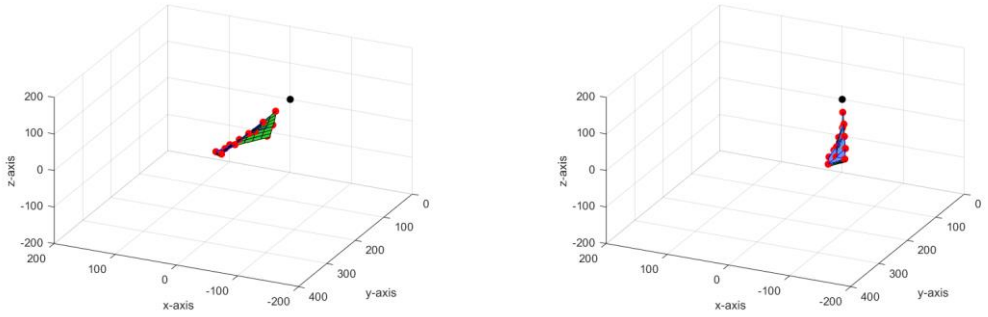

(g) t/T = 0.75 (h) t/T = 0.875

Figure 5.23: Comparison of VICON and CFD/CSD wing deformation (f = 8 Hz)

5.4 Summary

The goal of the present study was to validate the predictive capability of the coupled CFD/CSD solver for the case of an anisotropic flexible flapping wing modeled after a realistic flapping-wing MAV. Experiments were conducted on the test wing in hover at flap frequencies of 2 Hz, 4 Hz, 6 Hz and 8 Hz. Aerodynamic force measurements were conducted to analyzing the instantaneous lift and drag forces produced as well as the aerodynamic power time histories. VICON motion tracking experiments were performed to measure passive wing deformation throughout a flap cycle. The model analyzed by the coupled aeroelastic solver was constructed to replicate the flap kinematics, geometry and structure of the wing used during experimentation. The experimental results were used to validate the coupled CFD/CSD aeroelastic analysis and assess its predictive capability. The overall conclusions are as follows:

i. The coupled CFD/CSD model was able to satisfactorily predict instantaneous aerodynamic lift and drag. Mean lift and drag values were seen to vary quadratically with flap frequency. The lift force-time history was captured well and for flap

frequencies above 2 Hz, a periodic variation in the lift force-time history was observed. The peak magnitude in drag was underpredicted for all flap frequencies tested however, the temporal variation was well captured by the computational analysis.

ii. The time histories of aerodynamic power were investigated and predicted results agreed well with those measured during experimentation. As flap frequency increased, the measured and predicted instantaneous aerodynamic power trends exhibited better agreement. Experimental and computational mean aerodynamic power values versus flap frequency correlated well. The magnitude of lift-to-power ratio was slightly underpredicted by the coupled CFD/CSD analysis. However, a plateau in lift-to-power ratio is seen in both the experimental and computational results. Results from the force measurement studies show that inertial force subtraction may be a viable means of determine the lift and aerodynamic power produced by a flexible flapping wing. However, measuring drag force proves difficult due to the larger inertial forces acting in the same direction as drag.

iii. The coupled aeroelastic analysis was able to adequately predict the passive wing deformations due to aerodynamic and inertial forces. High frequency oscillations present in the experimental results were adequately captured in the computational results. At higher flap frequencies, there is a notable phase shift in the peak trailing edge displacement. The variation in instantaneous pitch angle matched well between the measured and predicted values. The pitch angle magnitude was slightly underpredicted especially toward outboard portion of the wing. As expected, peak pitch angle magnitude increased with increased flap frequency. The overall pitch

angle variation correlated well with the variation in instantaneous lift suggesting that wing deformation significantly influence lift production.

Chapter 6 Anisotropic Flexible Wing – Parametric Study

The chapter presents the results of a parametric study performed on the wing discussed in Chapter 5. The studies were conducted using the coupled CFD/CSD aeroelastic solver to investigate the aerodynamic forces and power as well as the immediate flowfield about the wing and passive wing deformations over time. While the coupled CFD/CSD analysis does have a high computational cost, the level of fidelity it provides allows for in-depth analysis of the wing's effect on the previously mentioned characteristics. The goals of this parametric study are to investigate the effect of wing flexibility on performance and determine which aspect of the wing structural design most directly impact performance.

6.1 Parametric Study Parameters

The wing studied is the anisotropic flexible wing discussed throughout Chapter 5. The computational model used in the parametric study is the same one described in Section 5.2 which can be referenced for additional detail on its development. The structural properties of the wing are displayed below in Table 6.1. The major load carrying components of the wing are the leading-edge spar, cross spar and root spar. A schematic of the anisotropic wing is shown in Fig. 6.1 for reference. The larger stiffness of the leading-edge spar, in comparison to the root and cross spars, aids in preventing significant spanwise deflection of the wing. Focus will be on how varying the flexural stiffness (EI) of the root and cross spars in three cases:

1. Root spar only
2. Cross spar only
3. Root spar and cross spar in conjunction

For all three groupings, the EI values of the respective members under consideration are reduced to 75%, 50%, 25% and 10% of their nominal value shown in Table 6.1. The flexural stiffness is reduced uniformly across a structural member mean the stiffness value does not vary along a given structural member. The 6 Hz flap frequency is analyzed because it is the flap frequency at the start of the plateau in mean lift-to-power ratio shown in Fig. 5.2 b. The goal is to investigate how varying wing flexibility affects wing performance including lift generation and lift-to-power ratio. Additionally, the flowfield and passive wing deformation over time will be analyzed to determine how wing compliance affects these aspects of the flapping wing.

Table 6.1**: Structural properties of anisotropic flexible wing**

Wing span, *b*	19.05 cm
Mean wing chord, $\bar{c}$	5.26 cm
Membrane thickness, *h*	0.80 mm
$EI_{root\ spar}$	6.24×10^{-4} N-m^2
$GJ_{root\ spar}$	8.27×10^{-4} N-m^2
$EI_{cross\ spar}$	3.27×10^{-4} N-m^2
$GJ_{cross\ spar}$	2.42×10^{-4} N-m^2
$EI_{leading\ edge\ spar}$	4.33×10^{-2} N-m^2
$GJ_{leading\ edge\ spar}$	3.21×10^{-2} N-m^2
$E_{foam\ sheet}$	1.83×10^{6} N-m^{-2}
$\nu_{foam\ sheet}$	0.3
$\rho_{carbon\ fiber}$	1433.0 kg-m^{-3}
$\rho_{plastic}$	1505.0 kg-m^{-3}
$\rho_{foam\ sheet}$	34.0 kg-m^{-3}

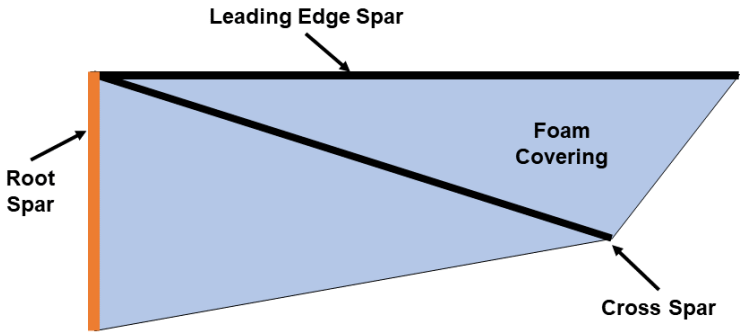

Figure 6.1: Schematic of anisotropic wing highlighting structural members

6.2 Aerodynamic Force and Power Comparison

6.2.1 Time-averaged Aerodynamic Force and Power

In this sub-section the mean aerodynamic force coefficients at varied structural stiffnesses. Note that when describing lift or drag, the reference coordinate system is the same one mentioned in Sub-section 5.3.2. Positive lift is said to act in the positive z-direction while drag acts in opposition to wing motion. Figure 6.2 shows mean aerodynamic lift and drag coefficients versus structural stiffness for the three cases tested. The case where only the root spar stiffness is varied is represented by the red circles while the cases where only the cross spar stiffness is varied and the root and cross spars are varied in conjunction are represented by blue squares and black triangles respectively. The stiffness values (displayed on the abscissa of the plot) are shown as a stiffness ratio in percent form where the actual stiffness of the component is normalized by its nominal value. Note that the point labeled “rigid” on the abscissa represents the case of an infinitely rigid wing which undergoes no deformation during flapping. For this case, the aeroelastic solver was run with no structural dynamics making it

effectively a pure CFD simulation. The wing was set at the initial 90° pitch angle and prescribed the same one degree-of-freedom flap kinematics as in the coupled CFD/CSD cases.

In Fig. 6.2a, as expected, the rigid case produces zero lift. For the rigid case, the mean drag coefficient (Fig. 6.2b) is approximately equal to 0.3. As the flexural stiffness is decreased, the mean lift coefficient (C_L) increases approximately linearly. However, the mean drag coefficient appears to vary quadratically. The mean C_D slightly increases for the 100% stiffness case with respect to the rigid case. In general, after the 100% stiffness case, the magnitude of mean C_D decreases with decreasing structural stiffness. In examining the mean aerodynamic power coefficient (C_P) trends in Fig. 6.2c, the variation in mean C_P with respect to stiffness is similar to that seen in the mean drag coefficient versus stiffness plot.

Up to the 25% stiffness case, the mean C_L, C_D and C_P results between the three cases tested are similar with the root and cross spars case (i.e. case 3) exhibiting slightly higher mean lift coefficients and slightly lower mean drag and power coefficients in comparison to the other two cases. However, at 10% stiffness, the case where only the cross spar stiffness is varied deviates from the expected trend. There is a notable decrease in mean C_L as well as a significant increase in mean C_D and mean C_P.

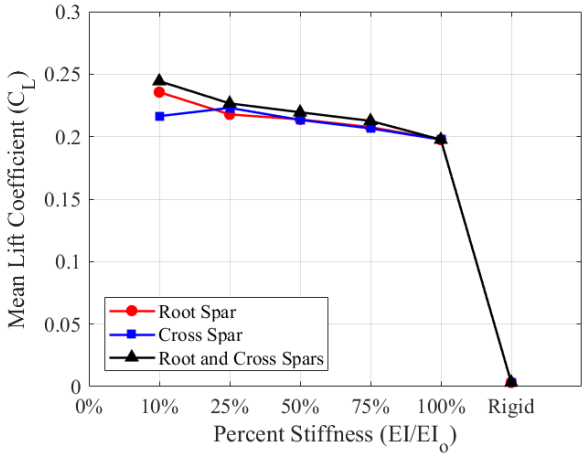

(a) Mean lift coefficient vs structural stiffness

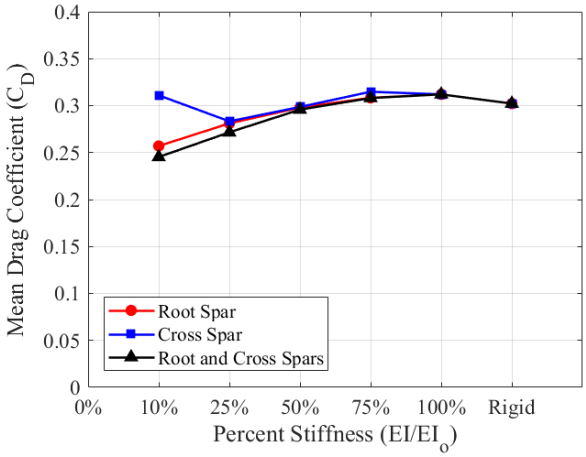

(b) Mean drag coefficient vs structural stiffness

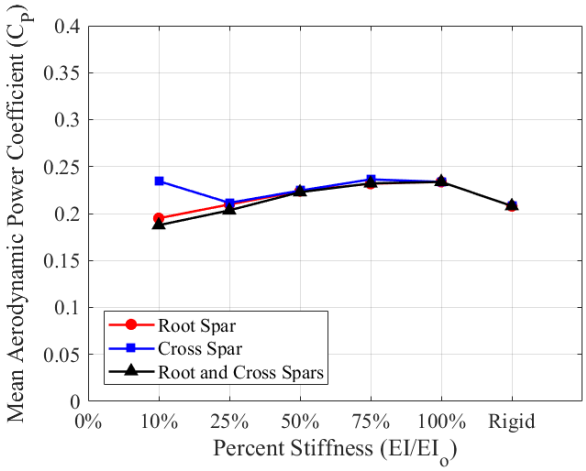

(c) Mean aerodynamic power coefficient vs structural stiffness

Figure 6.2: Mean aerodynamic coefficients vs structural stiffness (All 3 test cases)

To more directly assess how wing flexibility influences performance, two metrics are examined: 1) lift-to-drag ratio and 2) lift-to-power ratio (i.e. power loading). Figure 6.3a and 6.3b display lift-to-drag ratio and power loading versus stiffness for the three cases studied. Lift-to-drag ratio is calculated by dividing the mean lift coefficient by the mean drag coefficient while power loading is calculated by dividing the mean lift coefficient by the mean aerodynamic power coefficient.

Given that the mean C_D and mean C_P plots in Fig. 6.2 exhibited similar trends, the lift-to-drag ratio and power loading plots in Fig. 6.3 also exhibit similar trends. For all three cases tested, lift-to-drag ratio and power loading are seen to increase with decreasing stiffness ratio down to a stiffness ratio of 25%. The case were both the root and cross spars are changed in conjunction exhibits the highest L/D and power loading for all stiffness ratios tested. The highest lift-to-drag ratio and power loading values occur at a stiffness ratio of 10% where L/D equals 1.0 and power loading equals 1.3. When comparing the predicted L/D and power loading at nominal stiffness values, a 10% stiffness ratio allows for an increase in lift-to-drag ratio by 58.7% and an increase in power loading by 53.8%. It is important to note that at a stiffness ratio of 10%, the lift-to-drag ratio and power loading for the case where only the cross spar stiffness is varied decreases significantly. For this case, there is a 11.6% reduction in L/D and 12.5% reduction in power loading in comparison to the same case at a stiffness ratio of 25%.

Moving forward, analysis will focus on determining what aspects of the wing deformation and development of the flowfield about the wing increase lift production and overall performance of the wing as wing flexibility is increased. Additionally, it is

important to better understand what mechanisms are responsible for the decrease in wing performance for the case where only the cross spar stiffness is reduced from 25% to 10%.

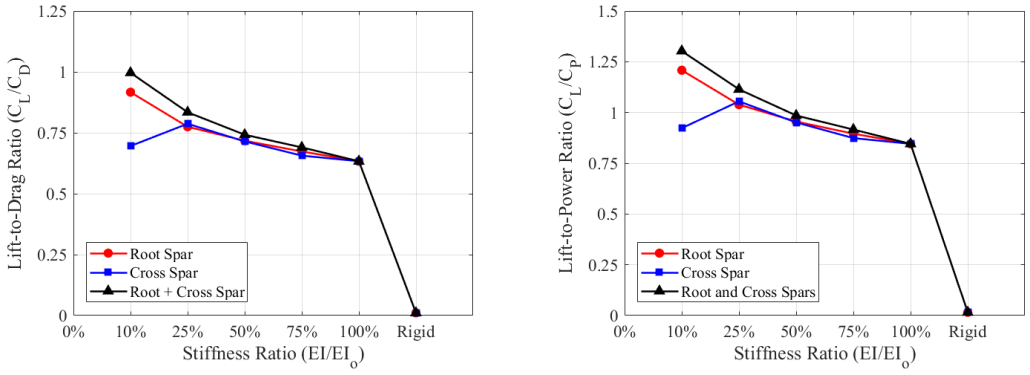

(a) Lift-to-drag ratio versus stiffness (b) Power loading versus stiffness

Figure 6.3: Comparison of lift-to-drag ratio and power loading versus wing stiffness

6.2.2 Aerodynamic Force and Power Time Histories

Figures 6.4, 6.5 and 6.6 respectively show the time history of lift, drag and aerodynamic power coefficients over the course of a flap cycle. The plots in Figs. 6.4a, 6.5a and 6.6a are for a stiffness ratio of 25% while Figs. 6.4b, 6.5b and 6.6b are for a stiffness ratio of 10%. In Fig. 6.4a, the rigid case produced essentially zero lift throughout the flap cycle. For the nominal case (100% EI), the variation in lift is periodic in nature and nearly symmetric between the forward and backward strokes. For a given flap stroke (forward stroke or backward stroke), instantaneous lift increases sharply at the start of a flap cycle. The peak in instantaneous lift occurs approximately a quarter of the way through a given flap stroke. After the peak in lift, the magnitude of lift decreases until mid-flap stroke (t/T = 0.25 or 0.75) at which point the lift trend

plateaus. Toward the end of the flap stroke, instantaneous lift approaches zero and the process repeats during the subsequent flap stroke.

For all cases at 25% EI in Fig. 6.4a, the variation in lift over time is similar. The time history of lift is sinusoidal-like in nature with a nonzero mean offset. The peak in lift is slightly before mid-flap stroke (approximately t/T = 0.20 or 0.70) with a magnitude similar to that seen in the 100% stiffness case. Unlike in the nominal 100% stiffness case, the decrease in the lift after the peak is more gradual for the 25% stiffness cases. Therefore, the average lift generated during a flap cycle is greater for the 25% stiffness cases as opposed to the nominal stiffness case.

In Fig. 6.4b, there is a notable difference between the cases at the 10% stiffness ratio. In the case where only the root spar stiffness is varied (case 1) the increase in lift at the beginning of a flap stroke is similar to that seen in the nominal stiffness case. However, instead of a distinct peak in lift forming, the lift time history plateaus and remains relatively constant for a major of the flap stroke. Toward the end of the flap stroke, lift magnitude drops as the wing starts the subsequent flap stroke. The case where the root and cross spars are varied in conjunction (case 3) exhibits a similar trend to that in case 1. The main difference is that toward the end of the plateau in lift force (approximately t/T = 0.33 or 0.83) there is a slight peak in lift prior to the decrease in lift at the end of the flap stroke. While the maximum magnitude in lift is lower in cases 1 and 3 in comparison to the nominal stiffness case, the plateaus in lift force during a majority of the flap strokes allow for greater averaged lift coefficients in cases 1 and 3.

In the case where only the cross spar stiffness is varied (case 2), the lift trend is vastly different than that described in cases 1 and 3. The lift time history for case 3

closely resembles that of the nominal stiffness case. However, the peaks in lift coefficient are slightly higher in case 3 in comparison to the nominal stiffness case. These results help to explain why the mean lift coefficient is significantly lower in case 2 as compared to cases 1 and 3 at a stiffness ratio of 10%.

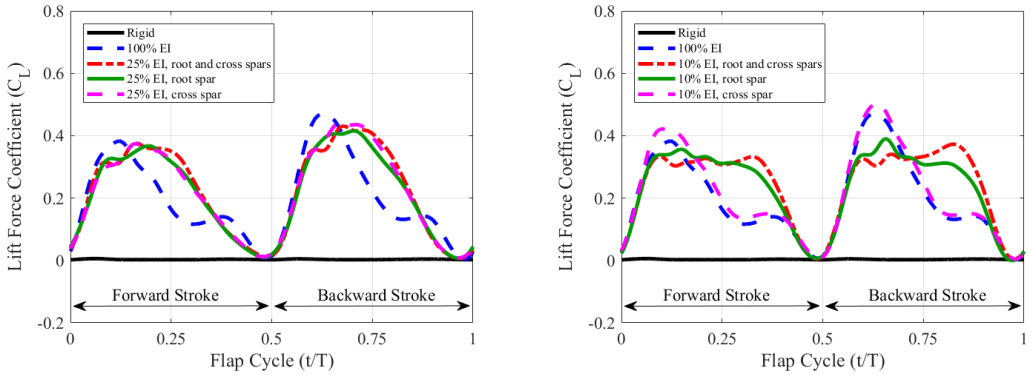

(a) C_L time history (25% stiffness ratio) (b) C_L time history (10% stiffness ratio)

Figure 6.4: Comparison of instantaneous lift vs time at 25% and 10% stiffness ratios

In Fig. 6.5, the variation in drag force time history is similar between all cases. The drag force trend exhibits a sinusoidal-like behavior which is expected given the sinusoidal-like flap kinematics. The 100% stiffness case has slightly larger peak magnitudes in drag compared to the rigid case which helps to explain why the time averaged C_D is highest for the nominal case. The drag force trends nearly collapse on top of one another for all cases at a 25% stiffness ratio (Fig. 6.5a) and have lower peak drag magnitudes in comparison to the rigid and 100% EI cases. In Fig. 6.5b, the peak drag force magnitudes are lowest for cases 1 and 3 at a 10% stiffness ratio. However, the drag force time history of the nominal case (100% stiffness ratio) and case 2 (i.e. cross spar only case) are nearly identical.

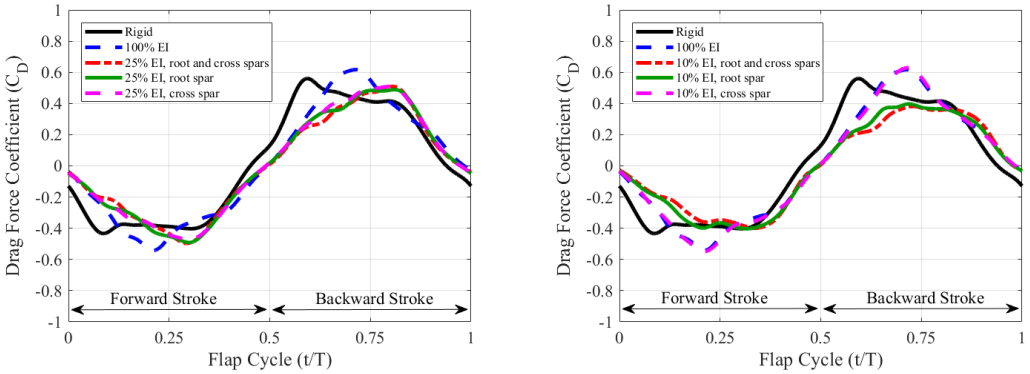

(a) C_D time history (25% stiffness ratio) (b) C_D time history (10% stiffness ratio)

Figure 6.5: Comparison of instantaneous drag vs time at 10% and 25% stiffness ratios

For the rigid case in Fig. 6.6, the aerodynamic power increases rapidly at the beginning of the flap stroke toward a distinct peak. After which, the magnitude of instantaneous C_P gradually lowers in value for most of the flap stroke and then sharply decreases toward the end of the flap stroke. This trend in power coefficient repeats itself in the subsequent flap stroke. In the nominal stiffness case, the temporal variation in C_P is similar to the lift time history in Fig. 6.4. The peak in C_P is greater in magnitude and has a larger value for a significant portion of the flap stroke when compared to the rigid case.

In Fig. 6.6a, the trends at a stiffness ratio of 25% nearly lay on top of one another. Unlike the rigid and nominal stiffness cases, the peak in aerodynamic power occurs after mid-flap stroke (t/T = 0.25 or 0.75). The magnitude of the peak in C_P is close to that seen in the rigid case. After the peak, the magnitude of C_P decreases at a rate similar to that seen in the 100% EI case at the end of a flap stroke. At a 10% stiffness ratio (Fig. 6.6b), the aerodynamic power coefficient trends increase at the start of a flap stroke and then plateau in a manner similar to the corresponding lift force time histories for case 1 and case 3. The maximum magnitude of C_P for cases 1 and 3 is

significantly lower than the rigid or nominal cases. For the case were only the cross spar stiffness is varied (case 2), the temporal variation in C_P is almost identical to the nominal wing stiffness case.

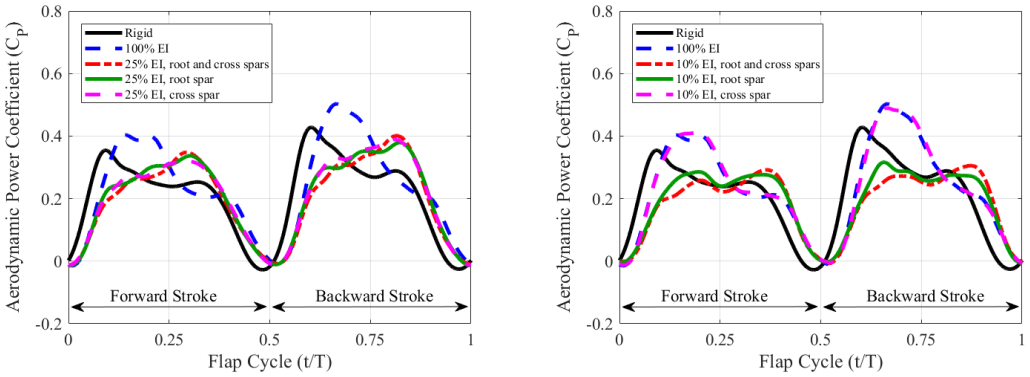

(a) C_P time history (25% stiffness ratio) (b) C_P time history (10% stiffness ratio)

Figure 6.6: Comparison of instantaneous aerodynamic power vs time at 10% and 25% stiffness ratios

Analysis of the aerodynamic coefficient time histories provides insight into how wing flexibility influences the temporal variation in lift, drag and aerodynamic power. For cases 1 and 3, decreasing wing stiffness allowed for the temporal variation in lift to remain constant over a larger portion of the flap cycle resulting in greater average mean lift values compared to the nominal stiffness case. Part of the reason for the decreased mean coefficient values for case 2 at 10% stiffness is that the temporal variation in the aerodynamic coefficients nearly match that of the nominal stiffness case which underperforms in comparison to the wings with lower structural stiffness. Varying wing flexibility influences the spanwise variation of wing deflection throughout the flap cycle. Thus, it is important to assess the sectional variation of the aerodynamic coefficients over the flap stroke to gauge how varied wing compliance impacts the aerodynamics both temporal and spatially.

6.2.3 Sectional Aerodynamic Coefficient Contour Plots

In this sub-section, the sectional aerodynamic coefficients will be discussed. The data is displayed using contour plots to show both the temporal and spatial variation in the coefficient values. Note that the contour plots show data from the forward stroke only. In the time history plots discussed in Sub-section 6.2.2, there were some differences in the data between the forward and backward strokes for a given case. However, they were similar enough that the general conclusions drawn from this discussion can be applied to both parts of the flap cycle. Thus, for brevity, only the forward stroke data will be discussed. In all the sectional aerodynamic coefficient contour plots, the wing flap direction is from left to right in the plot. Dashed black lines mark various azimuthal positions in the flap stroke ranging from 0° – 80°. The 0° flap angle position marks the start of the forward stroke and the 80° flap angle position marks the end of the forward stroke.

Figure 6.7 shows the sectional lift coefficient (C_l) contour plots where Fig. 6.7a represents data from the nominal stiffness case and Fig. 6.7b represents data at a 10% stiffness ratio where both the root and cross spar stiffness values are varied in conjunction (case 3). In Fig. 6.7a, much of the lift is produced during the first half of the flap stroke with the highest C_l values occurring toward the wing tip slightly before the 20° azimuthal position. Between the 20° and 40° azimuthal positions, the magnitude of lift production significantly decreases with most of the lift being produced near the wing tip. After mid-flap stroke, lift production is relatively low along the wing except for a slight increase in lift at the 60° azimuthal position toward the wing tip. In Fig. 6.7b, the highest C_l values also occur at the 20° azimuthal position near the wing tip.

However, lift production remains consistent after the 20° azimuthal position along the entire wing span until the 60° azimuthal position. After that point, lift drops off as the wing reaches the end of the flap stroke. Decreasing the stiffness of the root and cross spars allows for greater lift production along the wing span as well as increased lift production throughout the flap cycle in comparison to the nominal case.

Figures 6.7c and 6.7d are for the case where only the cross spar stiffness is varied at 25% and 10% stiffness respectively. For a stiffness ratio of 25%, lift production near the wing root increases between the 20° and 40° azimuthal positions. After mid-flap stroke lift production persists but diminishes from root to tip until the wing is at the 60° azimuthal position. After that point lift approaches zero as the wing nears the end of the flap stroke. At a stiffness ratio of 10%, the C_l contour is similar to that of the nominal stiffness case. While the peak in C_l is greater in magnitude, the overall temporal and spatial variations in C_l during the forward stroke closely resembles that of the nominal stiffness case. Reducing cross spar stiffness to 25% EI not only helps to increase lift at the wing root, which is counter-intuitive, but also prolongs lift production throughout the flap cycle. However, at a 10% stiffness ratio, the pattern of lift production resembles that of the nominal case and performance gains in lift production drop.

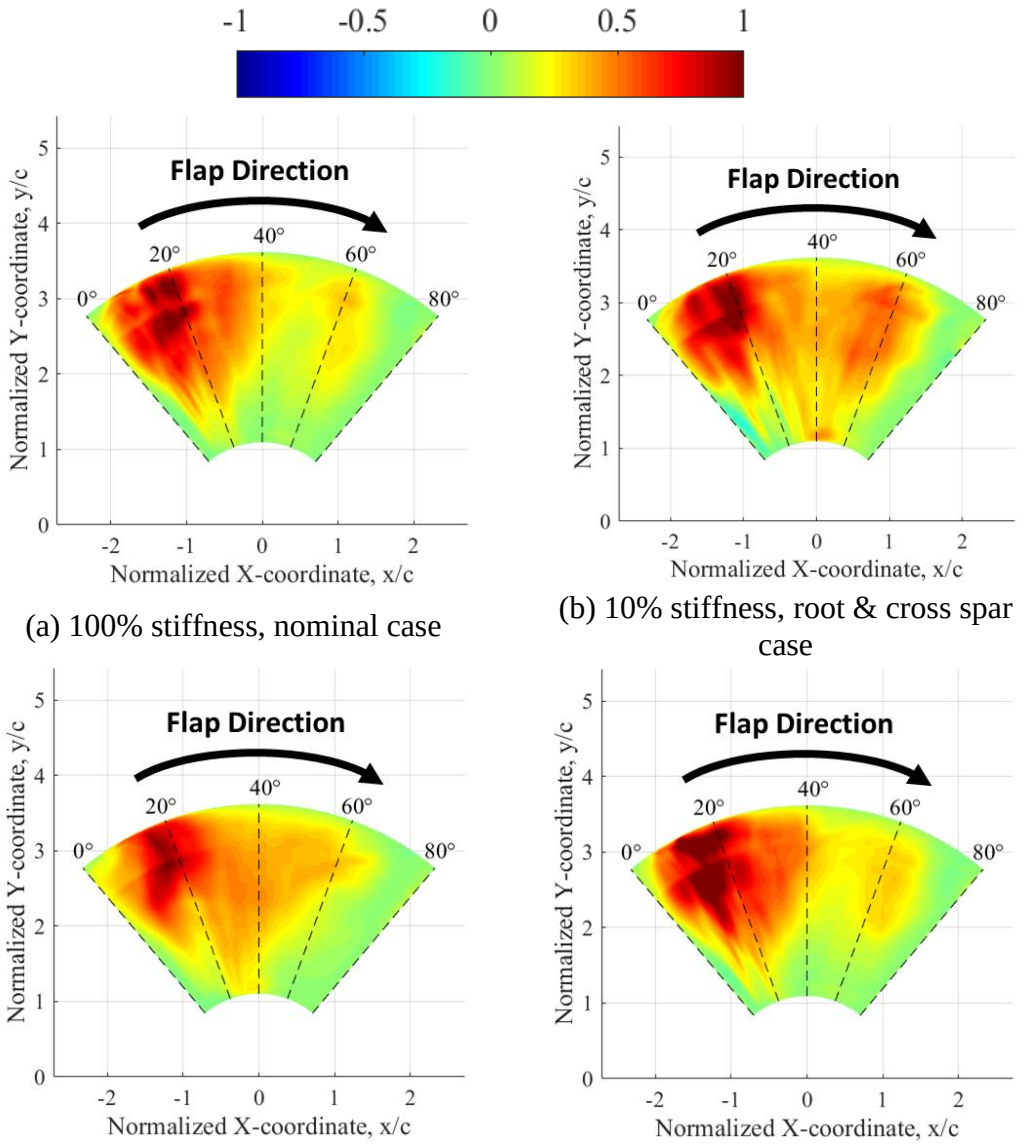

(a) 100% stiffness, nominal case

(b) 10% stiffness, root & cross spar case

(c) 25% stiffness, cross spar case

(d) 10% stiffness, cross spar case

Figure 6.7: Sectional lift coefficient contour plots

Figure 6.8 shows the sectional drag coefficient (C_d) contour plots where Fig. 6.8a represents data from the nominal stiffness case and Fig. 6.8b represents data at a 10% stiffness ratio for case 3. In Fig. 6.8a, similar to the corresponding C_l contour plot, the highest C_d values occur in the early part of the flap stroke at approximately the 20° azimuthal position toward the wing tip. Significant levels of drag are produced along the whole span of the wing for most of the forward stroke. In Fig. 6.8b, the magnitude

of sectional drag is lower during the first half of the flap stroke in comparison to the nominal stiffness case. Specifically, lower magnitudes in C_d are seen during toward the wing root and the peak in C_d near the wing tip is less significant than that of the 100% stiffness case.

Figures 6.8c and 6.8d are for the case where only the cross spar stiffness is varied at 25% and 10% stiffness respectively. For both stiffness ratio, the pattern in drag production during the forward stroke is similar. However, at 25% stiffness ratio, the magnitude of C_d is comparatively lower especially between the 20° and 40° azimuthal positions. Like the sectional C_l contour plots, the sectional C_d contour plots at nominal stiffness values and case 2 at a 10% stiffness ratio strongly resemble each other. In comparison the nominal stiffness case, reducing the root and cross spar stiffness in conjunction appears to lower the overall magnitude in sectional C_d as well as reduce the strong peaks in C_d toward the beginning of the flap stroke. When only the cross spar stiffness is reduced, the pattern of the sectional C_d contour plots at 25% and 10% stiffness ratios closely match that of the nominal stiffness case. However, at 25% stiffness, the magnitude of C_d is noticeably lower especially during the first half of the flap stroke.

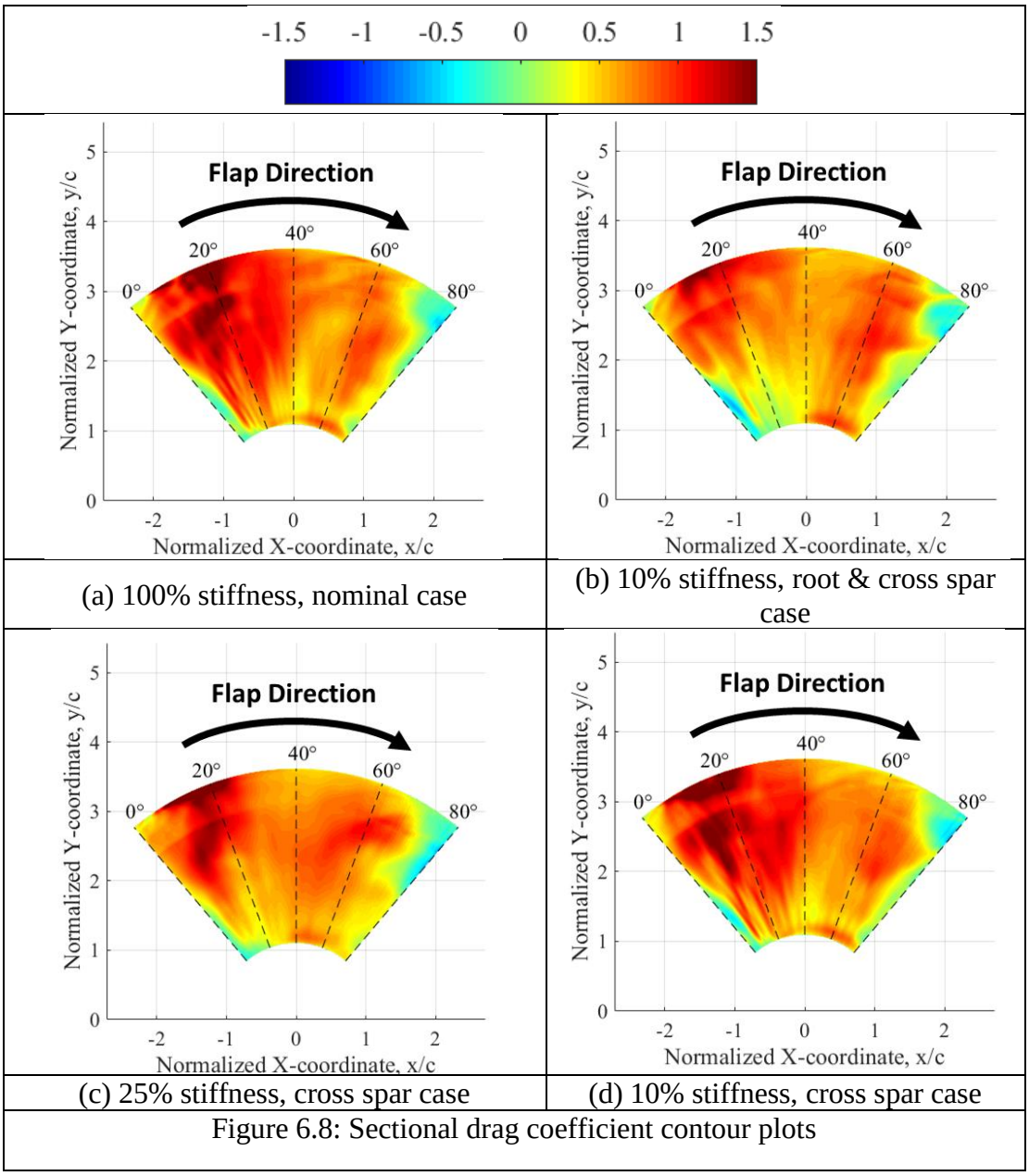

(a) 100% stiffness, nominal case

(b) 10% stiffness, root & cross spar case

(c) 25% stiffness, cross spar case

(d) 10% stiffness, cross spar case

Figure 6.8: Sectional drag coefficient contour plots

6.3 Wing Deformation Comparison

In addition to analyzing the wing forces, it is important to assess the impact of wing flexibility on the deformation of the wing over time. One of the major conclusions from Chapter 5 was that there was a strong correlation between the temporal variation

in wing deformation and the temporal variation in aerodynamic lift produced by the wing. The deformation of the different hypothetical test wings was compared using the plots of instantaneous pitch angle over time which are shown in Fig. 6.9. Figure 6.9a represents the data from the nominal stiffness case. The temporal variation of the pitch angle is similar across the span with the peak magnitude of pitch angle increasing from root to tip. At 75% span, the peak pitch values are approximately 56° and 54° during the forward and backward strokes respectively.

For case 3 at 10% stiffness (Fig. 6.9b), there is a distinct difference in the pitch angle variation for the more inboard portions of the wing compared to the outboard portions of the wing. At 0% and 25% span, the variation in pitch angle over a flap stroke exhibits a singular peak with the peak in pitch angle occurring slightly before mid-flap stroke (approximately t/T = 0.20 or 0.70). Maximum peak pitch angle magnitudes occur at 0% span with values of approximately 39° and 34° between the forward and backward strokes respectively. At 50% and 75% span, the instantaneous pitch angle time history exhibits a double peak behavior over a flap stroke. This double peak behavior causes the direction of wing twist to change over the course of the flap stroke such that for a portion of the flap stroke pitch angle magnitude increases along the span from root to tip. This behavior is not seen in the nominal wing case were the magnitude of wing pitch is always decreasing from root to tip.

For case 2 at a stiffness ratio of 25% (Fig. 6.9c), the peak pitch angle magnitudes are similar to those seen in the nominal stiffness case. However, near mid-flap stroke (t/T = 0.5 or 0.75) the pitch angle across the span of the wing is nearly consistent. Also, the variation in pitch angle over time strongly correlates to the corresponding C_L time

history in Fig. 6.4a. At a stiffness ratio of 10% (Fig. 6.9d), the pitch angle time histories are similar to those in Fig. 6.9a. The main difference is that the peak pitch angles are slightly lower in magnitude compared to the nominal stiffness case. This suggests that the extent of wing deformation is slightly greater for case 2 at 10% stiffness even though the temporal variation in wing deflection is similar to that of the 100% stiffness case.

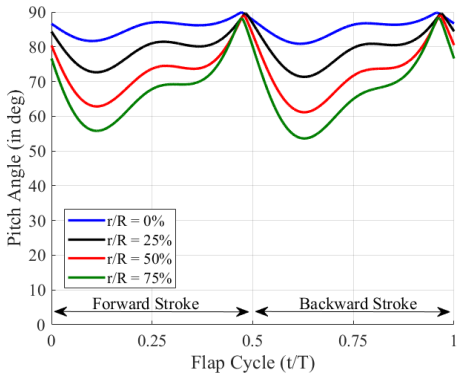

(a) 100% stiffness, nominal case

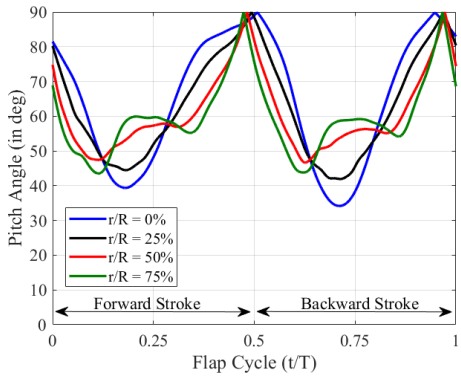

(b) 10% stiffness, root & cross spar case

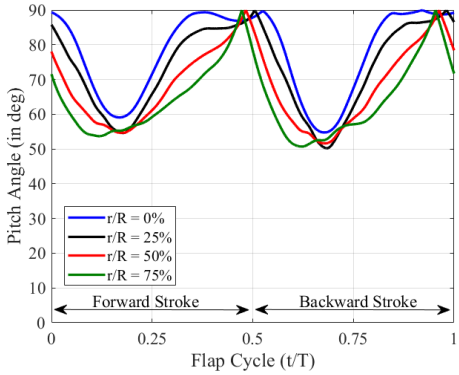

(c) 25% stiffness, cross spar case

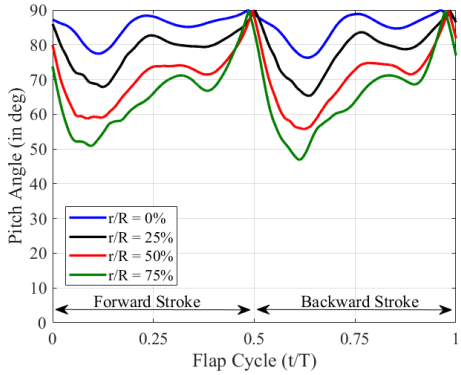

(d) 10% stiffness, cross spar case

Figure 6.9: Comparison of instantaneous pitch angle variation over time

Figures 6.10, 6.11, and 6.12, display the full wing deformation for the different spar stiffness cases discussed at various instances of the flap cycle. In Figs. 6.10, 6.11, and 6.12, the wing for the case in question is shown in green and the wing deformation for the nominal stiffness case is shown in grey for comparison purposes. The black

circular marker designates the origin of the graph. The flap axis passes through the origin and coincides with the z-axis. Figure 6.10 displays images for case 3 at 10% stiffness. The wing deformation present in case 3 at 10% stiffness is significantly larger in magnitude compared to the nominal stiffness case. Figures 6.11 and 6.12 display the images for case 2 at 25% and 10% stiffness ratios respectively. The 25% stiffness case exhibits notably greater wing deflections compared to the 100% stiffness case. However, the wing deformation at 10% stiffness ratio strongly coincides with the wing deformation of the nominal stiffness case such that the wing profiles overlap.

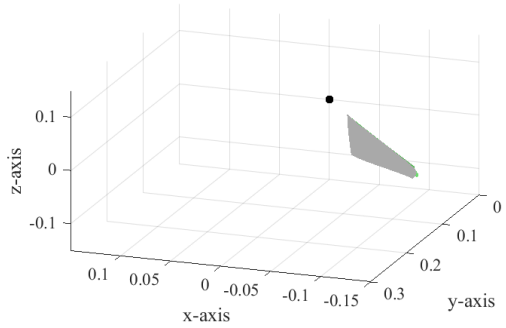

(a) t/T = 0.0

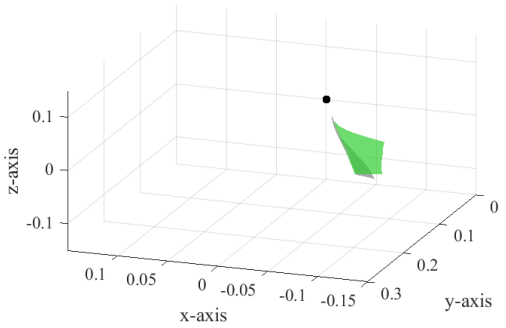

(b) t/T = 0.125

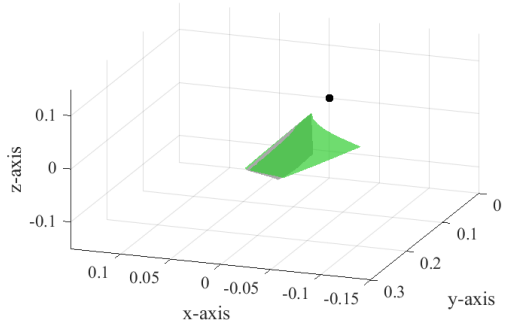

(c) t/T = 0.25

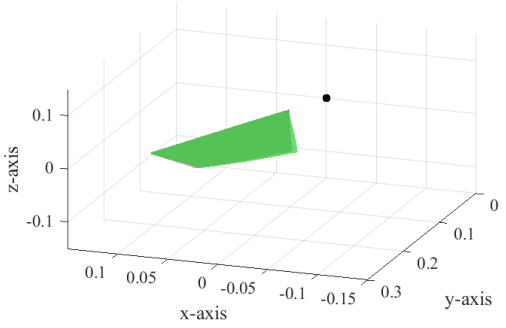

(d) t/T = 0.375

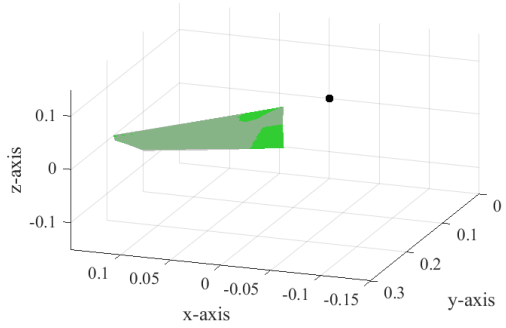

(e) t/T = 0.5

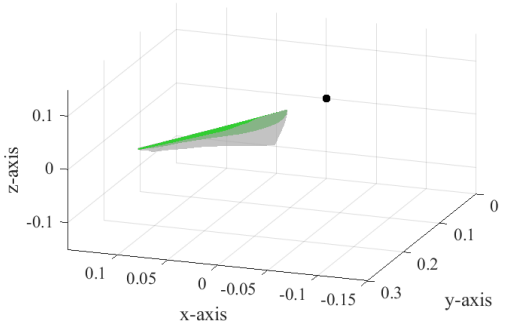

(f) t/T = 0.625

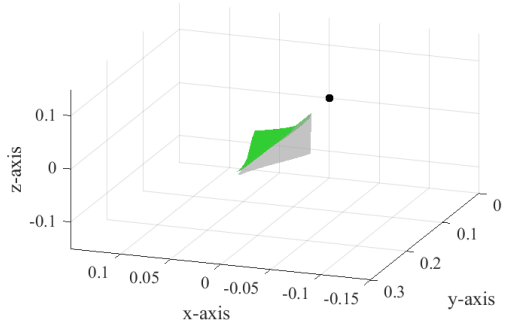

(g) t/T = 0.75

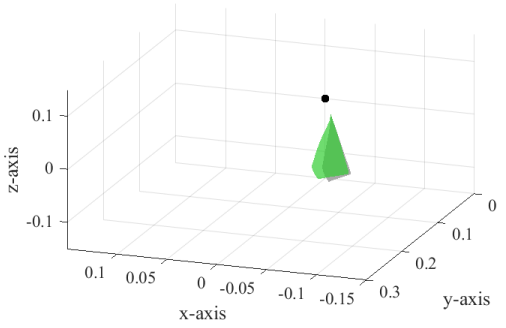

(h) t/T = 0.875

Figure 6.10: Comparison of full wing deformation (10% stiffness, root and cross spar case)

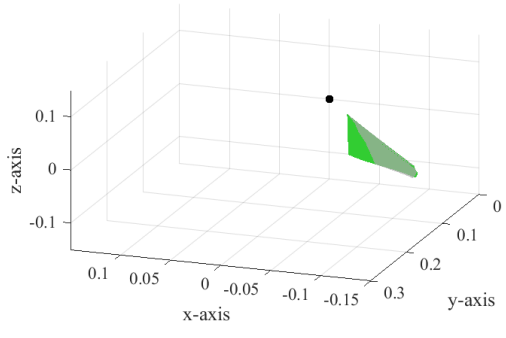

(a) t/T = 0.0

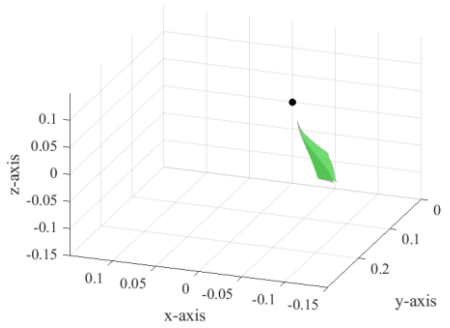

(b) t/T = 0.125

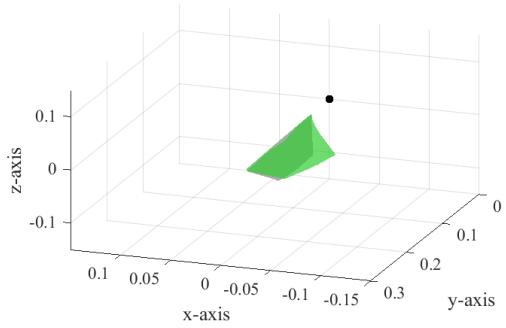

(c) t/T = 0.25

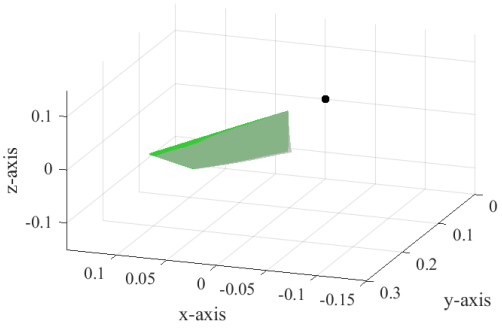

(d) t/T = 0.375

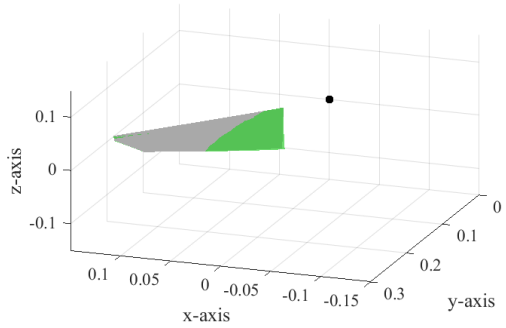

(e) t/T = 0.5

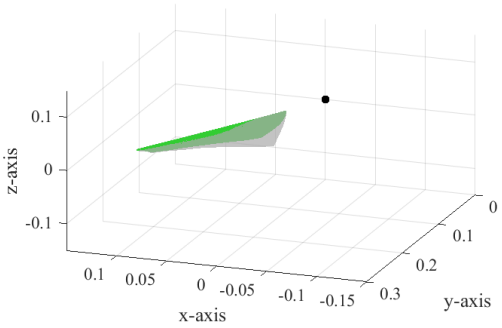

(f) t/T = 0.625

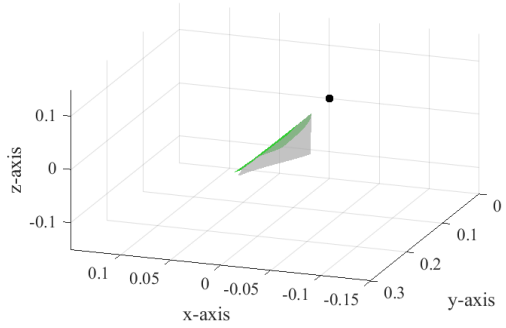

(g) t/T = 0.75

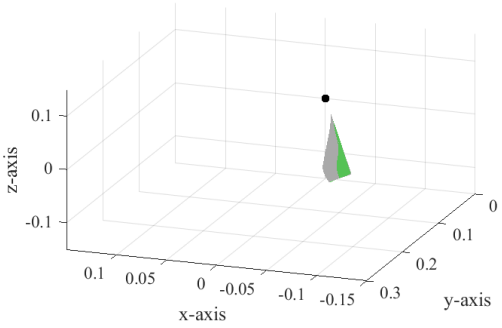

(h) t/T = 0.875

Figure 6.11: Comparison of full wing deformation (25% stiffness, cross spar case)

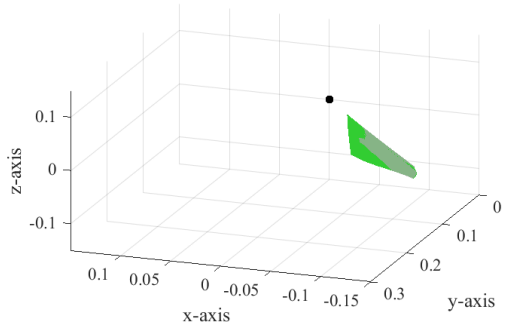

(a) t/T = 0.0

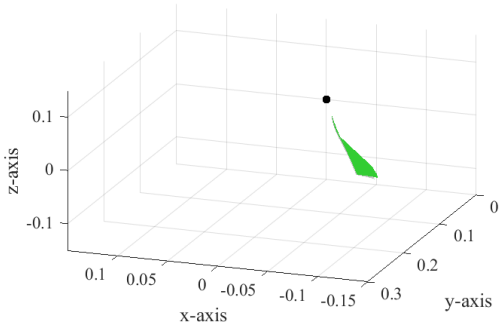

(b) t/T = 0.125

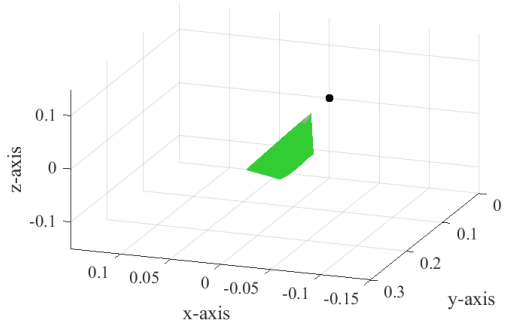

(c) t/T = 0.25

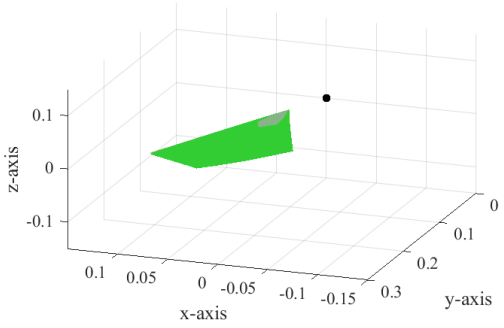

(d) t/T = 0.375

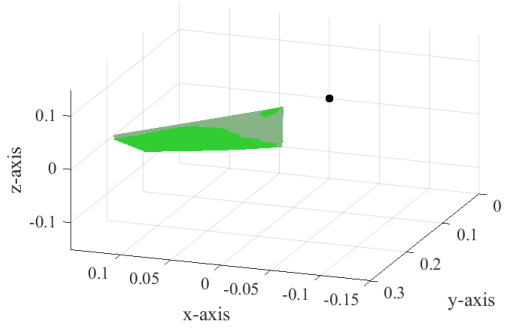

(e) t/T = 0.5

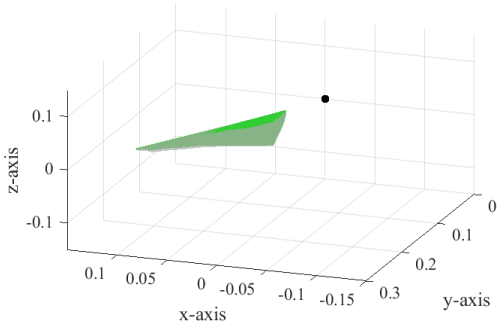

(f) t/T = 0.625

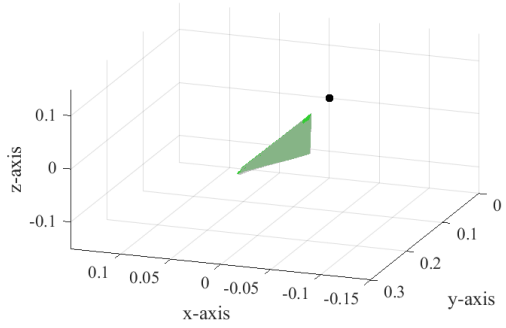

(g) t/T = 0.75

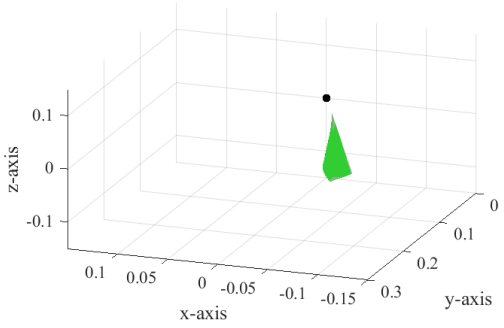

(h) t/T = 0.875

Figure 6.12: Comparison of full wing deformation (10% stiffness, cross spar case)

6.4 Flowfield Comparison

In Section 6.2, the time averaged aerodynamic coefficients and the aerodynamic coefficient time histories over a flap cycle were analyzed. In addition, the sectional aerodynamic coefficient contour plots were discussed. Results showed that in general, decreasing stiffness improved the aerodynamic performance of the wing with the cases where both the root and cross spar stiffnesses were reduced exhibiting the greatest performance gains. In Section 6.3, as the flexibility of the root and cross spars was increased, the pitch angle variation along the wing changed. For the nominal case, the variation in wing pitch was similar across the span with the magnitude change in wing pitch being greater toward the wing tip. For case 3 at a 10% stiffness ratio, the change in wing pitch magnitude was seen to be greater at the wing root compared to the wing tip. It is expected that increasing the flexibility (i.e., reducing stiffness) of the wing would allow for greater wing deformations while flapping. However, one needs to assess whether the improved performance is due to a redirection of the resultant force vector or if the difference in wing deformation significantly alters the formation of the flow structures about the wing.

Figures 6.13 – 6.16 show vorticity magnitude contours at various spanwise slices along the wing throughout the forward stroke. Note that in Figs. 6.13 – 6.16, the sub-figures (·)a – (·)h correspond to flap angles of 8° – 64° during the forward stroke in increments of 8°. These figures provide a qualitative means of visualizing the evolution of the LEV as well as other vortical flow structures along the wing span. Figure 6.13 displays the vorticity magnitude contours for the nominal stiffness case. During the start of the flap stroke (Figs. 6.13a–c), a LEV is beginning to form along the span of

the wing while vortices are being shed from the trailing edge. When the wing is near mid-flap stroke (Figs. 6.13d–f), the LEV near the wing root is coherently formed and remains in close proximity to the wing surface. However, toward the wing tip, the LEV is beginning to diffuse and detached from the wing. Toward the end of the flap stroke (Figs. 6.13g and 6.13h) the LEV near the wing root is still attached. Near the wing tip, vortical flow has become less coherent and highly separated flow is observed.

Figure 6.14 shows the vorticity magnitude contour plots for the case where the root and cross spar stiffnesses are varied at a stiffness ratio of 10%. At Ψ= 8° and 16° (Fig. 6.14a and 6.14b), the formation of the LEV along the span is similar to that of the nominal stiffness case. However, the size of the LEV is slightly smaller especially near the wing tip. In addition, distinct shear layers have formed along the trailing edge with the trailing edge vortices being less coherent. For much of the forward stroke (Figs. 6.14c–f), the LEV remains attached to the wing from root to tip. From Ψ = 24° – 48°, the LEV continues to grow in size yet remains attached to the wing surface. Near the wing tip, the LEV grows larger enough to encompass the entire wing chord at a given spanwise station. Near the end of the flap stroke (Figs. 6.14g and 6.14f), the LEVs near the wing tip begin to exhibit signs of breaking down and detaching from the wing while the LEVs near the wing root remain attached and coherent.

Figures 6.15 and 6.16 display the vorticity magnitude contours for the case where only the cross spar stiffness is varied at 25% and 10% stiffness ratios respectively. During the initial parts of the forward stroke, vortical flow develop in the 25% stiffness case (Figs. 6.15a–c) is similar to the nominal stiffness case at the corresponding flap angles. The formation of a coherent and attached LEV occurs later in the flap stroke in

comparison to the nominal stiffness case and case 3 at a 10% stiffness ratio especially toward the wing root. In Figs. 6.13 and 6.14 formation of a coherent LEV near the wing root occurs near $\Psi = 24°$. However, a LEV of similar coherence doesn't form near the wing root until $\Psi = 48°$ for case 3 at 25% stiffness (Fig. 6.15f). For $\Psi = 56°$ and 64°, the LEVs near the wing tip are highly diffuse and are starting to burst. For case 2 at 10%, the evolution of the vortical flowfield is similar to the nominal stiffness case. This helps to explain why this case exhibits similar force-time history compared to the 100% stiffness case.

Decreasing wing stiffness was seen to alter the formation of vortical structures about the wing particularly the LEV. The increased wing flexibility (i.e., decreased stiffness) of case 3 at a 10% stiffness ratio allowed for greater variation in wing twist to develop during flapping allowing for more favorable local pitch angles along the wing span. This aided in prolonging the sustainment of the LEV which in turn improves lift production. Compared to the nominal case, the LEV for case 3 at 10% stiffness was able to remain coherent and attached to the wing for a longer duration of the flap stroke. In addition, less separated flow was seen near the wing tip. For case 2 at 10% stiffness ratio, the evolution of the flowfield was similar to the nominal stiffness case which explains the similar aerodynamic performance discussed in Section 6.2.

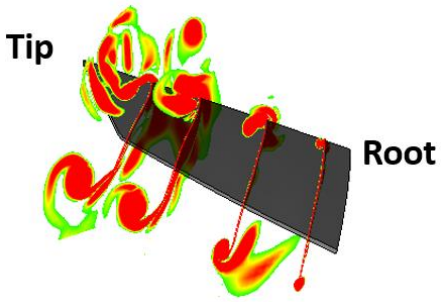

(a) Ψ = 8°

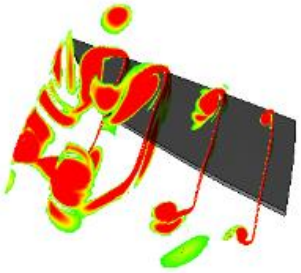

(b) Ψ = 16°

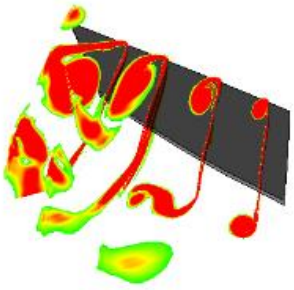

(c) Ψ = 24°

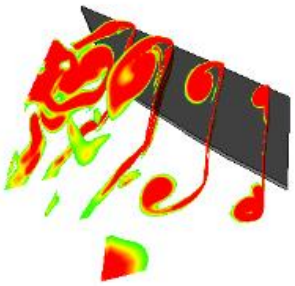

(d) Ψ = 32°

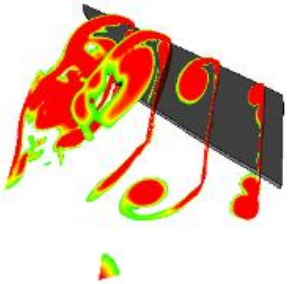

(e) Ψ = 40°

(f) Ψ = 48°

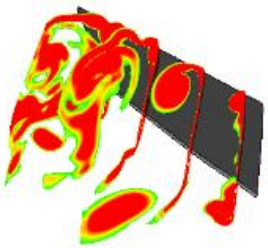

(g) Ψ = 56°

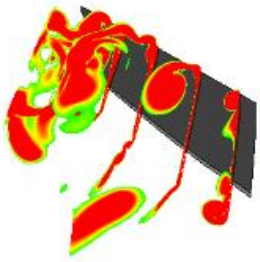

(h) Ψ = 64°

Figure 6.13: Vorticity magnitude contour at various instances of the forward stroke, 100% stiffness, nominal case

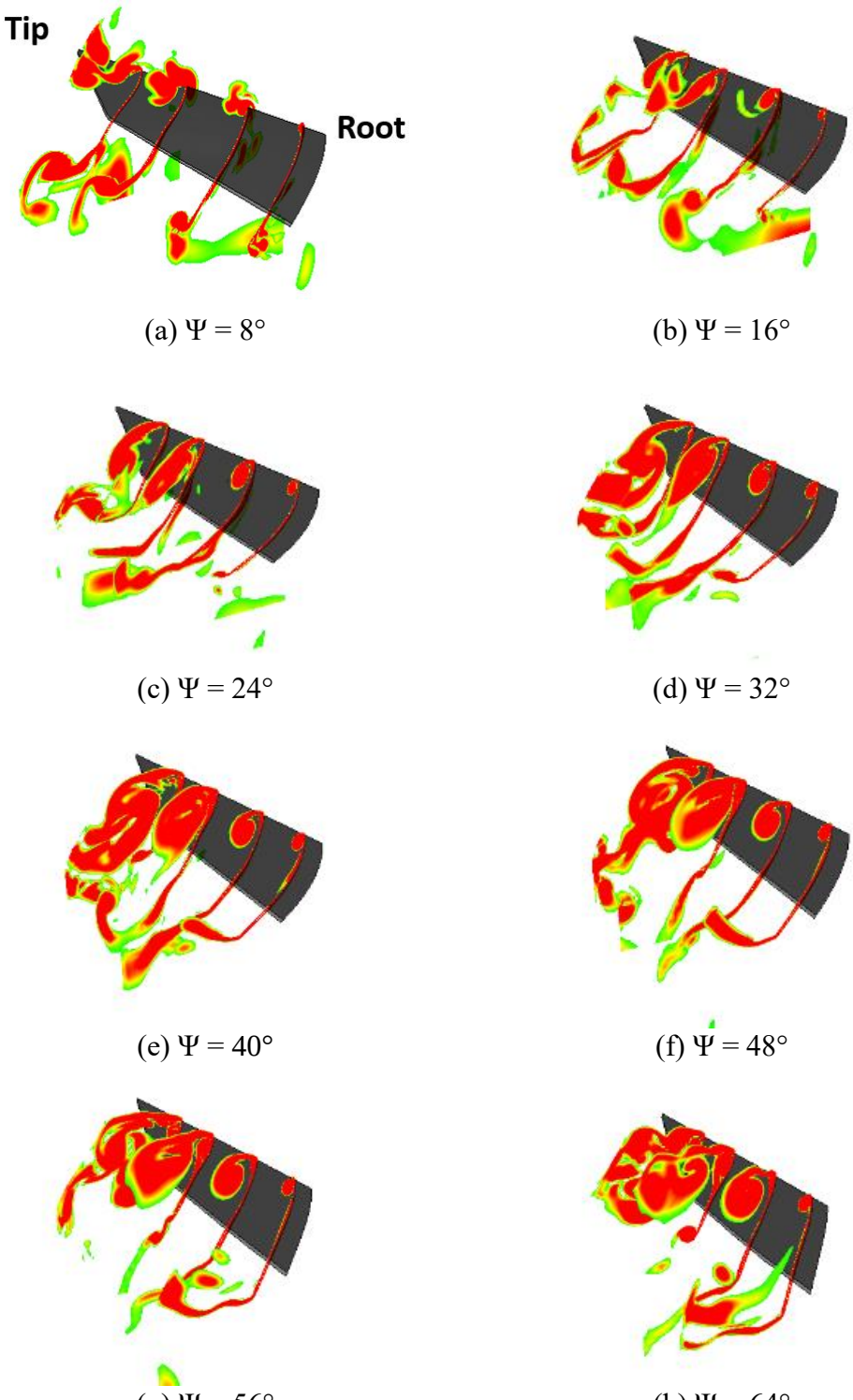

(a) Ψ = 8° (b) Ψ = 16°

(c) Ψ = 24° (d) Ψ = 32°

(e) Ψ = 40° (f) Ψ = 48°

(g) Ψ = 56° (h) Ψ = 64°

Figure 6.14: Vorticity magnitude contour at various instances of the forward stroke, 10% stiffness, root and cross spar case

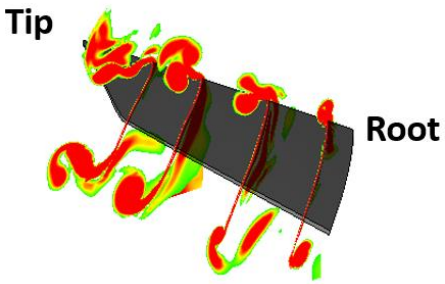

(a) Ψ = 8°

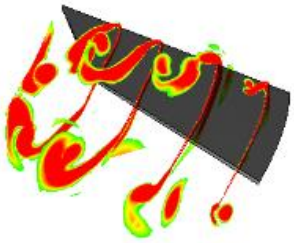

(b) Ψ = 16°

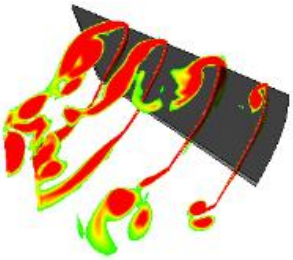

(c) Ψ = 24°

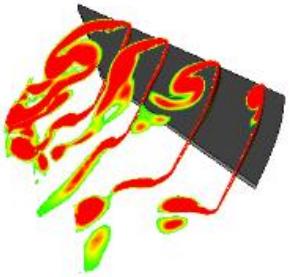

(d) Ψ = 32°

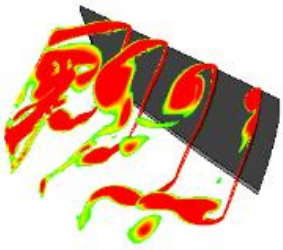

(e) Ψ = 40°

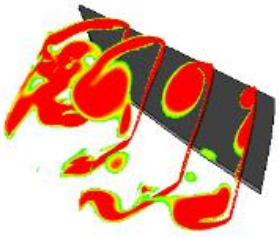

(f) Ψ = 48°

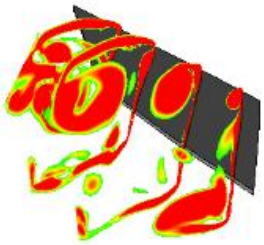

(g) Ψ = 56°

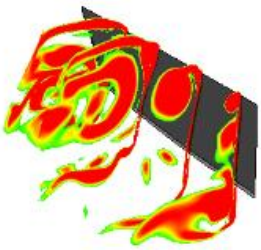

(h) Ψ = 64°

Figure 6.15: Vorticity magnitude contour at various instances of the forward stroke, 25% stiffness, cross spar case

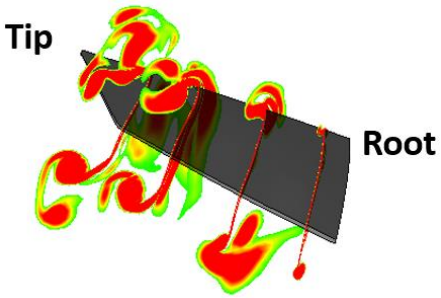

(a) Ψ = 8°

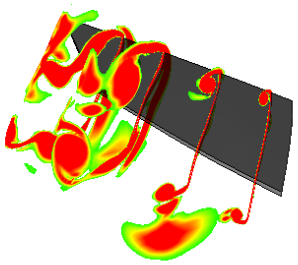

(b) Ψ = 16°

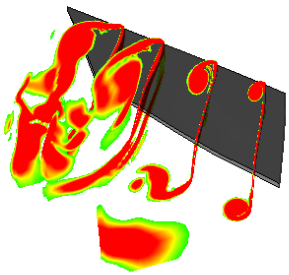

(c) Ψ = 24°

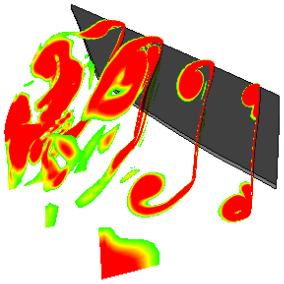

(d) Ψ = 32°

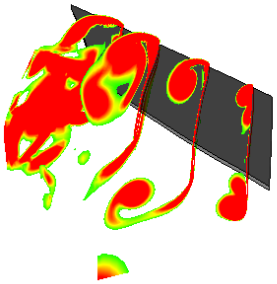

(e) Ψ = 40°

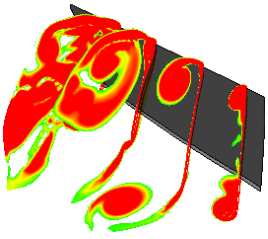

(f) Ψ = 48°

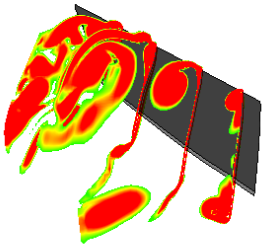

(g) Ψ = 56°

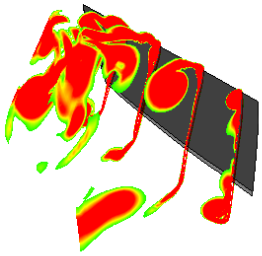

(h) Ψ = 64°

Figure 6.16: Vorticity magnitude contour at various instances of the forward stroke, 10% stiffness, cross spar case

6.5 Summary

The presented work is a continuation of the studies conducted in Chapter 5. The goal was to perform a parametric study using the coupled CFD/CSD solver to determine the influence of wing flexibility on wing performance. The structural and geometric properties from the anisotropic flexible flapping wing modeled in Chapter 5 were used as a baseline for the parametric study. The stiffness of the wing root and cross spars were varied in three groupings. In case 1, only the root spar stiffness was varied. In case 2, only the cross spar stiffness was varied. Lastly, in case 3, the stiffness of the root and cross spars were varied in conjunction. For all cases, the spar stiffness values were reduced to 75%, 50%, 25% and 10% of their nominal values. All simulations were conducted at a flap frequency of 6 Hz because it was at this frequency that performance characteristics began to plateau. The wing characteristics assessed include aerodynamic force time histories, wing pitch angle deformation and the vortical flowfield about the wing. The overall conclusions are as follows:

i. Overall, mean C_L values were seen to increased with decreased stiffness while mean C_D values were seen to decrease with decreased stiffness. For all three cases tested, lift-to-drag ratio and power loading are seen to increase with decreasing stiffness ratio down to a stiffness ratio of 25%. The case were both the root and cross spars are changed in conjunction exhibits the highest L/D and power loading for all stiffness ratios tested. The highest lift-to-drag ratio and power loading values occur at a stiffness ratio of 10% where L/D equals 1.0 and power loading equals 1.3. When comparing the predicted L/D and power loading at nominal stiffness values, a 10% stiffness ratio allows for an increase

in lift-to-drag ratio by 58.7% and an increase in power loading by 53.8%. It is important to note that at a stiffness ratio of 10%, the lift-to-drag ratio and power loading for the case where only the cross spar stiffness is varied decreases significantly.

ii. In analyzing the aerodynamic coefficient time histories, a stiffness ratio of 10% for cases 1 and 3 allowed for the temporal variation in lift to remain constant over a larger portion of the flap cycle. This resulted in greater average mean lift values compared to the nominal stiffness case. For case 2 at a 10% stiffness ratio, the temporal variation in the aerodynamic coefficients nearly match that of the nominal stiffness case which underperforms in comparison to the other hypothetical wings with lower structural stiffness.

iii. In comparing the sectional lift coefficient contours, case 3 at 10% stiffness allowed for greater lift production along the wing span as well as increased lift production throughout the flap cycle in comparison to the nominal case. Additionally, sectional drag coefficients were seen to be lower for case 3 at 10% stiffness relative to the 100% stiffness case. When just the cross spar stiffness is reduced to 25% EI, not only is there an increase in lift production at the wing root, which is counter-intuitive, but lift production is prolonged throughout the flap cycle. However, for the same case at a 10% stiffness ratio, the pattern of lift production resembles that of the nominal case and performance gains in lift drop off.

iv. In comparing the instantaneous pitch angle variations over time, the temporal variation of the pitch angle is similar across the span for the nominal stiffness

case with the peak magnitude of pitch angle increasing from root to tip. For case 3 at a 10% stiffness ratio, the variation in pitch angle at 0% and 25% span exhibits a singular peak during a flap stroke. However, at 50% and 75% span, the instantaneous pitch angle time history exhibits a double peak behavior over a flap stroke. This double peak behavior causes the direction of wing twist to change over the course of the flap stroke such that for a portion of the flap stroke pitch angle magnitude increases along the span from root to tip. This behavior is not seen in the nominal wing case were the magnitude of wing pitch is always decreasing from root to tip. For case 2 at a stiffness ratio of 25% the variation in pitch angle over time strongly correlates to the corresponding C_L time history. In case 2 at a stiffness ratio of 10%, the pitch angle time histories are similar to those of the nominal stiffness case.

v. In comparing the 100% stiffness case and case 3 at a stiffness ratio of 10%, it was seen that decreasing wing stiffness altered the formation of vortical structures about the wing particularly the LEV. The increased wing flexibility for more favorable wing twist along the wing span during flapping. This helped to prolong the sustainment of the LEV which in turn improves lift production. Compared to the nominal case, the LEV for case 3 at 10% stiffness was able to remain coherent and attached to the wing for a longer duration of the flap stroke. For case 2 at 10% stiffness ratio, the evolution of the flowfield was similar to the nominal stiffness case explaining the similar aerodynamic performance.

Chapter 7 Summary and Conclusions

7.1 Summary

A 3D, unsteady Reynolds-averaged Navier-Stokes solver (OVERTURNS) was coupled with a multi-body structural dynamics solver (MBDyn) to aid in the analysis of flapping wing problems with aeroelastic phenomena. The CFD solver was modified to facilitate in the propagation structural deformations applied at the wing surface throughout the CFD mesh via an inverse distance weighting (IDW) based scheme. The individual solvers as well as the coupled solver were validated against both experimental and computational studies. The validation studies consisted of in-house experimental tests as well as previous tests conducted by other researchers. Validation studies include:

1) Rigid bio-inspired wing with passive wing pitch
2) Flat plate undergoing single degree-of-freedom flapping
3) Zimmerman planform wing with structural compliance
4) Flexible isotropic rectangular planform wing in hover

Additional experimental and coupled CFD/CSD were conducted on a chordwise flexible wing with a carbon fiber wing covered by a mylar film. Experimental tests sought to measure the velocity about the wing using PIV as well as the passive wing deformations during flapping. The measured and predicted results were compared against one another.

Aerodynamic force-time history and passive wing deformation studies were conducted on an anisotropic flexible flapping wing modeled after the wing of a man-made flapping wing MAV. Accompanying CFD/CSD studies were performed on a

model of the anisotropic wing. Parametric studies on the anisotropic wing model were performed to investigate the effect of flexibility on wing performance. The major conclusions from the studies conducted are discussed in the next section.

7.2 Conclusions and Specific Contributions

The key conclusions from the series of validation and parametric studies are discussed below.

- **Rigid bio-inspired wing in hover:** The aerodynamic force-time histories predicted by the CFD solver correlate well with the experimental force-time histories for the translational pitch angles tested. The CFD solver was able to predict the salient flow features measured in the experimental PIV tests both spatially and temporally. Quantitatively, the CFD model was able to adequately capture the trend in LEV circulation strength over time measured during experimentation.
- **Flat plate undergoing single degree-of-freedom flap motion:** The CSD solver demonstrated the capability to model the large deformation of a thin flat plate subject to flapping motion prescribed at the root. The time history of vertical displacement at the tip of the flat plate agreed well with the computational results from other CSD solvers for the 5 Hz and 10 Hz flap frequencies. At a flap frequency of 30 Hz, the results tended to deviate from one another over time. This is mainly due to the highly nonlinear and chaotic wing deformations that occur at such a high flap frequency for this particular case.

- **Zimmerman planform wing with structural compliance:** The results predicted using the coupled CFD/CSD aeroelastic solver agreed well with the experimental and computational validation results for a wing with a small degree of structural compliance. There was excellent agreement with respect to the predicted wing tip displacement time histories. Similarly, good agreement was seen with respect to the lift coefficient time history. Additionally, there was satisfactory agreement of the predicted vorticity field, velocity field and velocity profiles with the experimental and computational validation data.
- **Flexible isotropic rectangular wing in hover:** Static and dynamic wing deformations predicted using the computational analysis correlated well with the experimental results for a set of wings with a significant level of structural compliance. The CFD/CSD solver was able to reasonably predict the trailing edge displacement of the wing as well as the instantaneous pitch angle variation over time. Computational studies show that using idealized kinematics may be sufficient for preliminary analysis. However, the measured experimental kinematics should be prescribed in the computational model to most accurately predict the deformation of the wing during flapping.
- **Chordwise flexible rectangular wing:** The coupled CFD/CSD model was able to predict the prominent aerodynamic flow features for the flexible flapping wing cases analyzed. The aeroelastic analysis demonstrated the ability to predict the general size, location and temporal evolution of the LEV for the various spanwise locations analyzed. The coupled aeroelastic analysis was able to adequately predict the passive wing deformations due to aerodynamic and

inertial forces. High frequency oscillations present in the experimental results were adequately captured in the computational results. At higher flap frequencies, there is a notable phase shift between the flapping motion and trailing edge deflection response. Instantaneous pitch angle variation results match well between the measured and predicted values. For a given flap frequency, the wing pitch angle variation was nearly uniform across the span of the wing throughout the flap cycle. The computational analysis was used to compare the lift, drag and aerodynamic power coefficient time histories for the flap frequencies tested. As expected, peak lift coefficient values increased with increased flap frequency. Peak aerodynamic power coefficients are nearly the same for all flap frequencies tested, however, the temporal variation differs between the cases tested. The 4 Hz case exhibits a double peak behavior while the 6 Hz and 8 Hz cases exhibit a single peak behavior within a given flap stroke.

- **Anisotropic flexible wing – Validation study:** The coupled CFD/CSD model was able to satisfactorily predict instantaneous aerodynamic lift and drag. Mean lift and drag values were seen to vary quadratically with flap frequency. The lift force-time history was well captured and for flap frequencies above 2 Hz, a periodic variation in the lift force-time history was observed. The peak magnitude in drag was underpredicted for all flap frequencies tested however, the temporal variation was well captured by the computational analysis. Predicted aerodynamic power time histories as well as mean aerodynamic power versus flap frequency trends agreed well with those measured during

experimentation. The magnitude of lift-to-power ratio was slightly underpredicted by the coupled CFD/CSD analysis, however, a plateau in lift-to-power ratio is seen in both the experimental and computational results. Results from the force measurement studies suggest that inertial force subtraction may be a viable means of determining the lift and aerodynamic power produced by a flexible flapping wing. However, measuring drag force proves difficult due to the larger inertial forces acting in the same direction as drag. The coupled aeroelastic analysis was able to adequately predict the passive wing deformations measured during flapping. The variation in instantaneous pitch angle matched well between the measured and predicted values. The pitch angle magnitude was slightly underpredicted especially toward outboard portions of the wing. The overall pitch angle variation correlated well with the variation in instantaneous lift suggesting that wing deformation significantly influence lift production.

- **Anisotropic flexible wing – Parametric study:** Overall, mean C_L values were seen to increase with decreased stiffness while mean C_D values were seen to decrease with decreased stiffness. For all three cases tested, lift-to-drag ratio and power loading are seen to increase with decreasing stiffness ratio down to a stiffness ratio of 25%. The case where both the root and cross spars are changed in conjunction exhibits the highest L/D and power loading for all stiffness ratios tested. In analyzing the aerodynamic coefficient time histories, a stiffness ratio of 10% for the case were the root and cross spar stiffness was varied allowed for the temporal variation in lift to remain constant over a larger

portion of the flap cycle. This resulted in greater average mean lift values compared to the nominal stiffness case. When analyzing the sectional lift coefficient contours, increased wing flexibility (i.e., reduced wing stiffness) allowed for greater lift production along the wing span as well as increased lift production throughout the flap cycle in comparison to the nominal case. Additionally, sectional drag coefficients were seen to be lower compared to the 100% stiffness case. However, these improvements in aerodynamic performance were not seen in the case where only the cross spar stiffness was reduced to 10% of its initial stiffness. In general, decreasing wing stiffness altered the formation of vortical structures about the wing especially the leading edge vortex. The increased wing flexibility allowed for a more favorable wing twist along the wing span during flapping. This helped to prolong the sustainment of the LEV which in turn improves lift production. Note that for the case where only the cross spar stiffness is reduced to 10% of its initial value, the development of the flowfield was similar to the nominal stiffness case explaining the similar aerodynamic performance.

The main contributions of this study toward the development and analysis of flapping wings are summarized below:

1. An inverse distance weighting scheme was implemented to manage the mesh deformation of structured, body-fitted curvilinear meshes in an efficient and robust manner. The efficacy of the scheme was demonstrated for a series of

different flexible flapping wing cases undergoing large, nonlinear deformations.

2. A range of experimental tests were conducted in air on a variety of structurally characterized flapping wings at MAV-scale. The experimental datasets include flowfield measurements via particle image velocimetry, passive wing deformation measurements via a VICON motion capture system and instantaneous wing force-time history measurements. The array of datasets provides experimental measurements against which to validate future computational analysis geared toward analyzing flexible flapping wings.

7.3 Recommendations for Future Work

The work presented in this dissertation is focused on furthering the development and analysis of flapping wings designs for micro air vehicles. While this dissertation presents experimental as well as computational means of investigating flapping wings, there are still additional areas of research to explore that would help to advance our understanding of the subject. In this section, future research topics are discussed that may help to further our understanding of flapping wing design.

1. The work presented in this dissertation focused on analyzing flexible flapping wings in the hover flight condition. However, a mission capable flapping wing MAV should be capable of efficient hover and forward flight. Parametric trade studies for a wing in hover as well as forward flight would provide insight into how wing design favors a given flight mode. Potential parameters to investigate

include the wing's flap kinematics, planform shape and the stiffness of its various structural members.

2. High-fidelity coupled CFD/CSD aeroelastic analysis provides a wealth of information when simulating the aeroelastic phenomena of flexible flapping wings. However, the high level of detailed information provided comes at the high computational cost. Currently, the limiting factor is the time associated with running fluid dynamics simulations using CPU-based Navier-Stokes solvers. The use of high-performance clusters helps to reduce simulation time but, requires a large financial investment and aren't widely available outside of large research or industrial institutions. The use of GPU-based Navier-Stokes solvers would greatly reduce computational time and the number of resources need to run coupled CFD/CSD simulations.
3. A number of experimental and numerical studies have looked into investigating flexible flapping wings and increase our understanding how wing compliance affects wing performance. While previous work has shown that for certain flight conditions, flexible wing outperform rigid wings. However, few studies have tried to determine if there is an ideal temporal variation in wing deformation for optimum hover performance of 3D flexible flapping wings. For example, rotor blades with hyperbolic twist and taper allow for optimum hover efficiency. Numerical studies can be conducted to help determine what combination of time-dependent wing twist and camber allows for more optimal hover efficiency. Studies could consist of prescribing wing twist and camber to a set

of flapping wings with representative planform shapes undergoing various flap kinematics.

4. The current coupled CFD/CSD solver could be combined with a trim algorithm to perform trim analysis for a flexible flapping wing. This would provide a truly comprehensive analysis (combining aerodynamics, structural dynamics and trim flight dynamics) to investigate how incorporating aeroelastic effects influences the trim of a flapping wing vehicle in hover as well as forward flight.
5. With respect to flapping wings, the design space of possible configurations is quite wide. Currently, accurate numerical exploration of the design space requires the use of high-fidelity CFD/CSD solvers, which have a high computational cost. Thus, parametric variations and trade studies may prove too costly in terms of time and computational resources to conduct for a wide range of design parameters. However, time-dependent adjoint-based CFD solvers may provide a means to determine optimal flapping wing designs in an acceptable amount of time. In contrast to other optimization techniques, the adjoint-based formulation allows for the computation of the sensitivity derivatives with respect to all design variables at a cost comparable to that of a single flow solution. This makes the time-dependent optimization of 3D turbulent flapping-wing flows feasible for practical applications. Optimization studies could consist of several design variables include flap kinematics, wing geometry, wing structural compliance and mass distribution throughout the wing structure. These optimization studies, performed using a high-fidelity aeroelastic analysis, can dramatically improve the performance and

fundamental understanding of current flapping wings. An adjoint-based optimization study provide insight into how flapping wing aeroelasticity affects performance and help to formulate a set of design principles for more efficient flapping MAVs.

Bibliography

[1]Taylor, J. W. R. and Munson, K., *Jane's pocket book of remotely piloted vehicles: robot aircraft today*. Collier Books, 1977.

[2]Donald, D., "U.S. Air Force Ends Predator Operations," *AIN Online*, 13-Mar-2018.

[3]"RQ-4 Global Hawk," *U.S. Air Force*, 27-Oct-2014. [Online]. Available: http://www.af.mil/About-Us/Fact-Sheets/Display/Article/104516/rq-4-global-hawk/. [Accessed: 16-Jul-2018].

[4]Ellis, F., "MQ-8B Fire Scout Data Sheet." Northrup Grumman Systems Corporation.

[5]Erwin, S. I., "Soaring Costs Not Likely to Slow Down Global Hawk," *National Defense*, 01-May-2006.

[6]McMichael, J. M. and Francis, M. S., "Micro Air Vehicles - Toward a New Dimension in Flight." Defense Advanced Research Projects Agency (DARPA), 07-Aug-1997.

[7]Ehley, B., "How Drones Could Help America's Infrastructure," *The Fiscal Times*, 03-Jul-2014.

[8]Clift, T., "Virginia Utility to Expand Use of Drones in Power Line Inspections," *Daily Press*, Newport News, VA, 04-Oct-2016.

[9]Mazur, M., "Six Ways Drone Are Revolutionizing Agriculture," *MIT Technology Review*, 20-Jul-2016.

[10]"Drones to venture into Fukushima containment vessels," *World Nuclear News*, London, England, 22-Mar-2018.

[11]Grasmeyer, J. M. and Keennon, M., "Development of the Black Widow micro air vehicle," presented at the 39th AIAA Aerospace Sciences Meeting and Exhibit, Reno, NV, 2001.

[12]Cosyn, P. and Vierendeels, J., "Design of fixed wing micro air vehicles," *The Aeronautical Journal*, vol. 111, no. 1119, pp. 315–326, May 2007.

[13]Woodside, P., "Skate SUAS Wins Border Security Product Challenge Award," *Aurora Flight Sciences - Public Relations*, Manassas, VA, 20-Mar-2012.

[14]"Wasp III," *U.S. Air Force*, 01-Nov-2007. [Online]. Available: http://www.af.mil/About-Us/Fact-Sheets/Display/Article/104480/wasp-iii/. [Accessed: 17-Jul-2018].

[15]Lian, Y., “Membrane and adaptively-shaped wings for micro air vehicles,” Doctor of philosophy, University of Florida, Department of Mechanical and Aerospace Engineering, Gainesville, Florida, 2003.

[16]Shyy, W., Ifju, P., and Viieru, D., “Membrane wing-based micro air vehicles,” *Applied Mechanics Review*, vol. 58, no. 4, pp. 283–301, Jul. 2005.

[17]DeLuca, A. M., Reeder, M. F., Freeman, J. A., and Ol, M. V., “Flexible-and rigid-wing micro air vehicle: lift and drag comparison,” *Journal of Aircraft*, vol. 43, no. 2, pp. 572–575, Mar. 2006.

[18]Gamble, B. and Reeder, M., “Experimental analysis of propeller-wing interactions for a micro air vehicle,” *Journal of Aircraft*, vol. 46, no. 1, pp. 65–73, Jan. 2009.

[19]Bohorquez, F. and Pines, D., “Hover performance of rotor blades at low Reynolds numbers for rotary wing micro air vehicles,” presented at the 2nd AIAA Unmanned Unlimited Systems Technologies and Operations, San Diego, CA, 2003.

[20]Bohorquez, F., Samuel, P., Sirohi, J., Pines, D., Rudd, L., and Perel, R., “Design, analysis, and hover performance of a rotary wing micro air vehicle,” *Journal of the American Helicopter Society*, vol. 48, no. 2, pp. 80–90, Apr. 2003.

[21]Sirohi, J., Tishchenko, M., and Chopra, I., “Design and testing of a micro aerial vehicle with a single rotor and turning vanes,” presented at the American Helicopter Society 61st Annual Forum Proceedings, Grapevine, TX, 2005.

[22]Hrishikeshavan, V., Sirohi, J., Tishchenko, M., and Chopra, I., “Design, development and testing of a shrouded single-rotor micro air vehicle with anti-torque vanes,” *Journal of the American Helicopter Society*, vol. 56, no. 1, Jan. 2011.

[23]Sanborn, J. K., “Marines Get a Closer Look at Black Hornet Micro Drone,” *Marine Corps Times*, Quantico, VA, 22-Sep-2015.

[24]Bouabdallah, S. *et al.*, “Towards palm-size autonomous helicopters,” *Journal of Intelligent and Robotic Systems*, vol. 61, no. 1–4, pp. 445–471, Jan. 2011.

[25]Fankhauser, P., Bouabdallah, S., Leutenegger, S., and Siegwart, R., “Modeling and decoupling control of the coax micro helicopter,” presented at the IEEE/RSJ International Conference on Intelligent Robots and Systems, San Francisco, CA, 2011.

[26]Wang, F., Wang, T., Chen, B. M., and Lee, T. H., “An indoor unmanned coaxial rotorcraft system with vision positioning,” presented at the 8th IEEE International Conference, Xiamen, China, 2010.

[27]George, S. and Samuel, P., “On the design and development of a coaxial nano rotorcraft,” presented at the 50th AIAA Aerospace Sciences Meeting Including the New Horizons Forum and Aerospace Exposition, Nashville, TN, 2012.

[28]Bohorquez, F., "Rotor hover performance and system design of an efficient coaxial rotary wing micro air vehicle," Doctor of philosophy, University of Maryland, Department of Aerospace Engineering, College Park, MD, 2007.

[29]Samuel, P., Sirohi, J., Rudd, L., Pines, D., and Perel, R., "Design and development of a micro coaxial rotorcraft," presented at the Proceedings of the AHS Vertical Lift Aircraft Design Conference, Alexandria VA, 2000.

[30]Paulos, J. and Yim, M., "Flight performance of a swashplateless micro air vehicle," presented at the 2015 IEE International Conference on Robotics and Automation, Seattle WA, 2015.

[31]"Parrot Drones SAS." [Online]. Available: https://www.parrot.com/us/drones/parrot-bebop-2#parrot-bebop-2-details. [Accessed: 19-Jul-2018].

[32]"Spreading Wings S900." [Online]. Available: https://www.dji.com/spreading-wings-s900. [Accessed: 19-Jul-2018].

[33]"Snipe Nano UAS." [Online]. Available: https://www.avinc.com/images/uploads/product_docs/Snipe_Datasheet_2018_Web.pdf. [Accessed: 19-Jul-2018].

[34]Ulrich, E., "Design, development, analysis and control of a bio-inspired robotic samara rotorcraft," Doctor of philosophy, University of Maryland, Department of Aerospace Engineering, College Park, MD, 2012.

[35]Benedict, M., "Fundamental understanding of the cycloidal-rotor concept for micr air vehicle applications," Doctor of philosophy, University of Maryland, Department of Aerospace Engineering, College Park, MD, 2010.

[36]Jarugumilli, T., "An experimental investigation of a micro air vehicle-scale cycloidal rotor in forward flight," Master of Science, University of Maryland, Department of Aerospace Engineering, College Park, MD, 2013.

[37]Shrestha, E., Hrishikeshavan, V., Benedict, M., Yeo, D., and Chopra, I., "Development of control strategies for a twin-cyclocopter in forward flight," *Journal of the American Helicopter Society*, vol. 61, no. 4, pp. 1–9, Oct. 2016.

[38]Pines, D. and Bohorquez, F., "Challenges facing future micro-air-vehicle development," *Journal of Aircraft*, vol. 43, no. 2, pp. 290–305, Mar. 2006.

[39]Shyy, W., Aono, H., Chimakurthi, S., Trizila, P., Kang, C., Cesnik, C., and Liu, H., "Recent progress in flapping wing aerodynamics and aeroelasticity," *Progress in Aerospace Sciences*, vol. 46, pp. 284–327, 2010.

[40]Mueller, T., “Aerodynamic measurements at low Reynolds numbers for fixed wing micro-air-vehicles,” Notre Dame Univ., Dept. of Aerospace and Mechanical Engineering, 2000.

[41]Brown, R. H. J., “The flight of birds - II. Wing function in relation to flight speed,” *Journal of Experimental Biology*, vol. 30, no. 1, pp. 90–103, Mar. 1953.

[42]Roget, B., Sitaraman, J., Harmon, R., Grauer, J., Hubbard, J., and Humbert, S., “Computational study of flexible wing ornithopter flight,” *Journal of Aircraft*, vol. 46, no. 6, pp. 2016–2031, Dec. 2009.

[43]Kinkade, A. S., “Ornithopter,” 0173217, 21-Nov-2002.

[44]Gerdes, J. *et al.*, “Robo Raven: A flapping-wing air vehicle with highly compliant and independently controlled wings,” *Soft Robotics*, vol. 1, no. 4, pp. 275–288, Dec. 2014.

[45]Pornsin-Sirirak, T. N., Tai, Y.-C., Ho, C.-M., and Keennon, M., “Microbat: A palm-sized electrically powered ornithopter,” presented at the Proceedings of NASA/JPL Workshop on Biomorphic Robotics, 2001.

[46]de Croon, G. C. H. E., de Clercq, K. M. E., Ruijsink, R., Remes, B., and de Wagter, C., “Design, aerodynamics and vision-based control of the DelFly,” *International Journal of Micro Air Vehicles*, vol. 1, no. 2, pp. 71–97, Jun. 2009.

[47]Badrya, C., Sridharan, A., Baeder, J., and Kroninger, C., “Multi-fidelity coupled trim analysis of a flapping-wing micro air vehicle flight,” *Journal of Aircraft*, vol. 54, no. 5, pp. 1614–1630, Jan. 2017.

[48]Zdunich, P. *et al.*, “Development and testing of the Mentor flapping-wing micro air vehicle,” *Journal of Aircraft*, vol. 44, no. 5, pp. 1701–1711, Sep. 2007.

[49]de Croon, G. C. H. E., Percin, M., Remes, B., Ruijsink, R., and de Wagter, C., “Introduction to Flapping Wing Design,” in *The Delfly*, Springer, Dordrecht, 2016.

[50]Wood, R. J., “The first takeoff of a biologically inspired at-scale robotic insect,” *IEEE transactions on robotics*, vol. 24, no. 2, pp. 341–347, Apr. 2008.

[51]Keennon, M., Klingebiel, K., Won, H., and Andriukov, A., “Development of the Nano Hummingbird: A tailless flapping wing micro air vehicle,” presented at the 50th AIAA Aerospace Sciences Meeting Including the New Horizons Forum and Aerospace Exposition, Nashville, TN, 2012.

[52]Coleman, D., Benedict, M., Hrishikeshavan, V., and Chopra, I., “Design, development and flight-testing of a robotic hummingbird,” presented at the American Helicopter Society 71st Annual Forum, 2015.

[53]Gaissert, N., Mugrauer, R., Mugrauer, G., Jebens, A., Jebens, K., and Knubben, E. M., “Inventing a micro aerial vehicle inspired by the mechanics of dragonfly flight,” presented at the Conference Towards Autonomous Robotic Systems, 2013, pp. 90–100.

[54]Anderson Jr, J. D., *Fundamentals of Aerodynamics*, 2nd ed. McGraw-Hill, 1991.

[55]McMasters, J. H. and Henderson, M. L., “Low-speed single-element aifoil synthesis,” Boeing Commericial Airplane Company, Seattle WA, Technical Report 19790015719, 1979.

[56]Mayo, D. and Leishman, J. G., “Comparison of the hovering efficiency of rotating wing and flapping wing micro air vehicles,” *Journal of the American Helicopter Society*, vol. 55, no. 2, p. 025001, Apr. 2010.

[57]Laitone, E., “Wind tunnel tests of wings at Reynolds numbers below 70000,” *Experiments in Fluids*, vol. 23, no. 5, pp. 405–409, Nov. 1997.

[58]Hein, B. and Chopra, I., “Hover performance of a micro air vehicle: Rotors at low Reynolds number,” *Journal of the American Helicopter Society*, vol. 52, no. 3, pp. 254–262, Jul. 2007.

[59]Dickinson, M., “Insect flight,” *Current Biology*, vol. 16, no. 9, pp. 309–314, 2006.

[60]Ward, T. A., Fearday, C. J., Salami, E., and Soin, N. B., “A bibliometric review of progress in micro air vehicle research,” *International Journal of Micro Air Vehicles*, vol. 9, no. 2, pp. 146–165, Jun. 2017.

[61]Weis-Fogh, T., “Quick estimates of flight fitness in hovering animals, including novel mechanisms for lift production,” *Journal of Experimental Biology*, vol. 59, no. 1, pp. 169–230, Aug. 1973.

[62]Ellington, C. P., “The aerodynamics of hovering insect flight. I. The quasi-steady analysis,” *Philosophical Transactions of the Royal Society B*, vol. 305, no. 1122, pp. 1–15, Feb. 1984.

[63]Ellington, C. P., “The aerodynamics of hovering insect flight. II. Morphological parameters,” *Philosophical Transactions of the Royal Society B*, vol. 305, no. 1122, pp. 17–40, Feb. 1984.

[64]Ellington, C. P., “The aerodynamics of hovering insect flight. III. Kinematics,” *Philosophical Transactions of the Royal Society B*, vol. 305, no. 1122, pp. 41–78, Feb. 1984.

[65]Ellington, C. P., “The aerodynamics of hovering insect flight. IV. Aerodynamic mechanisms,” *Philosophical Transactions of the Royal Society B*, vol. 305, no. 1122, pp. 79–113, Feb. 1984.

[66]Ellington, C. P., "The aerodynamics of hovering insect flight. V. A vortex theory," *Philosophical Transactions of the Royal Society B*, vol. 305, no. 1122, pp. 115–144, Feb. 1984.

[67]Ellington, C. P., "The aerodynamics of hovering insect flight. VI. Lift and power requirements," *Philosophical Transactions of the Royal Society B*, vol. 305, no. 1122, pp. 145–181, Feb. 1984.

[68]Francis, R. H. and Cohen, J., "The flow near a wing which starts suddenly from rest and then stalls," *Reports and Memoranda of the Aeronautical Research Committee*, no. 1561.

[69]Kramer, V. M., "Die Zunahme des Maximalauftriebes von TragflugeIn bei plotzlicher," *Z. Flugtech. Motorluftschiff*, vol. 23, pp. 185–189, Apr. 1932.

[70]McCroskey, W. J. and Fisher, R. K., "Detailed aerodynamic measurements on a model rotor in the blade stall regime," *Journal of the American Helicopter Society*, vol. 17, no. 1, pp. 20–30, 1972.

[71]Ericsson, L. E. and Reding, J. P., "Dynamic stall of helicopter blades," *Journal of the American Helicopter Society*, vol. 17, no. 1, pp. 10–19, 1972.

[72]Tarzanin, F. J., "Prediction of control loads due to blade stall," *Journal of the American Helicopter Society*, vol. 17, no. 2, pp. 33–46, 1972.

[73]Beddoes, T. S., "A synthesis of unsteady aerodynamic effects including stall hysteresis," *Vertica*, vol. 1, pp. 113–123, 1976.

[74]Leishman, J. G., *Principles of Helicopter Aerodynamics*. Cambridge University Press, 2006.

[75]Srygley, R. B. and Thomas, A. L. R., "Unconventional lift-generating mechanisms in free-flying butterflies," *Nature*, vol. 420, no. 6916, pp. 660–664, Dec. 2002.

[76]Ennos, A. R., "The importance of torsion in the design of insect wings," *Journal of Experimental Biology*, vol. 140, no. 1, pp. 137–160, Nov. 1988.

[77]Ennos, A. R., "The kinematics and aerodynamics of the free flight of some Diptera," *Journal of Experimental Biology*, vol. 142, no. 1, pp. 49–85, Mar. 1989.

[78]Ennos, A. R., "The inertial cause of wing rotation in diptera," *Journal of Experimental Biology*, vol. 140, no. 1, pp. 161–169, Nov. 1988.

[79]Combes, S. A. and Daniel, T. L., "Flexural stiffness in insect wings I. Scaling and the influence of wing venation," *Journal of Experimental Biology*, vol. 206, no. 17, pp. 2979–2987, Sep. 2003.

[80]Dickinson, M. H. and Gotz, K., "Unsteady aerodynamic performance of model wings at low Reynolds numbers," *Journal of Experimental Biology*, vol. 174, no. 1, pp. 45–64, Jan. 1993.

[81]Polhamus, E. C., "A concept of the vortex lift of sharp-edge delta wings based on a leading-edge suction analogy," NASA Langley Research Center, Hampton, VA, Technical Note D-3767, Dec. 1966.

[82]Ellington, C. P., Van Den Berg, C., Willmott, A. P., and Thomas, A., "Leading-edge vortices in insect flight," *Nature*, vol. 384, pp. 626–630, 1996.

[83]Ellington, C. P., "The novel aerodynamics of insect flight: applications to micro air vehicles," *Journal of Experimental Biology*, vol. 202, no. 23, pp. 3439–3448, Dec. 1999.

[84]Birch, J., Dickson, W. B., and Dickinson, M. H., "Force production and flow structure of the leading edge vortex on flapping wings at high and low Reynolds numbers," *Journal of Experimental Biology*, vol. 207, no. 7, pp. 1063–1072, Mar. 2004.

[85]Shyy, W. and Liu, H., "Flapping wings and aerodynamic lift: The role of leading-edge vortices," *AIAA Journal*, vol. 45, no. 12, pp. 2817–2819, Dec. 2007.

[86]Wojcik, C. and Buchholz, J., "Parameter variation and the leading-edge vortex of a rotating flat plate," *AIAA Journal*, vol. 52, no. 2, pp. 348–357, Jan. 2014.

[87]Stevens, P. *et al.*, "Experiments and computations of the lift of accelerating flat plates at incidence," *AIAA Journal*, Jul. 2017.

[88]Manar, F. and Jones, A., "Transient response of a single degree-of-freedom wing at high angle-of-attack and low Reynolds number," *AIAA Journal*, vol. 55, no. 11, pp. 3681–3692, Nov. 2017.

[89]Dickinson, M., Lehmann, F.-O., and Sane, S., "Wing rotation and the aerodynamic basis of insect flight," *Science*, vol. 284, no. 5422, pp. 1954–1960, Jun. 1999.

[90]Sane, S. and Dickinson, M. H., "The aerodynamic effects of wing rotation and a revised quasi-steady model of flapping flight," *Journal of Experimental Biology*, vol. 205, no. 8, pp. 1087–1096, Apr. 2002.

[91]Tuncer, I. H. and Platzer, M. F., "Thrust generation due to airfoil flapping," *AIAA Journal*, vol. 34, no. 2, pp. 324–331, Feb. 1996.

[92]Tuncer, I. H. and Platzer, M. F., "Computational study of flapping airfoil aerodynamics," *Journal of Aircraft*, vol. 37, no. 3, pp. 514–520, May 2000.

[93]Kang, C., Baik, Y., Bernal, L., Ol, M., and Shyy, W., "Fluid dynamics of pitching and plunging airfoils of Reynolds number between 10000 and 60000," presented at

the 47th AIAA Aerospace Sciences Meeting including The New Horizons Forum and Aerospace Exposition, 2009.

[94]Ashraf, M., Young, J., and Lai, J. C. S., "Reynolds number, thickness and camber effects on flapping airfoil propulsion," *Journal of Fluids and Structures*, vol. 27, no. 2, pp. 145–160, Feb. 2011.

[95]Sane, S., "The aerodynamics of insect flight," *Journal of Experimental Biology*, vol. 206, no. 23, pp. 4191–4208, Dec. 2003.

[96]Yuan, W., Lee, R., Hoogkamp, E., and Khalid, M., "Numerical and experimental simulations of flapping wings," *International Journal of Micro Air Vehicles*, vol. 2, no. 3, pp. 181–209, Sep. 2010.

[97]Birch, J. and Dickinson, M., "Spanwise flow and the attachment of the leading-edge vortex on insect wings," *Nature*, vol. 412, pp. 729–733.

[98]Sane, S. and Dickinson, M. H., "The control of flight force by a flapping wing: lift and drag production," *Journal of Experimental Biology*, vol. 204, no. 15, pp. 2607–2626, 2001.

[99]Willmott, A. P., Ellington, C. P., and Thomas, A., "Flow visualization and unsteady aerodynamics in the flight of the hawkmoth, Manduca sexta," *Philosophical Transactions of the Royal Society B: Biological Sciences*, vol. 352, no. 1351, pp. 303–316, 1997.

[100]Van Den Berg, C. and Ellington, C. P., "The three-dimensional leading-edge vortex of a 'hovering' model hawkmoth," *Philosophical Transactions of the Royal Society B: Biological Sciences*, vol. 352, no. 1351, pp. 329–340, 1997.

[101]Lentink, D. and Dickinson, M. H., "Rotational accelerations stabilize leading edge vortices on revoling fly wings," *Journal of Experimental Biology*, vol. 212, no. 16, pp. 2705–2719, Aug. 2009.

[102]Seshadri, P., Benedict, M., and Chopra, I., "Understanding micro air vehicle flapping-wing aerodynamics using force and flowfield measurements," *Journal of Aircraft*, vol. 50, no. 4, pp. 1070–1087, Jul. 2013.

[103]Liu, H. and Kawachi, K., "A numerical study of insect flight," *Journal of Computational Physics*, vol. 146, no. 1, pp. 124–156, 1998.

[104]Liu, H., Ellington, C. P., Kawachi, K., Van Den Berg, C., and Willmott, A. P., "A computational fluid dynamics study of hawkmoth hovering," *Journal of Experimental Biology*, vol. 201, no. 4, pp. 461–477, 1998.

[105]Sun, M. and Tang, J., "Unsteady aerodynamic force generation by a model fruit fly wing in flapping motion," *Journal of Experimental Biology*, vol. 205, no. 1, pp. 55–70, 2002.

[106]Ramamurti, R. and Sandberg, W., "Computational study of 3-D flapping foil flows," presented at the 39th Aerospace Sciences Meeting and Exhibit, Reno, NV, 2001.

[107]Badrya, C., Baeder, J., Amiraux, M., and Kroninger, C., "Parametric study of insect flapping performance using CFD," presented at the Fifth decennial AHS aeromechanics specialists' conference, Scottsdale, AZ, 2014.

[108]Zhang, H., Wen, C., and Yang, A., "Optimization of lift force for a bio-inspired flapping wing model in hovering flight," *International Journal of Micro Air Vehicles*, vol. 8, no. 2, pp. 92–108, May 2016.

[109]Jones, M. and Yamaleev, N., "Adjoint-based shape and kinematics optimization of flapping wing propulsive efficiency," presented at the 43rd AIAA Fluid Dynamics Conference, San Diego, CA, 2013.

[110]Heathcote, S., Wang, Z., and Gursul, I., "Effect of spanwise flexibility on flapping wing propulsion," *Journal of Fluids and Structures*, vol. 24, no. 2, pp. 183–199, 2008.

[111]Chimakurthi, S., Tang, J., Palacios, R., Cesnik, C., and Shyy, W., "Computational aeroelastic framework for analyzing flapping wing micro air vehicles," *AIAA Journal*, vol. 47, no. 8, pp. 1865–1878, Aug. 2009.

[112]Gordnier, R., Chimakurthi, S., Cesnik, C., and Attar, P., "High-fidelity aeroelastic computations of a flapping wing with spanwise flexibility," presented at the 49th AIAA Aerospace Sciences Meeting including the New Horizons Forum and Aerospace Exposition, Orlando, FL, 2011.

[113]Malhan, R., Lakshminarayan, V., Baeder, J., Chopra, I., Masarati, P., Morandini, M., and Quaranta, G., "CFD-CSD coupled aeroelastic analysis of flexible flapping wings for MAV applications: Methodology validation," presented at the 53rd AIAA/ASME/ASCE/AHS/ASC Structures, Structural Dynamics and Materials Conference, Honolulu, HI, 2012.

[114]Toomey, J. and Eldredge, J. D., "Numerical and experimental study of the fluid dynamics of a flapping wing with low order flexibility," *Physics of Fluids*, vol. 20, no. 7, p. 073603, May 2008.

[115]Heathcote, S., Martin, D., and Gursul, I., "Flexible flapping airfoil propulsion at zero freestream velocity," *AIAA Journal*, vol. 42, no. 11, pp. 2196–2204, Nov. 2004.

[116]Yin, B. and Luo, H., "Effect of wing inertia on hovering performance of flexible flapping wings," *Physics of Fluids*, vol. 22, no. 11, p. 111902, Nov. 2010.

[117]Sridhar, M. and Kang, C., "Aerodynamic performance of flexible flapping wings at bumblebee scale in hover flight," presented at the 53rd AIAA Aerospace Sciences Meeting, Kissimmee, FL, 2015.

[118]Hua, R.-N., Zhu, L., and Lu, X.-Y., "Locomotion of a flapping flexible plate," *Physics of Fluids*, vol. 25, no. 12, p. 121901, Dec. 2013.

[119]Walker, S. M., Thomas, A., and Taylor, G. K., "Deformable wing kinematics in free-flying hoverflies," *Journal of the Royal Society Interface*, vol. 7, no. 42, pp. 131–142, May 2009.

[120]Wu, P., Ifju, P., and Stanford, B., "Flapping wing structural deformation and thrust correlation study with flexible membrane wings," *AIAA Journal*, vol. 48, no. 9, pp. 2111–2122, Sep. 2010.

[121]Malhan, R., Benedict, M., and Chopra, I., "Experimental studies to understand the hover and forward flight performance of a MAV-scale flapping wing concept," *Journal of the American Helicopter Society*, vol. 57, no. 2, pp. 1–11, Apr. 2012.

[122]Singh, B. and Chopra, I., "Insect-Based hover-capable flapping wings for micro air vehicles: Experiments and analysis," *AIAA Journal*, vol. 46, no. 9, pp. 2115–2135, Sep. 2008.

[123]Willis, D. J., Israeli, E. R., Persson, P.-O., Drela, M., and Peraire, J., "A computational framework for fluid structure interaction in biologically inspired flapping flight," presented at the 25th AIAA Applied Aerodynamics Conference, Miami, FL, 2007.

[124]Vanella, M., Fitzgerald, T., Preidikman, S., Balaras, E., and Balachandran, B., "Influence of flexibility on the aerodynamic performance of a hovering wing," *Journal of Experimental Biology*, vol. 212, no. 1, pp. 95–105, Jan. 2009.

[125]Fitzgerald, T., Valdez, M., Vanella, M., Balaras, E., and Balachandran, B., "Flexible flapping systems: computational investigations into fluid-structure interactions," *The Aeronautical Journal*, vol. 115, no. 1172, pp. 593–604, Oct. 2011.

[126]Roccia, B., Preidikman, S., and Balachandran, B., "Computational dynamics of flapping wings in hover flight: A co-simulation strategy," *AIAA Journal*, vol. 55, no. 6, pp. 1806–1822, Apr. 2017.

[127]Preidikman, S., Roccia, B., Verstraete, M., Valdez, M., Mook, D., and Balachandran, B., "Computational aeroelasticity of flying robots with flexible wings," in *Aerial Robots - Aerodynamics, Control and Applications*, InTech, 2017.

[128]Chimakurthi, S., Stanford, B., Cesnik, C., and Shyy, W., "Flapping wing CFD/CSD aeroelastic formulation based on co-rotational shell finite element,"

presented at the 50th AIAA/ASME/AHS/ASC Structures, Structural Dynamics and Materials Conference, Palm Springs, CA, 2009.

[129]Mayo, D., Lankford, J., Benedict, M., and Chopra, I., "Experimental and computational analysis of rigid flapping wings for micro air vehicles," *Journal of Aircraft*, vol. 52, no. 4, pp. 1161–1178, Jul. 2015.

[130]Mayo, D., Lankford, J., Benedict, M., and Chopra, I., "Aeroelastic analysis of avian-based flexible flapping wings for micro air vehicles," *Journal of the American Helicopter Society*, vol. 60, no. 3, pp. 1–18, Jul. 2015.

[131]Lakshminarayan, V., "Computational investigation of micro-scale coaxial rotor aerodynamics in hover," Doctor of philosophy, University of Maryland, Department of Aerospace Engineering, College Park, MD, 2009.

[132]Amiraux, M., "Numerical simulation and validation of helicopter blade-vortex interaction using coupled CFD/CSD and the levels of aerodynamic modeling," Doctor of philosophy, University of Maryland, Department of Aerospace Engineering, College Park, MD, 2014.

[133]Barth, T., Pulliam, T., and Buning, P., "Navier-Stokes computations for exotic airfoils," presented at the 23rd Aerospace Sciences Meeting, Reno, NV, 1985.

[134]Duraisamy, K., "Studies in tip vortex formation, evolution and control," Doctor of philosophy, University of Maryland, Department of Aerospace Engineering, College Park, MD, 2005.

[135]Lee, Y., "On overset grids connectivity and vortex tracking in rotorcraft CFD," Doctor of philosophy, University of Maryland, Department of Aerospace Engineering, College Park, MD, 2008.

[136]White, F. and Corfield, I., *Viscous Fluid Flow*, vol. 3. New York: McGraw-Hill, 2006.

[137]Van Leer, B., "Towards the ultimate conservative difference scheme V. A second-order sequel to Godunov's method," *Journal of Computational Physics*, vol. 135, no. 2, pp. 229–248, Aug. 1997.

[138]Koren, B., "Upwind schemes, multigrid and defect correction for the steady Navier-Stokes equations," presented at the Proceedings of the 11th International Conference on Numerical Methods in Fluid Dynamics, Williamsburg, VA, 1988, pp. 344–348.

[139]Roe, P., "Approximate Riemann solvers, parameter vectors and difference schemes," *Journal of Computational Physics*, vol. 135, no. 2, pp. 250–258, Aug. 1997.

[140]Jameson, A. and Yoon, S., "Lower-Upper implicit schemes with multiple grids for the euler equations," *AIAA Journal*, vol. 25, no. 7, pp. 929–935, Jul. 1987.

[141]Yoon, S. and Jameson, A., "Lower-Upper Symmetric-Gauss-Seidel method for the Euler adn Navier-Stokes equations," *AIAA Journal*, vol. 26, no. 9, pp. 1025–1026, Sep. 1988.

[142]Pulliam, T., "Time accuracy and the use of implicit methods," presented at the 11th Computational Fluid Dynamics Conference, Orlando, FL, 1993, p. 3360.

[143]Spalart, P. and Allmaras, S., "A one-equation turbulence model for aerodynamic flows," presented at the 30th AIAA Aerospace Sciences Meeting & Exhibit, Reno, NV, 1992.

[144]Turkel, E., "Preconditioning techniques in computational fluid dynamics," *Annual Review of Fluid Mechanics*, vol. 31, no. 1, pp. 385–416, Jan. 1999.

[145]Buelow, P., Schwer, D., Feng, J., and Merkle, C., "A preconditioned dual-time, diagonalized ADI scheme for Unsteady Computations," presented at the 13th AIAA Computational Fluid Dynamics Conference, Snowmass Village CO, 1997.

[146]Pandya, S., Venkateswaran, S., and Pulliam, T., "Implementation of preconditioned dual-time procedures in OVERFLOW," presented at the 41st AIAA Aerospace Sciences Meeting and Exhibit, Reno, NV, 2003.

[147]Masarati, P., Morandini, M., and Mantegazza, P., "An efficient formulation for general-purpose multibody/multiphysics analysis," *Journal of Computational and Nonlinear Dynamics*, vol. 9, no. 4, pp. 1–9, Oct. 2014.

[148]Masarati, P., "Comprehensive multibody aeroservoelastic analysis of integrated rotorcraft active controls," Doctor of philosophy, Politecnico di Milano, Dipartimento di Ingegneria Aerospaziale, Milano, Italy, 2000.

[149]Masarati, P. and Mantegazza, P., "On the C0 discretisation of beams by finite elements and finite volumes," *L'Aerotecnica, missili e spazio*, vol. 75, no. 4, pp. 77–86, Jul. 1996.

[150]Ghiringhelli, G. L., Masarati, P., and Mantegazza, P., "Multibody implementation of finite volume C0 beams," *AIAA Journal*, vol. 38, no. 1, pp. 131–138, Jan. 2000.

[151]Witkowski, W., "4-Node combined shell element with semi-EAS-ANS strain interpolations in 6-parameter shell theories with drilling degrees of freedom," *Journal of Computational Mechanics*, vol. 43, no. 2, pp. 307–319, Jan. 2009.

[152]Merlini, T. and Morandini, M., "The helicoidal modeling in computational finite elasticity. Part I: Variational formulation," *International Journal of Solids and Structures*, vol. 41, no. 18–19, pp. 5351–5381, Sep. 2004.

[153]Pietraszkiewicz, W. and Eremeyev, V. A., "On natural strain measures of the nonlinear micropolar continuum," *International Journal of Solids and Structures*, vol. 46, no. 3–4, pp. 774–787, Feb. 2009.

[154]Morandini, M. and Masarati, P., "Implementation and validation of a 4-node shell finite element," presented at the ASME 2014 International Design Engineering Technical Conferences, Buffalo, NY, 2014.

[155]Quaranta, G., Masarati, P., and Mantegazza, P., "A conservative mesh-free approach for fluid-structure interface problems," presented at the International Conference on Computational Methods for Coupled Problems in Science and Engineering, Barcelona, Spain, 2005.

[156]Shepard, D., "A two-dimensional interpolation function for irregularly-space data," presented at the Association for Computing Machinary National Conference, 1968.

[157]Witteveen, J. and Bijl, H., "Explicit mesh deformation using inverse distance weighting interpolation," presented at the 19th AIAA Computational Fluid Dynamics, San Antonio, TX, 2009.

[158]Witteveen, J., "Explicit and robust inverse distance weighting mesh deformation for CFD," presented at the 48th AIAA Aerospace Sciences Meeting Including the New Horizons Forum and Aerospace Exposition, Orlando, FL, 2010.

[159]Luke, E., Collins, E., and Blades, E., "A fast mesh deformation method using explicit interpolation," *Journal of Computational Physics*, vol. 231, no. 2, pp. 586–601, Jan. 2012.

[160]Uyttersprot, L., "Inverse distance weighting mesh deformation: A robust and efficient method for unstructured meshes," Master of Science, Delft University of Technology, Department of Aerospace Engineering, Delft, Netherlands, 2014.

[161]Shoemake, K., "Animating rotation with quaternion curves," *ACM SIGGRAPH*, vol. 19, no. 3, pp. 245–254, Jul. 1985.

[162]Benedict, M., Coleman, D., Mayo, D., and Chopra, I., "Experiments on rigid wing undergoing hover-capable flapping kinematics at micro-air-vehicle-scale Reynolds numbers," *AIAA Journal*, vol. 54, no. 4, pp. 1145–1157, Apr. 2016.

[163]Wu, J. H. and Sun, M., "Unsteady aerodynamic forces of a flapping wing," *Journal of Experimental Biology*, vol. 207, no. 7, pp. 1137–1150, Mar. 2004.

[164]Aono, H., Chimakurthi, S., Wu, P., Sallstrom, E., Cesnik, C., Ifju, P., Ukeiley, L., and Shyy, W., "A computational and experimental study of flexible flapping wing aerodynamics," presented at the 48th AIAA Aerospace Sciences Meeting Including the New Horizons Forum and Aerospace Exposition, Orlando, FL, 2010, pp. 1–22.

[165]Funabashi, H. and Freudenstein, F., "Performance criteria for high-speed crank-and-rocker linkages - Part I: Plane crank-and-rocker linkages," *Journal of Mechanical Design*, vol. 101, no. 1, pp. 20–25, Jan. 1979.

[166]"Standard Test Method for Tensile Properties of Plastics," ASTM International, West Conshohocken, PA, ASTM Standard D638-14, 2015.

[167]Stanford, B., Miranda, J., Parker, G., and Beran, P., "The complicating effect of uncertain flapping wing kinematics on model validation," *International Journal of Micro Air Vehicles*, vol. 3, no. 3, pp. 143–148, Aug. 2011.

[168]Masarati, P., "Direct eigenanalysis of constrained system dynamics," *Institution of Mechanical Engineers*, vol. 223, no. 4, pp. 335–342, Jul. 2009.

[169]Combes, S. A. and Daniel, T. L., "Into thin air: contributions of aerodynamic and inertial-elastic forces to wing bending in the hawkmoth Manduca sexta," *Journal of Experimental Biology*, vol. 206, no. 17, pp. 2999–3006, Sep. 2003.